

PENN

CENTER for

MUSCULOSKELETAL

DISORDERS

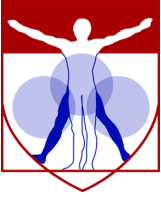
14th Annual Scientific Symposium/Retreat

Wednesday, November 15, 2017
BRB II/III Auditorium and Lobby
8:00am-6:30pm
www.med.upenn.edu/pcmd/

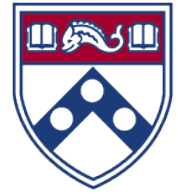
Table of Contents

	Page
Symposium Agenda.....	1
Penn Center for Musculoskeletal Disorders Components.....	2-12
Center Overview.....	2-3
Core I-Biomechanics.....	4
Core II-Histology.....	5
Core III-MicroCT.....	6
Pilot Grant Program.....	7-11
Visiting Professorship Series.....	12
Symposium Participants.....	13-17
Speaker Abstracts.....	18-27
Other Abstracts.....	P1-P74
Biomechanics.....	P1-P17
Histology.....	P18-P37
MicroCT.....	P38-P51
Miscellaneous.....	P52-P74
Notes.....	

We gratefully acknowledge the financial support provided by the National Institute of Arthritis, Musculoskeletal and Skin Diseases of the National Institutes of Health and the University of Pennsylvania Perelman School of Medicine for our Center.



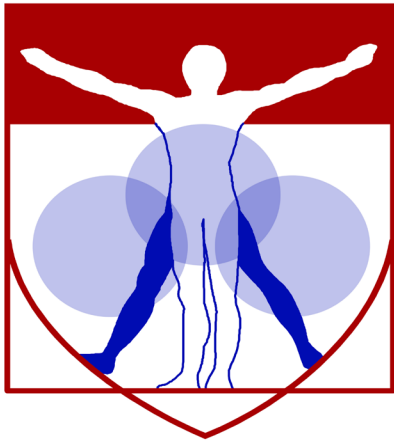
Penn Center for Musculoskeletal Disorders Scientific Symposium Agenda



November 15, 2017

BRB II/III Auditorium/Lobby ♦ University of Pennsylvania

- 8:00 – 9:00am **Registration and Poster Set-up**
- 9:00 – 9:20am **Welcome and Overview**
Louis J. Soslowsky, Ph.D.
- 9:20 – 10:20am **Session I: Affiliate Member Session** (Moderator: Robert Mauck, Ph.D.)
- ♦ *Evangelia Bellas, Ph.D., Temple University, “Engineering Adipose Tissue”*
 - ♦ *Megan Killian, Ph.D., University of Delaware, “The Role of Fibroblast Growth Factor Signaling during Tendon-Bone”*
 - ♦ *Lin Han, Ph.D., Drexel University, “Roles of Type V Collagen in TMJ Function and Disorder”*
- 10:20 – 11:05am **Poster Session (Even Numbered) and Break**
- 11:05 – 12:05pm **Session II: Pilot Grantee Session** (Moderator: Maurizio Pacifici, Ph.D.)
- ♦ *Chamith Rajapakse, Ph.D., “Assessment of Osteoporotic Hip Fracture Risk Using Computational Biomechanics”*
 - ♦ *Tejvir Khurana, M.D., Ph.D., “Role for IL15ra in Osteoblast Function and Cortical Bone Mineralization”*
 - ♦ *Oren Friedman, M.D., “Characterization of Septal Cartilage Manipulations and Tissue Engineering in Otolaryngology”*
- 12:05 – 12:50pm **Poster viewing and lunch (provided) in BRB Lobby**
- 12:50 – 1:50pm **Session II: Recent New Member Session** (Moderator: Xiaowei Sherry Liu, Ph.D.)
- ♦ *Shuying Yang, M.D., M.S., Ph.D., “Primary Cilia in Skeletal Development and Diseases”*
 - ♦ *Ellen Puré, Ph.D., A.B., “Defining the Impact of CD44 on Fibrillar Collagen Accumulation and Tensile Strength in Cutaneous Wound Healing”*
 - ♦ *Matthew Maltese, Ph.D., “Med Device Innovation in Academia – Entrepreneurship in the Publish-or-Perish Paradigm”*
- 1:50 – 2:35pm **Poster Session (Odd Numbered) and Break**
- 2:35 – 3:35pm **Keynote Speaker** (Moderator: Louis Soslowsky, Ph.D.)
“Toward Bioengineering Translation”
Kyriacos Athanasiou, Ph.D., Distinguished Professor, Department of Biomedical Engineering, University of California, Irvine
- 3:35 – 4:35pm **Session: Can Your Research Results Become a Product?** (Moderator: Mark Turco, M.D.)
- 4:35 – 4:50pm **Final Comments Preceding Poster Session and Reception**
- 4:50 – 6:20pm **Poster Session, Presentation of Poster Awards and Reception in BRB Lobby**

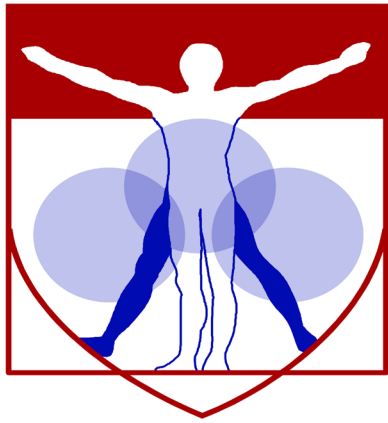


PENN

CENTER for
MUSCULOSKELETAL
DISORDERS

Center

Components



PENN

CENTER for
MUSCULOSKELETAL
DISORDERS

Center Overview

OVERVIEW OF THE PENN CENTER FOR MUSCULOSKELETAL DISORDERS

Director: Louis J. Soslowsky, PhD (soslowsk@upenn.edu)

Associate Director: Maurizio Pacifici, PhD (PacificiM@email.chop.edu)

Musculoskeletal-related conditions in the United States account for 132 million visits to physicians' offices, 29 million visits to emergency rooms, 15 million hospital outpatient visits, and cost over \$850 billion each year. Further, musculoskeletal injuries in the United States cause workers to miss more than 440 million days of work annually. In fact, more than one in four Americans has a musculoskeletal impairment. With the widespread increase in athletic and recreational activities, and the increase of the elderly population at large, these numbers are expected to rise substantially. Musculoskeletal injuries represent a critical health concern which must be better understood and better treated. To do so, a dedicated and focused strategic effort is required that optimizes research translation from the bench to the bedside in an efficient and effective manner.

The Penn Center for Musculoskeletal Disorders (PCMD) will continue to enhance the research productivity of, and provide critical resources and programs to, investigators to address multidisciplinary research strategies for musculoskeletal problems. The overall goal of this Center is to promote cooperative interactions among investigators, accelerate and enrich the effectiveness and efficiency of ongoing research, foster new collaborations and new research, and ultimately, translate our research efforts into better and new therapies for musculoskeletal disorders. The central theme of the Center will continue to be “Musculoskeletal Tissue Injury and Repair”. This theme is broad (as it includes all musculoskeletal tissue types, such as bone, cartilage, disc, ligament, meniscus, muscle, and tendon), focused (as takes advantage of commonalities in approaches across tissue types), and clinically significant (as it fosters development of assays, procedures and knowledge in preclinical animal and human models of translational relevance). It is important to note that our PCMD is not a “bone center” nor is it a “muscle center”. Rather, it is truly a “musculoskeletal center” and has emerged as the recognized home for musculoskeletal research across the Penn campus and as a technical and intellectual resource for the broader Philadelphia musculoskeletal research community.

One focus of our Center is to translate research themes, approaches, and paradigms that are consistent across different tissues. Musculoskeletal tissues have much in common and their similarities are often overlooked when focus is restricted to a single tissue type. For example, the role of inflammatory cytokines is well studied in several tissue injury and repair scenarios; yet specific findings in one tissue-type are not always known and applied in other tissues. Similarly, the availability of technologies for imaging blood vessel formation in vivo to monitor healing in a given tissue is not always known and available to researchers focusing on other tissues. Given that approaches routinely used to evaluate mechanisms in one tissue could aid researchers in other areas, our Center will work to foster this critical cross-talk.

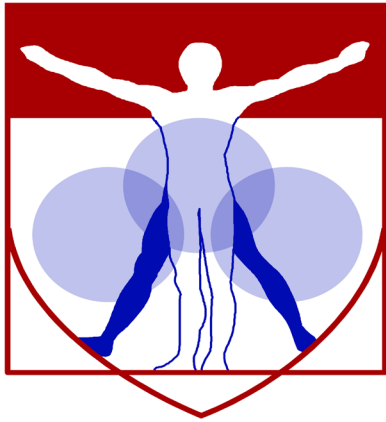
To provide a further focus for our Center, we will continue to develop programs with an emphasis on small animal models utilizing unique and sophisticated methods that can cross length scales to pre-clinical large animal models and human testing. Although large animal models for many human diseases exist and are essential for translational studies, small animals (e.g., mouse and rat) have become more commonly used for fundamental discovery of disease mechanism and initial therapeutic development due to availability of transgenic and knockout approaches and molecular tools, low cost, ease of handling and housing, and other practical issues. However, performing certain assays and experiments in mice and rats can be challenging and these difficulties often cannot be overcome in single investigator laboratories. The PCMD will provide unique expertise and sophisticated analytical tools to investigate musculoskeletal tissues across length scales.

Thus, the primary overall aims of this Center are to enhance and advance the research productivity of investigators in musculoskeletal tissue injury and repair by:

- Aim 1:** Providing innovation within critical resource core facilities in areas that cross disciplines, length scales, and hierarchies. These core facilities are μ CT Imaging, Biomechanics, and Histology.
- Aim 2:** Developing a pilot and feasibility grant program for investigators, with direct mentorship, whereby new approaches, ideas, and collaborations can be developed prior to seeking extramural funding.
- Aim 3:** Developing educational and research enrichment programs spanning tissue types, research approaches, and paradigms, through which members can learn from national leaders and from each other.

High quality musculoskeletal research is currently being conducted by many groups at Penn. While many bring sophisticated approaches to bear on musculoskeletal problems, few groups have the required expertise and facilities to perform high quality and specialized assays in their own labs. Furthermore, most investigators are not aware of approaches utilized, and results obtained, in other tissues that may have direct relevance on their research questions. Ultimately, close cooperation, communication, and collaboration among researchers across musculoskeletal tissue types and from a wide variety of disciplines will significantly enhance the research of our members. The Center will provide opportunities to integrate multi-disciplinary techniques to determine mechanisms for tissue function, injury, degeneration, repair, and regeneration, with the ultimate goal of advancing the diagnosis, treatment, and prevention of diseases and injuries of the musculoskeletal system.

In addition to the specific features described in this proposal, there is an intangible feature of our Center that should not be overlooked. Although our musculoskeletal program is strong nationally, the Penn biomedical research community is large and diverse. As such, the Center serves as an essential mechanism to highlight our successes and the importance and excitement of musculoskeletal research across campus, as well as to institutional leadership. Having a strong voice for musculoskeletal researchers is critical to support our collective and individual research goals. In these ways, the Center - with essential support from the P30 - has become and remains an indispensable resource and advocate for our community.



PENN

CENTER for
MUSCULOSKELETAL
DISORDERS

Core I

Biomechanics

Biomechanics Core

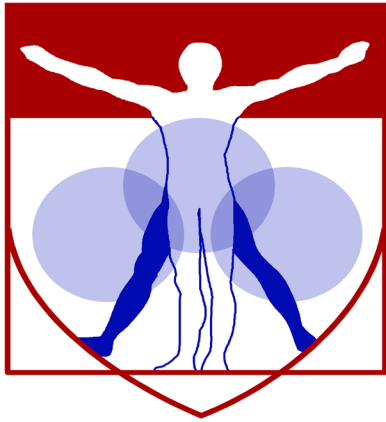
Core Director: Robert Mauck, Ph.D. (lemauck@mail.med.upenn.edu)

Technical Director: Snehal Shetye, Ph.D. (shetye@upenn.edu)

The overall objective of the Biomechanics Core is to develop and provide a wide range of innovative biomechanical approaches to evaluate musculoskeletal tissue function in the context of damage, repair, and regeneration, and to provide training and funding for new projects and collaborations utilizing these assays. Over the last decade, our Biomechanics Core at the Penn Center for Musculoskeletal Disorders (PCMD) has grown into a thriving resource for the University of Pennsylvania and Philadelphia area musculoskeletal research community. In this submission, we will further expand our services to meet the increased demand for specialized techniques and develop new and innovative methods that address the multi-scale mechanics of musculoskeletal tissues. These developments will provide customized services that enhance the research productivity of our members. The Specific Aims of the Biomechanics Core are:

- To provide guidance and training on the capabilities, advantages, and disadvantages of the various methodologies to assess musculoskeletal tissue biomechanical function through formal educational enrichment programs and one-on-one interactions
- To provide expertise and service for biomechanical assays of musculoskeletal tissues
- To develop innovative biomechanical testing techniques that will be applicable to Musculoskeletal research, and in particular those that provide information across tissue length scales
- To provide funding for the development of new projects and collaborations and to develop preliminary and/or feasibility data for investigators.

Successful completion of these aims will significantly enhance the environment and the capabilities of researchers at the University of Pennsylvania, leading to new approaches to address musculoskeletal disorders and new collaborations between Center faculties who may have not previously included biomechanical function approaches in their musculoskeletal research programs.



PENN

CENTER for
MUSCULOSKELETAL
DISORDERS

Core II

Histology

Histology Core

Overview and Mission

The mission of the Penn Center for Musculoskeletal Disorders (PCMD) Histology Core is to provide comprehensive, high quality histology services to musculoskeletal researchers at the University of Pennsylvania and the broader research community.

The Specific Aims of the core are:

- To provide guidance and training on the capabilities, advantages, and disadvantages of the various methodologies to assess musculoskeletal tissue structure and composition through formal educational enrichment programs and one-on-one interactions.
- To provide expertise and service for histological and histomorphometric assays of musculoskeletal tissues.
- To develop new histologically-based techniques that will be applicable to musculoskeletal research.
- To provide funding for development of new projects and collaborations and to develop preliminary and/or feasibility data for investigators.

Services Offered

The core offers a complete spectrum of services from sample preparation and processing, to sectioning, staining and analysis, with capabilities for paraffin, plastic and frozen histology. The core provides state of the art equipment in each of these areas, which can be accessed either on a self-service basis (upon completion of training) or a full-service basis through our full-time histology technician. Service fees are highly competitive, with significant subsidies offered for PCMD members.

- Consultation and protocol development (no charge for first 6 hours)
- Paraffin processing, embedding and sectioning
- Plastic processing and sectioning
- Frozen sectioning, including cryofilm method for undecalcified bone and teeth
- Routine histochemical staining
- Imaging and histoquantitation
- Training in histology techniques

If you are using the core for the first time, we highly recommend scheduling a meeting with one of the core co-directors and the core technician to discuss the scope of your project and specific needs.

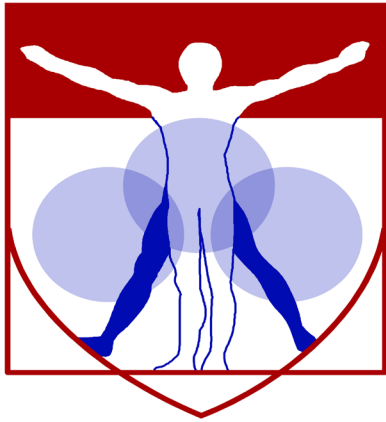
We are very happy to provide letters of support for grant applications. To request a letter, please contact the core co-directors and provide the project title, a brief description of the project and core services you propose to use.

Please visit the core website for more information: www.med.upenn.edu/pcmd/histologymain.html

Co-Directors

Ling Qin, Ph.D. (Plastic and Frozen Histology)
Associate Professor of Orthopaedic Surgery
qinling@mail.med.upenn.edu
215 898 6697

Lachlan Smith, Ph.D. (Paraffin Histology)
Assistant Professor of Neurosurgery
lachlans@mail.med.upenn.edu
215 746 2169



PENN

CENTER for
MUSCULOSKELETAL
DISORDERS

Core III

MicroCT

MicroCT Core

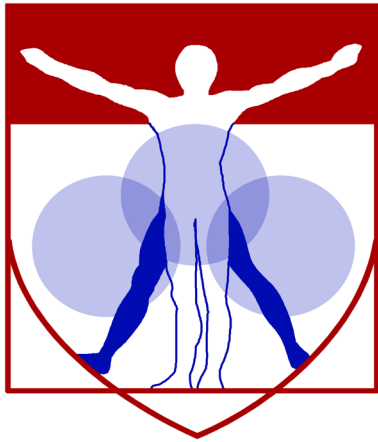
Director: X. Sherry Liu, Ph.D. (xiaoweil@mail.med.upenn.edu)

The development of high-resolution micro-CT (μ CT) during the past two decades has revolutionized the quantitative assessment of calcified and X-ray dense tissue morphology. With the capability of non-destructive, three-dimensional (3D) visualization of tissue structure, μ CT has largely supplanted traditional histomorphometry and become a gold standard for calcified tissue density and microstructure evaluation for many measures. Due to the low intrinsic X-ray contrast of non-mineralized tissues, traditional applications of μ CT in musculoskeletal research have been limited to mineralized tissue. However, the development of contrast-enhanced imaging methods has greatly broadened applications of μ CT to include musculoskeletal soft tissues as well. These cutting-edge image-based quantification methods not only enable characterization of soft-tissue morphology, but some also yield insight into tissue composition, such as glycosaminoglycan (GAG) density, which is associated with soft-tissue function and mechanics. Another important advance in the past decade is in vivo μ CT imaging of living small animals. Research of musculoskeletal tissue injury and repair has been progressively utilizing animal models of human disease. Unlike many assays that require sacrificing the animal to extract tissues for analysis, in vivo μ CT enables longitudinal evaluation of changes in a particular animal non-invasively over time. This new imaging strategy minimizes the number of animals required while enhancing statistical power. With these developments, μ CT can now provide a deep and quantitative understanding of the genetic influences on the skeleton, as well as remodeling events in hard and soft tissues during repair, treatment, and with altered loading scenarios. Further, a μ CT modality for clinical imaging of calcified tissue microstructure, called high-resolution peripheral quantitative CT (HR-pQCT), has recently been developed. This technology inaugurated a new era of non-invasive quantitative skeletal imaging, and has become a powerful tool for clinical research of musculoskeletal disorders. The overall objective of the μ CTIC is to offer a wide range of μ CT imaging approaches to evaluate musculoskeletal tissue injury and repair, and to provide training and consultation for new projects and collaborations utilizing these assays.

The Specific Aims for the μ CTIC are:

- To provide guidance and expertise on the use of μ CT imaging for musculoskeletal research through educational enrichment programs and one-on-one interactions
- To provide a range of μ CT imaging resources, expertise, and services for the study of the structure, function and physiology of the musculoskeletal system in laboratory animals and humans
- To develop new μ CT imaging-based techniques that will be applicable to musculoskeletal research
- 4) To provide funding for the development of new projects and collaborations and to develop preliminary and/or feasibility data for investigators.

Successful completion of these Aims will significantly enhance the environment and capabilities of researchers at the University of Pennsylvania, leading to novel and innovative approaches to address musculoskeletal disorders and to new collaborations between Core faculty who may not have previously included human and/or animal imaging in their musculoskeletal research programs.



PENN

CENTER for

MUSCULOSKELETAL

DISORDERS

Pilot Grant Program

PENN CENTER FOR MUSCULOSKELETAL DISORDERS PILOT AND FEASIBILITY GRANT PROGRAM

The Penn Center for Musculoskeletal Disorders has an ongoing Pilot and Feasibility Grant Program. Submissions should be related to musculoskeletal tissue injury and repair which is the broad focus of the Center and Grants are only eligible for Center members (if you are not a member but would like to become one, please contact pcmd@mail.med.upenn.edu). For more information on our Cores and Center in general, please see our web site at www.med.upenn.edu/pcmd. We are anticipating that the next Center grant submission deadline will be in Spring 2018.

Eligibility

- Only Full Center members are eligible. If you are not currently a member, please go to the link: <http://www.med.upenn.edu/pcmd/memberinfo.shtml>
- Categories of applicants include: 1) Established investigators with a proposal to test the feasibility of a new or innovative idea in musculoskeletal tissue injury and repair representing a clear and distinct departure from their ongoing research, 2) Established investigators with no previous work in musculoskeletal tissue injury and repair interested in testing the applicability of their expertise on a problem in this area, and 3) New investigators without significant extramural grant support as a Principal Investigator to develop a new project.
- Pilot and Feasibility Grants must use at least one of the Center's Research Cores.
- Pilot project awardees are eligible for one year, with a second year to be considered (budgets will be for \$20-50,000 per year and timelines should be for one or two years). The second year of funding, the dollar amount of which would only be for up to half the year one budget, will be considered based on the progress report submitted after the first year of funding and funding availability in the Center. Please note that second year funding will often not be awarded, and when awarded, will be done so primarily to new investigators; second year funding to senior investigators will be quite rare.
- It is expected that these Pilot grants will lead to funding through other independent, extramural mechanisms. Therefore, the likelihood of future extramural funding will enter into the evaluation of these proposals.

Format

• Applications should be formatted loosely in the style of an NIH R03 grant (<http://grants.nih.gov/grants/guide/pa-files/PA-13-304.html>). The main body of the application (Specific Aims through Research Design and Methods-sections 4-7 below) is limited to five pages. The application should be in a single pdf file. The format should be:

- 1) Cover Page (not NIH face page) with grant title, PI name (and co-PI name if applicable), affiliation, contact information
- 2) Budget and brief justification (note that equipment is not allowed) (Please use form PHS398, Page 4)
- 3) NIH Biosketch of PI (and co-PI if applicable) (in the new NIH format)
- 4) Specific Aims
- 5) Significance
- 6) Innovation
- 7) Approach
- 8) Brief Statement of Category of Investigator per guidelines above
- 9) Brief Statement of How this Funding will lead to other Extramural Funding
- 10) Human Subjects and/or Vertebrate Animal Subjects (if applicable)
- 11) Consultants (if applicable)
- 12) Literature Cited
- 13) Certification of Patient Oriented Research (if applicable)

Please do not hesitate to email pcmd@pennteam.upenn.edu with any questions or comments.

Penn Center for Musculoskeletal Disorders Pilot & Feasibility Grants
(all grants awarded since inception of Center)

Awarded 2017-2018

Nathaniel Dymant, Ph.D., Assistant Professor of Orthopaedic Surgery, “Murine anterior cruciate ligament reconstruction model to understand the cellular origins and mechanisms of repair”

Yangqing Gong, Ph.D., Research Assistant Professor of Medicine, “Role of plasminogen in mesenchymal stem cell function and post-injury bone regeneration”

Carla Scanzello, M.D., Ph.D., Assistant Professor of Medicine, “Importance of Macrophage Responses in Osteoarthritis”

Susan Volk, V.M.D., Ph.D., D.A.C.V.S., Assistant Professor of Small Animal Surgery, “The Regulatory Roles of Type III Collagen in the Cartilage Collagen Network: Implications for Osteoarthritis Prevention and Treatment”

Awarded 2016-2017

Joseph Baur, Ph.D., Assistant Professor of Physiology Institute for Diabetes, Obesity and Metabolism, “Targeting NAD metabolism in muscular dystrophy”

Yongwon Choi, Ph.D. Leonard Jarett Professor of Pathology and Lab Medicine, “Cell adhesion regulation of multiple-myeloma induced bone destruction”

X. Sherry Liu, Ph.D., Assistant Professor of Orthopaedic Surgery and Bioengineering, “Mechanical Consequences of Modeling- vs. Remodeling-Based Bone Formation” (*awarded extramural funding from the NSF Award #1661858*)

Hongtao Zhang, Ph.D., Research Assistant Professor, Department of Pathology and Lab Medicine, “Novel cartilage-targeting Fc fusion proteins as novel and effective treatments for osteoarthritis”

Awarded 2015-2016

Yeji Zhang, MD, PhD, Department of Physical Medicine and Rehabilitation, “Inhibition of ADAM-8 to reduce intervertebral disc degeneration” (*Awarded extramural funding from the VA Pilot Grant; VA Competitive Pilot Fund*)

Oren Friedman, MD, Department of Otorhinolaryngology, “Effect of injury to cartilage and recovery treatment with FGF-18”

Harvey Smith, MD, Department of Orthopaedic Surgery, “Impact of Pre-Culture and In Vivo Remobilization on Engineered Disc Replacement”

Tejvir Khurana, MD, PhD, Department of Physiology, “Role of the IL-15 / IL-15R α axis in modulating muscle-tendon-bone adaptation and repair”

Awarded 2014-2015

Joshua F. Baker, MD, MSCE, Department of Rheumatology & Epidemiology/Perelman School of Medicine: “*Assessment of Intramyocellular Fat Accumulation in Rheumatoid Arthritis Using MR Spectroscopy*”

Russ P. Carstens, MD, Department of Renal-Electrolyte and Hypertension Division, Perelman School of Medicine: “Roles of Epithelial Splicing Regulatory Proteins in Craniofacial Development” (*awarded extramural funding NIH 1R56DE024749 and awarded R01 NIDCR*)

Foteini Mourkioti, PhD, Department of Orthopaedic Surgery/Perelman School of Medicine: “A Novel Molecular Mechanism in Chronic Skeletal Muscle Injury” (*supported in part from the IRM*)

Chamith Rajapakse, PhD, Department of Radiology/Perelman School of Medicine: “Biomechanics of Hip Fracture Assessed by MRI” (*Awarded extramural funding from the NIH R01 AR068382*)

Awarded 2013-2014

X. Sherry Liu, PhD, Department of Orthopaedic Surgery, Perelman School of Medicine: “Structure and Strength Recovery in Post-Lactation Bone” (*awarded extramural funding from the NIH R03 AR065145 and NSF Career Award #1653216*)

Ling Qin, Ph.D., Department of Orthopaedic Surgery, Perelman School of Medicine: “Novel Anabolic Treatment for Radiation-Induced Osteoporosis” (*awarded extramural funding from the NIH R01AR066098*)

Lachlan Smith, Ph.D. Department of Orthopaedic Surgery, Perelman School of Medicine: “Molecular Mechanisms of Failed Vertebral Bone Formation in Mucopolysaccharidosis VII” (*awarded extramural funding from the NIH R03 AR065142 and the MPS Society*)

Hansell H. Stedman, MD, Department of Surgery, Perelman School of Medicine: “Molecular Pattern Recognition in Acute and Chronic Injury to Muscle and Myotendinous Junction” (*awarded extramural funding from the NIH R01NS094705*)

Awarded 2012-2013

Jason Burdick, PhD, Department of Bioengineering, School of Engineering and Applied Science: “Acellular Fibrous Scaffolds for Stem Cell Recruitment and Cartilage Repair” (*awarded extramural funding from the NIH R01 EB008722*)

James L. Carey, MD, MPH, Department of Orthopaedic Surgery, Perelman School of Medicine: “Development of a Large Animal Model of Osteochondritis Dissecans” (*awarded extramural funding from the NIH R01 EB008722*)

Andrew Kuntz, MD, Department of Orthopaedic Surgery, Perelman School of Medicine: “Effects of Intra-Articular Glenohumeral Injection of a Nonsteroidal Anti-Inflammatory Drug on Shoulder Joint Mechanics in a Rat Model”

Arjun Raj, PhD, Department of Bioengineering, School of Engineering and Applied Science: “Single Cell Analysis of Molecular and Micromechanical Heterogeneity in Mesenchymal Stem Cells and Engineered Tissues”

Awarded 2011-2012

Struan F.A. Grant, PhD, Department of Pediatrics, Children’s Hospital of Philadelphia and Perelman School of Medicine: “Utilization of CHIP-seq to Identify Genes Regulated by Osterix”

Motomi Enomoto-Iwamoto, DDS, PhD, Department of Orthopaedic Surgery, Children’s Hospital of Philadelphia and Perelman School of Medicine: “Tendon Repair by Retinoic Acid Receptor Agonists” (*awarded extramural funding from the NIH R21 AR062193*)

Ian N. Jacobs, MD, Department of Otorhinolaryngology: Head and Neck Surgery, Children’s Hospital of Philadelphia and Perelman School of Medicine: “A Pilot Study for the Development of a Rabbit In-Vivo Tissue- Engineered Cartilage Graft for Pediatric Laryngotracheal Reconstruction” (*awarded extramural funding from The Triological Society*)

Awarded 2010-2011

Susan W. Volk, VMD, PhD, Dipl ACVC, Department of Small Animal Surgery, School of Veterinary Medicine: “The Role of Type III Collagen in Bone Repair and Regeneration”

Jaimo Ahn, MD, PhD, Department of Orthopaedic Surgery, Perelman School of Medicine: “Toward the Identification of Molecular Pathway Alterations in Aged Fracture Healing: A Pilot Study Utilizing a Genetic Model of Senescence” (*awarded extramural funding from the NIH R03 AG040670*)

Shannon Fisher, MD, PhD, Department of Cell and Developmental Biology, Perelman School of Medicine: “Requirement for Osterix in Skull Formation and Maintenance of Adult Bone in Zebrafish” (*awarded extramural funding from the NIH R21 DE021509*)

Awarded 2010-2011 (Jointly with IOA)

Olena Jacenko, PhD, Department of Animal Biology, School of Veterinary Medicine: “Aging of the hematopoietic niche” *(awarded extramural funding from the NIH R01 DK088334-01)*

Eileen M. Shore, PhD, Departments of Orthopaedic Surgery and Genetics, Perelman School of Medicine: “Modulation of Progenitor Cell Differentiation through BMP Signaling” *(awarded extramural funding from the NIH R01 AR041916-15)*

Kurt D. Hankenson, DVM, PhD, Department of Animal Biology, School of Veterinary Medicine: “Notch Signaling in Bone Regeneration” *(awarded extramural funding from the DOD CDMRP)*

Awarded 2009-2010

Ling Qin, PhD, Department of Orthopaedic Surgery, School of Medicine: “Mechanisms of EGFR Action on Bone” *(awarded extramural funding from the NIH R01 DK095803)*

Steven Scherer, MD, PhD, Department of Neurology, Perelman School of Medicine: “Are N-cadherin and L1 Adhesion Molecules Required for Recovery of Muscle Strength after Nerve Injury?”

Nader M. Hebel, MD, Department of Orthopaedic Surgery, Perelman School of Medicine: “A Pre-Clinical Rodent Model of Intervertebral Disc Autograft Transplant” *(awarded extramural funding from the DOD/CDMRP/PROP OR090090)*

Awarded 2008-2009

Sunday O. Akintoye, BDS, DDS, MS, Department of Oral Medicine, School of Dental Medicine: “Orofacial Bone Marrow Stromal Cells Promote Bisphosphonate-Associated Jaw Osteonecrosis” *(awarded extramural funding from the NIDCR R21 DE022826)*

Margaret M. Chou, PhD, Departments of Cell and Developmental Biology, Perelman School of Medicine: “Mechanisms of TRE17/USP6 Function in the Etiology of Aneurysmal Bone Cyst” *(awarded extramural funding from the NIH-NCI R01 CA168452 and R21-CA18601)*

Kenneth W. Leichty, MD, Department of Surgery, Perelman School of Medicine: “The Role of Inflammation in Regenerative Fetal Tendon Wound Healing” *(awarded extramural funding from the NIH DP2 DK083085)*

Kathleen M. Loomes, MD, Department of Pediatrics, Children’s Hospital of Philadelphia: “The Role of Jag1 in Osteogenesis”

Eileen M. Shore, PhD, Departments of Orthopaedic Surgery and Genetics, Perelman School of Medicine: “Analysis of an ACVR1 Knock-in Mouse Model for FOP” *(awarded extramural funding from the NIH R01 AR041916-15S1)*

Awarded 2007-2008

Sherrill L. Adams, PhD, Department of Biochemistry, School of Dental Medicine: “Collagen III-deficient Mice as a Model for Musculoskeletal Wound Repair”

Kurt D. Hankenson, DVM, PhD, Department of Animal Biology, School of Veterinary Medicine: “Regulation of Bone Formation by Novel Activators of Canonical Wnt Signaling”

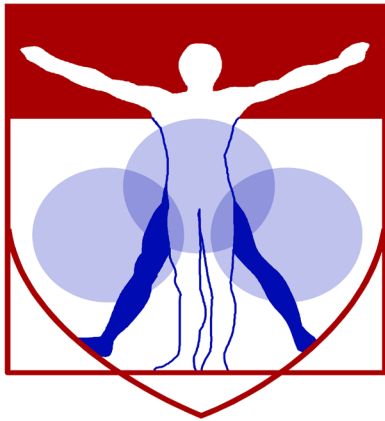
Awarded 2006-2007

Robert J. Pignolo, MD, PhD, Department of Medicine, Perelman School of Medicine: “Stem Cell Rescue of the Osteoporotic Phenotype in a Mouse Model of Accelerated Aging” *(awarded extramural funding from the NIH R01 AG028873)*

Robert L. Mauck, PhD, Department of Orthopaedic Surgery, Perelman School of Medicine “Meniscus Repair with a Novel Aligned Nanofiber Scaffold” *(awarded extramural funding from the NIH R01 AR056624 and the VA RR & D)*

Christopher S. Chen, MD PhD, Department of Bioengineering, School of Engineering and Applied Science:
“Mechanotransduction in Mesenchymal Stem Cells” (*awarded partial funding as Co-Investigator on NIH P41 EB001046*)

Pedro K. Beredjiklian, MD, Department of Orthopaedic Surgery, Perelman School of Medicine: “Role of Hyaluronic
Acid Receptors in Tendon Healing” (*awarded extramural funding from the NIH R21 AR052393*)



PENN

CENTER for

MUSCULOSKELETAL

DISORDERS

**Visiting
Professorship Series
2017-2018**

Visiting Professorship Series-Academic Year 2017-2018

Tuesday, September 12, 2017, 1:30-2:30pm/CRB Austrian Auditorium

Title: *Cartilage Repair and Osteoarthritis in Genetic Mouse Models.*

Linda Sandell, PhD, Mildred B. Simon Research Professor and Director of Research
Washington University

Tuesday, October 24, 2017, 1:30-2:30pm/JMB Class of '62 Auditorium

Title: *How can we improve translation of pre-clinical osteoarthritis research to patients?*

Christopher Little, BVMS, PhD, Director, Raymond Purves Bone & Joint Research Laboratories
Kolling Institute, Institute of Bone and Joint Research, University of Sydney

ANNUAL SCIENTIFIC SYMPOSIUM (all day event)

Wednesday, November 15, 2017, 7:30-6:00pm/BRB Auditorium

Title: *Strategies for Improving Bone Properties in Patients with Osteogenesis Imperfecta*

Matthew Warman, MD

Professor, Department of Genetics, Harvard Medical School

Tuesday, December 12, 2017, 1:30-2:30pm/ CRB Austrian Auditorium

Title: *Osteocytes and Bone Remodeling: They're Just Dying to do the Job.*

Mitchell B. Schaffler, PhD

CUNY and Wallace Coulter Distinguished Professor of Biomedical Engineering

Chairman, Department of Biomedical Engineering

The City College of New York, City University of New York

Tuesday, January 16, 2018, 1:30pm – 2:30pm, CRB Austrian Auditorium

Title: *Parathyroid hormone and related peptides signaling to the nucleus of osteoblasts*

Nicola C. Partridge, Ph.D.

Professor and Chair

Departments of Medicine, Biochemistry & Molecular Pharmacology,

& Basic Science & Craniofacial Biology

College of Dentistry, New York University School of Medicine

Tuesday, February 13, 2018, 1:30pm – 2:30pm, CRB Austrian Auditorium

Title: *Notch Signaling and the Skeleton*

Ernesto Canalis, M.D.

Professor of Orthopaedic Surgery and Medicine

Director of Center for Skeletal Research

University of Connecticut

Tuesday, March 27, 2018, 1:30pm – 2:30pm, CRB Austrian Auditorium

Title: *Modular inductive high-density cell culture systems for engineering complex tissues.*

Eben Alsberg, Ph.D.

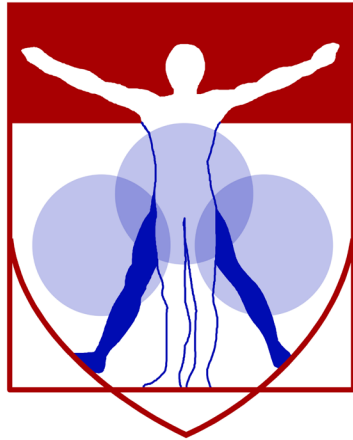
Professor of Biomedical Engineering and Orthopaedic Surgery

Director of ASCENT Lab

Case Western Reserve University

Tuesday, April 2018 TBD

Tuesday, May 2018 TBD



PENN

CENTER for
MUSCULOSKELETAL
DISORDERS

Symposium Participants

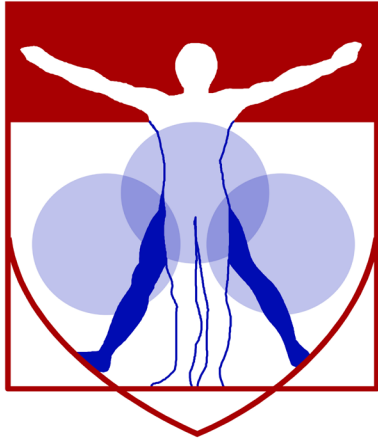
<u>Last Name</u>	<u>First Name</u>	<u>Email</u>	<u>Affiliation</u>
Abbasnia	Pegah	pegah.abbasnia@pennmedicine.upenn.edu	Penn Ortho
Agnello	Kimberly	kagnello@vet.upenn.edu	Penn Vet Clinical Studies
Ailavajhala	Ramya	tub58807@temple.edu	Temple Bioengineering
Akintoye	Sunday	akintoye@upenn.edu	Penn Dental
Alvarez-Urena	Pedro	pedroau@seas.upenn.edu	Penn Bioengineering
Arya	Lily	larya@obgyn.upenn.edu	Penn OBGYN
Ashinsky	Beth	Beth.ashinsky@gmail.com	Penn Ortho
Athanasiou	Kyriacos	athens@uci.edu	Univ of California, Irvine
Baker	Joshua	bakerjo@uphs.upenn.edu	Penn Rheumatology/Epidemiology
Bansal	Sonia	soniab@seas.upenn.edu	Penn Ortho
Barnum	Carrie	cbarnum@upenn.edu	Penn Ortho
Bautista	Catherine	cbaut@seas.upenn.edu	Penn Bioengineering
Baxter	Josh	josh.baxter@uphs.upenn.edu	Penn Ortho
Beach	Zakary	zakary.beach1@gmail.com	Penn Bioengineering
Bellas	Evangelia	Evangelia.bellas@temple.edu	Temple Bioengineering
Bendigo	Justin	jbendigo@pennmedicine.upenn.edu	Penn Ortho
Billings	Paul	BillingsP@email.chop.edu	CHOP Ortho
Boerckel	Joel	boerckel@pennmedicine.upenn.edu	Penn Ortho
Boland	Mary Regina	bolandm@mail.med.upenn.edu	Penn Biostatistics/Epidemiology
Bonnevie	Eddie	edbon@pennmedicine.upenn.edu	Penn Ortho
Boorman-Padgett	James	james.boormanpadgett@gmail.com	Penn Ortho
Buechter	Doug	dbuechte@its.jnj.com	DePuy Synthes
Carey	James	james.carey@uphs.upenn.edu	Penn Ortho
Caron	Bob	rcaron@pennmedicine.upenn.edu	Penn Ortho
Chakkalakal	Salin	salin.chakkalakal@gmail.com	Penn Ortho
Chandrasekaran	Prashant	pc487@drexel.edu	Drexel Biomedical Engineering
Cheema	Adnan	adnan.cheema@uphs.upenn.edu	Penn Ortho
Chen	Mengcun	chenmc0603@gmail.com	Penn Ortho
Chery	Daphney	dc679@drexel.edu	Drexel Biomedical Engineering
Chin	Matthew	mattchin@pennmedicine.upenn.edu	Penn Ortho
Chinipardaz	Zahra	zahrach@upenn.edu	Penn Dental
Collins	Joseph	jmcollin@seas.upenn.edu	Penn Bioengineering
Cotsarelis	George	cotsarel@mail.med.upenn.edu	Penn Dermatology
Cousminer	Diana	cousminerd@email.chop.edu	CHOP Human Genetics
Cresap	Anthony	anthonycresap@gmail.com	Penn Ortho
Dai	Eric	erican@seas.upenn.edu	Penn SEAS
Daniels	Ryan	rydan@pennmedicine.upenn.edu	Penn Ortho
Deepak	Vishwa	deepakv@pennmedicine.upenn.edu	Penn Dental
Degnan	Andrew	degnaana@email.chop.edu	Penn Radiology
Dekhne	Mihir	mdekhne@sas.upenn.edu	Penn Ortho
Demirtas	Ahmet	ademirta@villanova.edu	Villanova Mechanical Engineering
Diller	Wendy	w.diller@medtechinno.com	The MedTech Strategist
Dyment	Nat	dymment@mail.med.upenn.edu	Penn Ortho
Eby	Michael	michael.eby@uphs.upenn.edu	Penn Ortho
Esterhai	John	john.esterhai@uphs.upenn.edu	Penn Ortho
Falcon	Jessice	falcon@temple.edu	Temple Engineering
Farber	Daniel	Daniel.farber@uphs.upenn.edu	Penn Ortho
Freeman	Terry	theresa.freeman@jefferson.edu	Penn Ortho

Friedman	Oren	orenfriedman@hotmail.com	Penn Plastic Surgery
Fu	Chuanyun	cloudfcyhjy@gmail.com	Penn Dental
Fung	Ashley	afung@seas.upenn.edu	Penn Bioengineering
Galarrage	Jonathan	jgala@seas.upenn.edu	Penn SEAS
Gittings	Daniel	daniel.gittings@uphs.upenn.edu	Penn Ortho
Goel	Peeyush	pgoel@upenn.edu	Penn Ortho
Gonzalez	Michael	gonzalezm2@email.chop.edu	CHOP Ortho
Grant	Struan	grants@email.chop.edu	Division of Genetics
Graves	Dana	dtgraves@upenn.edu	Penn Dental Perio
Greer	Christopher	c.greer115@gmail.com	Penn Surgery
Gullbrand	Sarah	selinley516@gmail.com	Penn Ortho
Hamilton	Amber	amber@sas.upenn.edu	Penn Ortho
Han	Lin	lh535@drexel.edu	Drexel Biomedical Engineering
Harten	Robert	rharten@its.jnj.com	DePuy Synthes
Harvie	Heidi	hharvie@obgyn.upenn.edu	Penn OBGYN
Hast	Michael	hast@upenn.edu	Penn Ortho
Haughan	Joanne	jhaughan@vet.upenn.edu	Penn Vet Clinical Studies
He	Zhuohao	hezha@upenn.edu	Penn Pathology
Henning	Liz	ehenning@mail.med.upenn.edu	Penn Ortho
Himmelstein	Daniel	daniel.himmelstein@gmail.com	Penn SPATT
Ho-Fung	Victor	HOV@email.chop.edu	Penn Radiology
Hua	Phuong	pqh23@drexel.edu	Penn Ortho
Huang	Yan	huayan@upenn.edu	Penn Anatomy/Cell Biology
Hullfish	Todd	todd.hullfish@uphs.upenn.edu	Penn Ortho
Ita	Meagan	meita@seas.upenn.edu	Penn Bioengineering
Jeon	Hyeran	hjeon@upenn.edu	Penn Orthodontics
Jiang	Xi	jiangxi@upenn.edu	Penn Ortho
Joeng	Kyu Sang	joeng@bcm.edu	Baylor College of Medicine
Kandel	Shital	shitalkandel@gmail.com	Temple Engineering
Karchin	Jing	karchinj@mail.med.upenn.edu	Penn Pathology
Karchner	James	james.karchner@temple.edu	Temple Engineering
Karnawat	Vishakha	vishakha.karnawat@gmail.com	Penn Physiology
Kegelman	Chris	ckeg@seas.upenn.edu	Penn Bioengineering
Kelly	John	john.kelly@uphs.upenn.edu	Penn Ortho
Khurana	Tejvir	tsk@mail.med.upenn.edu	Penn Physiology
Killian	Megan	Killianm@udel.edu	Univ of Delaware Biomedical Engineering
Kim	Dong Hwa	kimdl@mail.med.upenn.edu	Penn Ortho
Kim	Minwook	kimminw@mail.med.upenn.edu	Penn Ortho
Klyde	Daniel	dklyde@seas.upenn.edu	Penn Bioengineering
Kolasinski	Sharon	sharon.kolasinski@uphs.upenn.edu	Penn Medicine
Koyama	Eiki	koyamae@email.chop.edu	CHOP Ortho
Kreeger	Karen	Karen.Kreeger@uphs.upenn.edu	Penn Communication
Kuntz	Andrew	andrew.kuntz@uphs.upenn.edu	Penn Ortho
Kwon	Mi	miykwon@seas.upenn.edu	Penn SEAS
Kyada	Rutvin	kyadarutvin@gmail.com	Temple Bioengineering
Lau	Yian Khai	adrianlau02@gmail.com	Penn Ortho
Leahy	Thomas	tpleahy@seas.upenn.edu	Penn Bioengineering
Leiphart	Ryan	rleip@seas.upenn.edu	Penn Bioengineering
Levin	L. Scott	scott.levin@uphs.upenn.edu	Penn Ortho

Lewis	Gregory	glewis1@pennstatehealth.psu.edu	Penn Ortho
Li	Qing	ql55@drexel.edu	Drexel Biomedical Engineering
Li	Xinhua	xinhuali@upenn.edu	Penn Dental
Li	Yihan	yihanl@seas.upenn.edu	Penn Bioengineering
Li	Ziqing	ziqingli@upenn.edu	Penn Dental
liang	dongming	dol@penncmedicine.upenn.edu	Penn Biochemistry/Biophysics
Linardi	Renata	rlinardi@upenn.edu	Penn Vet Clinical Studies
Liu	Min	minliu@upenn.edu	Penn Dental
Liu	X. Sherry	xiaowei.liu@gmail.com	Penn Ortho
Loebel	Claudia	loebelc@seas.upenn.edu	Penn SEAS
Long	Jason	jlong14@its.jnj.com	DePuy Synthes
Malayter	James	jmalayter@yahoo.com	Acuitive Technologies, Inc.
Maltese	Matthew	maltese@email.chop.edu	Penn Medicine
Mao	Qin	maoqin@upenn.edu	Penn Oral Surg./Pharmacology
Martin	Anthony	Anthony.martin@uphs.upenn.edu	Penn Ortho
Mason	Devon	dmason1@nd.edu	Penn Bioengineering
Mauck	Robert	lemauck@penncmedicine.upenn.edu	Penn Ortho
McCarrick-			
Walmlsey	Ruth	Mcc.walmsley@gmail.com	Penn Ortho
Millar	Sarah	millars@mail.med.upenn.edu	Penn Dermatology
Minnig	Molly	mminnig@sas.upenn.edu	Penn Ortho
Mohanraj	Bhavana	bhavana@biorez.com	Biorez
Morales	Leon	leonmorales89@gmail.com	Penn Surgery
Moussa	Fouad	moussaf@email.chop.edu	Penn Ortho
Mundy	Chrissy	matticolac@email.chop.edu	Penn Ortho
Newton	Joseph	josebr@seas.upenn.edu	Penn Bioengineering
Nguyen	Vu	vunguyen@upenn.edu	Penn Rheumatology
Novais	Emanuel	emanuel.j.novais@gmail.com	Penn Ortho
Nuss	Courtney	Cnuss37@gmail.com	Penn Ortho
Ortved	Kyla	kortved@vet.upenn.edu	Penn Vet Clinical Studies
Pacifici	Maurizio	pacificim@email.chop.edu	CHOP Ortho
Padalkar	Mugdha	tub84972@temple.edu	Temple Bioengineering
Park	Jino	jino.park@jefferson.edu	Penn Ortho
Park	Juyoung	orthosmile14@gmail.com	Penn Anatomy/Cell Biology
Pasha	Saba	pashas@email.chop.edu	Penn Ortho
Patel	Jay	jaymilanpatel@gmail.com	Penn Ortho
Peart	Natoya	npeart@upenn.edu	Penn Medicine
Peck	Sun	sunchung@penncmedicine.upenn.edu	Penn Ortho
Peredo	Ana	anapperedo@gmail.com	Penn Bioengineering
Pleshko	Nancy	npleshko@temple.edu	Penn Bioengineering
Puré	Ellen	epure@vet.upenn.edu	Penn Vet Clinical Studies
Qin	Ling	qinling@penncmedicine.upenn.edu	Penn Ortho
Querido	William	william.querido@temple.edu	Temple Engineering
Rabut	Emilie	erabut@upenn.edu	Penn Ortho
Raja	Harina	harina.a.raja@gmail.com	Penn Ortho
Rajapakse	Chamith	chamith@mail.med.upenn.edu	Penn Radiology
Reylander	Kimberly	reylanderk@email.chop.edu	CHOP Ortho
Riggin	Corinne	criggin@seas.upenn.edu	Penn Bioengineering
Risbud	Makarand	makarand.risbud@jefferson.edu	Penn Ortho

Rodriguez	Ashley	ashley.b.rodriguez0391@gmail.com	Penn Ortho
Rumpf	Emily	emily.rumpf@jefferson.edu	Penn Ortho
Rux	Danielle	ruxd@email.chop.edu	CHOP
Scanzello	Carla	cscanz@penntmedicine.upenn.edu	Penn Medicine
Schmidt	Elaine	schmidtelaine2@gmail.com	Penn Ortho
Scurato	Sharon	sscurato@radiuspharm.com	Radius Health
Sennett	Brian	Brian.sennett@uphs.upenn.edu	Penn Ortho
Sennett	Mac	sennett@mail.med.upenn.edu	Penn Ortho
Seravello	Donna	donnaser@upenn.edu	Penn Ortho
Shapses	Susan	shapses@rutgers.edu	Rutgers Environmental & Biological Sciences
Shetye	Snehal	shetye@upenn.edu	Penn Ortho
Shi	Dongliang	shidongliang2010@hotmail.com	Penn Biochemistry & Biophysics
Shore	Eileen	shore@penntmedicine.upenn.edu	Penn Ortho
Sidibe	David	dsidibe@upenn.edu	Penn Ortho
Sinha	Sayantani	sinhas@email.chop.edu	Penn Ortho
Smalley	Ryan	rynsmalley@gmail.com	Veterans Affairs Medical Center
Smith	Gail	smithgk@vet.upenn.edu	Penn Vet Clinical Studies
Smith	Harvey	harveysmith27@gmail.com	Penn Ortho
Smith	Lachlan	lachlans@penntmedicine.upenn.edu	Penn Neurosurgery
Smith	Lucas	smithlu@upenn.edu	Penn Chemical/Biomolecular
Song	Hee Kwon	hsong@uphs.upenn.edu	Penn Radiology
Soslowsky	Lou	soslowsk@upenn.edu	Penn Ortho
Sperry	Megan	sperrym@seas.upenn.edu	Penn Bioengineering
Spitsin	Serguei	spitsins@email.chop.edu	Penn CHOP
Sridharan	Anush	sridharana@email.chop.edu	Penn Radiology
Stankov	Sylvia	sstankov@penntmedicine.upenn.edu	Penn Ortho
Stanley	Alexandra	astanle@mail.med.upenn.edu	Penn Ortho
Stefanic	Neza	neza.stefanic@uphs.upenn.edu	Penn Ortho
Steinberg	David	david.steinberg@uphs.upenn.edu	Penn Ortho
Stoeckl	Brendan	bdstoeckl@gmail.com	Penn Ortho
Taylor	Brittany	b.taylor1888@gmail.com	Penn Ortho
Thomson	Euan	ethomso2@its.jnj.com	DePuy Synthes
Thornton	Angelique	thorntona1@email.chop.edu	Penn Ortho
Tichy	Elisia	etichy@mail.med.upenn.edu	Penn Ortho
Tomlinson	Ryan	ryan.tomlinson@jefferson.edu	Penn Ortho
Tower	Robert	rtower@penntmedicine.upenn.edu	Penn Ortho
Towler	Oscar	otowler@mail.med.upenn.edu	Penn Ortho
Tseng	Wei-Ju	weits@mail.med.upenn.edu	Penn Ortho
Tucker	Scott	stucker1@pennstatehealth.psu.edu	Penn State Medicine
Turco	Mark	turco@upenn.edu	Penn PCI
Ural	Ani	ani.ural@villanova.edu	Villanova Mechanical Engineering
Vega	Sebastian	sebv@seas.upenn.edu	Penn SEAS
Volk	Susan	swvolk@vet.upenn.edu	Penn Vet Clinical Studies
Waldorff	Erik	erikwaldorff@orthofix.com	Orthofix, Inc.
Wang	Bin	bin.wang@jefferson.edu	Thomas Jefferson Medicine
Wang	Chao	cw583@drexel.edu	Penn Bioengineering
Wang	Hong	whon@mail.med.upenn.edu	Penn Pathology
Wang	Luqiang	luqiang@mail.med.upenn.edu	Penn Ortho
Wang	Yaohui	ywang15@villanova.edu	Villanova Mechanical Engineering

Wehrli	Felix	wehrli@mail.med.upenn.edu	Penn Radiology
Weiss	Stephanie	weissn@gmail.com	Penn Ortho
Winkelstein	beth	winkelst@seas.upenn.edu	Penn Bioengineering
Wong	Hetty	Wonghe@pennmedicine.upenn.edu	Penn Medicine
Xu	Meiqi	mqx@mail.med.upenn.edu	Penn Ortho
Yang	Evan	yange3@email.chop.edu	Penn Ortho
Yang	Feikun	feikun@vet.upenn.edu	Penn Vet Clinical Studies
Yang	Shuying	shuying@upenn.edu	Penn Dental
Yang	Yanmei	yanmei.yang@jefferson.edu	Thomas Jefferson University
Yousefi	Farzad	farzadyousefi@gmail.com	Penn Ortho
Yu	Wenjing	wenjing@upenn.edu	Penn Anatomy/Cell Biology
Yuan	Gongsheng	gsyuan@upenn.edu	Penn Anatomy/Cell Biology
Zhang	Deyu	deyuz@mail.med.upenn.edu	Penn Ortho
Zhang	Qian	qian2@mail.med.upenn.edu	Penn Pathology
Zhang	Yeja	yeja.zhang@uphs.upenn.edu	Penn PM&R
Zhong	Leilei	zhongleilei8@gmail.com	Penn Ortho
Zhou	Cheng	zhoucz@mail.med.upenn.edu	Penn Rheumatology
Zhu	Xuming	xumingz@mail.med.upenn.edu	Penn Dermatology
Zintner	Shannon	smithsm@email.chop.edu	Penn Hematology
Zlotnick	Hannah	zlotnick@seas.upenn.edu	Penn Bioengineering



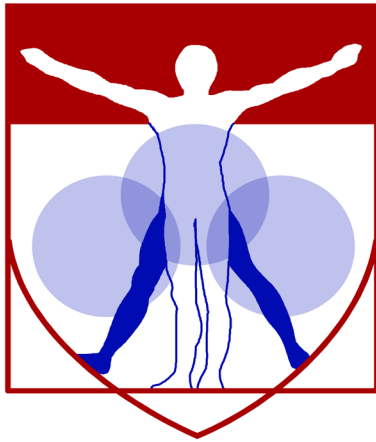
PENN

CENTER for

MUSCULOSKELETAL

DISORDERS

Abstracts



PENN

CENTER for

MUSCULOSKELETAL

DISORDERS

Speaker Abstracts

“Engineering Adipose Tissue”

Evangelia Bellas, Ph.D.
Assistant Professor of Bioengineering
Temple University

The overall research in the BellasFATLab focuses on engineering functional adipose tissue using 3D in vitro and fat-on-chip models for the study of such adipose tissue diseases such as obesity. As adipose tissue becomes obese, the adipocytes grow several fold in volume, but the surrounding vasculature does not increase to accommodate these changes, leaving the tissue hypoxic. This hypoxia leads to inflammation and fibrosis of the adipose tissue, causing metabolic dysfunction. We have developed a 3D in vitro model of the early changes during obesity to the adipose tissue microenvironment. Further, we will show how we can “trick” the adipocytes into thinking they are not experiencing a diseased, obese microenvironment.

The role of FGF signaling during the development of the tendon-bone attachment

Megan Killian
Assistant Professor of Bioengineering
University of Delaware

The transmission of active and passive loads from muscle to bone requires the attachment of tendon to bone. The formation and loading of attachments regulates the shape of our bones, providing uniquely patterned ridges along bone's surface. In the absence of muscle loading, the growth of these ridges is restricted during skeletal morphogenesis. In addition, morphogenetic factors like BMP4 have been recently shown to control the outgrowth of these structures at early stages of development. Our laboratory has recently shown that Fibroblast growth factor (FGF) signaling may act as a negative regulator of attachment and ridge size. Using novel transgenic strains for targeted deletion of FGF signaling in tendon progenitors, we have revealed a potential mechanism of regulating the surface shape of bone via FGFR1/2 ablation in tendon-progenitors (DKO mice). Using structural and morphometric analyses, we have found that loss of *Fgfr1* and *Fgfr2* in DKO mice led to aberrant patterning of the deltoid tuberosity and other attachment sites in both the forelimb and hindlimb. We have also found that DKO mice exhibit increased joint contraction and smaller tendon fibrils. This is the first study to interrogate the role of FGF signaling during postnatal growth of tendons and its role in bone shape. Our work aims to develop strategies for understanding the basic morphogenesis of the tendon-bone attachment, guided by FGF signaling. Aberrant joint growth in DKO mice suggests that *Fgf* signaling plays an important role in the structure and organization of tendons and ligaments, and that proper development of connective tissues contributes to joint maturation with age. Ongoing work is identifying the mechanical behavior of DKO and WT connective tissue as well as the adaptation of attachments to muscle unloading.

Roles of Type V Collagen in the Biomechanical Functions of Temporomandibular Joint

P. Chandrasekaran, Q. Li, M. Sun, L. J. Soslowsky, D. E. Birk, L. Han

The soft tissue in the temporomandibular joint (TMJ) is a unique hybrid of cartilaginous tissues. The articular disc (AD) is a fibrocartilage dominated by type I collagen (collagen I) fibers, while the mandibular cartilage (MC) has a bi-layered structure of fibrocartilage covering a hyaline cartilage layer. This specialized layout indicates that type V collagen, which initiates the fibrillogenesis of collagen I, is essential to the structural integrity of TMJ. Indeed, among classical Ehlers-Danlos Syndrome (EDS) patients who have genetic deficiency in COL5A1 gene, one salient symptom is the dysfunction of TMJ. To this end, the objective of this study is to determine the roles of type V collagen in the structure and mechanical properties of TMJ cartilaginous tissues. First, we established an atomic force microscopy (AFM)-based micromechanical method infrastructure to quantify the biomechanical properties of murine TMJ tissues, which is necessary for studying genetic deficiencies in animal models in vivo. In wild-type mice, using AFM-nanoindentation, we delineated the heterogeneity between the MC and AD. The surface of MC has substantially higher modulus than the AD, while the AD was highly heterogeneous, with lowest modulus found in the thinnest central region. Moreover, the surface of MC is dominated by randomly oriented collagen fibrils, a feature similar to knee cartilage, while the surface of AD consists of anteroposteriorly aligned fibers, a typical feature of fibrous tissues. Building on these findings, we studied the structural and biomechanical phenotype of TMJ mandibular cartilage in *Col5a1*^{+/-} mice. Upon the reduction of collagen V, there is a substantial increase in both the average and heterogeneity of collagen fibril diameters in the fibrous layer of MC. In accordance to the structural defects, *Col5a1*^{+/-} MC exhibits significant reduction of modulus. Furthermore, under the guidance of perlecan immunofluorescence labeling, we delineated the pericellular matrix (PCM) and further-removed territorial/interterritorial (T/IT)-ECM in the hyaline layer. In both regions, significant impairment of the modulus was detected. These results highlighted that type V collagen is not only critical to the fibrillogenesis in the fibrocartilage units, but also regulates the second hyaline layer of MC, a critical unit for the shock absorption of TMJ. Taken together, this study established a new, AFM-based engineering approach to study the development and disease of TMJ in murine models. The outcomes highlighted the critical role of type V collagen in the proper functions of TMJ. Our ongoing studies are evaluating the roles of type V collagen in the mechanotransduction of TMJ cells and TMJ disorder.

Assessment of Osteoporotic Hip Fracture Risk Using Computational Biomechanics

Chamith Rajapakse, Ph.D.
Research Assistant Professor, Radiology
University of Pennsylvania

Hip fracture is a devastating event. Within a year of the injury, 20-30% of patients die and 50% lose the ability to walk; in the United States these fractures account for 70% (\$12 billion) of the direct annual costs of fracture care. Ironically, more than half of the women who sustain a hip fracture would not have qualified for osteoporosis treatment by the current criteria, which are based on bone mineral density (BMD) measurements by dual energy X-ray absorptiometry (DXA). Thus, a better approach is needed to determine if an individual is at risk for hip fracture from a fall. Biomechanically, a hip will fracture if the impact force resulting from a fall is greater than the bone strength. Therefore, the ability to determine hip strength is critical for fracture risk assessment. The current best non-invasive tool for direct hip strength assessment is based on quantitative computed tomography (QCT) guided finite element models. However, due to ionizing-radiation dose restrictions, the spatial resolution of clinical QCT (0.6-1 mm) is not sufficient to resolve bone microstructure at the hip. We are developing a novel method for assessing hip strength in vivo using magnetic resonance imaging (MRI) coupled with biomechanics.

Lack of Interleukin 15 receptor α (Il15ra) impairs cortical bone mineralization.

Tejvir S. Khurana MD, PhD.

Professor of Physiology

Department of Physiology and Pennsylvania Muscle Institute

Perelman School of Medicine, University of Pennsylvania

Interleukin15 (Il15) and Il15 receptor α (Il15ra) mediate pro-inflammatory signaling. However, they are expressed in a number of tissues and cell types not directly involved in immunity where they are increasingly being recognized as undertaking diverse functional roles. IL15 and IL15RA are found in metabolically active tissues like muscle and bone, where we and others have shown they are also determinants of skeletal muscle properties and energy metabolism. In particular, Il15ra^{-/-} mice exhibit higher spontaneous activity, increased endurance and resistance to diet-induced obesity. Furthermore, the IL15/IL15RA axis is known to play a role in osteoclastogenesis, however, little is known about its role in osteoblast function and osteoblast/osteoclast coupling. Given the potential crosstalk between exercise activity, cytokine secretion and the musculoskeletal system we, in collaboration with Dr. Eileen Shore, used a variety of *in vivo*, *in vitro* and bioinformatic analyses to define the role IL15/IL15RA signaling on osteoblast function and bone mineralization.

We show that lack of IL15RA decreased bone mineralization in Il15ra^{-/-} knockout mice *in vivo* as well as in primary osteogenic cultures generated from these mice, suggesting a cell-autonomous effect on osteoblasts. Il15ra^{-/-} osteogenic cultures also had reduced *Rankl/Opg* mRNA ratio, indicating defective osteoblast/osteoclast coupling. We analyzed the transcriptome of primary pre-osteoblasts from normal and Il15ra^{-/-} mice and identified 1150 genes that were differentially expressed at a False Discovery Rate (FDR) of 5%. Of these, 844 transcripts were upregulated and 306 were downregulated in Il15ra^{-/-} cells. Using DAVID analysis, we grouped these genes into functional clusters related to metabolism, immune response, bone mineralization and morphogenesis. The transcriptome analysis was validated using qPCR of the most significant hits. Using bioinformatic approaches, we identified candidate genes, including *Cd200* and *Enpp1*, that could contribute to the reduced mineralization. Silencing *Il15ra* using shRNA in the calvarial osteoblast MC3T3-E1 cell line decreased ENPP1 activity. Together, these recently published data (*Loro et al. Bone 2017*) highlight an important cell-autonomous role for IL15RA in bone mineralization and osteoblast function. In the future, we plan to extend these studies focusing on signaling pathways and mechano-transduction mechanisms utilized by IL15RA. These studies may help determine the translational potential of targeting IL15/IL15RA signaling to improve bone health in response to ageing as well as inactivity/unloading and associated disease states .

Acknowledgement: The study was supported in part through a pilot grant for the Penn Center for Musculoskeletal Disorders-PCMD (P30AR069619). We thank members of the Biomechanics and MicroCT cores at the PCMD and the Penn Genomic Analysis Core and Molecular Profiling Core for their guidance and service.

Effect of injury to cartilage and recovery treatment with FGF-18

Oren Friedman & George R. Dodge
Departments of Orthopaedic Surgery & Otorhinolaryngology
University of Pennsylvania

The study of cartilage as autograft material in the reconstruction of the facial skeleton is a burgeoning area of tissue engineering and regenerative medicine. The translational relevance of this *in vitro* study is related to cartilage injury that occurs after it is harvested, and manipulated for purposes of reconstruction within the nasal superstructure and other facial skeletal structures. Clinically relevant applications include the repair of skeletal deformities associated with traumatic, congenital, cosmetic, and neoplastic related issues. The ideal implant material remains elusive and autograft cartilage in various forms is considered to be the best material for reconstruction of many facial osseo-cartilaginous structures. Since the amount of available septal cartilage is limited, any method to increase the volume and quality of septal cartilage would be transformative in facial plastic and reconstructive procedures. At present, there is an insufficient characterization of the cellular, and molecular changes that occur after cartilage has been harvested, and manipulated or injured to fit a given defect. In practice, the autograft cartilage is crushed, morselized, scraped, scraped, or shaved to increase plasticity and utilization potential based on the needs of the patient. In this study, we will clarify the changes that occur within cartilage from a structural and biomolecular perspective. We will further attempt to improve cartilage survival using a previously identified mitogenic growth factor, FGF-18 that has been shown to stabilize articular cartilage and increase chondrocyte function.

Cartilage grafting is required in rhinoplasty and other facial plastic and reconstructive procedures. In this presentation, we will first introduce the audience to basic concepts in rhinoplasty surgery. We will define the clinical problems in rhinoplasty associated with the limited amount of cartilage available from local sources in the head and neck, which is the problem we are aiming to solve through our research approaches. We will describe the manipulated cartilage characteristics and the clinically relevant implications of these findings on anticipated cartilage strength and survival in the rhinoplasty patient. Additionally, we will describe from this pilot project initial studies using the growth factor FGF-18 to augment or enhance cartilage characteristics in this area of the musculoskeletal system.

Primary Cilia in Skeletal Development and Diseases

Shuying Yang, MD, MS, PhD

Associate Professor

Department of Anatomy & Cell Biology

Primary cilia are membrane bounded microtubule-based organelles emanate from basal body templates. Primary cilia are existed on almost all vertebrate cells and have a variety of functions, including sensory reception and cellular signaling transduction. Cilia do not have ribosome; therefore, the ciliary proteins must be synthesized in the cytosol and transported to cilia by intraflagellar transport (IFT) bidirectional machinery. The core parts of the IFT machinery are IFT complex A and IFT complex B. Mutation of these IFT proteins caused serious diseases such as cancer, blindness, diabetes, severe cranial malformations, malposition of the heart, kidney cysts, and variety of skeletal abnormalities. Increasing studies have shown that primary cilia/IFT proteins are highly involved in skeletal disorders or diseases. However, the function and mechanism of IFT/cilia proteins in bone development and diseases are still largely undefined. By combining genetics, cell and molecular biology, and biochemistry technologies, our laboratory investigates the molecular basis by which IFT proteins and primary cilia regulate bone formation and diseases. In this talk, I will report our findings about IFT proteins in regulation of cilia formation and bone cell differentiation and function, and highlight the major effect of these proteins on bone and cartilage formation during development and in bone disease models.

Defining the Impact of CD44 on Fibrillar Collagen Accumulation and Tensile Strength in Cutaneous Wound Healing

Priya Govindaraju and Ellen Puré

Cutaneous wound healing occurs through blood clotting, inflammation, re-epithelialization and tissue remodeling. Stroma cell-dependent tissue remodeling involves dynamic restructuring of the fibrillar collagen rich extracellular matrix (ECM). Typically the response to injury is self-limiting and leads to restoration of normal skin function and biomechanics. However, persistent accumulation of fibrillar collagen, the principal ECM protein found in the skin, can result in hypertrophic scar formation and highly compromised skin function and aberrant biomechanical properties compared to normal skin. Hyaluronic acid (HA), the predominant glycosaminoglycan associated with the injury response is upregulated early following injury and persists during wound healing. Furthermore, evidence suggests that HA regulates collagen accumulation and impacts collagen architecture and thereby influences the outcome of wound healing. Thus, defining mechanisms that govern ECM dynamics is vital to understanding normal versus pathological hypertrophic scarring and developing approaches to prevent scarring.

The principle receptor for HA is CD44, an adhesion receptor expressed on nearly all cell types present in dermis. Although CD44 has been implicated in an array of inflammation and fibrosis such as leukocyte recruitment, T-cell extravasation, and HA metabolism, the role of CD44 in cutaneous wound healing and fibrillar collagen accumulation remains unknown. To define the role of CD44 we compared wound healing in wild-type (WT) and CD44 global knockout mice using a biopsy punch injury model. We found that CD44-deficient mice exhibit increased collagen synthesis leading to increased accumulation of fibrillar collagen at wound closure compared to WT mice. This increase in fibrillar collagen accumulation persisted after wound closure leading to reduced tensile strength thus, recapitulating a more severe scarring phenotype. These data indicate that CD44 plays a previously unknown role in fibrillar collagen accumulation during the response to cutaneous injury. We are currently investigating the mechanisms by which CD44-mediated signaling and/or CD44-ECM interactions regulates the dynamics of fibrillar collagen and thereby contributes to normal wound repair.

Med Device Innovation in Academia – Entrepreneurship in the Publish-or-Perish Paradigm

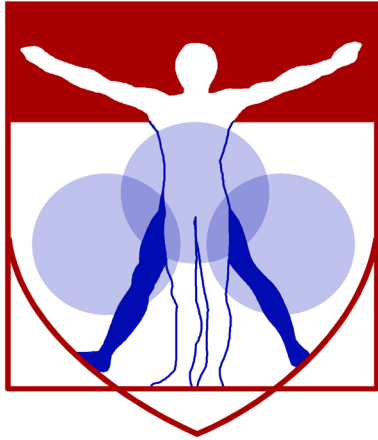
Matthew R. Maltese, PhD
Research Assistant Professor

Academic scientists are professionally incentivized to discover new things and write about them. Research funding is essential, and it comes when we align our scientific inquiry with the priorities of the funder which in turn are (hopefully) a reflection of societal need. Over the past decade we have witnessed a entrepreneurial revolution in our institution and in our country. Commercialization of an idea requires capitalistic thinking, which involves comparing market size with the cost of bringing a product to market (clinical trials, regulatory pathway, bench studies, IP, production, etc . . .). Scientists who want their ideas to go beyond publication and mature into products for the benefit of humankind must think of the entire pathway to commercialization at the ideation the stage. Then, when scientists choose to embark on the entrepreneurial journey they must understand two things: a) large portions of their day-to-day activity will not count toward academic promotion, and b) to bring their idea to the point where it helps society might require their temporary or permanent departure from academia. In this talk, we explore several examples of entrepreneur-scientists and how they brought their ideas to reality while maintaining their ties to academia. Several case example of translation of science to product, including some from the author, will be described. Audience attendees will gain and understanding of the commitment required, and extraordinary personal and professional satisfaction, that comes from academic entrepreneurship.

Toward bioengineering translation

Kyriacos A. Athanasiou, Ph.D.
Distinguished Professor, Biomedical Engineering
Director, DELTAi (Driving Engineering & Life-science Translational Advances @ Irvine)
(Editor-in-Chief, Annals of Biomedical Engineering
University of California, Irvine)

This presentation will cover three different areas: Articular cartilage healing and technology translation. Articular cartilage is arguably the tissue most pivotal for motion and overall function. This soft, white tissue that covers the ends of our long bones cannot heal by itself often progressing to osteoarthritis following injury. The demanding biomechanical milieu of a joint, plus cartilage's relative lack of cells and blood supply, renders this tissue almost unique in its inability to repair adequately. This presentation will describe our group's efforts toward helping joint cartilages, such as hyaline tissue, knee meniscus, and the TMJ disc, repair themselves via tissue engineering approaches. Central to our efforts is the understanding the biomechanical relationships at multiple dimensional levels. Also shown will be some of our latest results using various stem cell sources that indicate that cartilage regeneration is inexorably becoming a tractable problem. The second part of the presentation will be allocated on efforts to commercialize outcomes of our academe-based research. Specific examples and results will be presented to illustrate a specific pathway of commercializing research outcomes.



PENN

CENTER for

MUSCULOSKELETAL

DISORDERS

Biomechanics Abstracts

Nanostructure and Biomechanics of Fibrocartilage Pericellular Matrix: Roles of Collagen V

Chao Wang¹, Qing Li¹, Su-Jin Heo², Sheila M. Adams³, Mei Sun³, Motomi Enomoto-Iwamoto⁴, Robert L. Mauck², David E. Birk³, Lin Han¹

¹Drexel University, Philadelphia, PA; ²University of Pennsylvania, Philadelphia, PA;

³University of South Florida, Tampa, FL; ⁴University of Maryland, Baltimore, MD.

Disclosures: Chao Wang (N), Qing Li (N), Su-Jin Heo (N), Sheila M. Adams (N), Mei Sun (N), Motomi Enomoto-Iwamoto (N), Robert L. Mauck (N), David E. Birk (N), Lin Han (N).

INTRODUCTION: The pericellular matrix (PCM) is a structurally distinct, μm -sized domain [1]. Due to its immediate contact with each cell, PCM is pivotal in regulating cell-extracellular matrix (ECM) interactions. The importance of PCM in mechanobiology has been well recognized for chondrocytes in the compression-bearing hyaline cartilage [2]. However, for tension-bearing fibrocartilage, understanding of the PCM is very limited. Recent studies have shown that in fibrocartilage, the PCM exhibits distinct mechanical properties from the ECM [3], indicating a potential role of PCM in mediating cell strain and mechanosensing. In addition, the PCM is also the location for the early molecular events of cell-mediated ECM formation, wherein collagen V-mediated fibril nucleation, the initiation step in collagen I fibrillogenesis, takes place in the PCM [4]. Therefore, knowledge of biomechanical properties of the PCM can lay a foundation for understanding both the mechanotransduction of cells and the assembly of ECM in fibrocartilage. We hypothesize that collagen V is important in the regulation of structure and mechanical characteristics of fibrocartilage PCM. In this study, we query the roles of collagen V in fibrocartilage PCM by comparing wild-type (WT) versus heterozygous collagen V-null mice (*Col5a1*^{+/-}) menisci, the direct loading counterpart of knee cartilage.

METHODS: Medial menisci were harvested from 3-month WT and *Col5a1*^{+/-} C57BL/6J male mice. *Col5a1*^{-/-} mice were not included due to their embryonic lethality [5]. To reveal the localization of proteoglycans and collagens in the PCM, we applied immunofluorescence (IF) and histological imaging. To quantify the PCM mechanical properties, we prepared 6- μm -thick, unfixed horizontal cryo-sections [6] of the meniscus, and immuno-labelled the PCM with perlecan. Guided by IF-imaging, AFM-nanomechanical mapping was performed in PBS using a microspherical tip ($R \approx 2.25\mu\text{m}$, $k \approx 1\text{ N/m}$, μMasch) and an MFP-3D AFM. For each map, a 40×40 indentation grid was acquired over a $20 \times 20\ \mu\text{m}^2$ region of interest containing well-defined, ring-shaped PCM terrains. The effective indentation modulus, E_{ind} , was calculated by using finite thickness-corrected Hertz model [7]. To assess collagen fibril structure, SEM on horizontal sections and TEM on vertical sections [8] were performed. Two-sample *t*-test was used for statistical test at $\alpha = 0.05$.

RESULTS: WT meniscus PCM was rich in aggrecan and perlecan, resulting in concentrated sGAG (sulfated glycoaminoglycans) (Fig. 1a, c). While collagen V is distributed more in PCM, collagen VI, a cartilage PCM biomarker, is present in both PCM and ECM (Fig. 1c). The PCM contained network of porous, randomly oriented, thin fibrils, which was distinct from the ECM that is dominated by highly aligned, thick collagen I fibers along the circumferential direction (Fig. 1b). In comparison to the WT, *Col5a1*^{+/-} meniscus PCM exhibited larger fibril diameter and heterogeneity and fibril number than WT. Such effect was different from the ECM phenotype, which had similar average diameter, higher heterogeneity, but reduced fibril number (Fig. 2b). These structural defects contributed to a reduced E_{ind} in both the PCM and ECM for *Col5a1*^{+/-} meniscus. For both genotypes, the PCM had a lower E_{ind} than the ECM (Fig. 3c).

DISCUSSION: The unique composition, structure and mechanical features of meniscus PCM indicate that the PCM can play a critical role in mediating cell mechanotransduction during joint loading, when the cell-PCM units are interspersed between the aligned ECM fibers. Under tensile loading, stretching of ECM fibers leads to transverse compression of the PCM and cell. In response, osmotic pressure provided by negatively charged GAGs can resist transverse compression [9], thereby attenuating cell strain. It is thus possible for the PCM to mediate tensile mechanotransduction of fibrochondrocytes and to protect them from overloading. This hypothesis motivated our ongoing studies to directly measure the strain transmission from ECM to cell under tensile loading.

The differentiated phenotype of *Col5a1*^{+/-} PCM versus ECM provides new understanding of matrix assembly. Collagen V provides the necessary nucleation site for initiating collagen I fibrillogenesis [10]. The localization of collagen V provides direct evidence on its PCM-specific activities (Fig. 1c). Indeed, phenotype of *Col5a1*^{+/-} PCM illustrates that upon collagen V reduction, fibril nucleation occurs in a less controlled manner in the PCM, leading to higher fibril diameter, heterogeneity and increased fibril numbers (Fig. 2b). At a later stage, when fibrils assembled in the PCM undergo lateral growth in the interterritorial domain, the ones lacking the collagen V encounter less hindrance to lateral fusion, leading to the formation of abnormally thick fibrils and reduced fibril numbers (Fig. 2b). Therefore, our results show that the co-assembly of collagens V and I, which mainly takes place in the PCM [11], is necessary for maintaining the ECM fibril homogeneity by limiting fibril lateral growth in the ECM. As a result, reduction in collagen V leads to disrupted structural integrity for both PCM and ECM, resulting in reduced modulus (Fig. 3c).

SIGNIFICANCE: This is the first study on the unique structure and mechanical features of the fibrocartilage PCM, and the PCM-specific functions of collagen V. This knowledge will enable the development of novel PCM-based strategies in modulating cell mechanotransduction and fibrocartilage regeneration in vitro.

REFERENCES: [1] Poole, CA et al., *J. Orthop. Res.* 5:509-522, 1987. [2] Wilusz, RE et al., *Matrix Biol.* 39:25-32, 2014. [3] Sanchez-Adams, J et al., *J Orthop Res* 31:1218-1225, 2013. [4] Wenstrup, RJ et al., *J. Biol. Chem.* 279:53331-53337, 2004. [5] Wenstrup, RJ et al., *J. Cell. Biochem.* 92:113-124, 2004. [6] Kawamoto, T et al., *Methods Mol. Biol.* 1130:149-164, 2014. [7] Dimitriadis, EK et al., *Biophys. J.* 82:2798-2810, 2002. [8] Dunkman, AA et al., *Matrix Biol* 32:3-13, 2013. [9] Han, WM et al., *Nat. Mater.* 15:477-484, 2016. [10] Wenstrup, RJ et al., *J Biol Chem* 286:20455-20465, 2011. [11] Smith, SM et al., *Matrix Biol* 33:47-53, 2014.

ACKNOWLEDGEMENTS: This work was supported by NIH AR066824.

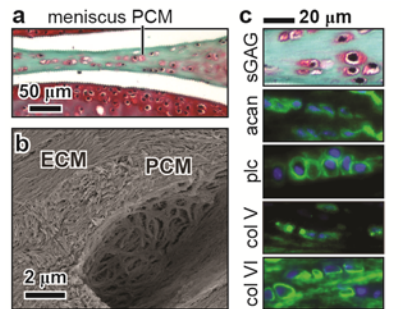


Fig. 1 a) Saf-O/Fast Green histology shows the PCM of meniscus in murine knees. b) SEM image highlights the random collagen fibril structure in the meniscus PCM. c) Histology and immunofluorescence images show that sGAGs, aggrecan (acan), perlecan (plc) and col V, but not col VI, are localized in the PCM.

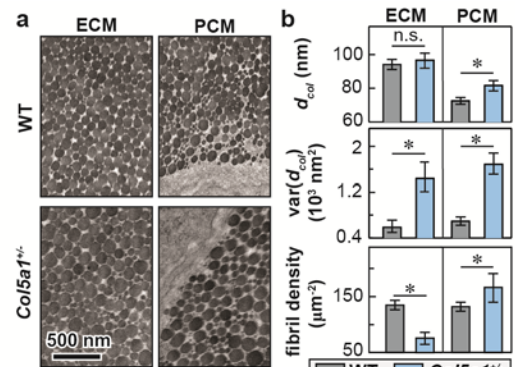


Fig. 2 Comparison of WT and *Col5a1*^{+/-} meniscus PCM and ECM fibril nanostructure. a) Representative TEM images. b) fibril diameter, variance and fibril density (mean \pm 95% CI from ≥ 300 fibrils from 3 animals for each, *: $p < 0.01$).

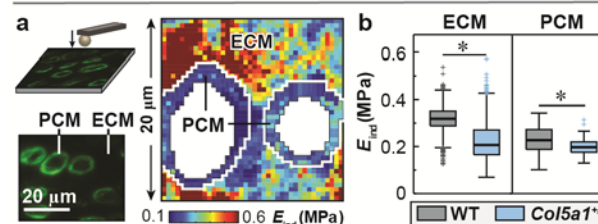


Fig. 3 a) IF-guided AFM: representative perlecan IF image from adult meniscus cryo-section and corresponding ECM-PCM modulus map via a microspherical tip in PBS ($R \approx 2.25\ \mu\text{m}$). b) Both the PCM and ECM shows reduced E_{ind} between in *Col5a1*^{+/-} meniscus in comparison to the WT control (*: $p < 0.001$, mean \pm 95% CI, ≥ 200 locations from 3 animals).

Structural and In Vivo Functional Measures Predict Achilles Tendon Fatigue Mechanics During Healing

Shetye SS, Freedman BR, Fryhofer GW, Riggan CN, Gordon JA, Thomas SJ, Farber DC, Soslowsky LJ
 McKay Orthopaedic Research Laboratory
 University of Pennsylvania, Philadelphia, PA

Disclosures: Shetye SS (N), Freedman BR (N), Fryhofer GW (N), Riggan CN (N), Gordon JA (N), Thomas SJ (N), Farber DC (N), Soslowsky LJ(N)

INTRODUCTION: The Achilles tendon is one of the most commonly injured tendons, affecting approximately 31 in 100,000 people each year [1]. Previous *laboratory* studies have shown that specific mechanical and material properties of the rat Achilles tendon in the post-injury period may be used to assess healing quality; however, direct *clinical* measurement of these mechanical properties is not yet possible [2-5]. Further, indirect functional measures, such as the “hop test” currently used clinically, are not capable of isolating specific tendon properties [6]. Therefore, the purpose of this study was to use multiple regression analyses to identify clinically measurable functional and structural outcomes capable of predicting the mechanical properties of healing Achilles tendon. We hypothesized that tendon properties, including cross sectional area (CSA), echogenicity, collagen fiber alignment, weight-bearing, and ankle range of motion would be strongly predictive of post-injury tendon fatigue mechanical properties.

METHODS: Study Design: Data used in this multiple regression statistical analysis study were obtained from previous studies using rat Achilles tendon blunt transection injury models, which incorporated post-injury immobilization and gradual return to treadmill activity ($n = 110$). Complete data sets needed for developing a robust regression model were acquired in the months of October and November 2016. Studies #1 [2] and #2 [3] investigated the role of surgical treatment (repaired [R] vs. non-repaired [NR]) and return to activity timing at 3 and 6 weeks post-injury in male rats. Study #3 [5] evaluated tendon healing at 3 and 6 weeks post-injury on injured female and ovariectomized (OVX) rats that underwent NR treatment. **Regression Modeling:** The predictor variables were: measures of collagen structure (echogenicity and circular standard deviation (CSD) (*high frequency ultrasound*)); active functional limb assessment (vertical, braking, propulsion, and lateral ground reaction force magnitudes (*gait analysis*)); tendon morphology (CSA (*laser-based measurement*)); and passive functional limb assessment (total ankle ROM, toe, and linear stiffness in dorsiflexion and plantarflexion (*passive ankle manipulation*)). Sex (M = [1,0], F = [0,1], OVX = [0,0]) and surgical treatment (NR = 1, R = 0) were inputted as categorical variables. The response variables were secant stiffness, hysteresis, laxity, secant modulus, and secondary phase slope (fatigue testing). Assumptions requisite for linear regression analysis were general linearity between single predictor and dependent variables, normality, nonmulticollinearity (Durbin-Watson), neutrality of the dependent variables, and lack of significant outliers. Step-wise backward elimination linear regression analysis was performed on the combined data set to select the best structural and functional variables for predicting mechanical properties. The resulting regression coefficients were then used to predict mechanical properties for all groups. **Statistical Significance Evaluation:** Coefficients of determination and two-tailed p-values were calculated for each regression model and significance was set at $p < 0.05$ for all tests (SPSS, IBM, Inc., Version 24, Armonk, NY).

RESULTS: All assumptions for multiple regression were satisfied and Durbin-Watson scores were greater than 1.62 for all models presented (Table 1). The chosen independent variables strongly predicted secant modulus and hysteresis ($R^2 > 0.74$, $p < 0.001$). Secant stiffness and laxity were moderately predicted by the chosen independent variables, with R^2 values of 0.34 and 0.46, respectively. Although statistically significant, the slope of the secondary phase was only weakly predicted by the independent variables. Repair type and plantarflexion linear stiffness were involved in predicting four of the five response variables. Sex was a contributing factor in predicting hysteresis, laxity, and secondary phase slope. Dorsiflexion linear stiffness, plantarflexion toe stiffness, lateral force, echogenicity, and total ankle ROM were not significantly predictive in any regression model.

DISCUSSION: The Achilles tendon typically operates under high and cyclic loading scenarios, which can result in tendinopathy and potentially lead to acute rupture. Following treatment and rehabilitation, injured tendons are expected to perform under similar physiologic cyclic loading conditions. Evaluation of tendon mechanics will be critical in making informed decisions regarding preparation to withstand these physiologic loads. Clinical assays such as ultrasound, gait analysis, and passive joint assessment cannot directly evaluate tendon fatigue properties. However, since many of these assays are generally simple to perform, but currently not employed in the clinic on a routine basis, defining their relative importance would be of great benefit to clinicians. Our regression results suggest that clinical evaluation of ankle joint stiffness into plantarflexion may serve as a viable metric for estimating and tracking tendon strength after injury. Further, CSA measurements may allow clinicians to predict the healing tendon’s efficiency in managing stored elastic energy (hysteresis) and ability in bearing load (secant modulus). Both parameters are crucial for allowing the tendon to resist failure under cyclic load during activities of daily living. Surprisingly, unlike ankle stiffness and cross-sectional area, parameters obtained from ultrasound (echogenicity, CSD) were not predictive of tendon fatigue properties, in contrast to a previous study [7]. Although both studies had similar coefficients of determination between echogenicity and secant stiffness, the other functional measures included in our model were more significantly predictive. Finally, in this study, CSA values were obtained using a laser-based technique not performed in humans; however, transverse plane ultrasound methods are in use clinically, and can provide similar area measurements that correlate very well to laboratory-based measurements [8]. Overall, clinically relevant in vivo functional measures were able to assess healing tendon quality by accurately predicting tendon fatigue mechanical properties.

SIGNIFICANCE: This study highlighted specific clinical measurements of tendon properties that reliably and significantly predicted the quality of tendon healing. This was achieved through controlled and rigorous laboratory experiments not generally feasible in the clinical setting.

REFERENCES: [1] Ganestam, et al., 2016. *KSSTA*.; 24(12):3730-3737 [2] Freedman, et al., 2016. *JOR* 2016, *In press* [3] Freedman, et al., 2016. *In review* [4] Pardes, et al., 2016 *J Biomech*. ;49(3):376-81 [5] Fryhofer, et al., 2016 *JAP*. ;121(5):1106-1114 [6] Chiodo, et al., 2010. *JAAOS*, 18:502-510. [7] Chamberlain, et al., *Annals of BME* 2013;41(3):477-87 [8] Smith, et al., *EVJ* 1994 ;26(6):460-5

ACKNOWLEDGEMENTS: This study was supported by NIH (R01AR064216, P30AR069619, T32AR007132, and TL1TR000138) and the NSF GRFP. We thank Jennica Tucker, Tyler Morris, Courtney Nuss, Robert Zanes, and Nabeel Salka for assistance.

Table 1 - Significant coefficient results using multiple regression analysis.

Response variable	R ²	p	CSA (mm ²)	CSD (°)	Dorsi.Toe Stiffness (N*mm/deg)	Plantar Lin Stiffness (N*mm/deg)	Vertical Force (%BW)	Propulsion Force (%BW)	Braking Force (%BW)	Ankle ROM (°)	Sex	Repair Type
Secant Stiffness (N/mm)	0.34	<0.001	---	---	---	-34.3	0.1	0.8	---	---	---	---
Hysteresis (MPa mm/mm)	0.74	<0.001	0.0003	---	-0.01	-0.04	---	---	---	-0.00006	0.008	0.002
Laxity (mm/mm)	0.46	<0.001	---	---	-19.9	2.3	---	---	---	---	2.3	-18.6
Secant Modulus (N/mm ²)	0.76	<0.001	-2.9	-3.3	---	-53.1	0.3	---	-0.9	---	---	-5.8
2 nd Phase Slope (mm/mm / % fatigue life)	0.11	0.036	---	---	---	---	---	---	---	---	0.017	0.016

Collagen V Haploinsufficiency Results in Deficient Mechanical and Structural Recovery of Injured Mouse Patellar Tendons

Snehal S. Shetye¹, Jessica M. Johnston¹, Brianne K. Connizzo¹, Kelsey A. Robinson¹, Julianne Huegel¹, Ashley B. Rodriguez¹, Mei Sun², Sheila M. Adams², David E. Birk², Louis J. Soslowsky¹

¹University of Pennsylvania, Philadelphia, PA, ²University of South Florida, Tampa, Florida

²Department of Molecular Pharmacology & Physiology, University of South Florida College of Medicine, Tampa, FL

Disclosures: Snehal S. Shetye (N), Jessica M. Johnston (N), Brianne K. Connizzo (N), Kelsey A. Robinson (N), Julianne Huegel (N), Ashley B. Rodriguez (N), Mei Sun (N), Sheila M. Adams (N), David E. Birk (N), Louis J. Soslowsky (N)

INTRODUCTION: Classic Ehlers-Danlos syndrome (EDS) patients suffer from connective tissue hyperelasticity, joint instability, and skin hyperextensibility due to mutations in the *Col5a1* and *Col5a2* genes with the most common being haploinsufficiency of the *Col5a1* gene. The role of collagen V in fibrillogenesis in tissues such as skin, cornea, and tendon has been firmly established [2], wherein collagen V haploinsufficiency leads to abnormal tissue development and altered collagen assembly. Patients with EDS display abnormal wound healing and scarring and recent studies have shown that injured skin from mice haploinsufficient for *Col5a1* have reduced tensile strength [3]. However, the role of collagen V in injured EDS tendons is unknown. Therefore, the objective of this study was to use the *Col5a1*^{+/−} mouse model to define the regulatory roles of collagen V in injured normal and classic EDS tendons. We hypothesized that tendons from heterozygous (HET) collagen V mice would heal more poorly (specifically, with decreased mechanical properties and increased fibril diameters) than tendons from wild-type (WT) mice.

METHODS: Adult male WT C57/BL6 and HET *Col5a1*^{+/−} EDS mice (n = 90) were used in an IACUC approved protocol. All animals underwent bilateral patellar tendon injury as described [4] at 120 days of age. Mice were then euthanized at 1, 3, or 6 weeks post injury. Uninjured tendons at 150 days of age were also assessed from both genotypes to determine baseline values for all properties. **Mechanics.** The patella-patellar tendon-tibia complexes were dissected from the knee and prepared for mechanical testing as described [5] at 3 and 6 weeks post injury. Tendons were subjected to a viscoelastic testing protocol as described [5, 6]. Tendon length was measured at nominal load prior to test initiation. **Histology.** Whole knees were grossly dissected (n=4/group at 1, 3, and 6 weeks post injury) and processed for paraffin sectioning. Coronal sections (7 μm) were stained with H&E. Each section was then evaluated for cellularity and cell shape (tendon proper only) [5]. **Electron Microscopy.** Samples for TEM (n=4/group at 3 and 6 weeks post injury) were prepared as described [4]. Ten non-overlapping digital images from cross-sections were obtained from the central (uninjured tendons) or injured areas of each specimen. Diameters were measured along the minor fibril axis. **Statistics.** Two-way ANOVAs with post-hoc Bonferroni tests were used to assess the effects of genotype and time on mechanical and structural properties. Non-parametric Kruskal-Wallis tests were used to analyze cell shape and cellularity results. Mann-Whitney tests (for nonparametric data) were used to compare fibril diameters between genotype at each time point.

RESULTS: Mechanical properties Uninjured HET tendons were significantly longer when compared with the uninjured WT tendons (Fig. 1A). No differences were observed in tendon length at 3 and 6 weeks post injury. Uninjured WT tendons were stiffer than HET tendons, as well as at 6 weeks post injury (Fig. 1B). HET tendons had significantly lower modulus when compared to WT tendons at 6 weeks post injury (Fig. 1C). **Histological observations** Both the HET and WT tendons showed the expected temporal tendon injury response with a significant decrease in cellularity and increased elongation of cells between 1 week and 6 weeks post injury. No differences were noted between genotypes at any time point (data not shown). **Electron microscopy** The median fibril diameter was larger for the HET tendons pre-injury and at 3 weeks post injury.

However, at 6 weeks post injury, the HET tendons had smaller median fibril diameter than WT patellar tendons (Fig. 2). Further, HET tendons had substantially altered fibril diameter distributions when compared to the WT tendons pre-injury and 3 weeks post injury (data not shown).

DISCUSSION: Overall, there was a diminished mechanical response from the HET patellar tendons before and after injury, which was consistent with our hypothesis. Specifically, we found a trend of decreased stiffness in the pre-injury HET group, which has also been observed for supraspinatus tendons in HET mice [7]. Post-injury, the wild type patellar tendons regained their pre-injury stiffness by 6 weeks, which was not the case for the HET tendons. It has been shown previously that *Col5a1* is significantly upregulated after injury in normal tissues [8]. However, this upregulation is diminished in the *Col5a1* HET group, which explains the inferior mechanical recovery at 3 and 6 weeks post injury. The trend of smaller uninjured wild type tendon fibrils as compared to those from HET tendons was expected, since a similar trend exists in supraspinatus tendons, skin, cornea and the flexor digitorum longus [2, 9, 10]. The HET tendons had smaller fibrils at 6 weeks post injury, potentially indicating failure in the healing response due to reduced collagen V upregulation. In contrast, the median fibril diameter of the WT tendons at 6 weeks was larger when compared to the median fibril diameter at 3 weeks. Future studies will further clarify the role of collagen V injury via an inducible *Col5a1* knock-out mouse model.

SIGNIFICANCE: These studies begin to define the role of collagen V in the temporal healing response of injured mouse patellar tendons.

REFERENCES: [1] Symoens S, et al. Hum Mutat. 33:1485-93, 2012. [2] Wenstrup RJ, et al. J Biol Chem. 279:53331-7, 2004. [3] Wenstrup RJ, et al. J Biol Chem. 279:53331-7, 2006. [4] Dunkman AA, et al. Matrix Biol. 32:3-13, 2013. [5] Dunkman AA, et al. Matrix Biol. 32(1):3-13, 2013. [6] Miller KS, et al. J Biomech Eng. 134(3):031007, 2012. [7] Connizzo et al. Interface Focus. 6(1):20150043, 2016. [8] Birk et al. J. Cell Biol. (1988) [9] Sun et al. J Cell Sci. (2011) [10] Connizzo et al. J Ortho. Res. (2015)

ACKNOWLEDGEMENTS: This study was supported by NIH/NIAMS AR065995, AR044745 and the Penn Center for Musculoskeletal Disorders (NIH/NIAMS, P30 AR0069619). We thank Carrie Barnum, Stephanie Weiss, and Dr. Cody Hillin for their assistance.

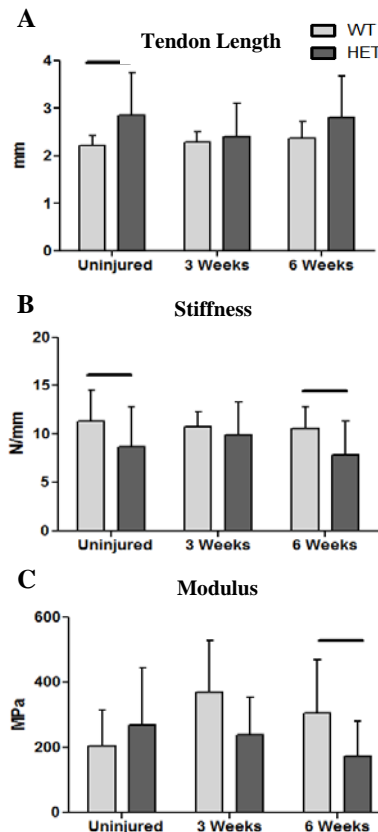


Figure 1 - (A) Tendon length was higher for the uninjured HET tendons as compared to the WT controls **(B)** Stiffness was significantly reduced for the uninjured HET tendons and at 6 weeks post injury. **(C)** The modulus of HET patellar tendons was significantly lower at 6 weeks post injury.

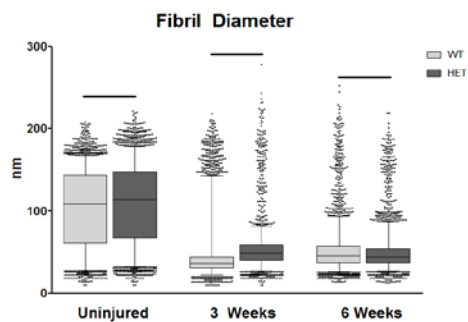


Figure 2 - Collagen fibril diameters for the HET tendons were significantly larger pre-injury and at 3 weeks post injury. In contrast, the WT tendons had a larger median fibril diameter at 6 weeks post injury. Boxplot whiskers span data between the 5th and 95th percentile. Data points outside this range are shown with individual markers.

Biceps Tenotomy in the Presence of a Supraspinatus Tear Alters the Adjacent Intact Tendons and Glenoid Cartilage

Zakary M Beach, Jennica J Tucker, Stephen J Thomas, Katherine E Reuther, Chancellor F Gray, Chang-Soo Lee, David L Glaser, Louis J Soslowsky
McKay Orthopaedic Research Laboratory, University of Pennsylvania, Philadelphia, PA

Soslowsk@upenn.edu

Disclosures: ZM Beach (N), JJ Tucker (N), SJ Thomas (N), KE Reuther (N), CF Gray (N), CS Lee (N), DL Glaser (N), LJ Soslowsky (N)

INTRODUCTION: A rotator cuff tear is a common injury in athletes and workers who repeatedly perform overhead movements, and it is not uncommon for this demographic to return to activity shortly after treatment. A biceps tenotomy is often performed in the presence of a rotator cuff tear to help reduce pain and improve joint function [1]. However, the effect of this procedure on the surrounding tissues in the glenohumeral joint is unknown. Therefore, the purpose of this study was to investigate the effect of a biceps tenotomy in the presence of a supraspinatus rotator cuff tear followed by overuse activity on ambulatory function and mechanical and histologic properties of the remaining rotator cuff tendons and glenohumeral articular cartilage. We hypothesized that a biceps tenotomy in the presence of a supraspinatus tear, followed by overuse, would result in adverse changes in the surrounding tissues demonstrated by a decrease in joint function, as well as decreased mechanics and increased cellular activity in the intact tendons and glenoid cartilage.

METHODS: *Experimental Design:* 46 adult male Sprague–Dawley rats underwent 4 weeks of overuse activity (downhill (10°) treadmill running at 17 m/min for 1h/day, 5 days/week) [2] to create a tendinopathic condition in the supraspinatus tendon. Next, the animals were randomized into two groups: unilateral detachment of the supraspinatus tendon alone (SO) or detachment of the supraspinatus and long head of the biceps tendons (SB), as previously described [3]. After surgery, animals were allowed 1 week of cage activity before returning to the overuse training over 2 weeks. After training, all animals underwent 5 weeks of overuse activity [4]. *Ambulatory Measurement:* Forelimb gait and ground reaction forces were quantified using an instrumented walkway [4]. Data was collected 1 day prior to tendon detachment to obtain baseline values and also at 3, 7, 14, 28, 42 and 56 days post-surgery. *Tendon Mechanical Testing:* Tendon testing was performed as previously described [3]. Briefly, stain lines were used to track optical strain. Cross-sectional area was measured using a custom laser device [5]. Tensile testing was performed as follows: preload to 0.08 N, preconditioning (10 cycles of 0.1-0.5 N at a rate of 1% strain/s), stress relaxation to 5% strain at a rate of 5% strain/s for 600 seconds, and ramp to failure at 0.3% strain/s. *Cartilage Mechanical Testing:* For cartilage thickness measurements [4], specimens were scanned using ultrasound. Each thickness map was divided into six regions, and a mean thickness was computed for each region. Utilizing a 0.5-mm-diameter, nonporous spherical indenter, cartilage indentation testing was performed [4]. Briefly, a preload (0.005 N) was followed by eight stepwise stress relaxation tests (8 μm ramp at 2 μm/second followed by a 300 second hold). Equilibrium elastic modulus was calculated, as described [6], at 20% indentation thickness and assuming Poisson's ratio ($\nu = 0.30$). *Histology:* Tendon samples were stained with hematoxylin and eosin, while cartilage samples were stained with safranin O, fast green and iron hematoxylin. Tendon sections were graded for cellularity and cell shape [4]. Cartilage sections were graded using a modified Mankin Score [7]. *Statistical Design:* For ambulation data, significance was assessed using a two-way ANOVA, followed by paired t-tests when appropriate. Multiple imputations for missing data (~15%) were conducted on the ambulatory measures. Tendon and cartilage mechanics were evaluated using t-tests. For histology, median grades were compared between groups using a Mann-Whitney test. Significance was set at $p < 0.05$.

RESULTS: Biceps tenotomy resulted in no differences in ambulatory measurements. The lower subscapularis tendon did not show any changes in the area of the insertion or midsubstance between groups. However, the upper subscapularis tendon was increased in the insertion area in the presence of the detachment of the long head of the biceps (Fig. 1). Increases in midsubstance areas were also found in the infraspinatus and upper subscapularis tendons (Fig. 2). An increase in tendon midsubstance elastic modulus was also seen in the upper subscapularis tendon (Fig. 3). Biceps tenotomy did not reveal changes in elastic modulus in the insertion of the infraspinatus, lower subscapularis or upper subscapularis tendons. Histology showed a significantly increased score for cell shape in the midsubstance of the infraspinatus tendon, signifying that the cells present may be more metabolically active. Results showed no differences in the lower or upper subscapularis tendons in cellularity or cell shape in any region. The biceps tenotomy group showed a significant decrease in glenoid articular cartilage thickness in the anterior-superior region and a significant increase in the superior region when compared to the intact long head of biceps tendon group (Fig. 4). The biceps tenotomy group also showed significantly greater equilibrium elastic modulus in the center and anterior-superior regions (Fig. 5). Histology showed significant increases in modified Mankin score in the biceps tenotomy group in the center, anterior-superior and posterior-superior regions of the glenoid articular cartilage.

DISCUSSION: Results suggest that the tissues in the surrounding joint are altered when a biceps tenotomy is performed in the presence of a supraspinatus only rotator cuff tear. The alterations seen in the infraspinatus and upper subscapularis tendons in the presence of a biceps tenotomy could be caused by an interruption in the anterior-posterior force balance, which has been shown to be important to joint health and function [8]. The altered mechanical properties of the glenoid articular cartilage, combined with the increased modified Mankin score, suggests that a biceps tenotomy in the presence of a supraspinatus tendon tear alters the loading in the superior half of the glenoid articular cartilage, which could be due to increased humeral head translation in the absence of the long head of the biceps tendon [9]. These findings show that the biceps tenotomy exacerbates the negative effects associated with overuse after a supraspinatus only tear [4]. Results indicate that the properties of the surrounding tendons and glenoid cartilage are negatively altered in the presence of the biceps tenotomy, perhaps due to decreased joint stability. Future studies are needed for further investigation concerning biceps tenotomy in the presence of a rotator cuff tear in humans to determine whether the short-term pain-relief of the biceps tenotomy results in increased joint damage long-term.

SIGNIFICANCE: This work demonstrates that a biceps tenotomy in the presence of a supraspinatus tendon rotator cuff tear negatively affects the surrounding tissues in the rotator cuff. Therefore, alternative methods of treatment should be explored that aim to address patient-specific problems while preserving long-term joint health.

REFERENCES: [1] Szabo I, et al., Sports Med Arthrosc, 2008. [2] Soslowsky LJ, et al., J Shoulder Elbow, 2000. [3] Peltz CD, et al., JOR, 2009. [4] Reuther KE, et al., JOR, 2012. [5] Favata M., PhD Thesis, University of Pennsylvania, 2006. [6] Hayes WC, et al., J Biomechanics, 1972. [7] Salo PT, et al., JOR, 2002. [8] Thomas SJ, et al., CORR, 2014. [9] Alexander S, et al., J Shoulder Elbow, 2013.

ACKNOWLEDGEMENTS: This study was funded by the NIH/NIAMS (R01 AR056658) and the Penn Center for Musculoskeletal Disorders (P30 AR069 619). The authors thank Daniel Choi, James Cirone, Brianne Connizzo, George Fryhofer and Nabeel Salka for their contributions.

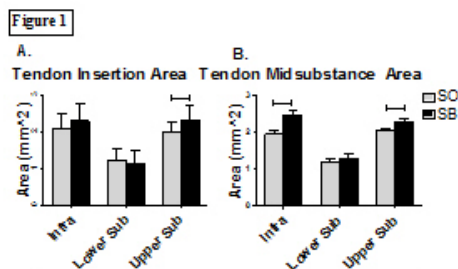


Fig 1. A) Infra and upper subscap tendon midsubstance area was increased in SB group. B) Upper subscap tendon insertion area was increased in SB group.

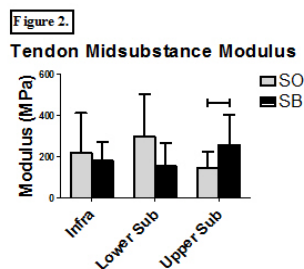


Fig 2. Upper subscap tendon midsubstance elastic modulus was increased in SB group.

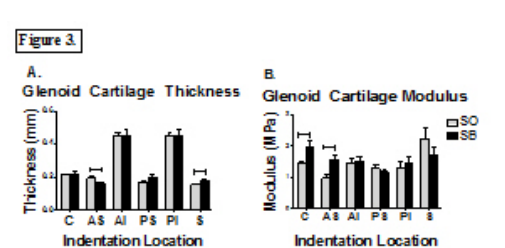


Fig 3. A) Glenoid cartilage thickness was altered in the anterior-superior and superior regions. B) Glenoid cartilage modulus was increased in the center and anterior-superior regions.

Reconstructing Proximal Humerus Fractures with Locking Plates: Don't Miss High?

Samir Mehta¹, Matthew Chin¹, Jennifer Sanville¹, Surena Namdari^{1,2}, and Michael W. Hast¹

¹University of Pennsylvania, Philadelphia, PA

²Rothman Institute, Thomas Jefferson University, Philadelphia, PA

hast@upenn.edu

Disclosures: Samir Mehta (2- AO North America, Smith and Nephew, Zimmer. 3B- Smith and Nephew, Synthes. 5- Amgen Co, Medtronic, Smith and Nephew. 7- Wolters Kluwer Health), Matthew Chin (N), Jennifer Sanville (N), Surena Namdari (1; DJ Orthopaedics, Miami Device Solutions. 2; DJ Orthopaedics. 3B; DJ Orthopaedics, Integra Life Sciences, Miami Device Solutions. 5; Arthrex, Integra, Zimmer. 7; Saunders/Moby-Elsevier.), Michael W. Hast (5; DePuy Synthes, Integra.)

INTRODUCTION: Upper extremity fractures account for one-third of the total incidence of fractures in the elderly [1] and the incidence of proximal humeral fractures significantly increases in osteoporotic bone [1,2]. Current rates of clinical failure are unacceptably high, with humeral head collapse, fixation failure, and hardware-related complications leading to revision rates between 27% and 59.2% in some studies [3,4]. Previous research has indicated that utilizing the calcar as an anchor point for screws is an effective method to provide medial column support (Fig 1) [5,6]. These studies make comparisons of groups that either utilize a calcar screw as an anchoring point or do not; however, they do not characterize the clinically relevant consequence of “missing” the calcar with screw placement during surgery. This study sought to elucidate the mechanisms associated with proximal and distal placement of locking plates in two-part proximal humeral fractures. We hypothesized that neutral placement of the plate would provide the best fixation, while distal and proximal plate locations would exhibit significant reductions in fixation strength.

METHODS: This study was first performed with 9 left osteoporotic humerus Sawbones models (Pacific Research). Specimens were assigned either neutral calcar screw insertion (SN; n=3), 8 mm distal calcar screw insertion (SD; n=3), or 8 mm proximal calcar screw insertion (SP; n=3) (Fig 1). The study was repeated and expanded with nine matched pairs of cadaveric specimens (4 M, 5 F, average age 81.2) in the following groups: CN, n=6; CD, n=6; CP, n=6. All specimens received a two-part 30° wedge osteotomy at the surgical neck of the humerus. Fractures were stabilized using locking proximal humerus plates (LCP Proximal Humerus, DePuy Synthes) with six locking screws. Quasi-static torsional stiffness tests were performed, and quasi-static axial compression tests at 0, +20, -20 degrees of ab/adduction were conducted for all specimens. Cadaveric specimens underwent an additional cyclic fatigue protocol consisting of axial compressive loads between 50-250 N for 5000 cycles at a rate of 1 Hz. A ramp to failure at a rate of 0.1 mm/s was performed after completion of the fatigue test. Maximum humeral head displacement during fatigue loading was measured with optical 3-D motion tracking techniques (OptiTrack), and ultimate load was recorded. One-way ANOVAs with alpha = 0.05 were performed to determine differences within the Sawbones and cadaveric groups.

RESULTS: In the Sawbones experiment, distal placement provided significantly improved construct stiffness over proximal placement in 3 out of 5 assays (Fig 2 and 3). In two cases, distal placement of the implant improved construct stiffness when compared to neutral placement. There were no significant biomechanical differences in angular or axial stiffness between the cadaveric groups. No significant differences were found for maximum displacement or ultimate load. In general, the Sawbones constructs were much more compliant than the cadaveric constructs.

DISCUSSION: Contrary to our overall hypothesis, the results from the Sawbones experiment suggest that distal implant placement is either equal to or stronger than neutral placement while proximal implant placement seems to decrease construct stiffness. However, the results from the cadaveric experiment did not provide similar significant results, as plate placement did not have a significant effect on torsional stiffness, axial stiffness, humeral head displacement, or ultimate load. Variations in human anatomy and bone mineral density led to variations in experimental data and future studies should include higher sample sizes. When comparing between the Sawbones and cadaveric models, it is clear that this surrogate for osteoporotic bones do not provide the same mechanical properties as the human condition. However, it is our belief that a Sawbones model, which includes realistic geometry, thinned cortical walls, and soft cancellous bone, provides a useful surrogate for biomechanical testing, despite the large decrease in mechanical strength.

SIGNIFICANCE/CLINICAL RELEVANCE: The purpose of this study was to provide guidance for surgeons who may not achieve idealized screw placement during a proximal humerus reconstruction. Results suggest that screws inserted below the calcar may act as an effective buttress to provide support to the medial column of the humerus, whereas “missing high” results in decreased construct stiffness.

REFERENCES: [1] Lee SH et al, Bone. 2002. [2] Aaron D, et al, JBJS Am. 2012. [3] Clavert P, et al, JSES. 2010. [4] Schnetzke M, et al, JBJS Am. 2016. [5] Katthagen JC, et al, Clin Biomech. 2014. [6] Bai L, et al, J Orthop Trauma. 2014.

ACKNOWLEDGEMENTS: This study was funded by DePuy Synthes (Grant SR 1005).

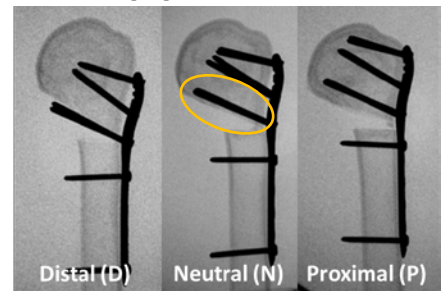


Fig 1: Fluoroscopic images of the 3 groups tested in the experiment. The screws circled in yellow are inserted into the calcar.

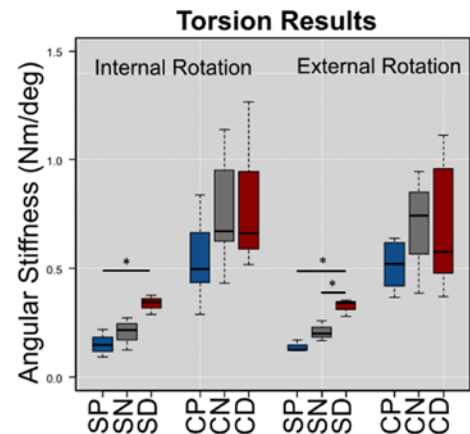


Fig 2: Plots of angular stiffnesses for Sawbones and cadaveric specimens. Significant differences between groups are marked with a *.

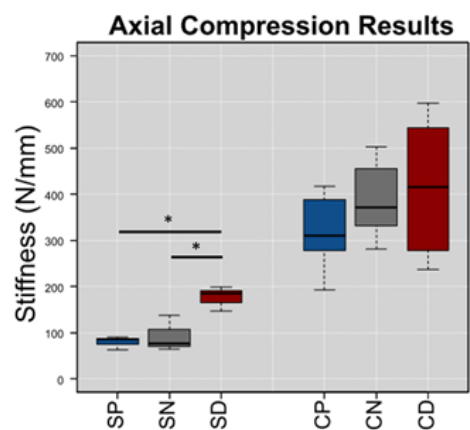


Fig 3: Plots of stiffnesses for Sawbones and cadaveric specimens during the 0° axial test. Significant differences between groups are marked with a *.

Identifying High Risk Activities after Superior Capsular Reconstruction with a Novel Multidisciplinary Model

Michael W. Hast, Elaine Schmidt, John D. Kelly IV, and Josh Baxter
University of Pennsylvania, Philadelphia, PA
hast@upenn.edu

Disclosures: Michael W. Hast (5; DePuy Synthes, Integra.), Elaine Schmidt (N), John D. Kelly (7; SLACK, Springer), Josh Baxter (N)

INTRODUCTION: Rotator cuff tears are painful and often debilitating injuries that are especially prevalent in older adults [1]. While many cuff tears can be surgically repaired, massive ‘irreparable’ tears present a special challenge for patients and shoulder surgeons alike. Superior capsular reconstruction (SCR) addresses this problem by utilizing a dermal allograft that spans the superior region of the glenohumeral joint. Preliminary studies indicate that SCR is effective in improving shoulder function [2]; however, the biomechanical limitations of this repair technique have yet to be sufficiently explored. The goal of this study was to identify activities of daily living (ADL) that may overburden the implanted graft and cause premature failure. To achieve this task, results from in vitro experiments and in vivo 3-D motion tracking sessions were used as inputs for the development of a musculoskeletal model capable of predicting graft failure (Fig 1).

METHODS: Six cadaveric upper extremities from 5 donors (4M, 1F, mean age 65.6 y.o) were used in this experiment. The specimens were skeletonized such that all muscle, tendon, and capsule tissues surrounding the shoulder joint were removed. The SCR repair was performed by an experienced surgeon following manufacturer’s protocol (Arthrex). Reflective markers were attached to the repaired shoulders so 3-D motions could be recorded. The potted humerus was then driven in a test frame (TA Instruments 3550) superiorly (relative to the scapula) at a rate of 0.5 mm/s until failure of the graft fixation occurred at the rim of the glenoid. Scapulae and humeri were 3-D scanned after failure (Afinia Einscan) and 3-D geometries and marker trajectories were used to create 6 degree-of-freedom simulations of the in vitro experiment in OpenSim [3]. The graft was modeled with four parallel ligament elements (green lines in Fig 1). Ligament resting lengths were based on fiber lengths when the shoulder was in the anatomic position. Physiological cross sectional area forces and normalized force-length curves were adjusted to reproduce the force displacement data that was measured experimentally. A 95% confidence interval of maximum graft strain before failure was created.

With institutional review board approval, upper extremity kinematics during activities of daily living were captured using motion analysis on 5 subjects (2M, 3F, mean age 22.0 y.o). Subjects performed the following activities of daily living multiple times: combing hair, forward reach, overhead reach, tucking the back of a shirt, washing their back, and washing their opposite shoulder. Using a boot-strapping technique, 95% confidence intervals for the three glenohumeral joint angles were calculated for each motion (Fig 2). The 3-D cone of glenohumeral rotation created by these bounds was explored by creating simulations that utilized every combination of the low, mean, and high thresholds of the 95% confidence intervals for the three rotations. Thus, 27 similar but different motions were created to thoroughly explore shoulder rotations that may take place during an activity of daily living. These simulations were run in a previously developed OpenSim upper extremity model [4] that was equipped with aforementioned model of an SCR graft. Graft strains were calculated for all 27 simulations, and compared to the previously defined 95% confidence interval of maximum graft strain (Fig 3).

RESULTS: Activities involving ligament-lengthening posterior shoulder rotation (back washing and shirt tucking) excessively strained the graft, which may cause graft failure. Fibers did not exceed their failure points during hair combing, forward reaching, overhead reaching, or shoulder washing motions. These activities largely resulted in shortening of the simulated graft fibers. Individual fiber lengths differed during motions, which at times caused some fibers to reach ultimate strains and “break” while others remained below their ultimate threshold.

DISCUSSION: This model identified post-surgical activity limitations that may better inform surgical outcome expectations. These results also demonstrate the capacity of coupling in vitro, in vivo, and in silico modeling techniques in one cohesive experiment. This approach has potential to provide valuable information to clinicians and rehabilitative specialists to manage patient expectations and guide rehabilitation. Future work will include modeling of glenohumeral contact forces and estimation of forces sustained by the grafts throughout activities.

SIGNIFICANCE/CLINICAL RELEVANCE: While SCR has shown promise as a repair strategy for massive irreparable rotator cuff tears, the biomechanical limitations of the grafts are still not well-defined. This paradigm could be repeated using patient specific motion data, and would act as an effective guide for rehabilitation protocols.

REFERENCES: [1] Templhof+ JSES 1999. [2] Hirahara+ Arthroscopy Tech 2015. [3] Delp+ IEEE Trans Biomed Eng 2007. [4] Saul+ Comp Meth Biomed Eng 2015.

ACKNOWLEDGMENTS: This study was funded by the University of Pennsylvania McCabe Pilot Award. The Musculoskeletal Transplant Foundation donated the grafts used in this study. Arthrex provided the anchors and suture. We thank Todd Hullfish and Annelise Slater for their help collecting motion capture data.

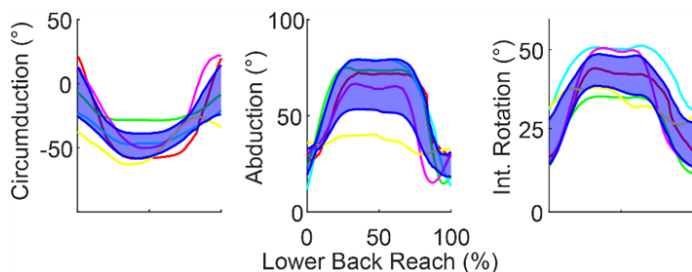


Fig 2: Plots showing the establishment of confidence intervals for the three shoulder rotations that make a motion. Non-blue lines represent the average motion for individual subjects, and the shaded blue region represents the 95% confidence interval for the population.

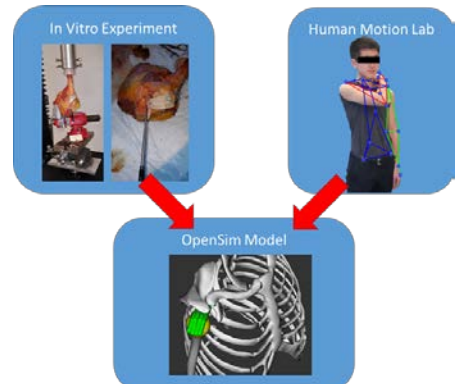


Fig 1: A general overview of the methods used in this experiment. In vitro data was used to inform the graft behavior, while in vivo data provided kinematic inputs to guide the motion of the upper extremity.

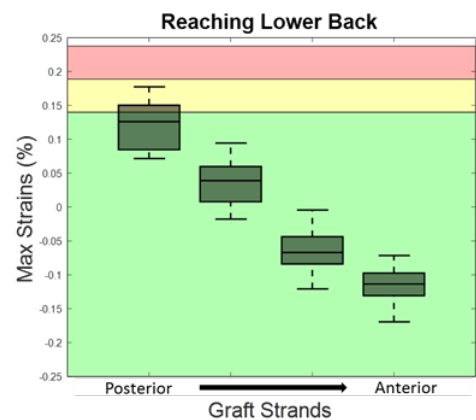


Fig 3: A box and whisker plot showing the distribution of maximum strains from simulations of reaching the lower back. The most posterior graft strand is strained the most and may break because it overlaps with the experimentally determined failure zone (yellow and red), as determined with in vitro testing.

Depth-Dependent Analysis of Cartilage Properties and Chondrocyte Function During Postnatal Growth

Minwook Kim¹, David R. Steinberg¹, Nancy Pleshko², Maurizio Pacifici³, Robert L. Mauck¹

¹McKay Orthopaedic Research Laboratory, University of Pennsylvania¹, Temple University², Children's Hospital of Philadelphia³, Philadelphia, PA
kimminw@mail.med.upenn.edu

DISCLOSURES: Nothing to report.

INTRODUCTION: Skeletal development and growth engender changes in the structure, mechanical properties, and cellular and molecular composition and organization in transient growth plate cartilage and permanent articular cartilage [1]. Transient cartilage undergoes endochondral ossification, and chondrocytes (CH) residing in the ossifying region rapidly divide, enlarge, and eventually undergo apoptosis [2]. Conversely, permanent cartilage retains its hyaline phenotype throughout development and adulthood. Given the diverse changes occurring in the tissues over time, we sought to determine whether they reflected cell autonomous processes and mechanisms and/or relied on interactions with the surrounding matrix [3]. To answer this question, we first evaluated age-related changes in cell and matrix properties in transient and permanent cartilage throughout the depth of the metaphysis as a function of postnatal age. Our focus was on the ECM as a whole, with particular attention given to the immediate peri-cellular environment (the so-called chondron inclusive of the CH and its immediate matrix [4]). We also assessed the cell autonomous differentiation of CHs from these different regions, and the role of the pericellular matrix (PCM) of the chondron in maintaining cartilage homeostasis under conditions that would otherwise promote hypertrophic conversion and ossification.

METHODS: **[Study 1]** Full thickness cartilage plugs (Ø4 mm; 1 plug/knee; n=3/age group) were obtained from femoral condyle at different prenatal and postnatal bovine stages that contain articular and subchondral tissue (Fetal: F=Ø4×18mm; Juvenile: J=Ø4×4.2; Adult: A= Ø4×1.5). To measure local mechanical properties at different depths, the plugs were divided into equal parts (Ø4×2 mm/piece), and local mechanical properties were measured using a custom-built compression device [5]. For local biochemical assessment of GAG, collagen, and calcium content, full thickness cartilage plugs were serially sectioned in 100 µm increments beginning at the articular surface and spanning to the subchondral bone. Paraffin sections were prepared for histology/immunohistochemistry and for FT-IRIS analysis to quantify collagen (Amide I), PG, PG/collagen, and collagen orientation. **[Study 2]** CHs and/or chondrons (CH+PCM) were isolated from top (J-r1) or bottom (J-r3) regions of juvenile cartilage (**Fig 1D**). These isolated CHs or chondrons from different regions were formed into pellets (250K cells/pellet) and cultured in osteogenic medium for 9 days. GAG, DNA and calcium content from the pellets and/or supernatant were determined. Significance was determined by two-way ANOVA with Tukey's post hoc (p<0.05).

RESULTS: **[Study 1]** Analysis of local modulus throughout tissue depth showed that fetal cartilage had the lowest properties, with little if any depth-dependent variation. With postnatal development, the overall functional properties and depth-dependent variations increased markedly (**Fig 1A**). Likewise, local GAG content generally increased with postnatal age. However, this change was more notable in regions that would eventually undergo endochondral ossification, but GAG content remained more steady in permanent cartilage (**Fig 1B**). FT-IRIS showed that the relative PG content (PG/collagen) decreased with age (**Fig 1C**). Further, Alcian blue staining showed that CHs located in the bottom-most regions (r2-r4) in each age group (F, J, A) had an enlarged cell morphology and evidence of local cell division compared to those in the top-most (r1) region. Immunostaining for type VI collagen, to identify the chondron boundary, reflected this enlargement and showed disruption of boundary during endochondral ossification (**Fig 1D**). **[Study 2]** In isolated cells/chondrons, at day 3, pellets formed with CHs from the bottom-most region (J-r3) released more GAG than those from the superficial zone. When the PCM was preserved during isolation, GAG release was significantly reduced. Interestingly, pellets formed from CHs isolated from superficial zone (J-r1) released less GAG than those that were isolated along with their PCM (**Fig 2A**). Consistent with the native tissue analysis, GAG production was greater in pellets from CHs or chondrons from the bottom-most (J-r3) region compared to those isolated from the top-most (J-r1) region (**Fig 2B**). However, GAG production on a per cell basis was similar between groups, suggesting that the greater GAG production was a consequence of increased division in cells from the bottom-most region (J-r3, **Fig 2C**). In comparison to cells from the superficial region, calcium deposition was higher in pellets formed from the bottom-most (J-r3) populations, regardless of whether PCM was present or not (**Fig 2D**).

DISCUSSION: In this study, we investigated the developmental- and age-related changes in cell and matrix in transient and permanent cartilage, and queried intrinsic capacity of CHs from different regions and the role of the PCM in maintaining cartilage homeostasis under osteoinductive conditions. Depth-dependent variation in content and properties became evident through the depth in juvenile tissue. Although GAG was abundant, even in fetal samples, the cartilage became increasingly stratified with greater collagen production. This suggests that the interaction of collagen and PG, along with the onset of normal mechanical loading, may regulate the deformation of cells and PCM and govern tissue formation [6]. Histological analysis of transient cartilage revealed a maturation process typified by enlarged cells and cell division, GAG production, and disruption of PCM. In pellet cultures in osteo-inductive conditions, CHs isolated from the bottom-most region (J-r3) released more GAG than those from the top-most region (J-r1). The PCM is thought to function as a transducer of external signals to CH within as well as a filter that captures formed matrix proteins. Even when this PCM was retained in pellet culture, CHs from the bottom most region (J-r3) showed an increased proliferation rate and calcium deposition in osteogenic conditions, while CHs from the top-most region (J-r1) did not show evidence of this hypertrophic conversion. Though the role of proteoglycans in cartilage calcification remains unclear [7], our data suggest that proper interactions between CHs and matrix proteins initially help to maintain function, but that CHs from different regions are cell autonomous in their eventual transition to hypertrophy. Ongoing studies are investigating changes in intracellular properties associated with changes in cartilage matrix, assessing the molecular factors/pathways that enable superficial CHs to support a permanent cartilage phenotype, and whether changes in pericellular matrix amount, composition, and mechanical properties influence CH fate decisions through the cartilage depth and with development and aging.

SIGNIFICANCE/CLINICAL RELEVANCE: This study demonstrates age-related changes in cell and matrix properties in cartilage through the depth and indicates a cell autonomous capacity of CHs from different regions and a role for the PCM as a transient matrix reservoir during cartilage development. **REFERENCES:** [1] Barbero+ 2004, [2] Schmid+ 1990, [3] DeGroot+ 1999, [4] Lee+ 1997, [5] Schinag+ 1997, [6] Jin+ 2001, [7] Hunter+ 1991. **ACKNOWLEDGEMENTS:** This work was supported by the NIH (R01 EB008722) and the Penn Center for Musculoskeletal Disorders.

Effect of Mineralized Collagen Fibril Orientation on Cortical Bone Fracture Resistance

Yaohui Wang and Ani Ural

Department of Mechanical Engineering, Villanova University, 800 Lancaster Avenue,
Villanova, PA

Bone is a hierarchically structured composite material which exhibits different fracture mechanisms at each length scale. At the submicroscale, the bone is composed of mineralized collagen fibrils. At this scale, the fracture processes in cortical bone have not been extensively studied in the literature. In this study, a novel approach to simulate the submicroscale fracture response in cortical bone was developed incorporating finite element models of unit cells of mineralized collagen fibrils. The models with varying fibril orientations were utilized to assess the influence of the fibril network pattern on the fracture behavior in cortical bone at the submicroscale.

Six sets of fibril networks were generated using a MATLAB script with a plywood structure incorporating fibril orientations of $0^\circ/90^\circ$, $0^\circ/60^\circ$, $0^\circ/30^\circ$, $\pm 15^\circ$, $\pm 30^\circ$, $\pm 45^\circ$. A fibril diameter distribution of 100 ± 5 nm was used in all models. Both longitudinal and transverse tensile loading with respect to the main fibril direction were applied to each model. Interfacial separation between the fibrils was represented by cohesive interface elements. Extended finite element (XFEM) cohesive fracture approach was applied to individual fibrils to account for fibril fracture. The material properties used in all the simulations were adapted from recent experimental data reported in the literature.

The simulation results showed that the interfacial separation dominates transverse loading as the interfaces are mostly perpendicular to the loading direction. The fibril fracture dominates longitudinal loading since the loading direction is approximately along the fibril direction. When the mineralized collagen fibril network was loaded in the transverse direction the mechanical properties (elastic modulus, ultimate strength, and fracture energy) increased as the orientation of fibrils deviated farther from the main fibril orientation whereas the opposite trend was observed under longitudinal loading. The fracture energy was much larger in longitudinal than transverse loading.

In conclusion, this study introduced a new modeling method to simulate the submicroscale fracture behavior of bone using a novel model generation approach and fracture mechanics-based finite element modeling. The results demonstrate the importance of the orientation of mineralized collagen fibrils with respect to the loading direction in determining cortical bone fracture behavior at the submicroscale.

Curvature dependence of nuclear rupture frequency revealed by AFM force spectroscopy

Irena Ivanovska, Yuntao Xia, Jerome Irianto and Dennis Discher

Nuclear deformations that occur during cell migration in constricting spaces can lead to nuclear envelope rupture with loss of many factors including DNA repair proteins. DNA repair is often compromised in cancer, and so fluorescence imaging of cancer cells was combined with single cell AFM-force spectroscopy to characterize in real-time any rupture and loss of repair factors. Deep indentations into the nucleus with AFM probes having low curvature do not cause rupture even when the tip dwells for minutes with forces of ~10 nN. However, poking the nucleus with tips having high curvature causes rupture events to increase dramatically in frequency. Repair factors mis-localization from the nucleus is restricted to cytoplasm, with no obvious leakage out of the cell. Softening the nucleus with Lamin- A knockdown dramatically increases probability of nuclear rupture even with indentation by low curvature at lower forces. The nuclear lamina is therefore mechano-protective against curvature-induced rupture.

Influence of Microcracks and Compositional Heterogeneity on Fracture Resistance of Cortical Bone

Ahmet Demirtas and Ani Ural,
Department of Mechanical Engineering, Villanova University

ABSTRACT

Several recent studies stated that long-term bisphosphonate (BP) treatment may influence the fracture resistance and can lead to atypical femoral fractures (AFF). Due to BP treatment, bone undergoes mechanical alterations including reduced bone tissue composition heterogeneity and increased microcrack density. The aim of this study is to investigate the effects of microcracks and tissue composition heterogeneity on the crack propagation behavior in human cortical bone by using finite element (FE) analysis.

Transverse microscopy images of cortical bone from the mid-diaphysis of tibiae of three donors aged 58, 70 and 81-year-old male was converted to 3D FE models. The fracture behavior of the model was investigated by modeling compact tension specimen tests incorporating cohesive extended finite element method in the osteons and interstitial bone and by cohesive interface elements at the cement lines. Total of 32 simulations were performed including homogeneous (HM) and heterogeneous (HT) material compositions, two different microcrack distributions, and two microcrack densities (5 and 10 microcracks/mm²) for all three models, and two clustered microcrack distribution for only one of the models. The effect of BP treatment was assessed by comparing the homogeneous models with 10 microcracks/mm² to heterogeneous models with 5 microcracks/mm² representing long-term BP-treated bone and healthy bone, respectively. Fracture resistance was assessed by comparing the crack volume between the models.

The simulation results showed that the crack volume was the highest in the models with no microcracks for both HM and HT material properties. Increasing the microcrack density resulted in lower crack volume in all models. Comparison of the two different random distribution of microcracks demonstrated the influence of the location and size of microcracks on the crack growth behavior in cortical bone. Microcracks with identical size and location led to different amounts of crack volume in each model indicating the influence of microstructure. Clustered microcracks had higher crack volume compared to models with distributed microcracks. On the other hand, the models representing long-term BP treatment predominantly had higher crack volumes compared to models representing healthy bone.

In summary, the results showed that the microcracks and increased tissue heterogeneity enhance the fracture resistance of bone, however, their distribution and location significantly affect the fracture behavior. Although limited number of additional microcracks that may form as a result of BP treatment do not individually impair fracture resistance, further changes in the tissue due to treatment such as reduction in material heterogeneity may lead to an overall decrease in fracture resistance. These results provide new information on the interaction of microcracks, tissue heterogeneity and fracture resistance and may improve the understanding of the influence of mechanical changes due to prolonged bisphosphonate use on the fracture behavior of cortical bone.

Aging Related Degenerative Mechanical Changes Manifest Earlier in Supraspinatus Tendons

Joseph B. Newton, George W. Fryhofer, Snehal S. Shetye, Ashley B. Rodriguez, Andrew F. Kuntz, and Louis J. Soslowsky
McKay Orthopaedic Research Laboratory, University of Pennsylvania, Philadelphia, PA

DISCLOSURES: Joseph B. Newton (N), George W. Fryhofer (N), Snehal S. Shetye (N), Ashley B. Rodriguez (N), Andrew F. Kuntz (N), Louis J. Soslowsky (N).

INTRODUCTION: Rotator cuff tendinopathy is a common condition affecting a large portion of the population and can result in pain and joint dysfunction. Advancing age is directly correlated with increased incidence of rotator cuff pathology, with over 90% involving injury to the supraspinatus tendon specifically [1-4]. However, the mechanism(s) by which tendon-specific changes with aging [5] may predispose the supraspinatus to injury relative to the other rotator cuff tendons is unclear. Therefore, the objective of this study was to define the age-related mechanical alterations in all four rotator cuff tendons to determine whether the supraspinatus is more susceptible to injury due to aging than the other rotator cuff tendons. We hypothesized that aging would preferentially affect supraspinatus tendon mechanics when compared to the subscapularis, infraspinatus and teres minor.

METHODS: Experimental design and sample preparation: 7-month juvenile (n=7-10), 18-month adult (n=7-10), and 27-month old (n=7-10) male F344XBN rats were obtained from the National Institute of Aging (IACUC approved). After 3 weeks of facility acclimation, all animals were sacrificed. Lower and upper subscapularis (LS & US, respectively [7]), supraspinatus (SS), infraspinatus (IS), and teres minor (TM), muscle-tendon complexes were then each carefully dissected from the scapula of the right shoulder and removed with the proximal humerus for mechanical testing. Muscle, along with extraneous tissue was removed from each tendon and cross-sectional area of each tendon was measured using a custom laser device [8]. Each humerus was potted in a custom acrylic cylinder secured with polymethyl-methacrylate, leaving the proximal humerus exposed. The

head of the humerus was secured using a self-tapping screw to prevent failure at the growth plate. **Mechanical testing:** The LS, US, SS, IS, and TM from each animal were mechanically tested independently on an Instron ElectroPuls E3000. The testing protocol

consisted of a 0.1N preload, preconditioning (30 cycles, 0.125% to 0.375% strain, 0.25 Hz), stress relaxation at 3% strain magnitude for 600s, frequency sweep at 3% strain (+/- 0.1875% strain at 0.1 Hz, 1.0 Hz, 2.0 Hz, and 10.0 Hz), stress relaxation at 6% strain magnitude for 600s, frequency sweep at 6% strain (+/- 0.1875% strain at 0.1 Hz, 1.0 Hz, 2.0 Hz, and 10.0 Hz), 300s rest at 0% strain, and a ramp to failure at 0.15% strain/second. Tendon toe and linear stiffness was calculated using a bilinear fit. Insertion site linear modulus was determined via optical tracking of stain lines at the insertion site. A 1-way ANOVA with Bonferroni post-hoc tests was used to compare the different ages for each tendon with significance set to $p < 0.05$.

RESULTS: There were no significant differences in cross-sectional area between any tendons across all age groups (data not shown). There was a significant decrease in percent relaxation at 3% strain between SS juvenile and adult groups, as well as IS juvenile to adult, and juvenile to old (Fig. 1). A significant decrease in percent relaxation at 6% strain was detected in all tendons between juvenile and old animals, and the SS and IS from juvenile to adult as well (Fig. 1). Toe stiffness of the US, SS, and IS was increased from juvenile to adult animals, and from juvenile to old animals in the US and IS (Fig. 2). Linear stiffness also increased in US and SS juvenile to adult, and US juvenile to old (Fig. 2). No differences in insertion site modulus were observed for any of the tendons across age (Fig. 3).

DISCUSSION: This study defines the effect of aging on the mechanical properties of the subscapularis, supraspinatus, infraspinatus, and teres minor tendons of the rotator cuff in a rat model. Supraspinatus structural properties (toe and linear stiffness) and its viscoelastic response (stress relaxation) displayed degenerative changes earlier in the aging process with consistent differences between juvenile and adult ages. These earlier changes were also observed in the upper subscapularis and infraspinatus, but not as consistently across properties. Surprisingly, these changes were not exacerbated further into old age, with no differences between the adult and old group in any of the tendons for any of the properties examined. Previous studies reported a steady and dramatic increase in supraspinatus tears in the aging human population [1-4]. Results from the animal model presented here demonstrate that supraspinatus tendon health is consistently affected earlier in the aging cycle, which may predispose the supraspinatus to injury due to other factors not present in this study such as overuse, high cholesterol, and diabetes [9-11]. Future studies will investigate the effect of aging on the healing response of the supraspinatus compared to the other rotator cuff tendons.

SIGNIFICANCE: This study highlights that supraspinatus degeneration initiates early in the aging cycle. These findings could potentially guide timely preventative therapeutic interventions to arrest the continued degeneration of this important rotator cuff tendon.

ACKNOWLEDGEMENTS: This study was supported by NIH/NIAMS (R01AR064216) and Penn Center for Musculoskeletal Disorders (P30AR069619).

REFERENCES: [1] Jempf JF et al., 1999. *Arthroscopy*, 15:56-66. [2] Minagawa H et al., 2013. *J Orthop Res*, 10:8-12. [3] Muto T et al., 2017. *J Sports Med*, 54:76293. [4] Krishnan SG et al., 2008. *Arthroscopy*, 24:324-8. [5] Svensson RB et al., 1985. *J Appl Physiol*, 121:1237-1246. [6] Reuther KE et al., 2014. *J Orthop Res*, 32:638-44. [7] Thomas S et al., 2013. *JSES*, 21:1687-1693. [8] Favata M et al., 2006. *J Orthop Res*, 24:2124-32. [9] Soslowsky LJ et al., 2000. *JSES*, 9:79-84. [10] Jungbluth K et al., 1999. *Arch Orthop Trauma Surg*, 119:280-4. [11] Sambandam SN et al., 2015. *W J Orthop*, 6:902-918.

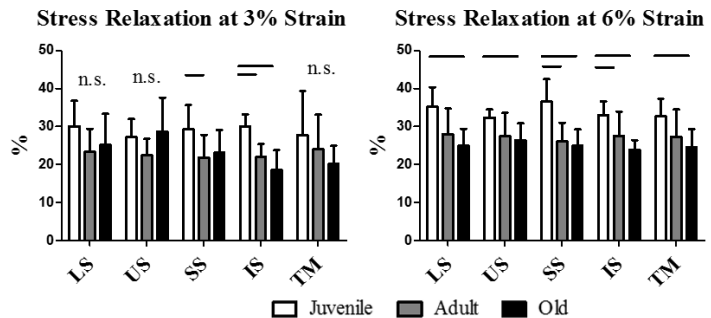


Fig 1. Percent relaxation of SS and IS is decreased at (A) 3% and (B) 6% strain between juvenile and adult. Percent relaxation of all tendons is decreased at (B) 6% strain from juvenile to old.

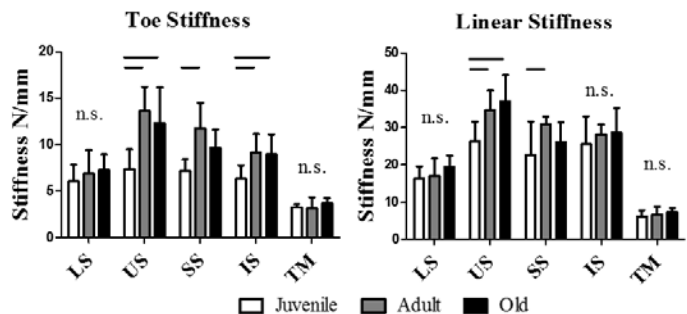


Fig 2. Toe (A) region stiffness increased in US, SS, and IS with age. Linear (B) stiffness also increased in US and SS with age.

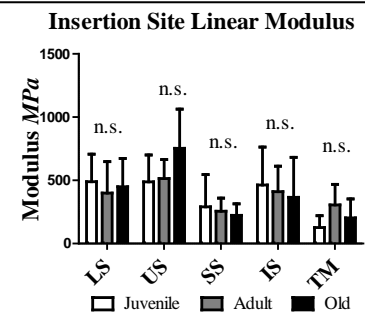


Fig 3. Insertion site linear modulus showed no changes.

Local Discontinuities in Aligned Fibrous Networks Reduce Tissue-to-Nuclear Strain Transmission

Tonia K. Tsinman,¹ Spencer E. Szczesny,¹ Su-Jin Heo,¹ Dawn M. Elliott,² Robert L. Mauck¹
¹University of Pennsylvania, Philadelphia, PA; ²University of Delaware, Newark, DE.

Disclosures: None.

Introduction: Tensile load bearing soft tissues, such as the knee meniscus, tendon, and the annulus fibrosus of the intervertebral disc, have an anisotropic and hierarchical organization. The extracellular matrix (ECM) of these tissues is comprised of aligned type I collagen whose organization is crucial for proper transmission of loads and strains across the ECM-to-cell length scales and subsequent normal mechanical signaling and homeostasis. During aging and pathologic remodeling, however, the ordered structure of these tissues is often lost. For instance, we recently reported that microscopic proteoglycan-rich domains emerge within the otherwise ordered collagenous ECM of the knee meniscus [1]. These micro-domains, with differing composition and mechanical properties, altered local strain transmission and created heterogeneous mechano-signaling patterns [1]. While the origin of these micro-domains remains to be determined, one hypothesis is that local interruptions of the fibrous architecture (i.e., local micro-damage) change the mechano-biologic stimuli received by resident cell populations, resulting in altered differentiation and matrix accumulation. To begin testing this hypothesis, this study developed an aligned polymer scaffold inclusive of local interruptions in the fibrous architecture in order to probe their impact on both macroscopic and cell scale strain transmission and signaling.

Methods: Aligned poly (ϵ -caprolactone) (PCL) scaffolds were fabricated by electrospinning 14.3% w/v PCL solution onto a rotating mandrel (as in [2]). Generated scaffolds were segmented into 1 x 6.5cm strips with the prevailing fiber direction oriented in the long axis of the scaffold. Small interruptions in the fibrous architecture were created by introducing two 0.4 cm incisions (oriented perpendicular to the fibers) spaced 2cm apart (Fig. 1a). To map strain at the macro-scale, strips were speckle coated, and grip-to-grip strain was applied in the fiber direction at a rate of 0.5%/s to 25%. Images were acquired during the test (at 15fps) and analyzed using Vic-2D (Correlated Solutions) to determine E_{11} Lagrangian strain across the sample. At least 200 points per sample were tracked. To determine Lagrangian strain at the cell scale (as well as to measure subcellular deformations), mesenchymal stem cells (MSCs)—isolated from juvenile bovine bone marrow and expanded through passage 1—were seeded onto scaffolds at a density of 10^5 cells/scaffold. Prior to seeding, scaffolds were hydrated through an ethanol gradient and coated overnight with 20 μ g/mL fibronectin. Seeded constructs were cultured for two days in a chemically defined medium to allow for cell attachment. To measure nuclear deformation (denoted as the change in nuclear aspect ratio, NAR, relative to baseline), cell-seeded scaffolds (with and without local incisions) were stained with Hoechst 33342 and uniaxial strain was applied in 3% grip-to-grip strain increments using a custom micromechanical test device mounted on top of an inverted fluorescent microscope [3], and nuclei of selected cells were imaged at 3, 6, 9, 12, and 15% strain steps using a 20X objective. The NAR was defined as the ratio of the long to short axis of the nucleus at each strain step, and was quantified using a custom MATLAB code ($n > 50$ for each group). The same software was used to calculate Lagrangian strains at the cellular level, based on the original and deformed positions of nuclear triads. Statistical differences were established using a two-way ANOVA with Bonferroni post-hoc testing to make comparisons between groups (significance threshold: $p < 0.05$).

Results: Strain mapping of intact speckle coated PCL scaffolds demonstrated relatively uniform ‘global’ E_{11} strain distributions that largely matched the magnitude of the applied grip-to-grip strain. As expected, introduction of discontinuities in the aligned fiber network resulted in non-uniform strain fields; most evident at 15% applied strain, where measured E_{11} strains were substantially diminished in the region located between the two incisions as compared to the outside edges of the scaffold (Fig. 1a). These ECM-level strain field alterations held true at the cellular level as well. Determination of ‘local’ Lagrangian strains through cell nuclei tracking showed similarity between locally and globally measured E_{11} strains of control and cut scaffolds (Fig. 1b), thus validating nuclear tracking as a method for Lagrangian strain mapping in this experimental system. Significant strain attenuation at the cellular level in the E_{11} and E_{22} directions was observed in the middle of the cut region compared to all other locations at all applied grip-to-grip strains (Fig. 2a). Importantly, local strain field perturbations were reflected in differences in nuclear deformation. Cells positioned along fully continuous fibers (uncut scaffolds, edge of cut scaffolds) showed a monotonic increase in NAR up to 23%. In contrast, the NAR of cells seeded in areas containing a fiber discontinuity (middle of cut scaffolds) did not change with the applied strain (Fig. 2b).

Discussion: This study shows that local interruptions in scaffolds composed of aligned nanofibers result in localized strain attenuation at the macroscopic (Fig. 1) and microscopic (Fig. 2) level. Diminished strain transfer was particularly evident at length scales relevant to the cellular mechano-response. Similar trends in NAR and local strain fields confirmed that strains in the principle directions influence the magnitude of nuclear deformation. Importantly, the local fiber discontinuities effected nuclear deformation *only* in regions within the defect, while cells residing in regions of uninterrupted fibers experienced similar deformations as those of uncut control samples. These data illustrate how local fiber disruption can generate distinct mechanical microenvironments within the same scaffold, with neighboring cells experiencing markedly different mechanical inputs based on local boundary conditions. Based on these data and our previous findings in native and engineered tissues [1], these micro-scale perturbations also likely result in different mechano-response. Future studies will focus on differential cellular mechano-signaling within the heterogeneous regions of these scaffolds.

Significance: This work developed an *in vitro* system in which cells within the same material framework can be exposed to markedly different micromechanical conditions. This platform will enable the exploration of how localized changes in the mechanical environment influence cellular response. In particular, future work using this system will query how perturbed local mechanics of native tissues due to micro-damage influences the development of differential cell-mediated ECM deposition and remodeling, potentially shedding light on the mechanism of formation of micro-domains in the meniscus.

References: [1] Han+ 2016. [2] Baker+ 2012. [3] Driscoll+2015.

Acknowledgements: This work was supported by the National Institutes of Health (R01 EB02425) and the Penn Center for Musculoskeletal Disorders.

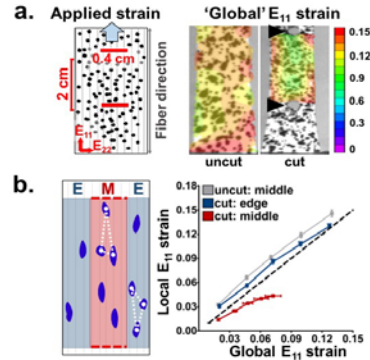


Figure 1. a) Schematic of the Vic-2D analysis set-up (left) and generated E_{11} Lagrangian strain maps for control and defected scaffolds at 15% applied strain (right). **b)** ‘Local strain’ calculation using cell-nuclei tracking. E_{11} strains in the middle of uncut scaffolds and middle and edge of cut scaffolds were compared to Vic-2D measurements (‘global strain’). Black dashed line = a 1:1 relation (slope of 1).

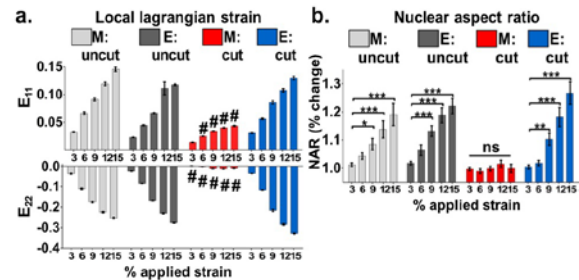


Figure 2. a) E_{11} and E_{22} measured through nuclear tracking (‘local strain’) at denoted applied strains. ‘M’=middle, ‘E’=edge, as in Fig. 1b. ‘Middle: cut’ cohort compared to all other groups at each strain. (#: $p < 0.001$) **b)** NAR (normalized to 0%) as a function of applied strain. ns: not significant, * $p < 0.05$, ** $p < 0.01$, *** $p < 0.001$.

Pericellular Matrix is Highly Sensitive to Cartilage Degeneration in Early Post-Traumatic Osteoarthritis

Daphney R. Chery¹, Qing Li¹, Junyu Lu¹, Biao Han¹, Ling Qin², X. Lucas Lu³, Motomi Enomoto-Iwamoto⁴, Lin Han¹
¹Drexel University, Philadelphia, PA; ²University of Pennsylvania, PA; ³University of Delaware, Newark, DE; ⁴University of Maryland, Baltimore, MD

Disclosures: D. R. Chery (N), Q. Li (N), J. Lu (N), B. Han (N), L. Qin (N), X. L. Lu (N), M. Enomoto-Iwamoto (N), L. Han (N).

INTRODUCTION: Post-traumatic osteoarthritis (PTOA) is the prevalent form of osteoarthritis in young adults, characterized by injury-induced breakdown of articular cartilage [1]. Specifically, PTOA induces irreversible changes in both the extracellular matrix (ECM) and chondrocyte activities, leading to the loss of joint function [2]. Currently, there is limited understanding of the cellular and matrix molecular mechanisms of PTOA, which hinders the development of early detection or intervention strategies [3]. This renders it important to study the pericellular matrix (PCM), the intermediate unit between the cell and ECM [4]. Since the PCM is in immediate contact with the cell, on one hand, the PCM could be more susceptible than the territorial/interterritorial matrix (T/IT-ECM) to elevated chondrocyte catabolic activities in OA; on the other hand, changes of PCM can directly influence the mechanotransduction of chondrocytes. Indeed, the importance of PCM is highlighted by the weakening of PCM in human OA cartilage [5], as well as the increased susceptibility to OA in mice lacking the PCM-specific molecule, collagen VI (*Col6a1*^{-/-}) [6]. To this end, the goal of this study is to elucidate the changes of PCM in early PTOA, and in doing so, to test if the PCM can serve as a potential target for early OA detection or intervention. Applying the destabilization of the medial meniscus (DMM) surgery [7], we induced mild-to-moderate PTOA in mice in a well-controlled time frame. This enabled us to study the changes of PCM in early OA (2 weeks after DMM) before the histological OA signs become detectable (4-8 weeks after) [7].

METHODS: *The DMM surgery* was performed on the right hind knees of 12-week-old male C57BL/6 WT mice, following established procedures [7]. The Sham control surgery was performed on the contralateral left knees. The mice were euthanized at 2 weeks after surgery. *Mechanical properties of the PCM.* Tibial condyles were harvested from both DMM and Sham knees ($n = 3$). Sagittal sections of un-demineralized, unfixed tibial joint were prepared via Kawamoto's film-assisted cryo-sectioning in OCT to expose the PCM [8]. We then labelled the PCM with antibodies of its biomarker, type VI collagen [9]. Using immunofluorescence (IF)-guided AFM nanomechanical mapping [10], we quantified the effective indentation modulus, E_{ind} , of the PCM and surrounding T/IT-ECM of Sham and DMM cartilage in PBS via microspherical tips ($R \approx 2.5 \mu\text{m}$, $k \approx 5.4 \text{ N/m}$, $10 \mu\text{m/s}$ rate, μMasch) and a MFP-3D AFM (Asylum Research) (Fig. 1a). Within each region of interest, nanomechanical mapping was performed as a 40×40 grid (1,600 indents) over a $20 \times 20 \mu\text{m}^2$ region containing ring-link PCM terrains (Fig. 1a). Values of E_{ind} were calculated via the finite thickness-corrected Hertz model [11]. In addition, we tested the modulus of freshly dissected, intact condyle cartilage ($n = 8$) via AFM-nanoindentation. *PCM and chondrocyte dimensions.* For additional mice ($n = 3$), freshly dissected tibias were fixed in 4% formaldehyde and stained with collagen VI antibodies [10]. Through-thickness imaging of cartilage ($\approx 50\text{-}100 \mu\text{m}$ thick [12]) were acquired over a sequence of roughly 50 serial sections using a laser scanning inverted confocal microscope (Zeiss LSM700). Full chondrons (chondrocyte + PCM) were selected for measuring their thickness and volume in ImageJ.

RESULTS: At 2 weeks post-DMM, despite the absence of histological signs, we detected substantial reduction of modulus on both intact joints and the cryo-sections for cartilage in the DMM joint (Fig. 1). Notably, the loss of E_{ind} for the PCM ($93 \pm 2\%$, mean \pm 95% CI) is significantly greater than the nearby T/IT-ECM regions ($85 \pm 3\%$) on the same sections (Fig. 1b). The reduction of modulus on intact cartilage was ($67 \pm 14\%$) (Fig. 1c). Confocal imaging did not detect changes in the volume of chondrocytes or the chondrons, suggesting the absence of macro-structural change in chondrocytes h at this early stage. However, we observed a significant increase in the PCM thickness along the vertical direction of cartilage in the DMM knee (Fig. 2).

DISCUSSION: This study provides direct mechanical evidences illustrating the high sensitivity of PCM to OA initiation factors. In articular cartilage, in comparison to the T/IT-ECM, the PCM has higher concentration of proteoglycans such as aggrecan, perlecan and biglycan [13], which are more susceptible to catabolic enzymatic degradation than collagen fibrils [14]. The compressive modulus of cartilaginous tissue highly relies on the proteoglycan content. Meanwhile, the PCM undergoes faster turnover than the T/IT-ECM [15]. These factors together contribute to the higher degree of modulus loss of the PCM than that of the T/IT-ECM (Fig. 1b) or whole tissue (Fig. 1c). Indeed, previous studies have shown that aggrecan degradation neo-epitopes are mainly localized in the PCM in both early human OA [5] and murine OA [14].

In addition to the mechanical changes, the PCM also undergoes significant swelling in the vertical direction, although at this time, chondrocyte hypertrophy is absent (Fig. 2b). In cartilage, each chondrocyte is confined in the PCM in the form of a chondron [4]. Changes of PCM dimension and loss of stiffness result in disrupted micromechanical niche of chondrocytes, and thus, can contribute to the altered chondrocyte mechanotransduction and hypertrophy in OA. Taken together, our results suggest that PCM is highly sensitive to early OA, and could be a potential target for early detection or intervention of OA. Ongoing studies are probing the spatiotemporal changes of PCM as well as their influences on chondrocyte activities in PTOA.

SIGNIFICANCE: This study shows that the degradation and swelling of cartilage PCM is an early event of PTOA, providing a basis for studying the PCM as a potential target for early OA detection and intervention.

REFERENCES: [1] Olson, SA et al. 2015. Post-Traumatic Arthritis Pathogenesis, Diagnosis and Management. [2] Lawrence, RC et al., *Arthritis Rheum* 58:26-35, 2008. [3] Anderson, DD et al., *J Orthop Res* 29:802-809, 2011. [4] Poole, CA et al., *J Orthop Res* 5:509-522, 1987. [5] Wilusz, RE et al., *Osteoarthritis Cartilage* 21:1895-1903, 2013. [6] Zelenski, NA et al., *Arthritis Rheumatol* 67:1286-1294, 2015. [7] Glasson, SS et al., *Osteoarthritis Cartilage* 15:1061-1069, 2007. [8] Kawamoto, T et al., *Methods Mol Biol* 1130:149-164, 2014. [9] Poole, CA et al., *Arthritis Rheum* 34:22-35, 1991. [10] Wilusz, RE et al., *J R Soc Interface* 9:2997-3007, 2012. [11] Dimitriadis, EK et al., *Biophys J* 82:2798-2810, 2002. [12] Li, J et al., *PLoS One* 9:e111939, 2014. [13] SundarRaj, N et al., *J Cell Sci* 108 (Pt 7):2663-2672, 1995. [14] Chambers, MG et al., *Arthritis Rheum* 44:1455-1465, 2001. [15] Quinn, TM et al., *Ann N Y Acad Sci* 878:420-441, 1999.

AKNOWLEDGEMENTS: This work was supported by NIH AR066824 and AR069619 to the Penn Center for Musculoskeletal Disorders (PCMD)

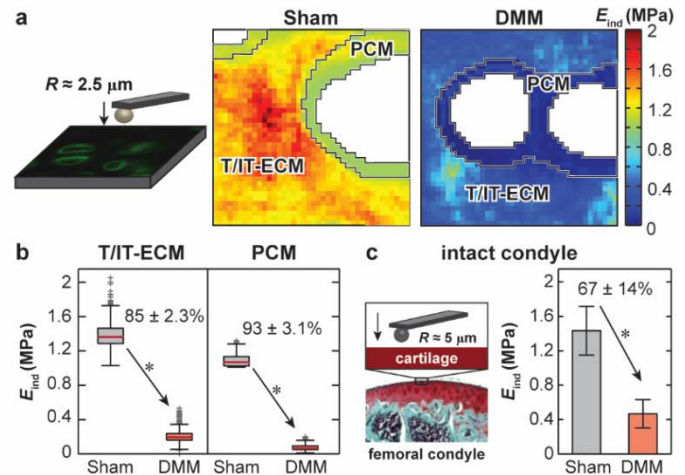


Fig. 1 a) Representative indentation modulus maps of Sham and DMM cartilage cryo-sections at 2-week after surgery measured via immunofluorescence-guided AFM. b) Distribution of E_{ind} for both T/IT-ECM and PCM (*: $p < 0.00001$, ≥ 3 locations from $n = 3$ animals). c) Modulus of intact condyle cartilage surface (mean \pm 95% CI, *: $p < 0.01$, $n = 8$).

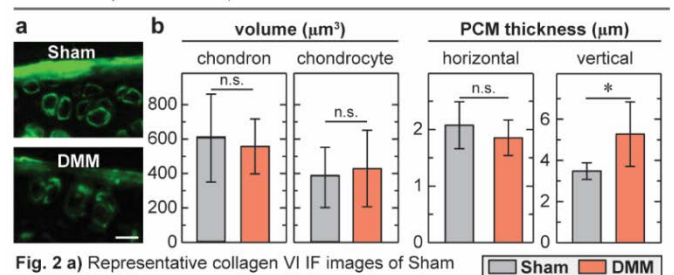


Fig. 2 a) Representative collagen VI IF images of Sham and DMM cartilage cryo-sections. b) Comparison of chondron and chondrocyte volumes, as well as PCM thickness between Sham and DMM cartilage (*: $p < 0.001$, ≥ 30 cells from $n = 3$ animals).

A Framework for Optimizing Hip Replacement Positioning Using Measurements of Subject-Specific Motions

Josh R. Baxter, Jenna Bernstein, Michael W. Hast
University of Pennsylvania, Philadelphia, PA, USA
josh.baxter@uphs.upenn.edu

Disclosures: Josh R. Baxter (N), Jenna Bernstein (N), Michael W. Hast (5; DePuy Synthes, Integra.)

INTRODUCTION: Total hip arthroplasty is a highly effective surgery for treating end-stage hip osteoarthritis. However, impingement between the femoral and acetabular components has been linked to poor outcomes, dislocations, and implant failure. Classic work by Lewinnek et al. [1] identified an acetabular cup ‘safe zone’ as a critical factor in dislocation risk, which has been challenged by a recent clinical study leveraging a larger cohort [2]. Activities of daily living associated with impingement and surgical placement of the acetabular component demonstrate large amounts of variability [2,3], highlighting the need for positioning recommendations based on patient-specific motions. Therefore, the objective of this study was to establish a simulation framework for optimizing acetabular cup positioning based on patient-specific movement biomechanics. Specifically, we aimed to develop a simulation tool using an open-source musculoskeletal modeling platform that can be implemented by the orthopaedic community to determine surgical placement based on implant geometry and patient-specific motions.

METHODS: Hip impingement was detected during activities of daily living using a modified musculoskeletal model (Fig. 1A, [5]) that simulated contact between the acetabular liner and neck of the femoral component. A generic hip replacement (grabcad.com/library/hip-replacement) was positioned so that the centroids of the acetabular liner and femoral head component were coincident. The musculoskeletal model was then scaled to fit anatomical landmarks of a healthy-young female (21 years, BMI: 31.1), who performed activities of daily living in this IRB approved study. Deep squats, shoe tying, and picking an object off the floor – each performed ten times – were measured using a 12-camera motion capture system. Ninety-five percent confidence intervals were calculated for each motion using a boot-strapping technique and used to evaluate the effects of acetabular cup positioning on impingement. The lower and upper confidence bounds of each activity were simulated in the subject-specific model and impingement between the acetabular cup and neck of the femoral component were recorded. The implications of cup positioning on impingement were tested by simulating all combinations of abduction [20 - 60°] and anteversion [0 - 40°] values in two-degree increments for a total of 441 simulations. Patient-specific positioning was optimized by identifying zones that resulted in no impingement throughout all the recorded activities.

RESULTS: Impingement was detected in 57% of cup positions in at least one of the tested motions (Fig. 1B). Increasing cup anteversion insured impingement-free motion during the studied tasks. Conversely, increased amounts of cup abduction were associated with greater incidences of impingement during squatting, shoe tying, and picking up an object. Deep squatting was the movement most likely to cause impingement and may be explained by the coupled flexion and internal rotation of the femur (Fig. 1C). Other primarily-sagittal motions – shoe tying with a bent trunk and picking up an object from the floor – also generated large amounts of hip flexion but required no greater than one-third the amount of internal rotation. In contrast, tying shoes by resting the foot on the contralateral knee generated large external rotation motions and impingement-free motion in all cup positions.

DISCUSSION: We developed a computational modeling framework to identify impingement ‘safe zones’ that are dictated by cup positioning and patient-specific motions. In addition to studying cup positioning and patient-specific motions, a myriad of other factors can be tested within this framework, such as implant geometry, femoral anatomy and positioning, and pelvic bony geometry. Current efforts are focused on optimizing implant positioning to minimize the amount of loading near the rim of the acetabular liner, which affects both wear and dislocation rates [4]. We used motion data from a healthy-young control to confirm that impingement detected using this framework was sensitive to both cup positioning and subject biomechanics. While this specific data set does not have clinical relevance, it has demonstrated a viable simulation framework that could be used to provide surgeons with guidance that could be leveraged to minimize impingement in patient populations.

Clinical studies have debated the ‘safe-zone’ for patients with total hip arthroplasty [1,2]. The current modeling framework allows researchers to understand the links between implant positioning, hip motion during high-risk activities, and mechanisms of dislocation and implant wear. Our results suggest that impingement occurs during these activities with component positioning that are within the range of patients that do not dislocate [2]. These findings support other causes of dislocation, which may include inadequate muscle strength, cup coverage, or soft-tissue constraints.

SIGNIFICANCE/CLINICAL RELEVANCE: Hip arthroplasty position may be optimized using an open-source musculoskeletal modeling paradigm to mitigate impingement risks and edge loading of the acetabular liner.

REFERENCES: [1] Lewinnek *et al.*, *JBJS*, 1978; [2] Esposito *et al.*; *J Arthroplasty*, 2015 [3] Hemmerich *et al.*, *JOR*, 2006; [4] Parvizi *et al.*, *CORR*, 2006

ACKNOWLEDGEMENTS: We thank Todd Hullfish and Annelise Slater for assisting in data collection and processing.

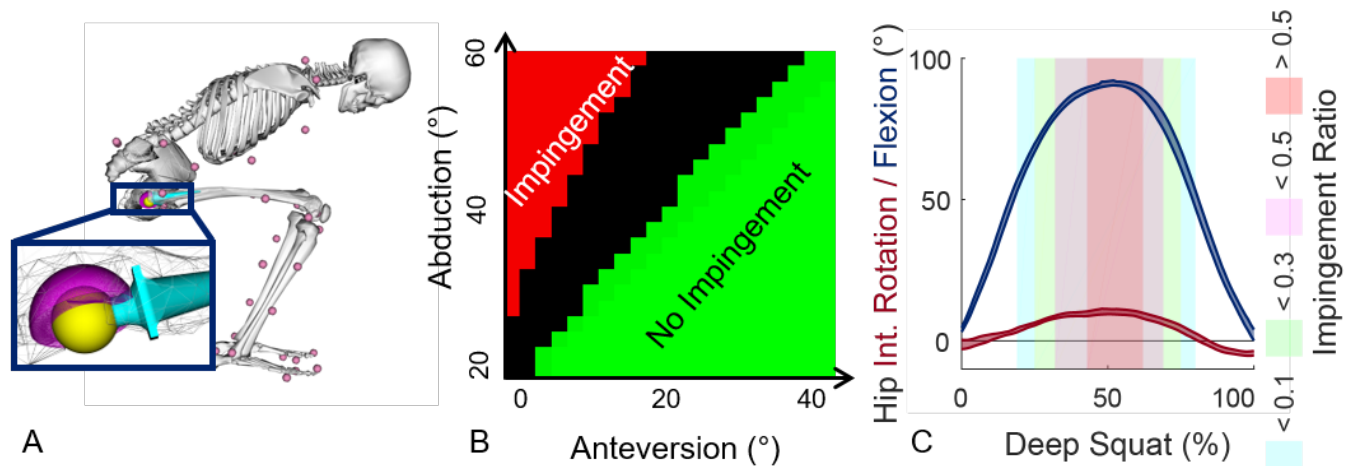


Fig1. (A) Hip impingement was detected using a subject-specific musculoskeletal model. (B) Hip impingement distributions are dependent on both cup positioning - abduction and anteversion – and movement task (green: no impingement ↔ red: impingement during all activities). (C) Deep squatting caused the most incidences of impingement, which may be caused by the coupled motion of hip flexion (blue) and internal rotation (red). Impingement ratios represent the ratio of cup positions that resulted in impingement at the highlighted portions of the task.

Plantarflexor Remodeling Following Achilles Tendon Rupture Repair: A Case Study

Josh R. Baxter, Todd Hullfish, Wen Chao
 University of Pennsylvania, Philadelphia, PA, USA
josh.baxter@uphs.upenn.edu

Disclosures: Josh R. Baxter (N), Todd Hullfish (N), Wen Chao (N)

INTRODUCTION: Achilles tendon ruptures lead to elongated tendons and reduced patient function. Despite these clinical correlates, the link between muscular shortening constraints imposed by altered tendon properties and muscle remodeling remain poorly understood. Animal studies have shown that muscles rapidly remodel in order to maintain sarcomere shortening dynamics [1,2]. However, the muscular response to extreme changes in shortening demands have not yet been described, which may provide critical information for clinical decision making.

Therefore, the purpose of this study was to establish a framework for linking muscle remodeling and functional deficits in patients recovering from Achilles tendon ruptures. In particular, we aim to identify clinically relevant benchmarks that will guide treatment and better manage expectations. This case study presents a framework that is actively being utilized in a prospective patient registry to confirm a mechanism for muscle remodeling and establish clinical benchmarks for patient success.

METHODS: A 27-year old male (1.83 m and 84 kg) presented with poor clinical outcomes 2.5 years following an acute Achilles tendon rupture that was surgically repaired by another provider using an open-reduction within 1 week of the initial injury. These poor outcomes were confirmed using a clinical outcome score (ATRS score of 49) [3], evaluation by a fellowship-trained foot and ankle surgeon, and inability to perform a single-leg heel raise. This functional assessment is part of an IRB approved research registry.

Plantarflexor architecture remodeling was quantified under ultrasonography by contrasting the medial gastrocnemius muscles of the affected and unaffected sides. Muscle thickness as well as fascicle length and pennation were quantified by identifying the superficial and deep aponeuroses and clearly identifiable fascicles.

Plantarflexor function was assessed through a battery of tests including isometric strength testing, single-leg heel raise, and walking. During these activities, the ultrasonography probe acquired images synchronously with motion capture and force plate data. Plantarflexion motion, torque, and power along with fascicle shortening dynamics were calculated to establish the link between muscular and patient function. Fascicle dynamics were tracked using an automated tracking routine that utilizes MATLAB's Computer Vision System Toolbox.

RESULTS: Muscle remodeling was clearly evident and likely explained the patient's functional limitations observed in this case study. The medial gastrocnemius fascicles of the affected side were 59% shorter, 162% more pennated, and 24% less thick compared to the unaffected side.

Plantarflexor isometric torque was reduced by almost 50% on the affected side, however the percentage of fascicle shortening (41% – 46%) was similar between sides (Table 1). These results suggest that both the affected and unaffected plantarflexor muscles were operating on similar portions of the force-length curves during isometric strength testing.

Despite drastic changes in muscle architecture and isometric strength, walking biomechanics did not differ between the affected and unaffected sides (Table 1). Toe off occurred at 15° plantarflexion with approximately 160 Nm of torque being generated. Gastrocnemius fascicles went through less than 1 cm of excursion, demonstrating how the Achilles tendon can efficiently store and return energy during cyclic tasks – even when constrained by muscular weakness.

DISCUSSION: Single-leg heel raises are a common clinical exam that demonstrated high sensitivity for muscle structure and function in this case study (Table 1). The affected limb generated one-third as much ankle rotation compared to the unaffected limb. These functional deficits appear to be explained by a 5-fold decrease in fascicle shortening. This decrease in fascicle shortening seems to be compounded by increased shortening pennation (48° compared to 36°), which resulted in a 14% decrease in force transmission along the Achilles tendon line of action.

This case study proposes a framework to rigorously quantify muscle remodeling in response to Achilles tendon injuries – establishing a means to prospectively study the implications of injury and treatments on joint function. Decreases in heel-raise function have been linked to tendon elongation of 3 cm following rupture [4], and our current findings suggest that fascicle remodeling occurs to compensate for tendon elongation at the cost of shortening capacity (Fig. 1). Further, these adaptations appear to be consistent with prior animal work that shows muscle remodeling following acute changes imposed on tendon traveling requirements [1,2].

SIGNIFICANCE/CLINICAL RELEVANCE: Skeletal muscle responds to tendon injuries in profound and deleterious ways. Utilizing a prospective approach to monitor patient progress may provide clinicians with additional information to tailor rehabilitation and return to activity timelines to optimize healing and long-term outcomes.

REFERENCES: [1] Koh and Herzog. J Biomech. 1998; [2] Burkholder and Lieber, J. Exp. Biology, 1998; [3] Nilsson-Helander K, et al. Am. J. Sports Med., 2007; [4] Silbernagel KG, et al. Am. J. Sports Med., 2012; [5] Willits K, et al. J. Bone Joint Surg. Am., 2010.

ACKNOWLEDGEMENTS: This study was supported by The Thomas B. McCabe and Jeannette E. Laws McCabe Fund

		Affected	Unaffected	% Change
Isometric	Torque	70 Nm	133 Nm	-47%
	Shortening	41% (1.9cm)	46% (5.1 cm)	≈ (-63%)
Walking	Plantarflexion	16°	15°	~
	Torque	160 Nm	156 Nm	~
Heel Raise	Shortening	< 1 cm	< 1 cm	~
	Plantarflexion	12°	40°	-70%
	Torque	140 Nm	140 Nm	~
	Power	100 W	260 W	-62%
	Shortening	1.0 cm	5.4 cm	5 times

Table 1. Functional differences between the affected and unaffected sides

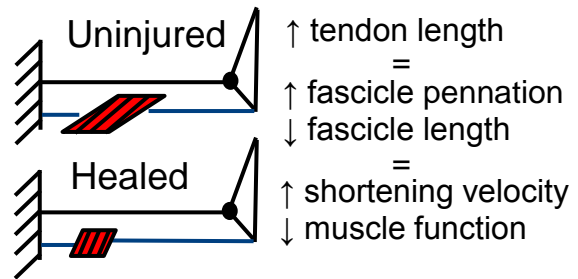


Fig 1. Achilles tendon lengthened following surgical repair [4], which appears to elicit muscle remodeling in order to maintain resting tendon tension. This muscle remodeling reduced muscle shortening and function in this study.

Competitive collegiate distance runners have structurally different Achilles Tendons than recreationally active young adults

Todd J. Hullfish, Kenton L Hagan, Ellen Casey, Josh R. Baxter
University of Pennsylvania, Philadelphia, PA
todd.hullfish@uphs.upenn.edu

Disclosures: Todd J. Hullfish (N), Kenton Hagan (N), Ellen Casey (N), Josh R. Baxter (N)

INTRODUCTION: Achilles tendinopathy is among the most commonly reported injuries in running athletes [1]. Repetitive tendon loading that reaches 12 times body weight is thought to be the driving factor in tendinopathy development in these athletes [2]. However, the progression of asymptomatic and symptomatic tendinopathies is not well understood [3]. Asymptomatic tendinopathy is thought to be a common precursor to tendon pain and reduced function; however, structural changes not associated with symptomatic tendinopathy have not yet been reported in athletic populations. Therefore, the aim of this study was to contrast Achilles tendon structure between healthy-young adults and collegiate cross-country runners. To accomplish this aim, we implemented an ultrasound imaging technique that quantifies tendon collagen organization.

METHODS: Twenty-two collegiate cross country runners (12 males; Age: 19 ± 1.5 , BMI: 20.3 ± 1.6) and twelve healthy controls (5 males; Age: 25 ± 2 ; BMI: 23.8 ± 2.4) participated in this IRB approved study. Running foot-strike pattern, lower-extremity injury history, years participated in collegiate cross country, and a clinical outcome questionnaire (VISA-A) were collected from the runners group. Longitudinal B-mode ultrasound images of the of the mid-substance of the right Achilles tendon were acquired while subjects lay prone on a treatment table with ankles placed in the resting position off the end of the table. Images were acquired using an 18 MHz transducer (L18-10L30H-4, SmartUs, TELEMED, Vilnius, Lithuania) with a scanning width of 3 cm (scan parameters: Dynamic Range: 72dB; frequency: 18 MHz; gain: 47 dB). Collagen organization was quantified in the ultrasound images using custom-written software. This image processing algorithm is a computational analog to crossed polarizer imaging, which assesses collagen fascicle alignment and quantifies tendon 'organization' as the circular standard deviation (CSD) of these collagen structures. To test our hypothesis that competitive-distance runners have structurally different tendons than their recreationally-active peers, we compared the measured CSD between the two groups using a one-way unpaired t-test. Secondary analyses were performed to determine if other runner characteristics, sex, BMI, foot-strike pattern (forefoot, mid-foot, and rear foot), and years running at the collegiate level are correlated with measurements of collagen organization. Unpaired two-way t-tests were performed to test differences explained by sex and foot-strike pattern.

RESULTS SECTION: All runners had an acceptably high VISA-A score (93.4 ± 8.05) and did not report dealing with pain originating from the tendon. Collagen alignment was 35% less organized in the runners compared to the controls. ($p < 0.001$, Fig. 1). Sex, BMI (Fig. 2), foot-strike pattern, or years running at the collegiate level had no effect on measurements of collagen alignment in the runners ($p > 0.1$).

DISCUSSION: Young adults who participate in competitive-distance running have structurally different tendons than recreationally-active young adults. These differences do not appear to be correlated with age, sex, BMI, foot-strike pattern, or years running at the collegiate level. The lack of correlation between these factors and CSD observed in this study could be partially attributed to the low variance among the runners; however, previous work has shown that these factors are not correlated with the development of tendinopathy. It remains unclear if these measurements of decreased tendon organization predict tendinopathy symptoms, though changes in tendon structure have been linked to functional losses associated with tendinopathy. This non-invasive imaging technique quantifies tendon structure and can be used to track changes in tendon structure to better characterize the progression of tendinopathy. Using this paradigm, we are prospectively quantifying tendon structure in distance runners throughout a competitive season in order to develop imaging biomarkers that may predict painful tendinopathy before symptoms manifest.

SIGNIFICANCE/CLINICAL RELEVANCE: Analyzing B-mode ultrasonography images may provide clinicians with early signs of tendinopathy and allow for preventative treatment and altered training schedules.

REFERENCES: [1] Doral+, *AJSM*, 2009; [2] Komi, *J Biomech*, 1990; [3] Riley, *Rheumatology*, 2004

ACKNOWLEDGEMENTS: We thank Annelise Slater and Neza Stefanic for assisting in data collection and processing, respectively. This work was supported by The Thomas B. McCabe and Jeannette E. Laws McCabe Fund.

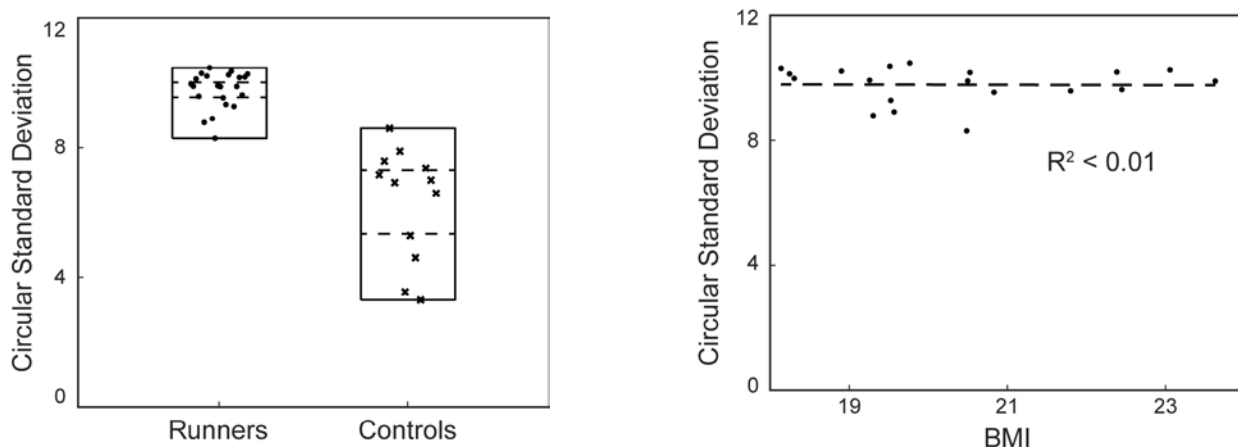


Fig 1. Measures of circular standard deviation are shown for both runners (dots) and controls (crosses). The ranges of these measurements are shown in the solid black rectangles 95% confidence intervals are shown as dotted lines.

Near Infrared Spectroscopy Predicts the Compositional and Biomechanical Properties of Porcine Engineered Cartilage

Shital Kandel¹, William Querido¹, Jessica M. Falcon¹, Farzad Yousefi¹, Daniel J. Reiners¹, Minwook Kim^{2,3}, Robert L. Mauck^{2,3}, Nancy Pleshko¹

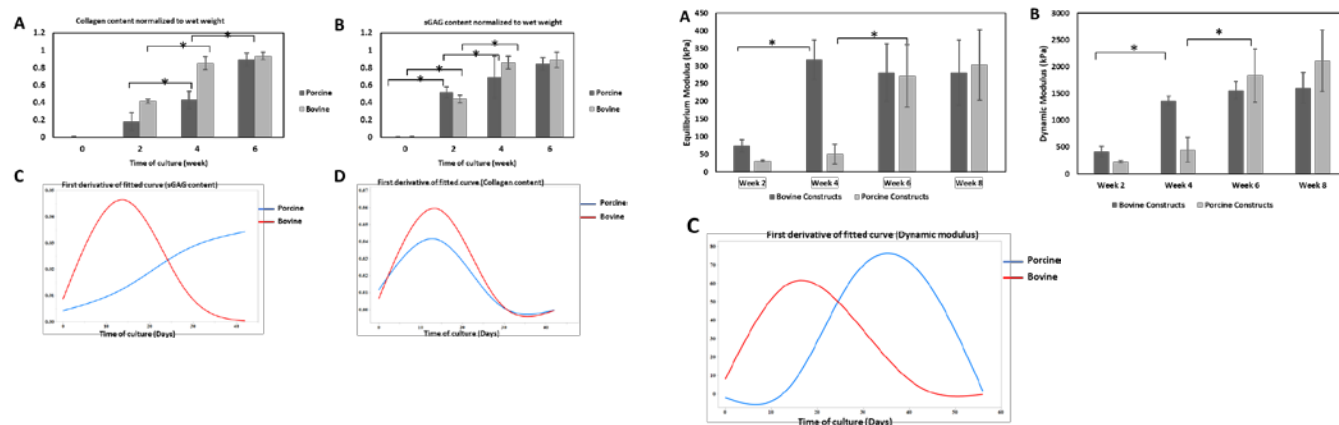
¹Department of Bioengineering, Temple University, Philadelphia, PA

^{2,3} Departments of Orthopaedic Surgery and Bioengineering, University of Pennsylvania, Philadelphia, Pennsylvania

Cartilage tissue engineering is a promising approach for the repair of chondral defects [1, 2]. Successful integration of engineered cartilage depends in part on construct maturity [2]. Hence, it is critical to determine the maturity of engineered cartilage *in vitro* prior to implantation. Gold standard techniques to determine compositional and mechanical properties are destructive. We have shown that near infrared (NIR) spectral data collected in a non-destructive manner correlates to compositional and biomechanical properties of bovine chondrocyte-based engineered cartilage [1]. In the current study, we used NIR spectroscopy to non-destructively assess properties of engineered cartilage grown with porcine chondrocytes. We hypothesized that NIR spectra along with multivariate partial least square (PLS) analysis could be used to predict the compositional and biomechanical properties of engineered cartilage.

Primary chondrocytes were isolated from articular cartilage of Yorkshire porcine stifle joints. Cells were encapsulated in hyaluronic acid (MeHA) hydrogels. NIR spectral data were collected from constructs at day 0 through day 42. Cartilage constructs were harvested on days 0, 14, 28, and 42 and sulfated glycosaminoglycan (sGAG) content and total collagen was measured using dimethylmethylene blue (DMMB) and chloramine T (hydroxyproline) assays, respectively. Mechanical testing was performed on a Bose Electroforce 3230 with a 1000N load cell.

Our results found that scaffolds seeded with either cell type showed a significant increase in normalized collagen content after week 4 and week 2 (Figure 1A) and normalized sGAG content after week 2 for both (Figure 1B). The first derivative of the fitted curve showed the maximum rate of construct maturation for sGAG content at week 2 (Figure 1C), week 2 for bovine collagen content but continued increasing for porcine (Figure 1D). Equilibrium modulus (Figure 2A) and dynamic modulus (Figure 2B) were comparable. However, the first derivative of the fitted curve of the dynamic modulus (Figure 2C) showed a difference in mechanical maturation. PLS analysis of NIR data for predicting biochemical composition and dynamic moduli of porcine constructs resulted in prediction models with 11.6%, 15.4% and 9.25% error for the calibration and validation of the dynamic modulus, sGAG content and collagen content, respectively. The current study demonstrates that non-destructive NIR spectroscopic data, along with multivariate analysis, can be used to predict the composition and biomechanical properties of engineered porcine chondrocyte-based cartilage constructs.



REFERENCES:

1. Yousefi, F, et al. Tissue Engineering: Part A, (2017).
2. Fisher et al. Biomaterials, 2014 35(7).

Finite Element Analysis of Intramedullary Nail Femur Fracture Fixation for Surgical Decision Support

Scott M. Tucker, MEng¹, Hwabok Wee, PhD¹, Gregory S. Lewis, PhD¹

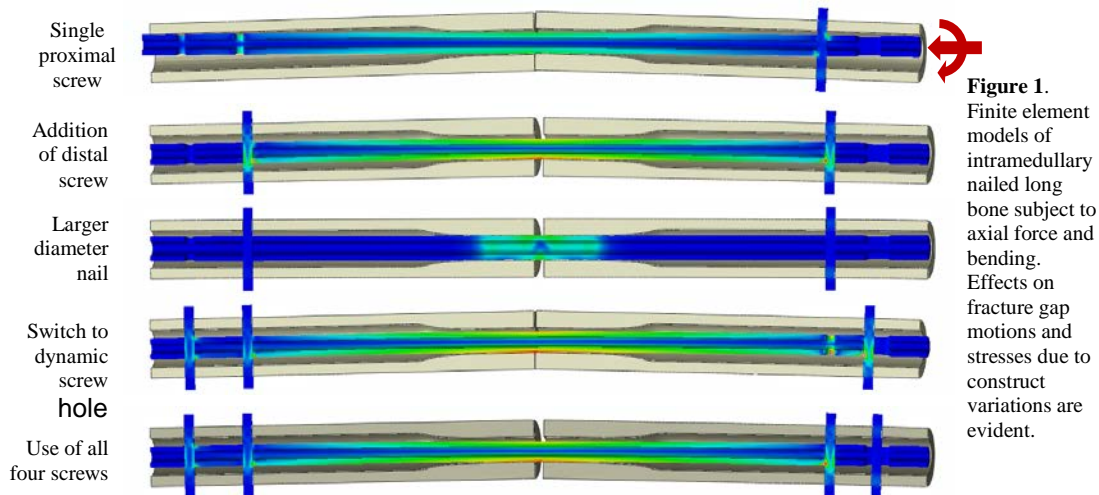
¹Pennsylvania State University College of Medicine, Hershey, PA, USA, glewis1@pennstatehealth.psu.edu

DISCLOSURES: No disclosures

INTRODUCTION: Fracture management constitutes a large portion of orthopaedic care. Intramedullary (IM) nails are commonly placed into the medullary cavities of diaphyseal and metaphyseal bone to stabilize fractures. Installation of an IM nail involves multiple decision points which a surgeon must navigate adequately for sufficient fracture fixation. Design considerations such as implant size, implant position, medullary canal reaming, and screw configuration will be influenced by patient factors such as bone quality and fracture geometry. It is understood that variations in fixation construct design variables influence the system biomechanics and healing process. However, surgeon intuition and precedent are currently the primary drivers for how these decisions are made. Computational modeling of fracture fixation constructs enables prediction of biomechanical outcomes based on model configuration. Importantly, design variables can be independently adjusted within simulations to isolate effects of individual design parameters. Simulation of all configurations of interest can be performed to yield a library of results. Specific results can then be interrogated and used to compare outcomes across design variable iteration. For example, a surgeon could search the library to assess the effect of using a longer or wider implant to fix the same fracture. Design simplification within the modeling database may be possible without sacrificing much accuracy of results. In this study we compare patient specific and generic model libraries of IM nail fixed femur fractures.

METHODS: Patient-specific femur models are segmented from CT scans of femur fracture patients. Generic femur models are developed from publicly available geometry (biomedtown.org). Bone is divided into trabecular and cortical materials with elastic moduli 155MPa and 16GPa, respectively. Intramedullary nail implants are rendered in SolidWorks (Dassault Systemes) with geometry and material properties based on implant manufacturer technical guides. Fractures are modeled based on the original patient image or on fracture classes outlined by the widely-used AO/OTA classification system. For each model an IM nail is aligned within the femur in SolidWorks. The femur is then reamed if indicated and bone and implant models are exported to Abaqus for meshing and simulation. Hard contact is modeled between implant and bone, implant and fixation screws, and bony fragments at the fracture site. A load of 2kN is applied to the proximal femur with loading orientation and femur boundary conditions as described by Eberle *et al*¹.

RESULTS: Generic simplified model results are shown in Figure 1. Altering design variables noticeably alters the resulting stress profile under combined axial and rotational loading.



DISCUSSION: This method has promise in the clinical management of femur fracture patients in providing specific biomechanics outcomes as a result of construct variation. As evident in Figure 1, increasing the diameter of the IM nail to match that of the medullary canal (third panel) has the most appreciable effect on reducing stress in both implant and screws. Interestingly, the use of 4 screws (fifth panel) produces a strikingly similar stress profile to the 2 screw case (second panel). Future development and comparison of more complex models such as patient-specific and generic bone models will help distinguish scenarios where a simple model adequately predicts outcome measures from those where more refinement is needed for accurate prediction. Additionally, modeling of more fracture types will show the fracture-specific biomechanical effects of design parameter variation.

SIGNIFICANCE/CLINICAL RELEVANCE: This study provides a novel tool orthopedists can utilize to gain insight into how their decisions can influence biomechanics. Additionally, this study will inform future modeling efforts and help determine when simplified models may achieve sufficient accuracy.

REFERENCES: 1. Eberle, Sebastian et al. "Type of Hip Fracture Determines Load Share in Intramedullary Osteosynthesis." *Clinical Orthopaedics and Related Research* 467.8 (2009): 1972–1980. *PMC*. Web. 23 Oct. 2017.

ACKNOWLEDGEMENTS: Support from AO Foundation and NSF I/UCRC Center for Healthcare Organization Transformation (CHOT), NSF I/UCRC grant #1067885

Chronic Nicotine Exposure Alters Tendon Vascularity and Viscoelasticity

Daniel J. Gittings; Corinne N. Riggan; James F. Boorman-Padgett; Stephanie N. Weiss; George W. Fryhofer; Daniel C. Farber; David R. Steinberg; Louis J. Soslowsky
 McKay Orthopaedic Research Laboratory, University of Pennsylvania, Philadelphia, PA
 daniel.gittings@uphs.upenn.edu

Disclosures:

D.J. Gittings: None. C.N. Riggan: None. J.F. Boorman-Padgett: None. S.N. Weiss: None. G.W. Fryhofer: None. D.C. Farber: 4; JMEA. D.R. Steinberg: 4; Johnson & Johnson. L.J. Soslowsky: 5; Bonti, Marine Polymer, OrthoFix.

INTRODUCTION: Tendon injuries are common and lead to significant disability. Smoking is a modifiable risk factor that has numerous adverse health effects, including association with tendon injuries. However, the effect of nicotine and smoking on tendon morphology and function is not well understood.¹ Therefore, the purpose of this study was to investigate the effect of chronic nicotine exposure on Achilles tendon (AT) and supraspinatus tendon (SS) structural and mechanical properties in a rat model. We hypothesized that chronic nicotine exposure would lead to tendinopathic changes as evidenced by altered tendon vascularity, tenocyte and extra-cellular matrix histology consistent with degeneration, and diminished mechanical properties.

METHODS: *Study Design:* Twenty male Sprague-Dawley rats (398±16g) were randomly allocated to groups exposed to either 0.9% saline (n=10) or 36mg/mL of nicotine (n=10) at a rate of 2.5 µL/hr through osmotic pumps for 12 weeks before being euthanized (IACUC approved). Timing for nicotine exposure was based on previous experiments and the nicotine concentration was based on the average tobacco user in the United States (14 cigarettes per day).^{2,3} Serum levels of cotinine, the predominant metabolite of nicotine, was measured every 4 weeks with an enzyme-linked immunosorbent assay at 450 nm to monitor the systemic release of nicotine. Osmotic pumps were exchanged after measurement of serum cotinine levels. *In vivo assays:* At 12 weeks, AT was imaged with contrast enhanced ultrasound (CE-US) to assess for vascularity (n=4/group). CE-US of AT was visualized in B-mode in the sagittal plane with a 21MHz center frequency ultrasound transducer and then video data was converted into echo-power data (linearization). Perfusion parameters were derived from this model including peak enhancement, rise time, time to peak, wash-in rate, wash-in area under the curve, and wash-in perfusion index as described.⁴ *Ex vivo assays:* Bilateral AT and SS were then harvested for ex vivo histologic structural (n=5/group) and biomechanical analysis (n=8-10/group) as described.^{5,6} Briefly, stain lines were used to track optical strain and cross-sectional area was measured using a custom laser device. Tensile testing was performed as follows: preload to 0.08 N, preconditioning (10 cycles of 0.1-0.5 N at a rate of 1% strain/s), stress relaxation at 5% strain for 600 seconds, and ramp to failure at 0.1% strain/s for AT and 0.3% strain/s for SS. *Analysis:* Statistical analysis was performed using Student's t-tests and Mann-Whitney U tests to compare parametric and non-parametric variables respectively. Significance was set at p<0.05 and trends at p<0.1.

RESULTS: AT CE-US demonstrated an increase in contrast wash-in rate and trend to decrease in rise time and time to peak in the nicotine group compared to the saline group, indicating an increase in tissue perfusion rate (Fig 1). No differences were found in the other amplitude-based CE-US measures.

Nicotine did not alter AT or SS histologic parameters (Fig. 2). AT percent relaxation, a measure of tendon viscoelasticity, was significantly increased with nicotine exposure compared to saline (Fig. 3a). Similarly, SS percent relaxation had an increased trend with nicotine exposure compared to the saline group (Fig. 3b). No differences in maximum load, maximum stress, stiffness, or modulus were observed with nicotine exposure in either AT or SS (n=6-10/group).

DISCUSSION: After chronic nicotine exposure at a clinically relevant dose modeling the average US smoker, AT perfusion rate increased and both AT and SS viscoelasticity were altered in this rat model. In a previous clinical study, CE-US detected a significant increase in vascularity in tendinopathic AT when compared to healthy human patients.⁷ Furthermore, nicotine has been shown to have pro-angiogenic effects that may represent a compensatory mechanism for nicotine's vasoconstricting effect.⁸ In our study, the changes in AT vascularity may suggest early tendinopathic changes to the tendon's structure following chronic nicotine exposure. Despite the changes in vascularity, we did not detect structural changes in cell shape or density. A previous study of porcine tenocytes exposed to nicotine found that alterations in matrix metalloproteinase (MMP) expression were dependent upon exposure to cyclic stretch.⁹ Throughout our study, animals were housed in cages and thus were not exposed to a high level of repetitive stimuli. Nicotine exposed tendons also had an increase in percent relaxation, a viscoelastic property, similar to changes seen in fibrotic tendon tissue post-injury. The addition of exercise or overuse as a physical stimulus to these nicotine exposed animals may manifest more dramatic changes to the tendon structure and composition. Further studies are also needed to assess the effect of nicotine dose on tendon properties and on healing of injured tissue.

SIGNIFICANCE: Chronic nicotine exposure alters tendon vascularity and viscoelasticity, which may predispose tendons to degeneration and injury.

REFERENCES: [1] Kwiatkowski TC, et al., Am J Orthop. 1996. [2] Ichinose R, et al., Acta Orthop. 2010. [3] O'Connor RJ, et al., Am J Epidemiol. 2006. [4] Chang K-V, et al., J Ultrasound Med. 2012. [5] Freedman BR, et al., JOR. 2016. [6] Thomopoulos S, et al., JBME. 2003. [7] Pingel J, et al., Am J Sports Med. 2013. [8] Zheng LW, et al., Bone. 2008. [9] Hatta T, et al., JOR. 2013.

ACKNOWLEDGEMENTS: This study was funded by the AFSH Resident/Fellow Fast Track Grant (Award 1271) and the NIH/NIAMS supported Penn Center for Musculoskeletal Disorders (P30 AR069619). The authors thank Zakary Beach, Courtney Nuss, Harina Raja, and Snehal Shetye.

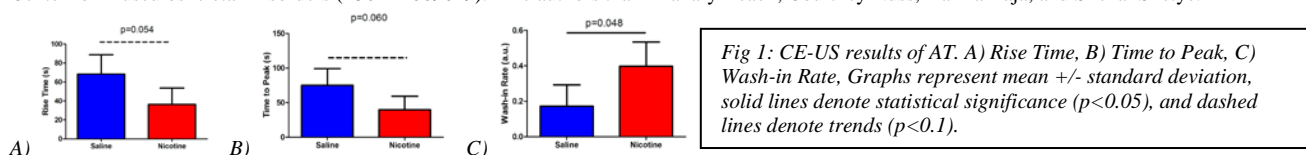


Fig 1: CE-US results of AT. A) Rise Time, B) Time to Peak, C) Wash-in Rate, Graphs represent mean +/- standard deviation, solid lines denote statistical significance (p<0.05), and dashed lines denote trends (p<0.1).

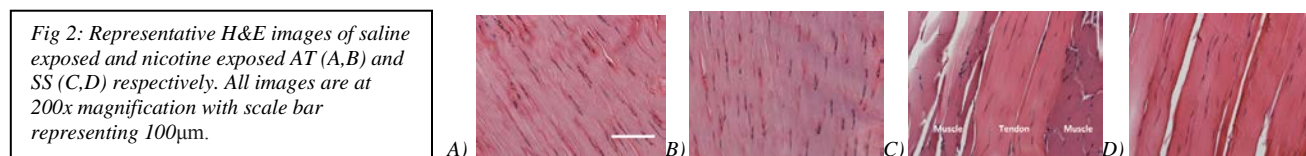


Fig 2: Representative H&E images of saline exposed and nicotine exposed AT (A,B) and SS (C,D) respectively. All images are at 200x magnification with scale bar representing 100µm.

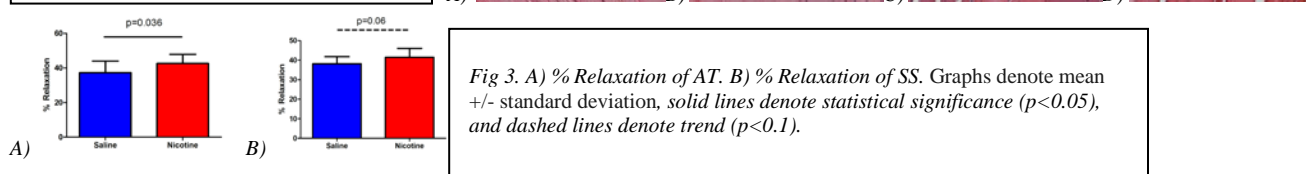
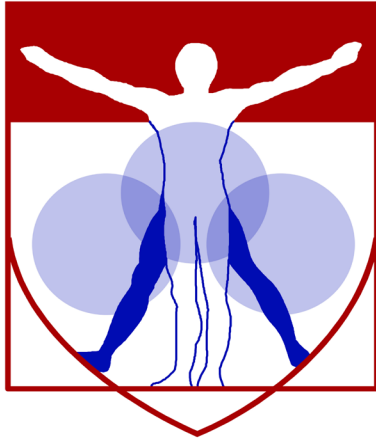


Fig 3. A) % Relaxation of AT. B) % Relaxation of SS. Graphs denote mean +/- standard deviation, solid lines denote statistical significance (p<0.05), and dashed lines denote trend (p<0.1).



PENN

CENTER for

MUSCULOSKELETAL

DISORDERS

Histology Abstracts

Development of Disc-Like Angle Ply Structures for Total Disc Replacement at Clinically Relevant Size Scales

Sarah E. Gullbrand,¹ Dong Hwa Kim,¹ Edward Bonnevie,¹ Beth G. Ashinsky,¹ Dawn M. Elliott,² Lachlan J. Smith,¹ Robert L. Mauck¹, Harvey E. Smith¹
¹University of Pennsylvania, Philadelphia, PA and Philadelphia VA Medical Center, Philadelphia, PA, ²University of Delaware, Newark, DE

Disclosures: None

Introduction: Replacement of the disc with a viable, tissue-engineered construct that mimics native disc structure and function is an attractive alternative to fusion or mechanical arthroplasty for the treatment of disc pathology. Towards this end, our group has developed disc-like angle ply structures (DAPS) sized for the rat caudal disc space that achieve near native composition and mechanical function with *in vitro* culture [1]. Composite tissue-engineered discs have also been developed by several other groups; however, the average size of constructs reported in the literature remains a fraction of the size of human discs [2,3]. In order to translate tissue-engineered disc replacement towards clinical use, successful fabrication and *in vivo* evaluation of these constructs at larger size scales is critically important. The purpose of this study was to evaluate the maturation of medium (rabbit lumbar disc equivalent) and large (goat/human cervical disc equivalent) sized DAPS constructs over 15 weeks of *in vitro* culture and after 5 weeks of subcutaneous implantation.

Methods: DAPS Fabrication, Culture and Subcutaneous Implantation: DAPS were fabricated in two sizes – medium (3 mm height x 10 mm diameter, NP diameter = 5 mm) and large (6 mm height x 20 mm diameter, NP diameter = 10 mm). The AF region of the DAPS was fabricated by electrospinning aligned sheets of 250-300 μm thick poly(ε-caprolactone) (PCL), and cutting the sheets into strips at a 30 degree angle. The strips were hydrated, coated with fibronectin and seeded with bovine AF cells (3,333 cells/mm²). Following 1 week of culture in chemically defined media with TGF-β3 (CM+), strips were coupled at opposing fiber angles (+/- 30°), and wound in a custom mold to form the circular AF region. The NP region of the DAPS was fabricated by seeding bovine NP cells in a 2% agarose hydrogel (20 million cells/mL), and culturing for 2 weeks in CM+ prior to combining with the AF region. The combined DAPS were cultured for either 5, 10 or 15 weeks in CM+ on an orbital shaker. After 5 weeks of pre-culture, DAPS of both size scales (n=6 per size) were implanted subcutaneously (SQ) in athymic rats for 5 weeks. **Viability, Metabolic Activity and Biochemistry:** At each *in vitro* and *in vivo* time point (n=4-6 per group), DAPS of each size were bisected. From one half-DAPS, GAG and collagen content were quantified via the DMMB assay and the OHP assay, respectively. From the remaining half DAPS, cell viability of the NP region was assessed via live-dead staining, and metabolic activity of the AF region was assessed via the MTT assay. **MRI and Mechanical Testing:** At each *in vitro* time point (n=3 per group), sagittal MRI T2 maps of the DAPS were obtained. Mechanical properties of the DAPS in unconfined compression (20 cycles compression, 0.24 MPa) were determined via a bi-linear fit of the stress-strain curve. **Histology:** DAPS (n=2 per group) were processed through paraffin, sectioned in the sagittal plane, and stained with Alcian blue (GAG) or picrosirius red (collagen). **Statistics and Correlation Analysis:** Significant differences in quantitative outcome measures were assessed via two-way ANOVA with Tukey's post-hoc test. Correlations between DAPS T2 values, biochemistry and mechanical properties were assessed using the *corr.test* function in R (r-project.org) for each size scale.

Results: In general, medium DAPS outperformed large DAPS with respect to AF and NP cell viability during *in vitro* culture and following subcutaneous implantation (Figure 1A, B). Subcutaneous implantation of the DAPS significantly increased AF cell metabolic activity in the medium DAPS, while NP cell viability was significantly reduced at both size scales compared to pre-implantation values. Analysis of compressive mechanical properties (Figure 1C, D), illustrated that medium DAPS matured more rapidly than large DAPS, as characterized by increases in toe modulus and reductions in transition strain at 10 weeks. AF T2 values significantly decreased from 5 to 15 weeks culture in both medium and large DAPS; NP T2 values were not affected by culture duration. NP and AF GAG and collagen content were significantly higher in medium DAPS compared to large DAPS, and reached maximal values after 15 weeks of culture at both size scales (Medium: NP GAG = 3.0% ww, AF GAG = 2.4% ww, NP collagen = 2.0% ww, AF collagen = 1.4% ww; Large: NP GAG=1.5% ww, AF GAG = 1.2% ww, NP collagen = 1.1% ww, AF collagen = 1.0% ww). NP GAG content was significantly reduced compared to pre-implantation values in both medium and large DAPS following SQ implantation. SQ implantation significantly increased NP collagen content in the medium DAPS, but did not affect AF collagen or GAG content at either size scale. Histology (Figure 2) confirmed quantitative biochemical analyses and further demonstrated the heterogeneity of matrix distribution present in the DAPS, particularly at the large size scale. Correlation analyses illustrated stronger correlations between MRI, biochemistry and mechanical properties in the medium DAPS than in large DAPS.

Discussion: Medium DAPS outperformed large DAPS, maturing more rapidly with more homogenous matrix distribution compared to large DAPS. Subcutaneous implantation was detrimental to cell viability and GAG content in the NP region independent of DAPS size, as we have previously observed in small DAPS sized for the rat caudal disc space [4]. In contrast, AF matrix content was maintained at pre-implantation values at both size scales following subcutaneous implantation, potentially due to infiltration of host cells into the outer layers of the AF. *In vitro* matrix distribution and *in vivo* performance of large DAPS could be further improved via the inclusion of nutrient channels, as has been utilized for cartilage tissue engineering, or via culture in a bioreactor [5,6]. Future work will evaluate the DAPS in a large animal model to further the translation of these constructs for the treatment of end stage disc degeneration.

Significance: We have demonstrated the feasibility of scaling up DAPS for total disc replacement to clinically relevant size scales. Clinical translation of tissue-engineered discs will offer an alternative to mechanical disc arthroplasty and fusion procedures, and may change the paradigm of clinical care for patients with disc pathology and associated axial spine and neurogenic extremity pain.

References: [1] Martin + 2015 ORS Proceedings [2] Bowles+ 2011 [3] Choy+2015 [4] Martin+2017 [5] Nims+2015 [6] Mauck+2000

Acknowledgments: This work was supported by the Department of Veterans' Affairs and the Penn Center for Musculoskeletal Disorders.

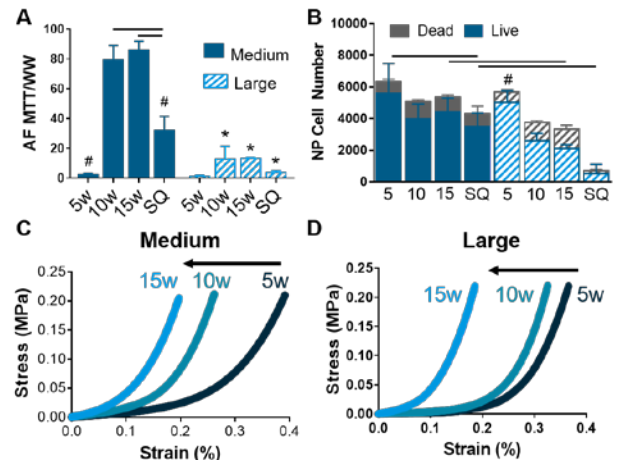


Figure 1. DAPS (A) AF cell metabolic activity, (B) NP cell viability for all experimental groups, and representative compressive stress-strain curves of (C) medium and (D) large DAPS. Bars denote significance, * = p<0.05 compared to medium at the same time point. # = p<0.05 compared to all other time points within a size.

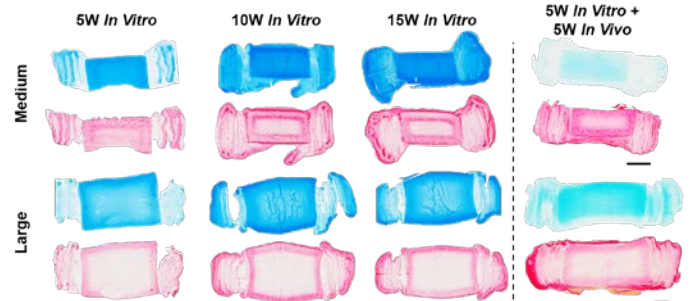


Figure 2. Alcian blue (top) and picrosirius red (bottom) stained sagittal histology section of DAPS in each experimental group (scale = 2 mm).

Nucleus Pulposus Cells have Epithelial Cell-Like Cytoskeleton and Highly Express N-Cadherin

Robert J Tower¹, Zuozen Tian², Brian Cosgrove¹, Robert L. Mauck^{1,2,3}, Motomi Enomoto-Iwamoto⁴, Ling Qin¹, and Yejia Zhang^{1,2,3}

¹Department of Orthopaedic Surgery, University of Pennsylvania, Philadelphia, PA ²Department of Physical Medicine and Rehabilitation, University of Pennsylvania, Philadelphia, PA ³Translational Musculoskeletal Research Center (TMRC), Corporal Michael J. Cresenz Veterans Affairs Medical Center, Philadelphia, PA ⁴Department of Orthopaedics, University of Maryland, Baltimore, MD
rtower@mail.med.upenn.edu

Disclosures: All authors declare no conflicts of interest

INTRODUCTION: Back pain related to intervertebral disc (IVD) degeneration is a common condition, believed to initiate in the nucleus pulposus (NP). Understanding the characteristics of the NP cells may help design strategies to prevent and/or revert IVD degeneration. In this study, we aim to examine actin cytoskeleton organization by staining filamentous actin (F-actin) with fluorescently-tagged phalloidin and analyzing gene expression profiles.

METHODS: All animal experimental procedures were approved by the Institutional Animal Care and Use Committee of the Corporal Michael J. Cresenz Veterans Affairs Medical Center in Philadelphia. For mouse tail injury model, twelve young adult (8 week old) female C57BL/6j mice (the Jackson Laboratory, Bar Harbor, ME, USA) were used in this study. Under anesthesia, the mouse tail IVDs were injured with a 26-G needle inserted under fluoroscopic guidance. Histological evaluation of Alcian Blue and Haematoxylin and Eosin (H&E) counter stained sections confirmed typical changes during injury. Tail IVDs with adjacent vertebral bodies were isolated, decalcified with 12.5% EDTA (Sigma), embedded in OCT compound (Tissue-Tek, Torrance, CA), and cryosectioned. Actin filaments were stained with Alexa fluor 488 phalloidin (Thermo Fisher Scientific), covered with mounting medium containing DAPI (Vector Laboratories, Burlingame, CA, USA), and imaged with a confocal microscope (Nikon Eclipse Ti, Nikon, Japan). For gene expression analyses, the lumbar and coccygeal vertebrae of 4 mice were isolated with a scalpel under a dissecting microscope: the gelatinous NP was scraped off with a scalpel. Annulus fibrosus (AF) tissues, identified by their concentric rings, were shaved off the cartilaginous endplate with a scalpel. Total cellular RNAs were extracted and the Mouse Extracellular Matrix & Adhesion Molecules RT Profiler PCR Array (Qiagen, Gaithersburg, MD) was used to profile the expression of 84 genes important for cell-cell and cell-matrix interactions.

RESULTS: In NP cells from intact IVDs, actin filaments are highly concentrated at the periphery of the cell, where they form a three-dimensional network beneath the plasma membrane (n=5; Figure 1A). This cell shape is reminiscent of that in the epithelium where cells exhibit cobblestone morphology. In injured IVDs, NP cells transition to a more oval shape and with a reduced cellular density (Figure 1B); actin filaments appear to have reorganized. Among the 84 genes examined, gene expression analyses showed cadherin 2 (*cdh2*; commonly known as neural (N)-cadherin) expressed higher in the NP than in AF, while secreted phosphoprotein 1 (*spp1*) was highly expressed in both the NP and AF. Thus, these genes were further examined by quantitative Real-Time PCR. NP, AF, and knee articular cartilage (AC) were isolated from a further 8 mice. The validated primer sets for *cdh2*, *spp1* and *b2m* were purchased (QuantiTect Primer, Qiagen, Gaithersburg, MD). Relative expression was calculated using the $2^{-\Delta\Delta C_t}$ method, normalized to *b2m* as an endogenous loading control. *Cdh2* gene expression was significantly higher in the NP compared to AF, which in turn was significantly higher than the AC. (n=8 for NP and AF; n=4 for AC, p<0.01; Figure 2A). *Spp1* was expressed at equally high levels in the NP, AF and AC (n=4, p>0.05; Figure 2B).

DISCUSSION: We were surprised to find that the normal NP cells represented a cobblestone organization (epithelial cell-like), and cells became oval shaped (considered chondrocyte-like) following injury. *Cdh2* gene is expressed higher in the NP than AF or AC, which would be linked to the unique morphology of NP cells. Future studies will include examination of gene expression and protein distribution of *Cdh2* and other epithelial cell makers, to elucidate the role of this intriguing cell phenotype in IVD degeneration.

SIGNIFICANCE/CLINICAL RELEVANCE: IVD degeneration is thought to initiate in the NP. NP cells reside in a high pressure and low nutrient environment, thus requires specialized physiological properties. A better understanding of the cytoskeleton and cell-cell interaction in normal NP and in response to injury may lead to better repair strategies for the degenerating disc.

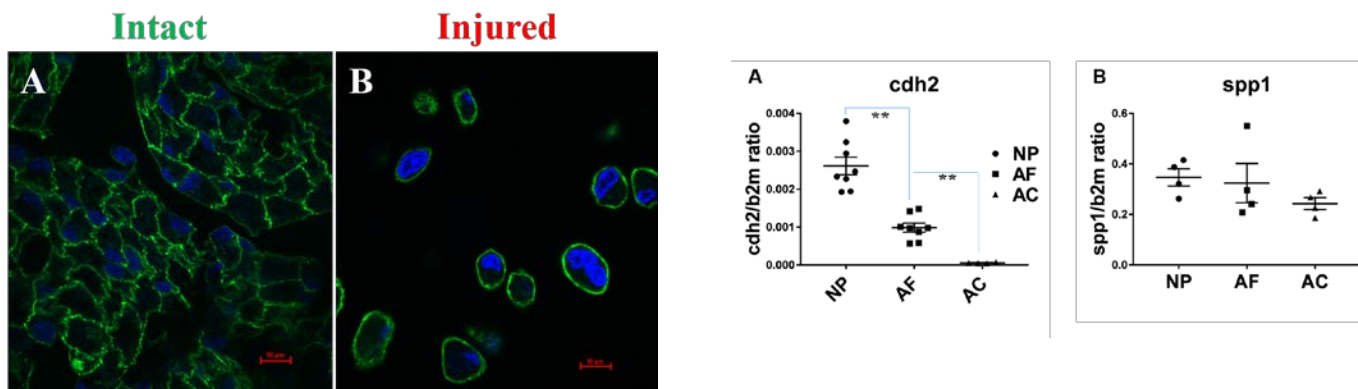


Figure 1 Injured tail nucleus pulposus cells proliferate. Green: F-actin cytoskeleton stained with phalloidin; Blue: cell nuclei stained with DAPI. Scale bar equals 10 um.

Figure 2 Gene expression by real time PCR in murine nucleus pulposus (NP), annulus fibrosus (AF) and articular cartilage (AC) tissue. *Cdh2*: cadherin 2; *spp1*: secreted phosphoprotein 1. Each point represents an individual animal; n=4-8. **p<0.01

Pathophysiological Role of ADAM8 (A Disintegrin and Metalloproteinase 8) in Intervertebral Disc Degeneration

Yeji Zhang, MD, PhD; Zuozen Tia, MS, Miersalijiang Yasen, MD, PhD; Robert Mauck, PhD, Maurizio Pacifici, PhD; Motomi Enomoto-Iwamoto, DDS, PhD.

INTRODUCTION:

Chronic back pain related to intervertebral disc (IVD) degeneration is a significant problem, costing billions of dollars in the U.S. alone. Despite the staggering disease burden, there is no current effective treatment to retard IVD degeneration and reduce associated pain because the etiology of IVD degeneration remains unclear. IVD degeneration is characterized by increased extracellular matrix degradation and a variety of cellular responses. ADAM8 (A Disintegrin And Metalloproteinase 8) is a membrane-anchored proteinase that is involved in cell-matrix and cell-cell interactions in physiological and pathological processes. Our results led to the hypothesis that ADAM8 is a key enzyme in the degenerative cascade in IVD tissues and represents a major, novel and potentially far-reaching step ahead in understanding disease etiology.

METHODS:

To examine expression and distribution of ADAM8 in IVD, degenerative annulus fibrosus and nucleus pulposus tissues were collected from patients undergoing surgery for back pain with appropriate institutional review board (IRB) approval. Degree of IVD degeneration was determined by MRI (grade V being the most degenerative). Distribution of ADAM8 in the IVD tissues was analyzed by immunostaining. ADAM8 and its specific proteolytic product, fibronectin fragments (FN-f; VRAA271), were quantified by Western blotting (n=3-4 for each grade). To examine the role of ADAM8 in IVD degeneration, we performed gain-of-function experiments in mice. Mature human ADAM8 ectodomain was generated in the HEK293T cell line (BioZyme, Apex, NC), labeled with the infrared dye (IRDye, Li-Cor Biosciences) and injected into the wild type mouse tail IVD. The ADAM8 or vehicle-injected IVD tissue was harvested 1-4 weeks after injection and subjected to histological inspection and immunostaining with an antibody to VDPIEN (neoepitope of cleaved aggrecan, a generous gift from Dr. J. Mort). We have also performed loss-of-function experiments in mice. The ADAM8 gene-inactivation mutant mice that harbor a point mutation, replacing the Glutamic acid at position 330 with a Glutamine (ADAM8E330Q/E330Q mice, generously provided by Dr. Anne Marie Malfait), were used to examine requirement of ADAM8 for IVD. We dissected IVDs from wild type and ADAM8E330Q/E330Q mice at 9 months of age and examined the neoepitope of the fibronectin fragment (FN-f) (VRAA271) by Western blotting. Aggrecan cleavage was examined by immunostaining.

RESULTS:

Immunostaining demonstrated that ADAM8 was expressed in human IVD tissues. Both ADAM8 and its proteolytic products (fibronectin fragments) were increased with IVD degeneration. These findings establish the clinical significance of ADAM8 in IVD degeneration. We observed that disorganized chondrocyte proliferation in IVDs was much more evident in the ADAM8-injected IVDs than in the PBS-injected IVDs in wild type mice. ADAM8-injected IVDs showed higher immunoreactivity to the antibody against the neoepitope of cleaved aggrecan, compared with the PBS-injected IVDs.

CONCLUSION:

These findings suggest that the ADAM8 proteolytic domain stimulates IVD degeneration. Inhibition of ADAM8 may be a valid therapeutic option for IVD degeneration and related back pain.

YAP and TAZ maintain cytoskeletal equilibrium by limiting actomyosin tension

Devon Mason^{1,2,3}, James Dawahare², Dung Nguyen², Yang Lin³, Sherry Voytik-Harbin⁴, Pinar Zorlutuna², Mervin Yoder³, and Joel Boerckel^{1,2}

¹ University of Pennsylvania, Philadelphia, PA ² University of Notre Dame, Notre Dame, IN ³ Indiana University, Indianapolis, IN ⁴ Purdue University, West Lafayette, IN

Email of presenter: dmason1@nd.edu

INTRODUCTION: Embryonic development and post-natal wound healing require coordinated multicellular migration. Migration requires spatiotemporal control of actomyosin contractility and adhesion to polarize cells in response to cell-cell and cell-matrix interactions. Extracellular conditions dictate focal adhesion formation that increase actomyosin contractility following by focal adhesion maturation. Actomyosin and focal adhesion remodeling reinforce one another and form a molecular clutch based cytoskeletal feedforward loop, however how the cytoskeleton is maintained at an optimal tensile equilibrium is unknown. Mechanotransducers coordinate transcriptional changes in response to extracellular cues in parallel to cytoskeletal mechanoadaptation. Transcriptional co-activators yes-associated protein (YAP) and transcriptional activator with PDZ-binding domain (TAZ) are such mechanotransductive factors that are activated by static and dynamic force and inhibited by cell-cell contact. However, the role that YAP and TAZ play in mechanotransductive control of cytoskeletal equilibrium is unknown.

METHODS: Endothelial colony forming cells (ECFCs) were depleted of YAP and/or TAZ using short interfering RNA (siRNA). Transfected cell monolayers were scratched and wound closure was tracked over time. Cells were fixed and immunocytochemistry was performed to visualize vinculin, β 1-integrin, YAP, TAZ, and actin (phalloidin). Cytoskeletal pre-stress was measured using nanoindentation and gene expression of YAP/TAZ target genes in actively migrating cells using qPCR.

RESULTS SECTION: YAP and/or TAZ depletion significantly decreased ECFC wound closure partially through a decrease in migration speed (Figure 1a-c). YAP and TAZ were nuclear (i.e. active) in leading edge cells which coincided with increased cytoskeletal pre-stress, measured as the apical cell modulus (Figure 1d&e). Actin polymerization and focal adhesion maturation significantly increased in YAP and/or TAZ depleted cells (Figure 2a-c). However, focal adhesions still remodeled in YAP/TAZ depleted cells, indicated by β 1-integrin endocytosis (Figure 2d). Instead, we found that YAP/TAZ deficiency increases myosin light chain (MLC) phosphorylation and myosin II inhibition using Y-27632 or blebbistatin normalized the cytoskeleton and partially restored migration (Figure 2e&f). We found that the YAP/TAZ target gene NUA2 family kinase 2 (NUAK2) is upregulated after YAP/TAZ depletion (data not shown). NUA2 upregulation sequesters myosin light chain phosphatase, preventing MLC dephosphorylation, promoting myosin II activation, and co-depletion of YAP/TAZ and NUA2 partially restored cytoskeletal structure and migration (data not shown)

DISCUSSION: YAP and TAZ are mechanotransductive transcriptional co-activators that mediate cell migration. We found that YAP and TAZ transcriptionally control cytoskeletal tension through control of myosin light chain phosphorylation. YAP and TAZ limit actomyosin tension by repressing the expression of NUA2, resulting in MLC dephosphorylation. Limiting pMLC allows adaptive actomyosin and focal adhesion remodeling that prevents cells from being anchored to their substrate and permits migration. Future work will study how YAP and TAZ mechanotransduction adapts the cytoskeleton in response to static and dynamic changes in cell-cell and cell-matrix conditions.

SIGNIFICANCE/CLINICAL RELEVANCE: YAP/TAZ activation are essential for endothelial cell migration by maintaining cytoskeletal equilibrium. Active YAP and TAZ are required for vasculogenesis and may be a viable target to promote vascular invasion into ischemic tissue to enhance wound repair.

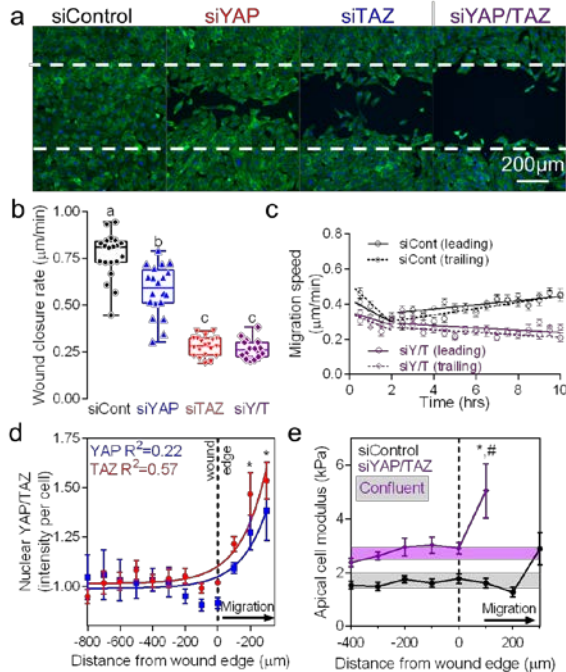


Figure 1: YAP and TAZ are essential for ECFC migration and control apical cell modulus. a) representative images of ECFC migration after 12 hours, phalloidin (green). b) Wound closure after 12 hours and c) live migration speed. d) Collective nuclear YAP/TAZ intensity and e) individual apical cell modulus in 100 μ m bins starting at the leading-edge.

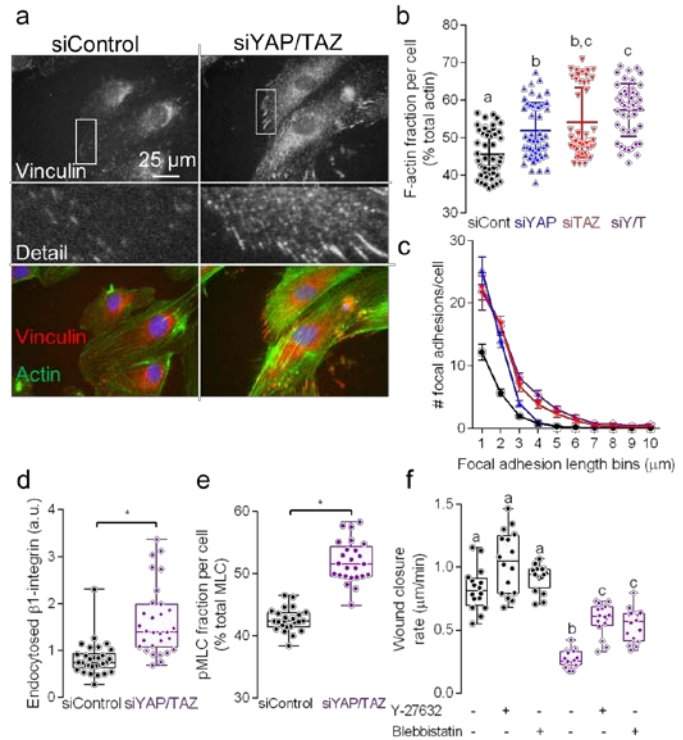


Figure 2: YAP and TAZ control focal adhesion remodeling through actomyosin tension to promote migration. a) representative images of ECFC focal adhesions. b) Percentage polymerized actin. c) Focal adhesion length histo d) Collective nuclear YAP/TAZ intensity and e) individual apical cell modulus in 100 μ m bins starting at the leading-edge cell.

Donor-Dependent Effects on the Survival and Extracellular Matrix Producing Capacity of Mesenchymal Stem Cells following Hypoxia and TGF- β Conditioning

Sun H. Peck^{1,2}, Justin R. Bendigo^{1,2}, George R. Dodge^{1,2}, Robert L. Mauck^{1,2}, Neil R. Malhotra², Lachlan J. Smith^{1,2}
¹Philadelphia VA Medical Center, Philadelphia, PA; ²University of Pennsylvania, Philadelphia, PA

Disclosures: SHP (N), JRB (N), GRD (N), RLM (N), NRM (N), LJS (N)

Introduction: In recent years, application of mesenchymal stem cells (MSCs) for regeneration of tissues such as the nucleus pulposus (NP) within the intervertebral disc and articular cartilage (AC) has received considerable attention [1,2]. Previous studies have shown that MSCs are capable of undergoing differentiation into multiple cell lineages [3], and specifically into NP or AC-like phenotypes under certain culture conditions [4,5]; however, a key challenge to the successful application of MSCs for NP or AC regeneration is the harsh *in vivo* environment, which is characterized by low nutrition and oxygen tension, both of which may negatively impact the survival and biosynthetic properties of MSCs [6]. Previously, we showed that conditioning MSCs using hypoxia and TGF- β during monolayer expansion enhanced subsequent survival of these cells in nutrient and oxygen poor culture conditions but did not significantly affect extracellular matrix (ECM) production capacity on a per cell basis [7]. We also demonstrated significant differences in global gene expression profiles of MSCs as a function of cell donor, independent of expansion conditions. The objective of this study was to investigate donor effects on MSC survival and ECM production under low nutrient and oxygen conditions subsequent to hypoxic and TGF- β exposure during monolayer expansion.

Methods: Cell Isolation and Monolayer Conditioning: Bone marrow-derived MSCs were isolated from 3 juvenile bovine long bones and expanded to confluence through a single initial passage in monolayer in normoxia (21% O₂) and basal medium (DMEM (4.5 g/L glucose) and 10% FBS) in independent cultures. MSCs from each donor were then passaged and expanded in basal medium for 1 additional week in one of four different conditions: 1. Normoxia (21% O₂; standard MSC expansion conditions); 2. Normoxia+TGF- β 3 (10 ng/mL); 3. Hypoxia (2% O₂); 4. Hypoxia+TGF- β 3. **Pellet Culture:** After monolayer expansion, cells were passaged and cultured in pellets (250,000 cells/pellet) in a simulated NP/AC-like environment (hypoxia (2% O₂), chemically defined media with low glucose (1 g/L) DMEM, no growth factors). After 2 weeks of culture, pellets were harvested and either fixed in formalin then processed for paraffin histology and immunohistochemistry (IHC) (n=2/donor), or analyzed for biochemical composition (n=5/donor). For histology, sections were stained with Alcian blue (glycosaminoglycans, GAG) or picosirius red (collagen). For IHC, sections were stained with antibodies specific for aggrecan (ACAN), Collagen I (COL1), or Collagen II (COL2). DNA (per pellet, surrogate for cell survival) and GAG (per DNA) contents were quantified using standard biochemical assays. Significant differences between groups were established using 2-way ANOVA with Bonferroni post-hoc tests (p<0.05).

Results: Cell Survival in Pellet Culture: For all 3 donors, DNA content for MSCs expanded under standard conditions (normoxia, without TGF- β 3), was approximately 20% of day 1 after 7 days, reflecting poor cell survival under low nutrient and low oxygen culture conditions (Fig 1). For MSCs conditioned in hypoxia, with or without TGF- β 3, DNA content was significantly higher than for MSCs expanded in normoxia, with or without TGF- β 3, reflecting improved cell survival. MSCs conditioned in hypoxia without TGF- β 3 had the highest percent survival. Examining donor-dependent effects, MSCs from Donor 1 were the least sensitive to expansion conditions with respect to survival in pellet culture, while MSCs from Donor 3 were the most sensitive, with significant differences in DNA content between all expansion conditions. Averaging results for all 3 donors, significant differences in percent cell survival as a function of expansion condition were the same as those for Donor 1. **Extracellular Matrix Production:** For Donors 1 and 2, GAG per DNA for MSCs conditioned with TGF- β 3 (under either normoxia or hypoxia) was significantly higher compared to MSCs expanded without TGF- β 3 (Fig 2). In contrast, for Donor 3, higher GAG content was present for MSCs conditioned in hypoxia compared to normoxia treated groups, but there were no significant effects of TGF- β 3. When results for all 3 donors were averaged, there were no significant differences in GAG per DNA as a function of expansion condition. Histological results supported biochemical assay results, where pellets formed from MSCs conditioned in hypoxia, with and without TGF- β 3, were larger, reflecting enhanced cell survival, and pellets with higher GAG content stained more intensely with Alcian blue and ACAN (Fig 3A, B). Pellets also stained positively for collagen with no clear differences as a function of donor or expansion condition, with COL2 staining more intensely than COL1 (Fig 3C).

Discussion: The results of this study demonstrate that conditioning in hypoxia during monolayer expansion leads to improved survival of cells in NP/AC-like conditions. In our previous study, no differences in GAG synthesis between the various expansion culture conditions were observed. Similarly, in the current study, when individual donor results were averaged, GAG production did not change as a function of expansion condition. Interestingly, however, when MSC donors were analyzed individually, significant differences in GAG production as a function of expansion condition were present. Likewise, significant differences in MSC survival as a function of expansion condition were present for individual donors that were not discernable when results for donors were combined. These findings highlight the importance of considering donor-specific factors such as age, sex, and other biological differences that may affect the response of MSCs to microenvironmental stimuli in the application of these cells in NP and AC regenerative therapeutics.

Significance: These results highlight the importance of considering the intrinsic biological differences present in the patient population when developing cell-based therapies as certain patients may be better candidates for autologous MSC implantation for disc or cartilage regeneration than others. Elucidating the molecular mechanisms that control the donor-dependent differences in cell survival and matrix production will pave the way for more effective cell-based therapies for intervertebral disc and articular cartilage repair.

References: [1] Sakai+ Spine, 2005. [2] Johnson+ Science, 2012. [3] Pittenger+ Science, 1999. [4] Smith+ Tissue Eng A, 2013. [5] Johnstone+ Clin Orthop Relat Res, 1999. [6] Farrell+ OAC, 2014. [7] Peck+ ORS Trans, 2017.

Acknowledgements: Department of Veteran's Affairs, National Institutes of Health, Penn Center for Musculoskeletal Disorders

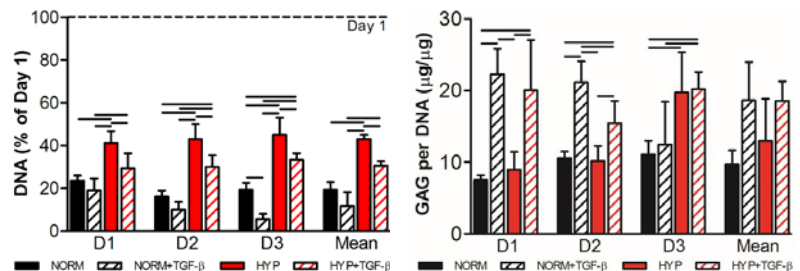


Figure 1. MSC survival (DNA) in pellet culture following monolayer conditioning as a percentage of Day 1. D: Donor; Mean: average of all 3 donors; n=5; all significance bars represent p<0.05.

Figure 2. GAG content of MSC pellets following monolayer conditioning. Normalized to DNA content. D: Donor; Mean: average of all 3 donors; n=5; all significance bars represent p<0.05.

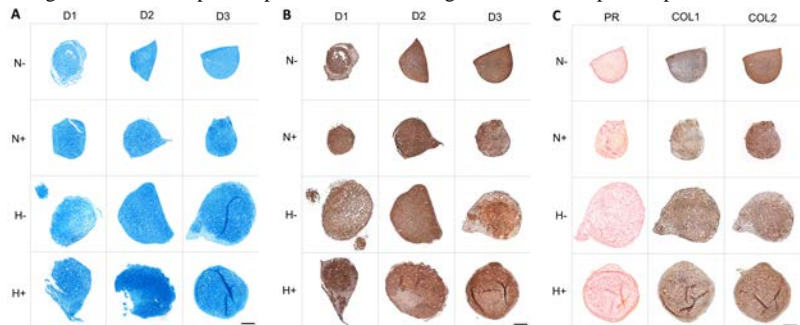


Figure 3. Composition of MSC pellets following monolayer conditioning. A. Alcian blue, B. Aggrecan, C. Representative images from donor 3 of Picosirius red (PR), Collagen 1 (COL1), Collagen 2 (COL2). D: Donor; N-: normoxia, N+: normoxia+TGF- β 3, H-: hypoxia, H+: hypoxia+TGF- β 3. Scale bar = 200 μ m.

Characterization of p16^{ink4a} conditional null mice's intervertebral disc

Novais EJ^{1,2}, Diekman BO³, M.V. Risbud¹

¹Thomas Jefferson University, PA ²University of Minho, Portugal, ³University of North Carolina School of Medicine, NC

Disclosures: Novais EJ: None. Diekman BO: None. M.V. Risbud: None.

INTRODUCTION:

Intervertebral disc (IVD) degeneration is the main cause of back pain, one of the most common diseases¹. Therefore disorders affecting the IVD, due to the inherent pain and disability associated with them have become a serious problem for Global Health². The etiology of disc disease is multifactorial, being related to abnormal mechanical loading, genetic background, obesity and aging³.

Recent studies have shown that senescence may play a role in IVD degeneration and aging in humans^{4,5}. The major characteristics of cell senescence are: high expression of p16 (encoded by the *Ink4a/Arf* locus, also known as *Cdkn2a*), an unique secretory phenotype (SASP), cell growth arrest, apoptosis resistance and altered gene expression⁵. Promising results have been shown by partial reverting age related diseases by selectively removing p16 positive cells^{6,7}. So, to understand the role of p16 and senescence in the intervertebral disc aging, we characterized the spinal phenotype of p16^{ink4a} conditional null mice that have been aged for 18 months.

METHODS:

The spines from 18 month old *AgcCreERT2-p16^{ink4a}^{fl/fl}* mice following tamoxifen injections (25 mg/kg bwt, i.p.) at 4 and 12 month were harvested and dissected. Motion segments were decalcified, embedded in paraffin and 7 μ m sections were cut from 3 lumbar levels from 12 animals (6 wild type and 6 p16^{ink4a} conditional null mice). Safranin and Pico-Sirius staining was used for morphological grading done by 4 blinded observers. Immunohistological staining for matrix proteins (Collagen 1a, collagen 2a and aggrecan); nucleus pulposus phenotypic markers (NP) (Glut1, CA3 and Keratine19); senescent markers (p19, p21 and H2AX) and SASP (IL1 β , Il6, MCP1 and MMP13) were used for characterizing.

RESULTS:

Both mice showed little signs of disc degeneration as evidenced from Tompson grading in both nucleus pulposus and annulus fibrosus compartments. Safranin and Pico-Sirius staining showed no differences between the matrix composition between both cKO and wild type animals. Both mice showed similar staining for matrix proteins, NP markers as well as senescence and SASP markers. Interestingly, ARF (p19) expression was increased in p16^{ink4a} cKO compare to WT.

DISCUSSION:

Based on these results we conclude that in contrast to what has been suggested by previous studies, p16 is not crucial for the maintenance of senescence in the IVD compartment. It is possible that by the increasing p19 and its downstream pathway, disc cells can bypass the absence of p16. We hypothesize that p16 is not necessary for NP cell senescence.

SIGNIFICANCE:

Senescence and p16 have been shown to be related with aging diseases and, particularly, IVD degeneration. Thus, uncovering the mechanisms behind these pathways can play a role for better understanding the pathology of age-related IVD degeneration.

REFERENCES:

1. US Burden of Disease Collaborators. The state of US health, 1990-2010: burden of diseases, injuries, and risk factors. *JAMA* (2013).
2. Cheung, K. M. C. *et al.* Prevalence and pattern of lumbar magnetic resonance imaging changes in a population study of one thousand forty-three individuals. *Spine* (2009).
3. Setton, L. a & Chen, J. *et al.* Mechanobiology of the intervertebral disc and relevance to disc degeneration. *J. Bone Joint Surg.* (2006).
4. Eisenstein, D. *et al.* Senescence in human intervertebral discs. *Eur Spine J.* (2006).
5. Deursen, J. M. *et al.* The role of senescent cells in ageing. *Nature.* (2014).
6. Baker, D. J. *et al.* Naturally occurring p16^{ink4a}-positive cells shorten healthy lifespan. *Nature* (2016).
7. Zhu, Y. *et al.* The Achilles' heel of senescent cells: from transcriptome to senolytic drugs. *Aging Cell* (2015).

ACKNOWLEDGEMENTS:

This work was supported by NIH grants: AR064733, and AR055655

Provision of Latent TGF- β Improves Cell Viability in Human-Sized Disc-Like Angle Ply Structures (DAPS)

Dong Hwa Kim,¹ Sarah E. Gullbrand,¹ Dawn M. Elliott,² Lachlan J. Smith,¹ Harvey E. Smith,¹ Robert L. Mauck¹

¹University of Pennsylvania, Philadelphia, PA and Philadelphia VA Medical Center, Philadelphia, PA, ²University of Delaware, Newark, DE

Introduction: A number of disc tissue engineering strategies have emerged for the replacement of degenerate discs [1,2], with some recent studies showing promise *in vivo* [3,4]. Our group recently developed disc-like angle ply structures (DAPS) sized for the rat tail (small, 1.5 mm high \times 4 mm diameter) and showed that these constructs achieved near native composition [3, 5]. However, a major challenge remains in scaling these constructs to human size, where homogeneous matrix deposition will be required throughout a large expanse [6]. Transforming growth factor-beta (TGF- β) is one of the most widely utilized mediators for tissue engineering, as it can spur matrix formation [7]. However, our findings and that of others has shown that supplementation with active TGF- β results in heterogeneous matrix accumulation, concentrated near the periphery. To overcome this limitation, one recent publication described the provision of latent TGF- β alongside active TGF, and showed that this enhanced cell and matrix distribution constructs for cartilage regeneration [8]. In the present study, beginning with a chemically defined medium [5], we assessed the impact of latent TGF- β supplementation on nucleus pulposus (NP) matrix production and distribution in a 3D-hydrogel and DAPS culture system sized for human application.

Methods: *NP cell-laden agarose hydrogel culture:* NP cells were encapsulated in a 2% agarose hydrogel at a density of 20 million cells/mL. Constructs (diameter: 10 mm, thickness: 4 mm) were cultured for 5 weeks in one of three media conditions: chemically defined media (CDM) with 10 ng/ml TGF- β 3 (Active TGF), CDM with 43 ng/ml latent TGF- β 1 (Latent TGF), or Active + Latent TGF media (Active + Latent TGF). *Large sized DAPS fabrication and culture:* Large sized DAPS (6 mm \times 20 mm outer diameter, NP diameter = 10 mm) were next fabricated. Electrospun poly(ϵ -caprolactone) (PCL) aligned sheets (thickness: 250-300 μ m) were used for developing the AF region of the DAPS by cutting sheets into strips at a 30 degree angle [3]. Bovine AF cells (3,333 cells/mm²) were seeded onto the strips and cultured for 1 week in chemically defined media containing active TGF. To form the circular AF region, with alternating fiber orientations in each layer, strips were coupled and wrapped concentrically using a custom mold [5]. To fabricate the NP region of the DAPS, bovine NP cells were encapsulated in 2% agarose (20 million cells/mL) and cultured for 2 weeks in chemically defined media containing active TGF alone, or active + latent TGF prior to combining with the AF region. *Viability, mechanical properties, histological assessment and quantitative T2 MRI:* Construct halves were stained with by Live/Dead for cell viability. A custom MATLAB program was used to automate counting of cells in each region. Compression testing of DAPS was carried out as in [5]. Additional samples were stained with alcian blue and picrosirius red to visualize proteoglycans and collagen, respectively. Structure and NP hydration were also assessed by quantitative T2 MRI, as in [5].

Results: Regional assessment of viability at 5 weeks showed a depth-dependent decline in viability in Active and Latent TGF-supplemented NP agarose constructs, especially in the central region. In contrast, simultaneous Active + Latent TGF supplementation resulted in a more homogeneous distribution of living cells (Fig. 1A). Histology also showed intense staining for GAGs though the tissue sections in this Active + Latent TGF supplemented construct (Fig. 1B). Next, large sized DAPS were successfully fabricated and cultured in media containing Active TGF with/without Latent TGF for up to 10 weeks (Fig. 2A). Active + Latent TGF-supplemented DAPS had a significantly higher cell viability in the center of NP region compared to those cultured in Active TGF alone (Fig. 2B, C). The transition strain also significantly decreased in the Active + Latent TGF-supplemented DAPS at 10 weeks. However, there were no significant difference in the toe region modulus between Active TGF and Active + Latent TGF DAPS at this time point (Fig. 2D). For both groups, histology showed intense staining for GAGs and collagen at the tissue periphery, but far less collagen staining in the tissue interior (Fig. 2E). NP and AF T2 values of Active + Latent TGF-supplemented DAPS were similar to that of Active TGF alone cultured DAPS (Fig. 3A, B).

Discussion: This study explored the impact of Active TGF and Latent TGF supplementation on the homogeneous growth and maturation of large sized DAPS *in vitro*. Our findings demonstrate that combination of Active TGF with Latent TGF is essential for establishing disc-like ECM content with homogeneous cell viability in these large NP cell-laden hydrogel constructs. Notably, despite the increased cellularity, Active TGF mixed with Latent TGF had no impact on construct properties. Furthermore, we noted persistent heterogeneity in matrix distribution under these conditions. These findings suggest that while provision Latent TGF can improve cell viability in these large constructs, additional work is required to optimize matrix deposition.

Significance: Our findings suggest that the combination of Active TGF with Latent TGF can mitigate gradients in viability observed in large tissue constructs. Further optimization of this growth is essential for improving the human translation of tissue engineered discs.

References: [1] Mizuno+ 2004 Spine [2] Mizuno+ 2006 Biomaterials [3] Martin+ 2014 Acta Biomater. [4] Bowles+ 2011 PNAS [5] Gullbrand+ 2017 ISSLS proceedings [6] Bian+ 2009 Osteoarthr. Cartilage [7] Richardson+ 2006 Stem Cells [8] Albros+ 2016 Biomaterials

Acknowledgments: This work was supported by the Department of Veterans Affairs and the Penn Center for Musculoskeletal Disorders.

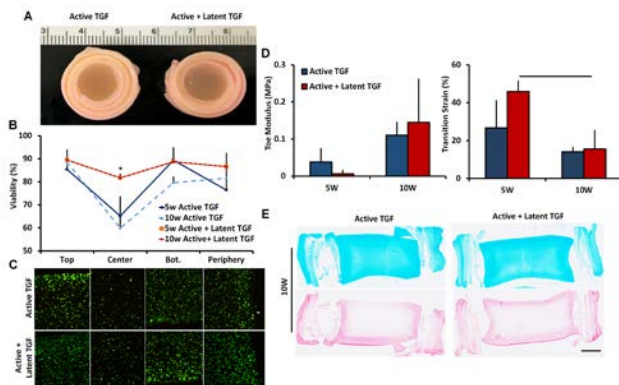


Figure 2. A: Gross appearance of DAPS cultured for 10 weeks. B: Quantification of viability. C: Live/Dead viability staining. D: Mechanical properties of DAPS. E. Alcian blue (top) and picrosirius red (bottom) stained DAPS at 10 weeks (scale = 2 mm).

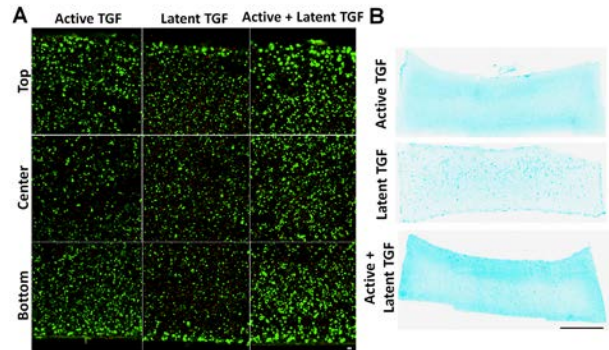


Figure 1. A: Representative of Live/Dead staining of NP cell-laden agarose gels cultured in three different media formulations for 5 weeks (Bar = 10 μ m). B: Alcian Blue staining of proteoglycans (Bar = 2mm)

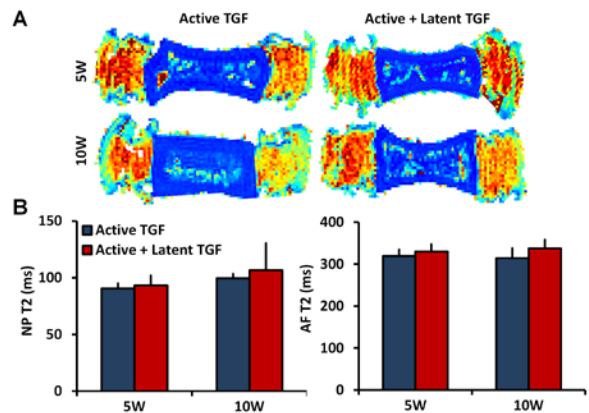


Figure 3. A. Composite T2 maps for each experimental group. B. NP and AF T2 values over 10 weeks culture.

Prior focal radiation causes atrophic nonunion fracture in mice

Luqiang Wang¹, Abhishek Chandra¹, Robert J Tower¹, Jaimo Ahn¹, Yejia Zhang^{1,2}, Ling Qin¹

¹Department of Orthopaedic Surgery and ²Department of Physical Medicine and Rehabilitation, University of Pennsylvania, Philadelphia, PA 19104, USA
luqiang@mail.med.upenn.edu

Disclosures: Wang (none), Chandra (none), Tower (none), Ahn (Merck Inc; Skelegen LLC), Zhang (none), Qin (none).

Introduction: Unlike many other tissues that healing with a scar, bone is a unique one that can regenerate completely after injury. However, up to 5-10% of bone fractures have delayed or nonunion healing. Among them, atrophic nonunion is especially challenging for the physician and thus is a major clinical burden in skeletal trauma treatment. Patients treated with radiotherapy (e.g. cancer, heterotopic ossification) are less likely to regenerate bone and more prone to develop fracture nonunion within the irradiated area even after several years of treatment. To better understand the relationship between radiation and fracture nonunion, we investigated the fracture healing process in mouse long bones with prior focal radiation.

Methods: All procedures were approved by our institution's Animal Care and Use Committee. **Animals-** Two-month-old male WT (C57BL/6) mice or Col2-Cre Rosa-Tomato mice in a C57BL/6J background received radiation (8 Gy twice, day 1 and day 3) at the midshaft of right tibiae (5 mm in diameter) from a focal irradiator (SARRP, Xstrahl). Two weeks later, closed transverse fractures were made within the irradiated area and the same area in the contralateral legs via a blunt guillotine with a pre-inserted intramedullary pin. **μ CT-** Bilateral tibiae were harvested at scheduled time points and scanned by vivaCT 40 (Scanco Medical AG) at a resolution of 10.5 μ m for measuring callus volume (CV), bone volume (BV), and bone volume fraction (BV/CV). **Histology and immunohistochemistry (IHC)** - Tibiae were fixed in 4% PFA, decalcified in 10% EDTA, and processed for paraffin or frozen sections followed by Safranin-O/fast green staining or IHC. For EdU staining, mice received 1.6 mg/kg EdU at 3 h before sacrifice. **Mechanical testing-** Tibiae harvested at 6 weeks after fracture were placed on a 3-point bending fixture and loaded with mechanical force at the previously fractured site using an Instron 5542. The force to failure curve was recorded for analyzing peak load, stiffness, and energy to failure. **Periosteal mesenchymal progenitor isolation-** Mice long bones were dissected free of surrounding tissues and digested in 2 mg/mL collagenase A and 2.5 mg/mL trypsin. The first 5 min digested cells were discarded. Periosteal mesenchymal progenitors were released by a subsequent 20 min digest and cultured in 15% α MEM for standard osteogenic and chondrogenic differentiation. **Statistics-** Data are expressed as means \pm SEM and analyzed by paired, two-tailed Student's t-test.

Results: At two weeks after radiation and right before fracture, bone marrow hematopoietic components in the irradiated region had already recovered but the periosteal cellularity was significantly lower compared to non-irradiated bone. Three days after fracture, compared to that in control, the periosteum layer in irradiated bones expanded much less at the proximal side of fracture, the region close to the growth plate, and did not expand at all at the distal side of fracture, the region close to the ankle (Fig. 1A). Consistently, EdU staining indicated less proliferation within the prior irradiated periosteum at the proximal site and almost no proliferation at the distal side compared to non-irradiated bone (Fig. 1B). Consequently, at 1 and 2 weeks after fracture, CV and BV were drastically decreased in irradiated bones at the proximal side with virtually no bone detected distal to the fracture line (Fig. 2). Histology uncovered that, while the irradiated bones attempted to heal through endochondral and intramembranous ossifications at the proximal side albeit at much less robust level compared to control, only cells with fibrotic morphology and type 1 collagen matrix were detected at the distal side (Fig. 3). Those cells did not stain for osteogenic (osterix and osteocalcin) or chondrogenic (Sox9 and type 2 Collagen) markers (data not shown). They did not express VEGF, leading to no vessel infiltration (Fig. 4) and no osteoclasts in the area (data not shown). Lineage tracing using Col2-Cre Rosa-Td Tomato mice that specifically label bone mesenchymal lineage cells, including periosteal progenitors [1], revealed that these fibrotic cells are not originated from periosteal progenitors (Fig. 5). At 4 and 6 weeks after fracture, the bony callus at the proximal side appeared to drape over the fibrous tissue of the distal side but without consolidation (Fig. 6, arrows). This resulted in a nonunion in the entire irradiated cohort (n=11 mice). Mechanical testing confirmed a drastically decreased peak load (-86%), stiffness (-75%), and energy to failure (-73%). Culturing periosteal mesenchymal progenitors under hypoxia conditions (0.1% oxygen) showed that radiation suppresses cell proliferation and inhibits osteogenic differentiation but not chondrogenic differentiation (data not shown).

Discussion: This location-dependent healing in prior irradiated bones demonstrates that both periosteum insult and a lack of surrounding vasculature are critical elements leading to fracture nonunion. This partially explains why fracture healing is difficult to achieve in patients who have been treated with radiotherapy. In our animal model, fibrous tissue instead of bone/cartilage is formed at the distal end of fracture after radiation, and these fibrous cells lack chondrogenic and osteogenic differentiation ability. These changes mimic clinical atrophic nonunion in which primarily fibrous tissue is detected at the fracture ends. Although the origin of this fibrous tissue is currently unknown, our data indicated that they do not come from periosteum. One possible source could be the surrounding muscle resident cells.

Significance: We establish a highly reliable, nonsurgical, and clinically relevant atrophic nonunion fracture model in mice for future investigations that will be relevant to patients undergoing radiotherapy but more broadly for those with atrophic nonunion. Particularly, identifying the source and characteristics of fibrous tissue may pave a way to resolve this clinically challenging disease.

References: 1.Chandra, A., et al., J Bone Miner Res, 2017. 32(2): p. 360-372.

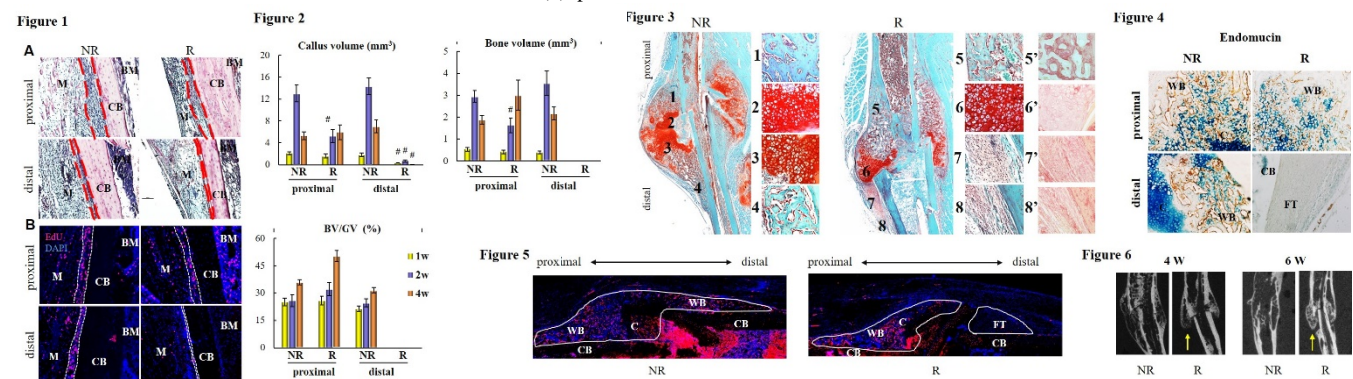


Figure 1. Prior radiation reduces periosteum responses toward fracture. HE (A) and EdU (B) stainings of fractured bones at 3 days post fracture. Dash lines depict periosteum. NR: non-irradiated; R: irradiated; CB: cortical bone; M: muscle; BM: bone marrow. **Figure 2.** Prior radiation has distinct effects on callus formation at two ends of the fracture line. MicroCT analysis of callus volume (CV) and bone volume (BV) within the callus at 1, 2, and 4 weeks after fracture. n= 6 mice/group. #: p<0.05 R vs NR. **Figure 3.** Fibrous tissue (images 7 and 8) is formed at the fracture distal end in prior irradiated bone at 2 weeks after fracture as shown by Safranin-O/fast green staining. Images 1-8 are magnified images for areas shown on the left panel. Images 5'-8' are Picro-Sirius red staining of the same sites as images 5-8. **Figure 4.** Fibrous tissues formed at 2 weeks after fracture at the distal end in prior irradiated bone are devoid of vessel invasion as shown by IHC of endomucin (a marker for endothelial cells, brown). CB: cortical bone, C: cartilage, WB: woven bone, FT: fibrous tissue. **Figure 5.** The fibrous tissue at 2 weeks post fracture in prior irradiated Col2-Cre Rosa-Tomato mice contains no Tomato positive cells. CB: cortical bone, C: cartilage, WB: woven bone, FT: fibrous tissue. **Figure 6.** Representative microCT images of nonirradiated and irradiated fracture callus at 4 and 6 weeks post fracture.

DNA damage in constricted migration impairs differentiation of myoblasts

Lucas R. Smith, Jerome Irianto, Dennis E. Discher

Introduction: Tissue regeneration often relies upon a stem cell's ability to proliferate, migrate, and differentiate to form new tissue. Chronic tissue injuries are often associated with fibrosis states that poses dense connective tissue networks with small pores and compromised the tissue regenerative capacity. Recent studies show that constricted migration of cancer cells causes DNA damage, genomic instability, and phenotypic alterations. Skeletal muscle has both a local stem cell population that is highly migratory and becomes fibrotic in diseased states. Thus, *we hypothesized that muscle progenitors incur DNA damage and have impaired differentiation after constricted migration, which may account for defects in regenerative capacity of fibrotic muscle.*

Methods: Both a murine myoblast cell line (C2C12) and a human rhabdomyosarcoma, muscle progenitor cancer, (Rh30) were used. Cells were placed on top of a transwell membrane with either small 3 μm or large 8 μm pores and allowed to migrate through the membrane for 24-48 hours. Immunofluorescent imaging was used to count γH2AX foci within the nucleus as a marker DNA damage as well as the presence of nuclear blebbing indicated from lamin staining. DNA damage was chemically induced with etoposide. Myoblasts were differentiated with low serum and stained for the presence of sarcomeric myosin to quantify differentiation. Serial transwell experiments used migrated cells from the bottom of a membrane that were expanded and then seeded on the top of another membrane.

Results: We find C2C12 myoblasts and Rh30 cells accumulate DNA damage as γH2AX foci (110% C2C12 and 60%, Rh30) after migration through rigid small pores that is mitigated in migration through large pores. After constricted migration, 32% of C2C12 cells show rupture of the nuclear lamina even though replication and proliferation rate are unaffected, with similar results for Rh30. Further rounds of constricted migration cause further accumulation of DNA damage that does not recover, even after 1 week in culture. Myoblast differentiation is temporally reduced by 55% in cells migrating through small pores and nearly eliminated after 3 rounds of transwell migration through small pores. Chemical induction of DNA damage in C2C12 myoblasts reduced differentiation by 80% demonstrating DNA damage as a plausible mechanism for impaired differentiation.

Conclusions: The stresses induced by constricted migration through small pores causes DNA damage and nuclear disruption in myoblasts. Constricted migration impedes the differentiation capacity of myoblasts and is compounded by serial migration. This work establishes constricted migration as a plausible mechanism for impaired differentiation, particularly in a fibrotic environment with increasingly small pores.

The Perichondrium is Enriched for Mesenchymal Progenitors that Initiate Canal Formation during the Development of the Secondary Ossification Center

Robert J Tower, Wei Tong, Chider Chen, Haoruo Jia, Motomi Enomoto-Iwamoto, Songtao Shi, Ling Qin

Long bone development progresses through the formation of the embryonic primary ossification center (POC) and the postnatal secondary ossification center (SOC). Several studies have elucidated the mechanisms behind POC formation, while much remains unknown regarding SOC development. Using Col2-Cre;tdTomato transgenic mice and in vitro techniques, we demonstrate the presence of an undifferentiated mesenchymal stem cell population enriched in the highly fluorescent (tomato^H) perichondrium of the epiphyseal cartilage prior to SOC initiation. In vitro, these tomato^H cells possess increased proliferative ($p < 0.05$), as well as osteogenic ($p < 0.001$) and adipogenic ($p < 0.001$) differentiation potentials. In vivo, perichondrial cells were found to show increased proliferation, visualized by Edu injection, and contained the stem and progenitor markers PDGFRb, CD44 and CD105 only after becoming part of the advancing SOC canal, which was also found to be populated by GDF5⁺ progenitor cells (observed using the GDF5-Cre;confetti transgenic mice) typically associated with cells lining the joints. These cells were able to give rise to several cell types within the formed epiphyseal bone, including osteoblasts, osteocytes, adipocytes and pericytes, along with their known role in the formation of the articular cartilage. In contrast to the POC, our results also demonstrate that it is the perichondrium, and not invading blood vessels, driven by hypertrophic chondrocyte-derived VEGF, which initiates and forms the invading SOC canal, coinciding with a cleavage of the chondrogenic matrix, visualized by VDIPEN and NITEGE staining. This perichondrium-derived canal was found to be the main source of VEGF, resulting in immature, filipodia-rich blood vessels (visualized by CD31 and endomucin staining) trailing behind the leading canal front. Later, epiphyseal chondrocytes outside the canal began expressing VEGF, driving angiogenesis and resulting in a shift to blood vessel invasion now leading bone cavity expansion. Our results suggest the presence of undifferentiated mesenchymal stem cells populating the perichondrium of the epiphyseal cartilage of developing bones with a unique ability to initiate the formation of the SOC canal. These results support an important role for the perichondrium and highlight its potential use as a source of multipotent progenitor cells which could be used in the treatment of bone and cartilage-related disease such as osteoarthritis.

Meniscus Cell Migration Through Dense Fibrous Networks Is Regulated By Nuclear Mechanics

Su Chin Heo¹, Kwang Hoon Song¹, Xuan Cao¹, Breanna N. Seiber¹, Vivek B. Shenoy¹, Jason A. Burdick¹, Robert L. Mauck¹
¹University of Pennsylvania, Philadelphia, PA

Disclosures: Su-Jin Heo (N), Kwang Hoon Song (N), Xuan Cao (N), Breanna N. Seiber (N), Vivek B. Shenoy (N), Jason A Burdick (N), Robert L. Mauck (N)

INTRODUCTION: Cell migration to a wound site is required for tissue repair [1]. However, the small pores of dense connective tissue extracellular matrix (ECM) present an obstacle to migration. This is primarily the result of the cell nucleus, the largest and stiffest organelle in the cell [2]. Modulating nuclear stiffness is, therefore, one potential strategy for enhancing cell mobility that could be leveraged to improve repair of dense connective tissues. Previously, we showed that Trichostatin A (TSA, a histone deacetylase inhibitor) induced chromatin relaxation and decreased nuclear stiffness in adult meniscus cells (aMCs), enhancing their migration through micron-sized pores using a transwell assay [3]. Here, we extend this work to a physiologic context, and determine whether such chemically induced nuclear softening modulates migration through fiber networks of varying porosity and through native tissue.

METHODS: To assess migration through nanofiber networks, a custom-PDMS chamber was implemented [3]. The system consisted of a top reservoir containing basal growth media (BM) and a bottom reservoir containing BM supplemented with 200 ng/mL PDGF (as a chemoattractant, Fig. 1A). Fluorescently labeled (Cell Tracker) poly(ϵ -caprolactone)/poly(ethylene oxide) (PCL/PEO) composite aligned fibrous scaffolds (composed of 0%, 25% or 50% sacrificial PEO fibers, Fig. 1B) were interposed between the two reservoirs (Fig. 1A). Adult meniscus cells (aMCs, passage 1) were seeded on the top of each scaffold and cultured in BM with/without TSA (200 ng/ml) for an additional 2 days (Fig. 1A). After a total of 3 days, 3D reconstructions of cells and scaffolds were obtained from confocal z-stacks to quantify infiltration [3].

Additionally, a cell/ECM model was developed in which the nucleus was taken to be a compressible neo-Hookean solid and the critical force required to pull the nucleus through these fiber networks was predicted (COMSOL Inc., Stockholm). To assess the impact of nuclear softening in the longer term, aMCs were seeded onto PCL/PEO 25% aligned scaffolds, and cultured in TGF- β 3 containing chondrogenic media for 4 weeks. TSA was applied once a week for 1 day (Fig. 2A). At 4 weeks, cryosections were obtained and stained with Picrosirius Red and DAPI. To quantify cell infiltration into the constructs, cell nuclei through the scaffold depth were counted using Image J. Finally, to investigate the role of nuclear softening on migration in native tissue, meniscus tissue explants (6 mm diameter, 6 mm height, Fig. 3A) were devitalized at their periphery and re-colonization was evaluated over time. For this, cells along the periphery of the explants were selectively lysed via a 2-cycle freeze-thaw process (-20°C for 30 min followed by thawing at room temperature for 30 min, repeated twice on Day -2, Fig. 3A). Freeze-thawed explants were treated with TSA for 1 day (Day -1, Fig. 3A) and the explants were then cultured in fresh BM for an additional 3 days. At day 3, LIVE/DEAD staining was used to assess the number of live cells within 1 mm of the periphery in 8 regions of the cutting plane using Image J. Statistical analysis was carried out in Graphpad Prism; sample number for each assay is as indicated in the figure legends.

RESULTS: Cell infiltration depth increased as a function of PEO content in the absence of TSA [(-)TSA, Fig. 1C] and TSA treatment [(+)TSA] enhanced this infiltration into scaffolds of lower porosity (lower % PEO groups, <25%) (Fig. 1C). The cell model predicted a decrease in critical force for nuclear entry into the scaffold as the PEO content (and so porosity [4]) increased (Fig. 1D). Consistent with the experimental data, the model predicted no effect of nuclear softening at higher PEO percentages (~50%). Taken together, these findings suggest that decreasing nuclear mechanics and/or increasing scaffold porosity enhance interstitial cell infiltration into dense fiber networks. In longer term cultures, control groups [(-)TSA], showed collagen deposition only at the border of the constructs (Fig. 2B). With TSA treatment [(+)TSA, 1x per week], the deposition and distribution of collagen was increased (Fig. 2B). Similarly, DAPI-stained cross-sections revealed a greater depth of aMC infiltration into scaffolds treated with TSA [Fig. 2C, D]. In native tissue, the 2-cycle

freeze-thaw process effectively eliminated live cells at the explant periphery (Day -2, Fig. 3B, D), while preserving viability in the center (Fig. 3B). A greater number of these viable cells migrated into the previously devitalized border region over three days of TSA treatment, compared to untreated control groups (Fig. 3C and D).

DISCUSSION: This work shows that both decreasing meniscus cell nuclear mechanics (via chromatin decondensation) and increasing scaffold porosity (via removal of sacrificial fibers) enhances adult meniscus cell interstitial migration in dense fibrous networks. The finding of increased collagen deposition in scaffolds subjected to repeated TSA treatment also suggests that de-condensation does not permanently interrupt cellular phenotype or matrix forming capacity. Notably, nuclear softening enhanced migration even in the context of dense, adult, meniscus ECM, suggesting that mobility of cells can be increased while preserving the loadbearing structure of the native tissue. Ongoing studies are reducing this finding to practice via the programmed release of de-condensing agents from implanted nanofibrous scaffolds, and testing this as a therapeutic in a large animal (ovine) model of endogenous meniscus repair.

SIGNIFICANCE: Our findings support the concept that decreasing physical impediments to migration through nuclear softening can improve dense connective tissue repair by enabling more cells to migrate to and colonize the wound site after injury. This will have widespread application in the promotion of endogenous repair in all poorly healing dense connective tissues.

REFERENCES: [1] Mauck+ 2015 ABME [2] Davidson+ 2014 Cell Mol Bioeng. [3] Heo+ 2017 ORS. [4] Baker+ 2008 Biomaterials.

ACKNOWLEDGEMENTS: This work was supported by the National Institutes of Health (AR056624 and EB02425).

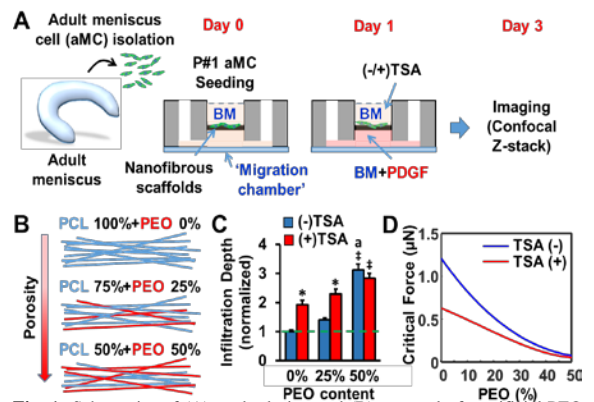


Fig. 1: Schematics of (A) study design and (B) removal of sacrificial PEO fibers to increase porosity. (C) Quantification of cell infiltration [n = 30, *p<0.05 vs (-) TSA, ‡p<0.05 vs 0% PEO, †p<0.05 vs 25% PEO, mean ± SEM, normalized to the control 0% PEO group]. (D) Predicted force required for nuclear entry into the scaffold as a function of PEO content.

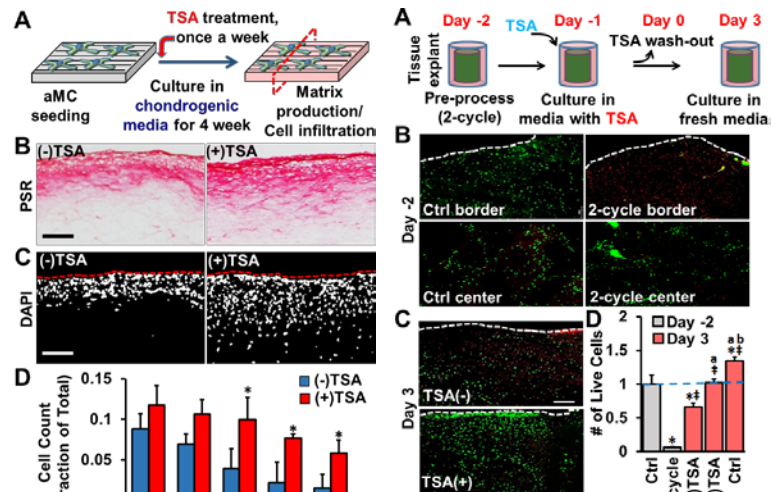


Fig. 2: (A) Schematic of study design. Representative cross-sections of aMC-laden nanofibrous constructs at week 4 stained for collagen (PSR: picrosirius red staining, B) and cell nuclei (DAPI, C), bar = 100 μm. (D) Quantification of MFC infiltration with/without TSA treatment [n = 3 images, *p<0.05 vs. (-)TSA, mean ± SD].

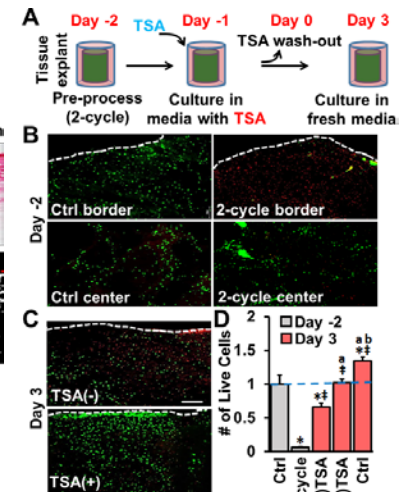


Fig. 3: (A) Study design. (B) Representative Live (green)/Dead (red) images at the periphery or center of control explants (Ctrl) and freeze-thawed explants (2-cycle) at day -2. (C) Live/Dead staining 3 days post TSA treatment. (D) Quantification of live cells at the periphery [n = 24-32 images from 3-4 explants, normalized to cell number in ctrl groups at day -2 (dashed line), mean ± SEM, *p<0.05 vs. Ctrl, †p<0.05 vs. 2-cycle, ‡p<0.05 vs. (-)TSA, †p<0.05 vs. (+)TSA].

Collagen GFP Reporter Mice Reveal Unique Subsets Of Cells Within The Tendon Midsubstance

Xi Jiang¹, Courtney Thompson², Pegah Abbasnia¹, Nicholas Oyster¹, Nathaniel A Dymnt¹
¹University of Pennsylvania, Philadelphia, PA, ²University of Notre Dame, South Bend, IN
 Email of Presenting Author: dymnt@upenn.edu

Disclosures: None.

INTRODUCTION: Heterogeneity within tendons and ligaments has traditionally been defined at the tissue level. Although, cells residing within the tendon fascicle, known as internal tendon fibroblasts or tenocytes, have classically been regarded as a homogenous population. Recent work has suggested that cells at multiple stages of the lineage exist within the internal population [1]. *In vivo* tools are needed to identify the progenitors and more mature cell types to better understand this lineage. To this end, our lab has identified lineage tracing and GFP reporter mouse lines that map to certain subset of cells within the tenocyte population. We previously reported that Col1a1(3.6kb)-CFP mice containing a 3.6kb fragment of the Col1a1 promoter display similar expression to Scx-GFP within multiple tendons and ligaments [2]. In addition, we demonstrated that Col1a1(2.3kb)-GFP, with a truncated 2.3kb region of the Col1a1 promoter, and Col6a1-GFP transgenic mice display expression in only a subset of cells within the tendon fascicle. The objectives of the current study are 1) to quantify the number of Col1a1(2.3kb)-GFP+ and Col6a1-GFP+ cells within multiple tendons and ligaments at different stages of growth and 2) to measure endogenous gene expression profiles of laser captured GFP+ cells using a microfluidic qPCR array to further define the level of cellular heterogeneity.

METHODS: Transgenic Mice. All animals and procedures were approved by UPenn's IACUC. Two transgenic mouse lines were used in this study: 1) **Col2.3GFP** - Col1a1(2.3kb)-GFP mice contain 2.3kb of the Col1a1 promoter driving GFP expression [3] and 2) **Col6GFP** - BAC containing Col6a1 promoter driving GFP expression (acquired from MMRRC). Experimental Design. Fore- and hindlimbs were isolated from P4, P14, and P28 mice for cryohistological analysis while knees from P14 mice were isolated for LCM and qPCR. The patellar tendon (**PT**), cruciate ligaments (**ACL/PCL**), Achilles tendon (**AT**), and supraspinatus tendon (**ST**) were analyzed for histology (n=4-5/group). For LCM, **Col2.3+** and **Col6+** cells were isolated from the PT and compared to **ACL/PCL**, articular cartilage (**AC**), and *whole* PT midsubstance controls from Col2.3GFP (**Col2.3PT**) and Col6GFP (**Col6PT**) sections (n=4/group). Cryohistology. Limbs were fixed in formalin, embedded, counterstained with DAPI, and imaged on the Zeiss Axio Scan.Z1. Laser capture microscopy (LCM). Knees were fixed in 4% PFA, embedded, and sectioned using CryoJane system. Slides were dehydrated and GFP+ cells or larger regions of tissue were isolated using the ArcturusXT laser capture microscope. Microfluidic qPCR Array. RNA was extracted from LCM samples, converted to cDNA, and preamplified for 93 targets and 3 housekeeping genes. qPCR reactions for 96 samples and 96 genes were run on Fluidigm's 96.96 Dynamic Array IFC yielding 9,216 individual Ct reactions. Image Quantification. The GFP intensity was recorded for each cell within the tendon/ligament midsubstance. An equivalent minimum threshold was applied and the percentage of GFP+ cells was computed. Statistics. One-way ANOVAs with either tissue type or age as fixed factors were used to analyze the number of GFP+ cells in the histological sections. Principal component analysis and hierarchical clustering were used to summarize the qPCR data.

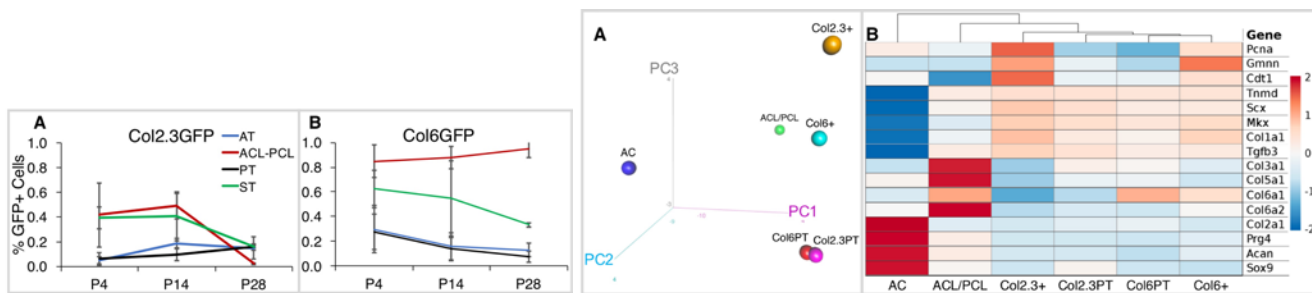
RESULTS: Age and tissue dependence of fluorescent reporters. Both tissue type and age had an effect on Col2.3GFP and Col6GFP expression (Fig. 1; p<0.05). Col2.3GFP expression increased in both the AT and PT with age (Fig. 1A). Conversely, Col2.3GFP was higher in the ACL/PCL and ST at P4 and P14 but significantly dropped at P28 (p<0.05). Col6GFP expression was highest in the cruciate ligaments (ACL/PCL) at all three ages (Fig. 2B). There was an increasing trend in Col6GFP expression in the ACL/PCL with age while the three tendons all decreased with age. Interestingly, the AT showed a regional variation in both reporter lines (data not shown). The region of the AT midsubstance proximal to the enthesis but adjacent to the calcaneus displayed elevated Col2.3GFP expression at P4 and P14 with a significant drop at P28, similar to the ACL/PCL. Additionally, this region of the AT had the highest Col6GFP expression at all time points. Endogenous gene expression indicates Col2.3GFP+ cells are more unique than Col6GFP+ cells in the PT. Principal component analysis of the 93 target genes and 6 cell/tissue types (Col2.3+, Col6+, Col2.3PT, Col6PT, ACL/PCL, and AC) revealed that 92% (57+26+9%) of the total variance was accounted for in the first 3 principal components. PC scores indicated that AC was the most different (Fig. 2A). However, Col2.3+ cells were more unique from *whole* PT samples than Col6+ cells (Fig. 2A). In fact, Col2.3+ cells expressed higher levels of cell cycle genes (Pcna, Gmn, Cdt1) (Fig. 2B). The tendon samples expressed higher levels of tenogenic markers (Tnmd, Scx, Mxx, Col1a1, Tgfb3) while the ACL/PCL expressed higher levels of other collagens (Col3a1, Col5a1, Col6a1, Col6a2). Finally, the AC samples had the highest levels of cartilage-related genes (Col2a1, Prg4, Acan, Sox9).

DISCUSSION: In order to better understand tendon pathologies and to develop improved repair strategies, we must first improve our understanding of the tendon lineage, including markers that define cells at multiple stages of the lineage and signaling pathways that regulate the differentiation of progenitors into mature tenocytes. We utilized two GFP reporter strains in this study to demonstrate a level of cellular heterogeneity within the internal tendon fibroblast (i.e., tenocyte) population that has not been appreciated previously. The Col2.3+ cells may be of particular interest as they display significant changes in expression with age (Fig. 1A) as well as larger differences in endogenous gene expression compared to *whole* PT controls than the Col6+ population (Fig. 2). Col2.3GFP's age-related expression changes correlate with changes in mineral apposition rate in these tissues during growth [4]. In addition, these cells also express higher levels of cell cycle genes. Therefore, we hypothesize that Col2.3GFP is a marker of an actively growing cell phenotype with increased proliferation, metabolic activity, and ECM production. A hypothesis that we will test in future studies.

SIGNIFICANCE: An improved understanding of the cellular markers and signaling pathways that define and regulate the tendon lineage will be crucial to developing new therapies to attenuate the progression of pathologies and improve repair outcomes following injury. The anatomical and temporal differences in GFP expression found in this study indicate that cells within the tendon midsubstance are not as homogeneous as previously thought. Using these model systems, we aim to identify the phenotype and function of these cells during normal processes of growth, homeostasis, and repair.

REFERENCES: 1. Dymnt N, et al., PLOS One, 2014; 2. Dymnt N, et al., ORS, 2016; 3. Kalajzic I, et al., JBMR, 2001; 4. Dymnt N, et al., Dev Biol, 2015.

ACKNOWLEDGEMENTS: Work supported by NIH grants R00 AR067283, P30 AR069619, and startup funds from Dept. Orthopaedic Surgery at UPenn.



Prestrain Regulates Sensation of Fibrous Microenvironments by Annulus Fibrosus Cells

Edward D. Bonnevie^{1,2}, Tonia Tsinman^{1,2}, Sarah Gullbrand^{1,2}, Dawn M. Elliott³, Robert L. Mauck^{1,2}

¹University of Pennsylvania, Philadelphia, PA, ²Philadelphia VA Medical Center, Philadelphia, PA, ³University of Delaware, Newark, DE

DISCLOSURES: Nothing to report.

INTRODUCTION: Hallmarks of intervertebral disc degeneration include proteoglycan loss from the nucleus pulposus (NP) and collapse of disc height. In a healthy state, the AF serves not only to connect adjacent vertebrae, but also to confine the osmotic swelling pressure of the NP. In fact, in a healthy state, this osmotic prestress against the AF leads to baseline strains (i.e., prestrain) that surpass 10%¹. This loss of disc pressurization can alter whole disc mechanics and, on a microstructural level, modulate the prestressed state of the annulus fibrosus (AF). In the context of degeneration, this loss of NP swelling and AF prestress likely have mechanobiological consequences on the resident cells. Indeed, it is becoming increasingly well understood that factors such as microenvironmental stiffness (which is modulated by the degree of prestrain) and organization can regulate the most basic of cell functions, including differentiation², proliferation³, and gene expression³. With this role of the microenvironment in mind, we hypothesized that prestrain in fibrous networks dictates AF cell homeostasis and mechano-sensation, and analyzed how prestrain dictates baseline cellular and nuclear morphology, focal adhesion formation, and contractility-dependent transcription factor localization (i.e., YAP/TAZ).

METHODS: Electrospun scaffolds were fabricated as previously described⁴. Briefly, poly(ϵ -caprolactone) was extruded through a charged spinneret and deposited onto a grounded, rotating mandrel (13 m/s aligned, 2 m/s nonaligned). A custom tensioning device was developed to image prestressed scaffolds within an ESEM, and fiber alignment as a function of strain was calculated via FFT analysis in ImageJ. Polyacrylamide gels were fabricated using standard protocols at either 5 kPa or 55 kPa stiffness and coated with collagen. Annulus fibrosus cells were isolated from bovine caudal discs via collagenase digestion and utilized at passage 1. Cells were seeded onto either aligned or nonaligned, fibronectin-coated scaffolds in a free swelling state or onto scaffolds that were already strained to 9% strain (prestrain). Scaffolds were cultured for 24 hours prior to analysis. For cell imaging, scaffolds were fixed, stained, and imaged while still in their prestressed state. Analyses were conducted in ImageJ and MATLAB, and one- and two-way ANOVA were performed.

RESULTS: As expected, scaffolds exhibited significant strain-stiffening behavior in a manner reminiscent of the toe-region of native fibrous tissues⁴. SEM of free swelling and prestrained scaffolds revealed significant fiber straightening and realignment with stretch (**Fig 1A**). Both aligned and nonaligned fiber networks exhibited strain-dependent organization, with nonaligned networks remaining more disorganized (even at 13.5% strain) than free swelling aligned networks (**Fig 1A**). In a similar manner, prestress in fibrous networks promoted nuclear alignment in the fiber and strain direction (**Fig 1B**). Additionally, within nonaligned networks, nuclear aspect ratio trended higher ($p = 0.1$) in prestrained scaffolds, while in aligned networks, prestrain significantly increased nuclear aspect ratio (**Fig 1C**). Similarly, cell aspect ratio increased for cells seeded onto aligned prestrained scaffolds, but on nonaligned networks, there was no effect of prestrain (**Fig 2AB**). Interestingly, focal adhesion formation in these fibrous environments (assessed via paxillin staining) revealed a significant decrease in total focal adhesion area for cells seeded on aligned prestrained networks (**Fig 2C**). To assess cellular perception of substrate stiffness, we assayed YAP/TAZ nuclear translocation on both 2D and fibrous substrates. Surprisingly, the strain-stiffened, aligned scaffolds had significantly decreased nuclear YAP/TAZ (**Fig 2D**).

Conversely, on 2D planar substrates, increasing substrate stiffness resulted in increased YAP/TAZ translocation to the nucleus (**Fig 2EF**), confirming the YAP/TAZ mechanical rheostat function in AF cells. These data suggest a disconnect between cell sensation of 2D and 3D fibrous environments regulated by cell morphology (**Fig 2G**).

DISCUSSION: These studies tested the hypothesis that pre-strain in fibrous environments alters cellular perception of the microenvironment to direct homeostasis. We found that prestrain does indeed alter the mechanics and topography (i.e., fiber morphology) of engineered fibrous environments, and that cells respond to these changes. Specifically, prestrain in aligned networks promoted cellular and nuclear elongation in the fiber direction. Interestingly, and counter-intuitively, these changes led to decreased nuclear YAP/TAZ. Additionally, we found a disconnect between cell sensation of stiffness in 2D versus 3D fibrous environments (**Fig 2G**). While increased nuclear YAP and cellular contractility could be expected in a strain-stiffened environment (as is seen on 2D surfaces), we instead observed that cell spreading in 1D along the prestrained template led to a lower focal adhesion area and decreased YAP in the nucleus. When extrapolated to *in vivo* situations, it is possible that fibrous prestress promotes the elevated aspect ratios of healthy AF cells and inhibits fibrotic responses such as hypercellularity and CTGF expression, both of which are downstream of YAP/TAZ activation³. In the context of disc degeneration, where osmotic swelling and consequently prestrain is lost, these findings indicate that aligned, prestrained fibrous environments may help to suppress the fibrotic responses that promote aberrant remodeling.

SIGNIFICANCE: This work introduces fibrous prestrain as a microenvironmental cue in AF mechanobiology. In aligned fibrous environments, prestrain promotes 1D cell elongation, creating a disconnect between sensation of 2D and 3D fibrous environments as highlighted by YAP/TAZ translocation.

REFERENCES: [1] Michalek+ 2009, [2] Engler+ 2006, [3] Piccolo+ 2014, [4] Nerurkar+ 2007.

ACKNOWLEDGEMENTS: This study was supported by the NIH (R01 EB02425, T32 AR53461-11, and P30 AR069619).

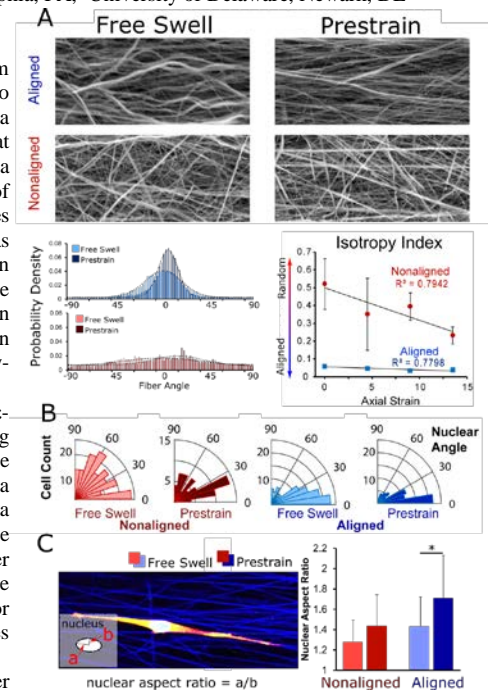


Figure 1: (A) Strain in electrospun scaffolds promotes fiber straightening and alignment, and increases organization ($n = 3$). Prestrain promotes nuclear (B) alignment and (C) elongation. ($n > 40$ cells/group, * $p < 0.05$)

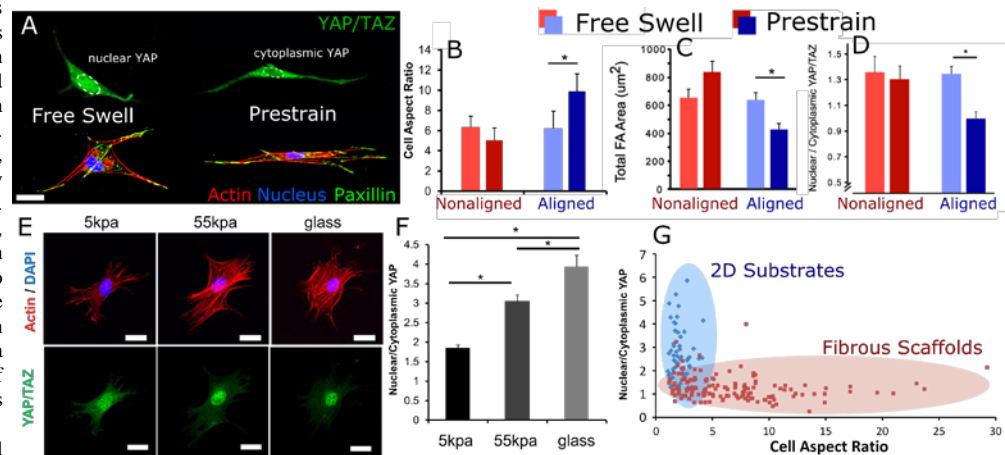


Figure 2: (A) Cells were stained for YAP/TAZ and paxillin in their strained states. Prestress in aligned networks (B) increased cell aspect ratio, and decreased (C) focal adhesion area and (D) nuclear YAP/TAZ. (EF) In 2D, YAP/TAZ increased with increased substrate stiffness. (G) YAP/TAZ vs cell aspect ratio highlights a disconnect in environmental sensing. ($n > 14-40$ cells/group, * $p < 0.05$, bar = 25 μm)

Conditional deletion of IFT80 in chondrocytes impairs fracture healing in mice

Min Liu¹, Mohammed Alharbi², Dana Graves², Shuying Yang¹

¹Dept. of Anatomy and Cell Biology, ²Dept. of Periodontics, School of Dental Medicine, University of Pennsylvania, Philadelphia, PA

INTRODUCTION: Primary cilia are essential cellular organelles projecting from the cell surface to sense and transduce developmental signaling. They have complicated structures containing microtubule-based internal structures and mother centriole formed basal body. Intraflagellar transport (IFT) operated by IFT proteins and motors are indispensable for cilia formation and function. Mutations in IFT proteins cause various human diseases. Over the last few decades, major advances have occurred in understanding the roles of these proteins in bone development and remodeling. However, the precise role and mechanism of IFT protein in regulating bone repair after fracture has not been studied. In this study, we investigated the effect of conditional deletion of IFT80 in chondrocyte on bone healing after femur fracture in mice.

METHODS: IFT80^{f/f} mouse model, which has two LoxP sites flanking exon 6 of IFT80, has been generated in our lab. Col2a1-CreER mouse, from the Jackson Laboratory, has strong tamoxifen-inducible Cre expression primarily in chondrogenic lineage cells. IFT80^{f/f} mice were crossed with Col2a1-CreER mice to produce Col2a1; IFT80^{f/f} mice. IFT80^{f/f} mice were used as control. Femur fracture was performed in 12-week-old male mice from both Col2a1; IFT80^{f/f} and IFT80^{f/f} mice groups. Tamoxifen was injected intraperitoneally at Days 3, 5, and 7 post fractures to delete IFT80 in chondrocytes. Mice were sacrificed at day 9 and 21 post fracture, and the femur samples were collected for histological analysis of endochondral bone formation, and immunofluorescence staining for the markers of chondrogenesis. MicroCT imaging was carried out at the fracture line to exam the bone reconstruction at day 9 or 21 post fracture. In addition, primary chondrocytes were isolated and cultured from IFT80^{f/f} mice at postnatal day 5, and then infected with adenovirus, which overexpress either Cre or GFP. Ad-Cre infection generally yields ~90% deletion of IFT80 in IFT80^{f/f} Chondrocytes. Ad-GFP treated cells were used as a control. Immunofluorescence staining was performed to visualize cilia structure. At day 14 following chondrogenic media induction, alcian blue staining was used to detect the sulfated proteoglycan deposits. Additionally, mRNA and protein levels of the markers of ciliogenesis and chondrogenesis were measured.

RESULTS: The histological evaluation revealed that Col2a1; IFT80^{f/f} mice formed smaller fracture calluses than IFT80^{f/f} (control) mice. The max-width and max-callus area were 31% and 47% smaller when compared to the control mice (Fig.1A). By performing safranin O staining, we found that IFT80^{f/f} mice exhibited more newly-formed cartilage area than Col2a1; IFT80^{f/f} mice (Fig.1B). X-ray image were conducted at Days 0, 7, 14 and 21 post fractures. Serial radiographic analysis of fractured femurs in both groups revealed marked differences in the formation of the fracture callus and a significant healing delay in Col2a1; IFT80^{f/f} mice (Fig.2A). To determine whether conditional knockout of IFT80 affects the bony union, we performed micro-CT scanning of bony tissues at the fracture site at 21 days following fracture surgery. 3D reconstruction of the fracture site showed that there were large amounts of high-density bony tissues covering almost the entire fracture gap in the control IFT80 mice (Fig.2B). Conversely, the fracture gap of Col2a1; IFT80^{f/f} mice were clearly observed and were partially covered mostly by low-density and porous woven bony tissue. Quantitative measurements of the newly formed bone at the fracture gap confirmed that Col2a1; IFT80^{f/f} mice had significantly lower BV/TV, Tb-N, Tb-Th and greater Tb-Sp (Fig.2C). In addition, in vitro study showed that IFT80 deletion in primary chondrocytes dramatically reduced cell differentiation, proliferation, cilia formation and cilia length. IFT deletion altered gene expression of chondrogenetic markers and TGF- β signaling transduction.

DISCUSSION: Present study demonstrates that conditional knockout of IFT80 in chondrocytes significantly delayed the fracture healing. Our data suggests that deletion of IFT80 protein impairs chondrocyte differentiation and TGF- β signaling, possibly by disruption of receptor endocytosis at the pocket region of the primary cilia. Thus, our study for the first time reveals that IFT80 protein plays an essential role in fracture repair.

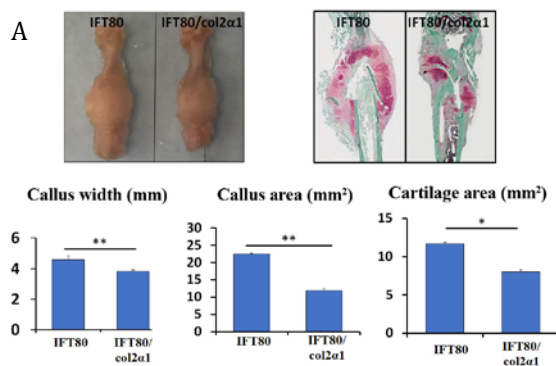


Figure 1: Histomorphometric measurements of callus width, callus area and cartilage area.

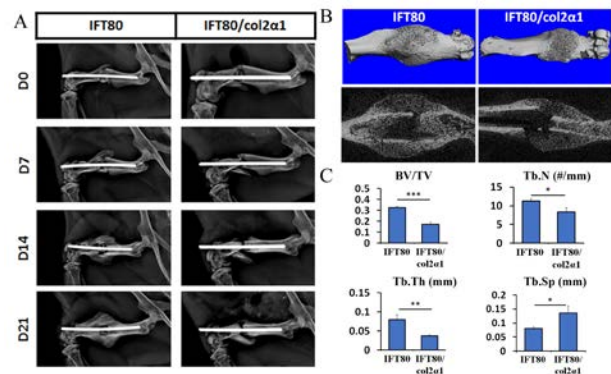


Figure 2: Serial radiographic images of fractured femurs and MicroCT analysis.

Hox Genes in the Adult Skeleton: Patterning Cues Beyond Embryonic Development

Danielle Rux¹, Jane Song², Kyriel Pineault³, Ilea Swinehart⁴, Aleesa Schlientz⁴, Steven Goldstein⁵, Kenneth Kozloff⁵, Daniel Lucas³, and Deneen Wellik^{2,3,4}

¹*Orthopaedic Research, Children's Hospital of Philadelphia;* ²*Program in Cell and Molecular Biology;* ³*Department of Cell and Developmental Biology;* ⁴*Department of Internal Medicine, Division of Molecular Medicine & Genetics, and* ⁵*Department of Orthopaedic Surgery, University of Michigan, Ann Arbor, MI*

The mammalian skeleton boasts a remarkable capacity to completely restore the original structure and function of bone following injury. Interestingly, the biological processes of fracture repair recapitulate many of the mechanisms of embryonic skeletal development. The *Hox* genes are critical regulators of skeletal development, yet the function of these genes during adult fracture repair is largely unknown. Ongoing research in the Wellik lab is focused on understanding the role(s) of these genes in this context.

The *Hox* genes encode evolutionarily conserved transcription factors that are imperative for patterning of the axial and limb skeleton in the developing embryo. Specifically, *Hox11* genes function to instruct growth and morphology of the lumbar elements of the axial skeleton and the zeugopod elements (radius/ulna and tibia/fibula) of the limbs. Previous work using a *Hox11:eGFP* allele showed that *Hox11* is expressed through the latest stages of embryonic development. We have now discovered that *Hox11* genes continue to be expressed in the adult skeleton and are largely restricted to the previously characterized PDGFR⁺/CD51⁺/Leptin Receptor(LepR)⁺ mesenchymal stem/stromal cell (MSC) population in bone marrow. These *Hox11*-expressing MSCs expand in response to fracture injury and are maintained throughout repair. Loss of *Hox11* function results in a significantly reduced ability to generate cartilage early in repair, and at late stages, the hard callus persists and is incompletely remodeled. Together, our data suggests that *Hox11* functions in MSCs at multiple stages of repair, first, for endochondral ossification and later for bone remodeling. In addition, we show more generally that the *Hox* expression pattern established during embryonic development is maintained in the adult skeleton. Overall, this research provides novel evidence that *Hox* genes have critical roles beyond embryonic patterning and that these genes are expressed and function in adult MSCs.

IFT80 and primary cilia is required for intervertebral disc development and maintenance

Xinhua Li¹, Jormay Lim¹, Zuoze Tian², Xue Yuan³, Yeji Zhang² and Shuying Yang^{1*}

¹Department of Anatomy and Cell Biology, School of Dental Medicine, University of Pennsylvania; ²Department of Physical Medicine & Rehabilitation, Perelman School of Medicine, University of Pennsylvania, Philadelphia, PA; Department of Physical Medicine & Rehabilitation, Perelman School of Medicine, University of Pennsylvania, Philadelphia, PA; Translational Musculoskeletal Research Center (TMRC), Corporal Michael J. Crescenzo Veterans Affairs Medical Center, Philadelphia, PA. ³Department of Oral Biology, School of Dental Medicine, University of Buffalo, State University of New York, Buffalo, NY, United States; *Corresponding author: Dr. Shuying Yang, shuyingy@upenn.edu

This work was supported by a National Institute of Health grant DE023105 (S. Yang) and AR061052 (S. Yang)

Abstract:

Intervertebral disc degeneration (IVDD) is one of most common musculoskeletal diseases all over the world. Mechanotransduction plays a particularly prominent role in IVD normal function and dysfunction with aging and/or injury. Previous studies have demonstrated that primary cilia play mechanosensory and chemosensory functions in bone cells; and intact ciliary structure and ciliary transport mediated by intraflagellar transport proteins (IFTs) are important for cilia formation and Hedgehog signaling pathways in bone formation. However, it is largely unknown whether and how cilia and IFT proteins are involved in intervertebral disc (IVD) development and maintenance. To address these unknown questions, we first utilized the IVD tail injury model to characterize whether the cilia number and length were affected in the injured IVD mouse and human samples. By performing immune fluorescence staining for acetylated tubulin which marks the primary cilia, we found that the cilia number is significantly reduced in the injured IVD compared to the normal ones. To determine how ciliary IFT80, IFT complex B protein, affects IVD development, we generated the mice with cartilage specific deletion of IFT80 by crossing the Collagen type II Cre ER (Col2CreERT) mice with IFT80 floxed mice that we generated previously. IFT80 gene was deleted after postnatal tamoxifen intraperitoneal injection. The lumbar IVDs of IFT80 deleted mice and control mice were isolated, decalcified, and paraffin embedded for histology or immunofluorescent imaging. The Safranin O fast green stain and hematoxylin & eosin stain revealed a noticeable phenotype in intervertebral disc in the IFT80-deleted mice compared to IFT80 floxed mice: the chondrocytes were disorganized and column indexes were much less in growth plate (GP); annulus fibrosis (AF) were disorganized and fissured; the endplate cartilage (EPC) were thinner, and the cells were underdeveloped and smaller; the shape of nucleus pulposus (NP) were changed from oval to irregular. The Immunofluorescent staining results showed the cilia number in the intervertebral disc were significantly less than that in the IFT80-intact mice. Taken together, our data suggested that cilia and IFT80 are important for the maintenance of IVD structure and function in mice.

Meniscus Maturation is Accompanied by Marked Compositional and Structural Reorganization

Sonia Bansal^{1,2}, Niobra M. Keah^{1,2}, Olivia C. O'Reilly¹, Feini Qu^{1,2}, Robert L. Mauck^{1,2}, Miltiadis H. Zgonis^{1,2}

¹McKay Orthopaedic Research Laboratory, University of Pennsylvania, Philadelphia, PA

²Translational Musculoskeletal Research Center, Philadelphia VA Medical Center, Philadelphia, PA

Disclosures: No disclosures to report.

INTRODUCTION: The menisci are semi-lunar shaped fibrocartilaginous wedges located between the femur and the tibial plateau and support the structure and mechanical function of the knee joint^{1,2}. Understanding meniscus structure and function is particularly important given the high incidence of meniscal pathology^{3,4}, and its association with progressive joint degeneration⁵. In the adult, the menisci are comprised primarily of circumferentially aligned type I collagen bundles, which function to convert compressive forces into tensile hoop stresses^{6,7}. In addition to circumferential fibers, the meniscus contains "radial tie fibers" that originate at the meniscus periphery and interdigitate amongst the circumferential fiber population^{1,2,6-8}. These radial tie fibers (RTFs) vary in size, spatial distribution, and in their degree of arborization⁸, and are thought to bind circumferential fibers together and protect against longitudinal splitting of the circumferentially-aligned collagen bundles^{6,9,10}. Interestingly, a recent study suggested that radial tears that interrupt circumferential fibers do not increase contact stresses until they reach ~90% of the meniscus width¹¹. This suggests alternative methods for strain transmission in the meniscus, a potential role of the RTFs. However, the morphology and composition of these structures during tissue formation and maturation has not yet been elucidated. To further this understanding, we quantified RTF area fraction and thickness as a function of tissue location and developmental state.

METHODS: Medial menisci (n=6/age) were harvested from fetal (mid-gestation), juvenile (6 month) and adult (skeletal mature) cows. Fetal menisci were divided into anterior and posterior regions. Juvenile and adult menisci were divided into four equal regions: anterior horn, anterior body (Body-A), posterior body (Body-P), and posterior horn. Each region was then cryosectioned into 10 μ m thick slices spanning the entire cross section and fixed in 4% PFA. For each cross section, three zones were examined at high power: the outer (O), middle (M), and inner (I) zones. First, sections were stained with Safranin O/Fast Green for proteoglycans and fibrous tissue, respectively, as well as with Picrosirius Red and a modified Masson's Trichrome with Verhoff stain to visualize collagen and elastin fibers. Next, unstained sections were imaged at 10X magnification via second harmonic generation (SHG, 840 nm excitation). Maximum projections spanning 4.8 ± 1.2 microns of the tissue depth were generated in each zone and the area fraction with positive SHG signal was computed as a measure of RTF area fraction. Additionally, RTF fiber thickness was estimated using the FIJI plugin BoneJ. Fiber area fraction and thickness were compared across regions, zones, and developmental states using ANOVA ($p \leq 0.05$) with Tukey's post-hoc tests; data are presented graphically as the mean value in each region and zone.

RESULTS: As expected, meniscal tissue size increased with age. Histological analysis showed increased proteoglycan content from the inner to the outer zone with increasing age, via Safranin O staining (Figure 1). Likewise, Masson's Trichrome revealed increasing collagen staining throughout the entire meniscus with increasing age. SHG imaging revealed that RTF fiber area ranged from 8% to 43%, with both age and region being significant factors ($p < 0.0001$). Adult menisci showed significant differences in RTF fiber area between zones, whereas juvenile and fetal menisci did not show significant differences ($p = 0.135$ and 0.143 , respectively). In the adult, central body regions had a lower RTF fiber area than the anterior or posterior horns (Figure 2). The thickness of RTFs also varied significantly with age ($p < 0.0001$). Juvenile and fetal menisci showed no significant differences in RTF thickness with respect to regions or zones, while adult menisci had significant differences in RTF thickness as a function of region ($p < 0.02$) and zone ($p < 0.005$) (Figure 2).

DISCUSSION: This study provides evidence for marked compositional and structural changes in the knee meniscus as a function of maturation. Fetal menisci were characterized by lower levels of collagen (Masson's Trichrome) and proteoglycan (SafO/Fast Green) compared to both juvenile and adult tissue. Additionally, radial tie fibers in fetal tissue are poorly developed compared to adult specimens. Specifically, we observed an increase in RTF thickness as well as emergent heterogeneity in RTF fiber area in the adult. The higher RTF fiber area and size in the outer region of the mature posterior horn may underlie the reported higher stiffness in this region⁶. This specialization in meniscus structure was concentrated in the horns of the tissue, potentially reflecting the more complicated mechanical loading environment of the meniscus insertion site. Future work will determine the structure-function implications¹² of these findings, as well as the mechanisms governing RTF development during maturation. This improved understanding will inform engineering design towards the fabrication of functional meniscus replacements.

SIGNIFICANCE: This study demonstrates that radial tie fibers in the meniscus show spatially varying and age-dependent patterns, and will inform tissue engineering strategies to create functional and anatomically correct meniscal replacements.

References: [1] Kambic+, J. Orthop. Res. 2005. [2] Chevrier+, J. Orthop. Res. 2009. [3] Merriam+, J. Sports Med. 2015. [4] Mordecai+, World J. Orthop. 2014. [5] Fairbank+, J Bone Jt. Surg. 1948. [6] Skaggs+, J. Orthop. Res. 1994. [7] Makris+, Biomaterials 2011. [8] Andrews+, J Anat. 2014. [9] Mauck+, Tissue Eng. Part B. 2009. [10] Bullough+, J Bone Jt. Surg. 1970. [11] Bedi+, J. Bone Jt. Surg. 2010. [12] Li+, SB3C Conference. 2016.

Acknowledgments: This work was supported by an OREF New Investigator Grant, the NIH, and the Department of Veterans Affairs.

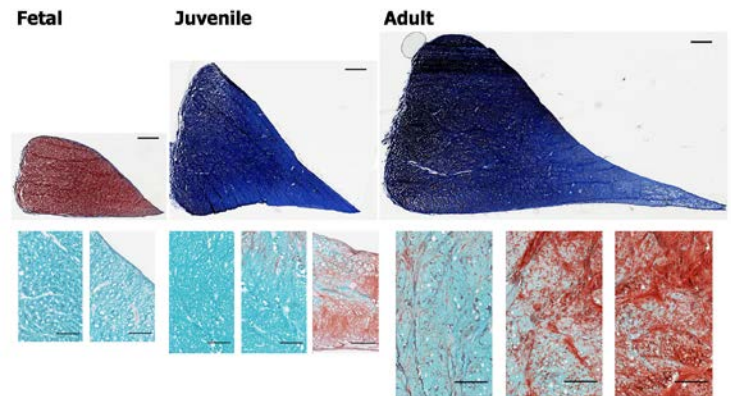


Figure 1 -- Histological staining of fetal, juvenile, and adult menisci. Top row: Masson's Trichrome, posterior sections, Scale bar = 2 mm. Bottom row: Safranin O/Fast Green, anterior sections, Scale bar = 500 μ m.

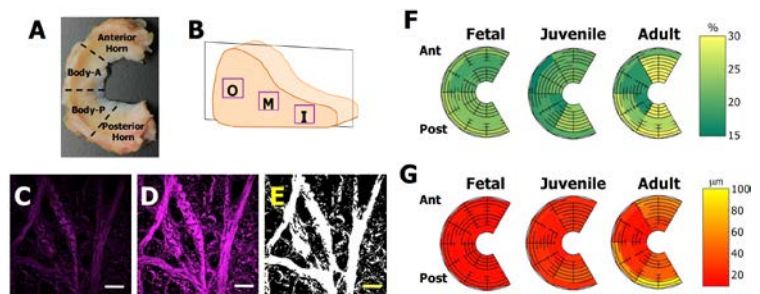


Figure 2 – Schematic illustration of (A) meniscal regions and (B) outer (O) middle (M) and inner (I) zones with sectioning plane. Original SHG image (C), Maximum Projection (D), and binarized (E) images. Scale Bar = 200 μ m. Colors maps denoting RTF fiber area (F) ranging from 15% to 30% and mean fiber thickness (G) ranging from 10 to 100 μ m.

Post-natal deletion of *Gnas* alters adipose tissue properties during progression of heterotopic ossification

John T. Fong, Niambi Brewer, Deyu Zhang, Frederick S. Kaplan, Robert J. Pignolo, and Eileen M. Shore

Progressive Osseous Heteroplasia (POH), a rare genetic disorder, is clinically characterized by heterotopic ossification (HO) that initiates in the subcutaneous soft tissues then progresses into the deeper connective tissues (Pignolo et al., 2015; Shore et al., 2002). POH is caused by inactivation of *GNAS*, a gene that encodes the alpha subunit of stimulatory G proteins (Gs α). Previous work by our group has demonstrated that adipose derived stromal cells (AdSCs) from *Gnas*^{p-KO} mice exhibit enhanced osteogenic and impaired adipogenic potential *in vitro* (Liu et al., 2012; Pignolo et al., 2011). These data support that osteogenesis and heterotopic bone in POH occurs at the expense of adipogenesis. The pathophysiology of POH is still poorly understood. In this study, we examined the mechanisms and the signals that lead to initiation and development of heterotopic bone in POH. In order to consistently and reliably induce HO for our study, *Gnas*-null mice (*Gnas*^{fl/fl}; *Cre-ER*^{T2} or *Gnas*^{fl/fl}; *Ai9*^{fl/fl}; *Cre-ER*^{T2}) injected with 4-hydroxy tamoxifen were used. The natural history of HO formation in these mice was investigated by cross-sectional and longitudinal studies, and heterotopic bone was evaluated by histology. Our results indicate that *Gnas* inactivation leads to (i) altered adipose tissue with enhanced collagen accumulation in subcutaneous tissues, and (ii) elevated BMP/SMAD1/5/9 signaling. These data suggest that changes in the tissue micro-environment could misdirect resident mesenchymal stem cells to osteogenic differentiation. Additionally, for the first time, we provide *in vivo* evidence, through fluorescence-tagged cell transplant experiments, supporting that AdSCs contribute to heterotopic ossification in POH. Together, our data provide insights into the pathophysiology of POH and other *GNAS*-related disorders and serve as a foundation for future studies to identify therapeutic strategies for *GNAS*-related heterotopic ossification.

(Presented at Eleventh Fellows Forum on Metabolic Bone Diseases, Denver, CO, September 6-7, 2017.)

Regulation of phalangeal joint development by ACVR1 in fibrodysplasia ossificans progressiva

Authors: O. Will Towler^{1,4,5}, Frederick S. Kaplan^{1,2,4}, & Eileen M. Shore^{1,3,4,5}

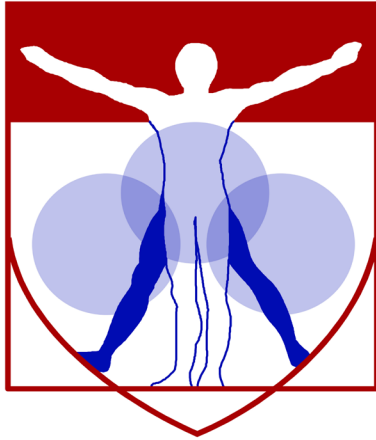
Departments of Orthopaedic Surgery¹, Medicine², Genetics³; the Center for Research in FOP and Related Disorders⁴; Cell and Molecular Biology Graduate Group⁵; Perelman School of Medicine at the University of Pennsylvania, Philadelphia

Fibrodysplasia ossificans progressiva (FOP; MIM #135100) is a genetic disease of heterotopic ossification accompanied by short, laterally deviated great toes caused by an activating mutation in the BMP receptor ACVR1/ALK2. To investigate the skeletal developmental phenotype of FOP, we used a conditional knock-in mouse model (MGI:5763014) with the FOP ACVR1 R206H mutation to examine digit and joint formation *in vivo*. Mice expressing the FOP mutation globally or in limb mesenchymal cells (*Prrxl1*+) exhibit stunted hindlimb first digits similar to FOP patients and generalized delayed digit development. Three-dimensional whole-mount pSmad1/5 immunohistochemistry and imaging of embryonic mouse limbs revealed unrestricted BMP signaling throughout the developing digit rays of mutant animals, supporting that BMP pathway activity from the mutant receptor was insufficiently inhibited in the joint space. Expressing the mutation only in joint progenitor cells using *Gdf5-Cre* showed that mutation activity in these cells alone was sufficient to produce the joint and digit phenotype. Histological analyses revealed disorganized, interphalangeal chondrocyte proliferation in both models, supporting the hypothesis that the phenotype is due to improper spatiotemporal activation of a chondrogenic pathway in the joint space by BMP pathway signaling through the mutant ACVR1 receptor during skeletal development.

Gambogic amide, a TrkA agonist, augments skeletal adaptation to mechanical loading without inducing hyperalgesia

Phuong Q. Hua, Ryan E. Tomlinson
Thomas Jefferson University, Philadelphia, PA

The periosteal and endosteal surfaces of mature bone are densely innervated by sensory nerves expressing TrkA, the high-affinity receptor for nerve growth factor (NGF). In previous work, we demonstrated that inhibition of TrkA signaling diminished load-induced bone formation. Similarly, administration of exogenous NGF significantly increased load-induced bone formation through activation of Wnt signaling, albeit with the induction of substantial mechanical and thermal hyperalgesia in adult mice. Here, we tested the ability of gambogic amide (GA), a recently identified robust small-molecule agonist for TrkA, to affect load-induced bone formation. The right forelimb of adult C57BL/6J mice (n = 7-8 per group) was subjected to non-damaging axial compression (3 N, 100 cycles, 2 Hz rest-inserted) for three consecutive days. GA (0.4 mg/kg) or vehicle (DMSO) was administered one hour prior to the first bout of loading. Calcein (10 mg/kg) and alizarin red (30 mg/kg) were administered 3 and 8 days after the initial bout of loading. Behavioral analysis was used to assess pain up to one week after loading. Contrary to our expectations, GA treatment was not associated with diminished use of the loaded forelimb, by forelimb asymmetry testing. In fact, GA-treated mice used the loaded forelimb significantly more than control mice at two time points (one and four days). To further examine GA-induced hyperalgesia, we performed hotplate sensitivity testing at 55 °C. In these experiments, we found a similar effect of GA treatment; thermal sensitivity in GA-treated mice was significantly decreased one day after the final bout of loading. These results suggest a potential paradoxical analgesic effect of GA. Importantly; load-induced bone formation was assessed by dynamic histomorphometry using undecalcified sections from the mid-diaphysis of loaded and non-loaded forelimbs. Here, we observed a significant increase in relative periosteal bone formation rate (+63%) in GA-treated mice as compared to control. In total, the results from our study demonstrate that gambogic amide has a beneficial effect on load-induced bone formation without inducing the hyperalgesia observed following exogenous administration of NGF.



PENN

CENTER for

MUSCULOSKELETAL

DISORDERS

MicroCT Abstracts

The Effect of Remobilization on the *In Vivo* Function of an Endplate-Modified Engineered Disc

Sarah E. Gullbrand,¹ Beth G. Ashinsky,¹ Dong Hwa Kim,¹ Lachlan J. Smith,¹ Dawn M. Elliott,² Harvey E. Smith,¹ Robert L. Mauck¹
¹University of Pennsylvania, Philadelphia, PA and Philadelphia VA Medical Center, Philadelphia, PA, ²University of Delaware, Newark, DE

Disclosures: None

Introduction: A promising alternative to fusion surgery for intervertebral disc pathology is total disc replacement with a cellular, engineered whole disc construct that restores normal structure and mechanical function to the spine. To this end, our group developed endplate-modified disc-like angle-ply structures (eDAPS) that mimic the structure and function of the native disc. Our previous work showed that, over a 5 week period of implantation in the rat tail disc space, eDAPS outperformed DAPS implanted without endplates with respect to construct composition and integration [1]. However, this previous work utilized an external fixator to immobilize the segment post-implantation. Chronic immobilization is known to be detrimental to disc health [2], and thus the eventual restoration of physiologic loading to the implanted eDAPS will be essential for integration and long term viability. The purpose of this study was therefore to elucidate the impact of remobilization (via fixator removal) on eDAPS structure, composition and mechanics.

Methods: eDAPS Fabrication and Culture: eDAPS sized for the rat caudal disc space were fabricated by concentrically wrapping aligned, angled strips of electrospun PCL nanofibers to form the AF region, and filling the center with a hyaluronic acid hydrogel to form the NP region [3]. Both regions were seeded with bovine disc cells (2×10^6 cells/AF and 6×10^5 cells/NP), and combined after two weeks culture with acellular porous PCL endplates to form the eDAPS. eDAPS were pre-cultured for 5 weeks in chemically defined media with TGF- β 3. **Implantation:** 32 athymic, male, retired breeder rats were anesthetized, and Kirschner wires were passed through the C8 and C9 caudal vertebral bodies, allowing for external fixator placement [4]. eDAPS were implanted following removal of the C8-C9 disc and a partial corpectomy of the adjacent vertebral bodies. The effects of remobilization (R) via external fixator removal were investigated after 5 weeks or 10 weeks of implantation, with endpoints of 10 weeks (10W R, n=6) and 20 weeks (20W R, n=10), respectively. Control groups included animals with external fixators left in place for 10 (10W F, n=5) and 20 weeks (20W F, n=11). **MRI:** T2 mapping of the eDAPS was performed at 4.7T (16 echoes, TE/TR = 7.84 ms/2,000 ms, FOV = 15x15 mm²). Average T2 maps were generated for each time point using a custom MATLAB code. **μ CT Imaging and Radiographs:** In the 20W R and 20W F groups, the PCL endplates were rendered radiopaque via the inclusion of zirconia nanoparticles [5]. Implanted motion segments were subjected to μ CT scanning at 3 μ m resolution before and after application of 3N compressive loading (Scanco μ CT50 Compression Device) to identify functional bony integration of the constructs. Lateral tail radiographs were taken immediately post-operative (PO), and at 10, 15 and 20 weeks PO. The angulation of the vertebral bodies (VB) of the implanted motion segment was quantified in MATLAB. **Mechanical Testing:** 3-4 vertebra-eDAPS-vertebra segments in each experimental group, and 4 native rat tail vertebra-disc-vertebra segments were subjected to compression testing (20 cycles, 0 to 3N, 0.05 Hz), followed by tension to failure for eDAPS samples. Mechanical properties were quantified via a bilinear fit to the 20th cycle. Significant differences in quantitative outcomes were assessed via a one-way ANOVA with Tukey's post-hoc tests.

Results: NP T2 values (Fig. 1) were maintained at native levels for up to 20 weeks *in vivo*; there were no significant differences in NP T2 across experimental groups. The toe and linear region moduli (Fig. 2A) of eDAPS implanted motion segments were not significantly different from native rat tail motion segments, and there were no significant differences between experimental groups. Maximum strain was significantly greater in the 10W R group compared to the native rat tail disc; no other significant differences between groups or compared to native discs were found for transition and maximum strains (not shown). Tensile load to failure after 10 weeks implantation ranged from 4-8 N. Radiographic analysis revealed a progressive increase in vertebral body angle in eDAPS implanted motion segments following remobilization. Vertebral body angle (Fig. 2B) also increased from PO to 10 weeks in the fixed group, but remained stable from 10 to 20 weeks. Vertebral body angle was significantly higher in the remobilized group (9.6°) compared to the fixed group (5.0°) at 20 weeks. Vertebral body angulation in the remobilized group was further evident on μ CT, and led to shearing of the implanted eDAPS under physiologic compressive loading. In contrast, the eDAPS remained well aligned in the fixed group, resulting in uniform axial compression of the implanted construct similar to the native disc (Fig. 3).

Discussion: These data suggest that long-term *in vivo* implantation of the eDAPS results in maintenance of construct composition and functional integration. While mechanical properties and MRI T2 values were not different between fixed and remobilized groups, remobilization had adverse effects on motion segment morphology, regardless of whether the external fixator was removed at 5 or 10 weeks post-implantation. It is likely that even after 10 weeks *in vivo*, eDAPS integration is not sufficient to fully support restoration of native loading, particularly in the hypermobile rat caudal spine, which lacks stabilizing posterior elements. Ongoing work is further investigating the biochemistry, histology and tensile properties of the 20 week implantation groups. Future work will evaluate the eDAPS in larger pre-clinical animal models, which have a more human-like morphology and motion.

Significance: Current surgical strategies for treating disc pathology do not restore native disc structure or function. A tissue-engineered disc replacement capable of integrating with the native environment, while maintaining composition and mechanical function, will significantly advance treatment options for patients with degenerative spinal pathology.

References: [1] Gullbrand+2017 *ORS Proceedings* [2] Wuertz+2009 [3] Martin+2017 [4] Martin+2014 [5] Martin+2015.

Acknowledgments: This work was supported by the Department of Veterans' Affairs and the Penn Center for Musculoskeletal Disorders.

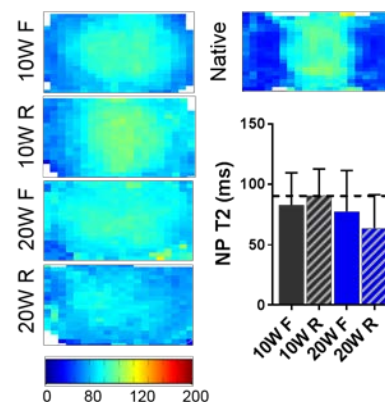


Figure 1. Average T2 maps for each experimental group, and quantification of NP T2. Dashed line = native rat tail NP

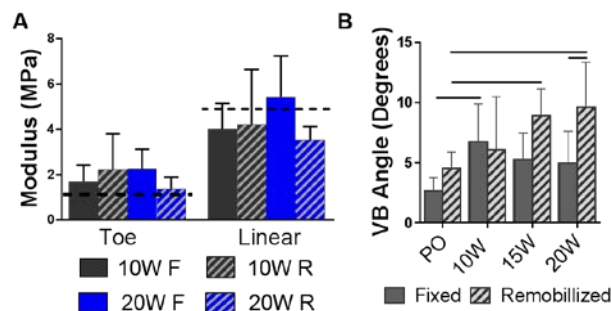


Figure 2. (A) Moduli for each experimental group. Dashed lines = native rat tail properties. (B) Vertebral body angle over time for fixed and remobilized groups. Bars denote significance.

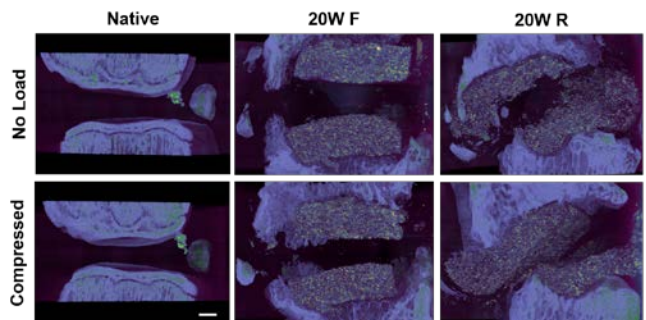


Figure 3. 3D reconstructions of μ CT scans of motion segments from the fixed and remobilized groups, compared to the native rat tail disc, before and after application of 3N compression using the Scanco *in situ* compression device. Color scale represents bone mineral density.

Peak Trabecular Bone Microarchitecture, but not Bone Mass, Predicts Rate of Estrogen-Deficiency-Induced Bone Loss

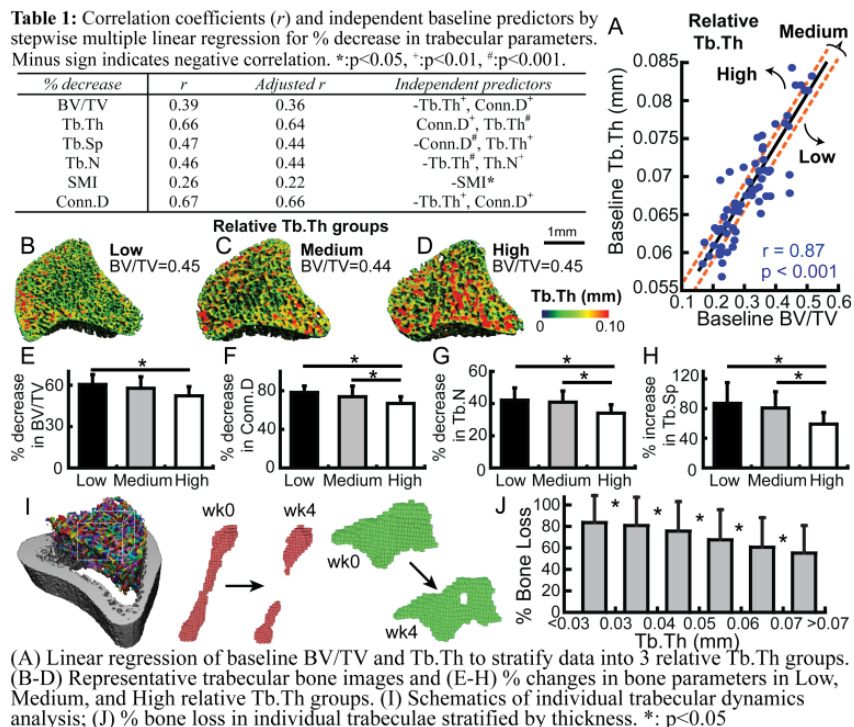
Yihan Li, Wei-Ju Tseng, Chantal de Bakker, Hongbo Zhao, X. Sherry Liu

Reduced estrogen levels during menopause lead to accelerated bone remodeling, resulting in low bone mass and increased fracture risk. Peak bone mass is a significant predictor of postmenopausal osteoporosis. However, it is not clear if rates of postmenopausal bone loss depend on peak bone mass and bone microarchitecture. To establish this relationship, we used *in vivo* μ CT to longitudinally track tibial bone changes in 62 rats (4-5 mo old) from 0 to 4 wks post-OVX.

Bone volume fraction (BV/TV) decreased 56% over 4 wks post-OVX. There was no correlation between baseline BV/TV and % decrease in BV/TV. Among all the baseline bone microarchitecture parameters, only trabecular thickness (Tb.Th) showed a trend of correlation with the extent of post-OVX bone loss ($r=-0.21$, $p=0.097$). Stepwise multiple linear regressions suggested that the combination of baseline Tb.Th and connectivity density (Conn.D) was an important predictor for % decrease in BV/TV, Tb.Th, Tb spacing (Tb.Sp) and Conn.D (adjusted $r=0.36-0.66$, Table 1).

To further examine the influence of Tb.Th regardless of BV/TV on OVX bone loss, rats were stratified by the relative baseline Tb.Th (adjusted by BV/TV) into 3 groups: Low, Medium, and High relative Tb.Th (Fig 1A-D). No difference of baseline BV/TV was found among the 3 groups. In contrast, bone loss rate was 15% lower in the High and 5% lower in the Medium compared to the Low relative Tb.Th group, respectively (Fig 1E). Similar results were found for % decrease in Conn.D, Tb number (Tb.N), and Tb.Sp (Fig 1F-H). Next, we used individual trabecular dynamics (ITD) analyses to track bone loss that occurred in each individual trabecula based on precisely aligned pre- and post-OVX μ CT images (Fig 1I). 11,862 trabeculae from 24 rats were analyzed and categorized to 6 groups based on their Tb.Th (Fig 1J). ANOVA test showed significant difference between all Tb.Th groups, suggesting thicker trabeculae led to less bone loss. Moreover, trabeculae that went through connectivity deterioration (Fig 1I) had 14% lower Tb.Th than trabeculae that remained intact post-OVX.

In summary, the extent of OVX bone loss was affected by peak bone microarchitecture, most notably the trabecular thickness. Thicker trabeculae are less likely to be disconnected or perforated in response to OVX, resulting less degree of bone loss. Given the same bone mass (BV/TV), a trabecular bone phenotype with thin trabeculae may be a risk factor toward accelerated postmenopausal bone loss.



Cyclic Treatment Regimen Rescues Parathyroid Hormone (PTH) Discontinuation-Induced Bone Loss and Microarchitecture Deterioration

¹Tseng W-J; ¹Zhao H; ¹Lee W; ¹Liu Y; ¹Li Y; ¹de Bakker C; ¹Qin L; +¹Liu XS
 +¹McKay Orthopaedic Research Laboratory, Department of Orthopaedic Surgery, University of Pennsylvania, Philadelphia, PA

Despite the potent effect of intermittent PTH treatment on promoting new bone formation, BMD rapidly decreases upon PTH discontinuation. To uncover the mechanisms behind this adverse phenomenon, we first examined the changes in tibial bone microarchitecture in ovariectomized (OVX) rats by *in vivo* μ CT. 18 4-mo-old rats underwent OVX surgery and developed osteopenia for 4wks (50% reduction in BV/TV). Bone loss continued in VEH-treated rats (n=9) for 12 weeks. In contrast, 3-wk PTH treatment (40 μ g/kg, n=9) led to 97% and 27% greater BV/TV and Tb.Th, respectively, in the PTH vs. VEH group. Intriguingly, 1 wk after the withdrawal (wk4), BV/TV and Tb.Th continued to show trends of improvement. Trends of bone deterioration appeared during the 2nd and 3rd wk of PTH withdrawal (wk 5 and 6), with a 28% decrease in BV/TV at wk 6 vs. wk 4 (Fig 1A). Histology (n=6/group) suggested that 3-wk PTH treatment led to 117% greater osteoblast # (Ob.N/BS) and 55% and 70% lower osteoclast # (Oc.N/BS) and adipocyte # (Adi.N/Ma.Ar), respectively, than VEH group. After 1-wk withdrawal from PTH, Ob.N/BS decreased 82% but remained 36% greater than VEH, and Oc.N/BS and Adi.N/Ma.Ar continued to be suppressed. 2wk after PTH discontinuation, there was no remaining difference in Ob.N/BS and Oc.N/BS from VEH while Adi.N/Ma.Ar was 56% lower than VEH group (Fig 1BCD).

The continuous anabolic window upon early withdrawal from PTH offers a new mechanism in support of a cyclic administration regimen with repeated cycles of on and off PTH treatment. Next, 3 treatment regimens were examined in OVX rats: VEH (n=3, 18-wk saline), PTH-VEH (n=6, 9-wk PTH followed by 9-wk saline), and Cyclic PTH (n=7, 3-wk PTH followed by 3-wk saline, 3 cycles). In the PTH-VEH group, 9-wk PTH led to a 97% increase in BV/TV, followed by a 72% decrease after 9-wk discontinuation, with no difference from VEH group at wk 18. Similar trends were found for Tb.Th (Fig 2). In contrast, in the Cyclic PTH group, the first cycle of 3-wk PTH on and 3-wk off prevented reduction in BV/TV and led to a 33% increase in Tb.Th. BV/TV stabilized and Tb.Th continued to increase during the 2nd and 3rd cycles. At wk18, BV/TV and Tb.Th in Cyclic PTH rats were greater than both PTH-VEH and VEH rats (p<0.05, Fig 2AB).

In summary, our study discovered a continuous anabolic window upon early withdrawal from PTH which allowed the cyclic treatment regimen to maximize the total duration and efficacy of PTH treatment on bone microarchitecture.

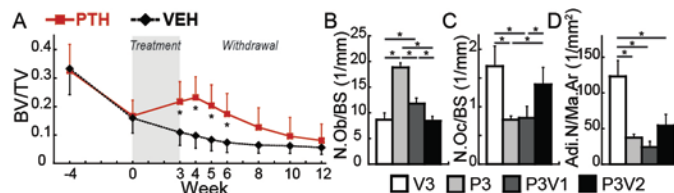


Fig 1 (A) Changes in BV/TV in 12-wk VEH treated, and 3-wk PTH followed by 9-wk VEH treated OVX rats. (B-D) Comparisons in cellular activities among rats with 3-wk VEH (V3) and PTH (P3), and 3-wk PTH followed by 1- and 2- wk VEH treatments (P3V1 and P3V2). * difference between treatment groups (p<0.05).

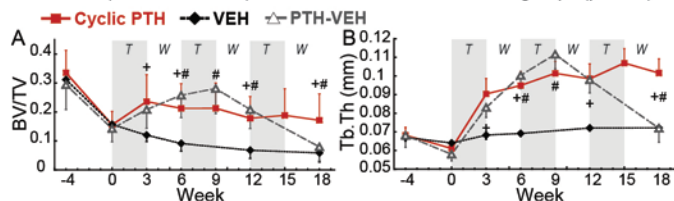


Fig 2 (A-B) Changes in trabecular bone microstructure in VEH, PTH-VEH, and Cyclic PTH-treated OVX rats. + difference between Cyclic PTH and VEH groups (p<0.05). # difference between Cyclic PTH and PTH-VEH groups (p<0.05). T: Treatment, W: Withdrawal in the Cyclic PTH group.

The Porcine Accessory Carpal as a Model for Biologic Joint Replacement for Trapeziometacarpal Osteoarthritis

Stoeckl BD^{1,2}, Hast MW¹, Sennett ML^{1,2}, Kim M^{1,2}, Eby MR^{1,2}, Schaer TP³, Mauck RL^{1,2,4}, Steinberg DR^{1,2}

¹ Department of Orthopaedic Surgery, University of Pennsylvania, Philadelphia, PA ² Translational Musculoskeletal Research Center, Philadelphia VA Medical Center, Philadelphia, PA ³ Penn Vet Center for Medical Translation, Comparative Orthopaedic Research Laboratory, School of Veterinary Medicine, University of Pennsylvania, Kennett Square, PA ⁴ Department of Bioengineering, University of Pennsylvania, Philadelphia, PA

Introduction: Trapeziometacarpal (TMC) osteoarthritis (OA) is one of the most common conditions affecting middle and older aged adults¹. Given that the opposable thumb is central to all activities of daily living, loss of function has a significant impact on quality of life. Patients with TMC OA are initially managed with activity modification, non-steroidal anti-inflammatory drugs, splinting, and occasionally corticosteroid injections². These conservative treatments often fail in the long term, and many patients will eventually require surgical intervention. However, most of these procedures are destructive, involving removal of all or part of the trapezium, and replacement with tendon, fascia, or an artificial substrate or implant². While effective at reducing pain, these procedures compromise grip strength and, in some cases, result in subsidence and disfigurement of the hand². Efforts to replace articular cartilage (and bone) with living, functional tissue have matured substantially over the last two decades³, as has technology for generating constructs that can match the anatomical complexity and geometry of native articulating surfaces^{3,4}. For these technologies to progress towards translation, appropriate large animal models are required. In this study, we explored the porcine accessory carpal (AC) bone as a model for TMC OA, with the goal of using this to evaluate a tissue-engineered biologic joint replacement.

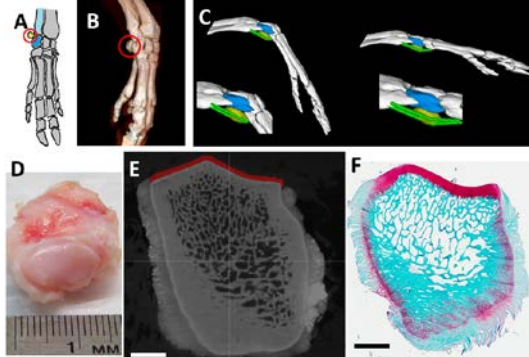


Figure 1: (A) Position of the AC (yellow) with respect to the ulnar carpal (blue) and ulna (light blue). (B) CT visualization with the AC identified (red circle). (C) OpenSim model showing position of the AC (yellow) relative to the ulnar carpal (blue) in flexion (left) and extension (right). (D) Gross view of cartilage surface of the AC. (E) μ CT slice in ITK-SNAP showing segmented cartilage in red. Scale = 3mm. (F) Safranin O/ Fast Green stained section of AC. Scale = 3mm.

Methods: The forelimbs of skeletally mature Yucatan minipigs under general anesthesia were imaged with a portable 8-slice CT scanner (CereTom, Neurologica). DICOM files were exported and opened in ITK-SNAP⁵, where the bones were individually segmented. Using this information, a 3D model was generated in OpenSim, and the relative motion of the AC and normal and shear contact forces were evaluated through a range of flexion angles. Next, five AC bones were isolated from the right forelimbs of adult Yucatan minipigs from an unrelated study. A custom indentation testing setup was used to evaluate cartilage mechanics along the midline of the AC articular surface via stress relaxation tests. The saddle-shaped articular cartilage surface was indented with a 2 mm diameter spherical indenter in three locations (superior, middle, and inferior). Four compressive ramps (10% strain each) were applied, with a 600s relaxation between each step. The equilibrium modulus was calculated from the second step. Samples were then fixed in formalin and imaged via μ CT (VivaCT 75, Scanco medical), before and after immersion in Lugol's solution (5% I₂, 10% KI in water) to enhance cartilage contrast. DICOMs from the initial scan were imported into ITK-SNAP and the bone was segmented. A surface mesh was exported and opened in Meshlab (ISTI), where the mesh was smoothed and simplified. This mesh was imported into Solidworks (Dassault Systèmes) and a 3D object was created in order to compute the bone volume and surface features. Scans post Lugol's treatment were manually registered with the bone scan and processed similarly, with the cartilage layer segmented in a semi-automated manner. Cartilage thickness was determined across the 3D object with a grid spacing of 1.25 mm. After imaging, samples were decalcified, processed into paraffin, sectioned, and stained with



Figure 2: Solidworks models of five AC bones and the corresponding cartilage surfaces (in red). Scale = 5mm.

Safranin O and fast green to visualize cartilage, bone, and fibrous tissue. Statistical analysis was by one-way ANOVA with Tukey's posthoc testing, and Pearson correlation of animal weight against cartilage volume and surface area.

Results: The cartilage surface of the pig AC consists of a main saddle-shape that articulates with the ulnar carpal bone and a secondary facet that interacts with the ulna (Fig 1A-B). The remainder of the bone is embedded in fibrous tissue (Fig 1F). When the unloaded hoof extends, this fibrous tissue sheath goes into tension and causes the AC to articulate slightly distally, resulting in estimated contact forces in the range of 138N compression and 21N shear (Fig 1C). Across five donors, the AC had the same basic shape and geometry, but showed a high degree of inter-subject variation in both shape (Fig 2) and in size (Fig 3B). AC volume (Pearson $r = -0.1065$) did not correlate with animal weight, while cartilage surface area was negatively correlated (Pearson $r = -0.6507$). The average thickness of the AC articular cartilage ranged from 310-420 microns within the contour of the main articulating surface. There was a trend towards greater thickness on the superior and middle regions compared to the inferior region (Fig 3A). Interestingly, there was more variation in the size and shape of the cartilage surface than there was in the thickness. The equilibrium modulus in the superior, middle, and inferior regions was 1.17 ± 0.20 , 1.63 ± 0.16 , and 1.54 ± 0.12 MPa, respectively (Fig 3C), with the superior region trending softer than the middle and inferior regions ($p=0.14$).

Discussion: We evaluated the geometric, histologic, and mechanical properties of the accessory carpal bone and cartilage in a Yucatan minipig model. This bone and articulating surface bears anatomic similarities to the human TMC in terms of its saddle-shaped cartilage surface as well as its load bearing function. While there was variation in geometry between subjects, several trends emerged. Specifically, the superior aspect was thicker and softer, while the inferior aspect was thinner and stiffer. These data provide benchmarks for the generation of anatomic models and living engineered replacements for the AC cartilage and bone⁴. The consistency in cartilage thickness suggests that CT rendering, using a clinical scanner, may provide sufficient resolution for implant generation, a priori, without the need for high resolution scanning of isolated tissue. This will enable ex vivo production and maturation of engineered constructs on an individualized basis. Having established these principles, future studies will focus on the creation of anatomic molds to create engineered bone coupled to an engineered articular cartilage surface. Ultimately, these engineered osteochondral units will be used for biologic joint resurfacing of the AC in a large animal model, advancing the state of the art in the treatment of TMC osteoarthritis.

Significance: This study defined the anatomic and mechanical features of the porcine AC bone and cartilage, a first step in the development of a large animal model to rigorously evaluate biologic resurfacing strategies for the treatment of TMC osteoarthritis.

References: [1] Becker+, Clin Orthop Relat Res, 2013. [2] Wajon+, Cochrane Database Syst Rev, 2015. [3] O'Connell+ J Knee Surg, 2012. [4] Saxena+ Tissue Eng Part A, 2016. [5] Yushkevich+, Neuroimage, 2006. **Acknowledgements:** Supported by the Department of Veterans' Affairs.

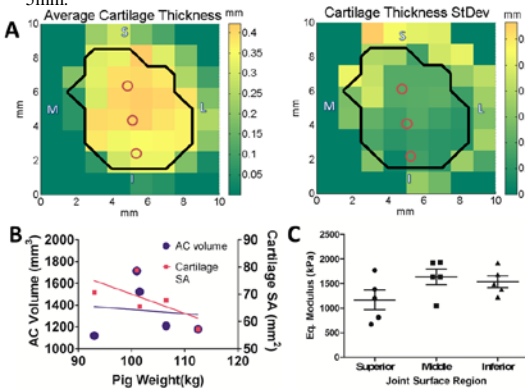


Figure 3: (A) Average (left) and standard deviation (right) thickness maps of the main articulating surface overlaid on top of a profile indicating the average cartilage perimeter (black line). Indentation test location indicated by red circles. (B) Correlation analysis of animal weight and cartilage volume and surface area. (C) Equilibrium modulus at three locations along the midline of the AC articular cartilage. $N = 5$, $p = 0.14$.

Proteasome inhibitor bortezomib is a novel therapeutic agent for focal radiation-induced osteoporosis

Abhishek Chandra^{1,8,9}, Luqiang Wang¹, Tiffany Young¹, Leilei Zhong¹, Wei-Ju Tseng¹, Michael A. Levine^{2,3,4}, Keith Cengel⁵, X. Sherry Liu¹, Yejia Zhang^{1,6},
⁷ Robert J. Pignolo, and Ling Qin¹

¹Departments of Orthopaedic Surgery, ⁵Radiation Oncology, ²Pediatrics, ⁶Physical Medicine and Rehabilitation, Perelman School of Medicine, University of Pennsylvania. ³Division of Endocrinology and Diabetes, ⁴Center for Bone Health, Children's Hospital of Philadelphia, ⁷Translational Musculoskeletal Research Center (TMRC), Corporal Michael J. Crescenz Veterans Affairs Medical Center, Philadelphia, Pennsylvania, USA.

⁸Department of Physiology and Biomedical Engineering, ⁹Medicine, Mayo Clinic, Rochester, Minnesota, USA.

Disclosures: Abhishek Chandra (none), Luqiang Wang (none), Tiffany Young (none), Leilei Zhong (none), Wei-Ju Tseng (none), Michael A. Levine (none) Keith Cengel (none), X.Sherry Liu (none), Yejia Zhang (none)and Ling Qin (none).

Introduction: Osteoporosis and its resulted fracture are unwanted consequences for cancer patients receiving clinical radiotherapy. We have been in constant pursuit of an anabolic drug that could sustain constant recovery of bone post-radiotherapy. Studies from our lab and other groups have shown that focal radiation eliminates the osteoclasts after a transient increase; hence any kind of recovery is solely possible through anabolic drugs. Anabolic agents, recombinant human parathyroid hormone (rhPTH1-34, teriparatide) and Sclerostin antibody (Scl-Ab) significantly improved bone architecture post-radiotherapy. DNA damage is one of the most deleterious events post-radiotherapy, creating double strand breaks (DSBs) which are then repaired by non-homologous end joining (NHEJ)/DNA repair proteins. We previously demonstrated that Wnt3a in vitro and rhPTH 1-34 and Scl-Ab in vivo could suppress radiation-induced DNA damage as measured by γ H2AX (DSB marker) foci levels. Since several components of the NHEJ pathway, such as Ku70 and DNA-PKc, are regulated by Ubiquitin-Proteasome based protein degradation, we aim to test whether Bortezomib (Bzb), a proteasome inhibitor and a FDA-approved drug for the treatment of multiple myeloma could restore bone structure after radiation damage.

Methods: *Small animal radiation research platform (SARRP) radiation and Bzb treatment.* All procedures were approved by our institution's Animal Care and Use Committee. Two-month-old male WT (C57BL6) mice received two 8 Gy doses delivered on days 1 and 3 to the distal metaphyseal region of the right femurs from SARRP (Xstrahl), a clinically relevant focal irradiator that is designed to mimic the typical femur dose constraints for whole pelvis intensity modulated radiotherapy for patients with prostate, rectal, or endometrial cancers. Following radiation, WT mice were subcutaneously injected with either vehicle or Bzb (1 mg/kg) twice a week for 4 weeks. On day 28, bilateral femurs (radiated and non-radiated) were harvested for μ CT, histology, and histomorphometry, and serum were collected for bone markers. For dynamic labeling, calcein (15 mg/kg) and xylenol orange (90 mg/kg) were injected at 9 and 2 days, respectively, before euthanization. *μ CT-* The metaphysis of distal femur was scanned by μ CT 35 (Scanco Medical AG) at 6 μ m resolution followed by calculation of trabecular bone structural parameters (n=6/group). *Histomorphometry-* After μ CT scanning, femurs were processed for plastic embedding for static and dynamic histomorphometric analysis. *Histology-* Col2-Cre Rosa-Tomato (Col2/Tomato) mice were used for monitoring osteolineage cells. At 2 weeks post radiation, femurs (n=3/group) were harvested for frozen embedding followed by TUNEL staining (Apoptag[®] TM, Millipore). *Cell death detection-* Ethidium Bromide (EB)/Acridine Orange (AO) staining was used for detection of apoptotic cells. *Immunofluorescence-* After radiation, cells were fixed with 4% paraformaldehyde and incubated with antibodies against γ -H2AX and caspase 3 followed by Alexa-conjugated fluorescent secondary antibodies and DAPI staining. *Single cell gel electrophoresis-* Comet assay was performed using the alkaline conditions of the Trevigen Comet Assay[®] kit. *Statistics:* Data are expressed as means \pm SEM and analyzed by paired, two-tailed Student's t-test for comparison of radiated and non-radiated legs and by unpaired, two-tailed Student's t-test for comparison of vehicle and Bzb-treated samples.

Results: As reported earlier, distal femoral metaphysis of adult mice that was focally irradiated by SARRP suffered dramatic trabecular bone loss compared to contralateral femur (BMD: -57%; BV/TV: -63%; Conn.Dens.: -80%; Tb.N: -39%; SMI: +69%; Tb.Sp: +76%) (Fig.1). Strikingly, bi-weekly injections of Bzb for 4-weeks showed a remarkable recovery in trabecular bone architecture as compared to the radiated bones in vehicle treated animals (BMD: +3-fold; BV/TV: +3.6-fold; Conn.Dens.: +4.7-fold; Tb.N: +86.7%; SMI: -52.7%; Tb.Sp: -51.9%). It is interesting to note that Bzb-treated radiated bones had significantly higher bone apposition than vehicle treated non-radiated femurs. We observed significant increase in osteoblast number (Ob.N/BS, Fig.1 C) and mineralizing surface (Fig. 1D) in Bzb treated radiated femurs, but only a modest but significant increase in bone formation rate. Osteoclasts identified by morphology at 4 weeks (Fig. 1E), or TRAP staining at 2 weeks (Fig.1F), show a significant decrease post-irradiation, indicating limited role of resorption to be considered for therapeutic. Bzb treatment decreased osteoclast number (Fig. 1 E,F) and reduced CTX-I levels as compared to vehicle group (Fig. 1G). Immunofluorescence imaging to detect apoptosis revealed an 11.6-fold increase in TUNEL⁺ bone surfaces osteoblasts (Fig.2A,B), which were significantly reduced by Bzb treatment. In a calvarial organ culture system, a 4-fold increase in cleaved-caspase 3, an apoptosis marker, by radiation was significantly mitigated in the presence of 20nM MG132, a Bzb functional analog (Fig. 2C). Similar results were observed in bone marrow osteoprogenitor and UMR-106 osteoblastic cell cultures. Radiation induced double strand breaks (DSBs) in primary calvarial osteoblastic cells as detected by γ H2AX immunofluorescence (Fig.3A) and western blots (Fig.3B) were mitigated by 20nM of MG132 pre-treatment prior to radiation. Components of NHEJ-DNA repair pathway, Ku70 and DNA-PKc were moderately increased after 4h of radiation, but significantly elevated starting 30min in osteoblastic cells, and calvarial organ cultures (Fig.3C). Finally, by COMET assay measuring DNA damage, knockdown of Ku70 mRNA abolished MG132-induced DNA repair in radiated osteoblasts (data not shown).

Discussion: Taking together our data suggests that functional suppression of proteasome function in radiated osteoblasts and progenitors by Bzb stimulates DNA repair and survival in osteoblasts, resulting in effective healing and improved architecture of radiated bones. Since we are experiencing sustained bone recovery post-radiotherapy at 1mg/kg, a dose-dependent study could further decrease any concern with the systemic nature of this treatment.

Significance: Proteasome Inhibitor class of drugs such as Bzb, which have a strong anti-tumor effect while sparing the normal tissues, could potentially mitigate the concerns attached to its potential as an anabolic therapeutic for radiotherapy induced osteoporosis.

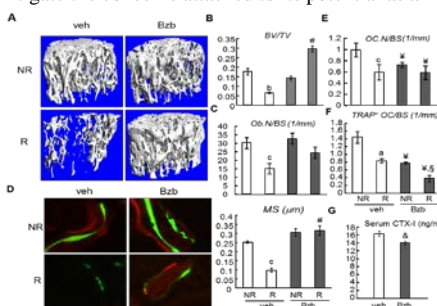


Figure 1. Bortezomib can alleviate radiation induced bone loss by promoting anabolic bone formation and suppression of bone resorption.

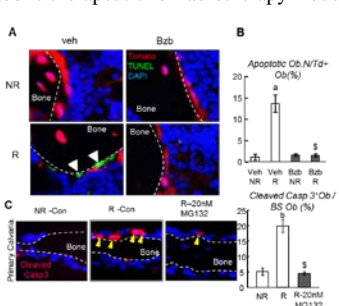


Figure 2. Proteasome inhibitors protects osteoblasts from radiation induced apoptosis

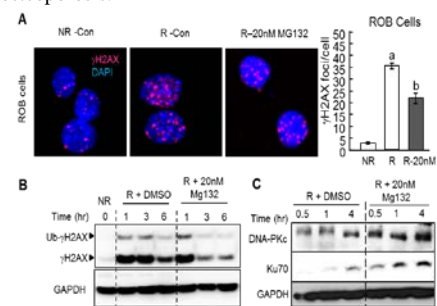


Figure 3. Proteasome suppression improves DNA repair in radiated osteoblasts via NHEJ pathway

Acknowledgement- This work was supported by the National Institute of Health (R01DK095803 to LQ), Penn Center for Musculoskeletal Disorders P30AR06919 (NIAMS/NIH) and ASBMR Junior Faculty Osteoporosis Basic Research Award (to LQ).

Subchondral bone plate sclerosis during late osteoarthritis is caused by loading-induced reduction in Sclerostin

Haoruo Jia^{1,2}, Xiaoyuan Ma^{1,3}, Yulong Wei^{1,4}, Wei Tong^{1,4}, Robert J. Tower¹, Abhishek Chandra¹, Luqiang Wang¹, Zeyang Sun^{1,5}, Zhaochun Yang⁶, Farid Badar⁷, Kairui Zhang⁸, Wei-ju Tseng¹, Ina Kramer⁹, Michaela Kneissel⁹, Yang Xia⁷, X.Sherry Liu¹, James H-C. Wang⁶, Lin Han¹⁰, Motomi Enomoto-Iwamoto^{11,12}, Ling Qin¹

¹Department of Orthopaedic Surgery School of Medicine, University of Pennsylvania, Philadelphia, Pennsylvania, 19104, USA. ²Department of Orthopaedics, The First Affiliated Hospital of the Medical College, Shihezi University, ShiHeZi, Xinjiang, China. ³Department of Orthopaedics, Shandong University Qilu Hospital, Jinan, Shandong, China. ⁴Department of Orthopaedics, Union Hospital, Tongji Medical College Huazhong University of Science and Technology, Wuhan, Hubei, China. ⁵School of Engineering and Applied Science, University of Pennsylvania, Philadelphia, Pennsylvania, 19104, USA. ⁶Department of Orthopaedic Surgery, University of Pittsburgh School of Medicine, Pennsylvania, 15213, USA. ⁷Department of Physics and Center for Biomedical Research, Oakland University, Rochester, Michigan, 48309, USA. ⁸Department of Orthopaedics and Traumatology, Nanfang Hospital Southern Medical University, Guangzhou, China. ⁹Musculoskeletal Disease Area, Novartis Institutes for BioMedical Research, Basel, Switzerland. ¹⁰School of Biomedical Engineering, Science and Health Systems, Drexel University, Philadelphia, Pennsylvania, 19104, USA. ¹¹Department of Surgery, The Children's Hospital of Philadelphia, Pennsylvania, 19104, USA. ¹²Department of Orthopaedics School of Medicine, University of Maryland, Baltimore, Maryland, 21201, USA.

OBJECTIVE: To establish an unbiased 3D approach that quantifies subchondral bone plate (SBP) changes in mouse joints and to investigate the mechanism that mediates SBP sclerosis at a late stage of osteoarthritis (OA).

DESIGN: A new micro-CT protocol was developed to characterize the entire SBP thickness in the distal femur of a mouse knee. Four mouse models with severe joint OA were generated: cartilage-specific Egfr knockout (CKO) mice at 2 months after surgical destabilization of the medial meniscus (DMM), aged Egfr CKO mice, wild-type (WT) mice at 10 months after DMM, and WT mice after DMM plus hemisection of the meniscus (DMMH) surgery. Additionally, SOST (Sclerostin) KO mice were subjected to DMMH surgery. Knee joints were examined by micro-CT, histology, and immunohistochemistry.

RESULTS: 3D micro-CT analysis of the mouse distal femur revealed a positive correlation between SBP thickness and the loading status in normal knees. In late OA models, SBP sclerosis was restricted to the areas under severely eroded articular cartilage. This was accompanied by elevated bone formation at the bone marrow side of the SBP and a drastic reduction of Sclerostin in osteocytes within the SBP. Unlike WT, SOST KO mice did not further increase SBP thickness in response to DMMH.

CONCLUSIONS: Since focal stress on SBP underlying the cartilage damage site increases at late OA, our work establishes mechanical loading-induced attenuation of Sclerostin and elevation of bone formation along the SBP surface as the major mechanism for subchondral bone phenotypes associated with late stage OA in mice. This article is protected by copyright. All rights reserved.

Naproxen, but not Aspirin, Increases Risk and Impairs Repair of Stress Fracture

Jino Park¹, Camilo S. Restrepo², Javad Parvizi^{1,2}, Ryan E. Tomlinson¹

¹ Thomas Jefferson University, Philadelphia, PA, USA

² Rothman Institute, Philadelphia, PA, USA

Skeletal stress fractures are painful, debilitating injuries caused by the formation and propagation of cracks in bone. In physically active populations, such as athletes, military recruits, and performers, stress fracture incidence is as high as 50%. Furthermore, these individuals are among the 30 million daily users of non-steroidal anti-inflammatory drugs (NSAIDs), the most commonly consumed class of medications worldwide. While effective in subduing pain and inflammation by preventing the synthesis of PGE₂ through COX1 and/or COX2, NSAIDs have been previously linked to impaired fracture healing. However, the overall effect of chronic NSAID use on skeletal health remains poorly understood. Recently, Hughes et al. found that US soldiers prescribed any NSAID have a 2.5 fold increased risk of future stress fracture. Similarly, we found that patients treated at the Rothman Institute for a stress fracture had a history of NSAID usage about twice the national average. Thus, we hypothesized that chronic NSAID use may predispose habitually loaded bones to stress fracture. To test this hypothesis, C57BL/6J mice were subjected to six bouts of axial forelimb compression (3 N, 100 cycles) over two weeks, starting at 16 weeks of age. Drinking water was used to administer naproxen (68 mg/L), aspirin (624 mg/L), or vehicle (control) starting 24 hours before loading. By dynamic histomorphometry, naproxen-treated mice had a sharply diminished rPs.BFR/BS (-74%) but aspirin-treated mice were not different than control. Although stiffness, ultimate stress, and bone mineral density were not affected by treatment, femurs from naproxen-treated mice had significantly decreased toughness (-35%) that was not evidenced in aspirin-treated mice, as compared to control. In total, these results indicate that naproxen, but not aspirin, increases stress fracture risk by limiting skeletal adaptation to repetitive loads and decreasing overall toughness, potentially by disrupting collagen synthesis and/or organization. In a separate experiment, C57BL/6J mice were subjected to an ulnar stress fracture generated by a single bout of fatigue loading at 16 weeks of age. Drinking water with naproxen, aspirin, or vehicle was provided 24 hours before loading. MicroCT analysis after 7 days indicated a marked decrease in woven bone volume (-27%) and span ($p=0.09$) in the naproxen-treated group, but not in the aspirin-treated group. Behavioral analysis in the week after stress fracture revealed normal forelimb use in both aspirin- and naproxen-treated mice ($p > 0.05$ vs. baseline) whereas control mice favored the uninjured forelimb until day 7 ($p < 0.05$). Thus, aspirin and naproxen had similar analgesic efficacy following stress fracture, but only naproxen impaired stress fracture repair. In summary, the substitution of aspirin for naproxen in patients at-risk for stress fracture may reduce injury rates and improve recovery times.

Antimicrobial peptide combined with BMP2-modified MSCs promotes bone repair

Min Liu¹, Zunpeng Liu², Xue Yuan², Yeji Zhang³, Shuying Yang^{1,2}

¹ Department of Anatomy and Cell Biology, School of Dental Medicine, University of Pennsylvania, ² Department of Oral Biology, School of Dental Medicine, University of Buffalo, The State University of New York, ³ Departments of Physical Medicine and Rehabilitation, School of Medicine, University of Pennsylvania

INTRODUCTION: Repair and regeneration of inflammation-caused bone loss remains a clinical challenge. LL37 is an antimicrobial peptide, which plays critical roles in cell migration, cytokine production, apoptosis, and angiogenesis. It has been associated with the regulation of wound healing, immune responses, and neovascularization in injured tissues. Migration of stem cells to the affected site and promotion of vascularization are essential for tissue engineering therapy, including bone regeneration. However, it is largely unknown whether LL37 affects mesenchymal stem cells (MSCs) behavior and bone morphogenic protein 2 (BMP2) mediated bone repair during bone pathologic remodeling process.

METHODS: We performed both *in vitro* and *in vivo* studies. MSCs was isolated and cultured from femurs and tibias of C57BL/6J mice. To investigate the cellular proliferation effect of LL37 on MSCs, the MTS assay was performed using the MTS cell proliferation kit. The cell proliferation rate of MSCs treated with BMP2 adenovirus and cultured with or without LL37 was assayed. Additionally, the effect of LL37 on osteogenic differentiation was examined by ALP activity assay and Alizarin Red staining. The *in vivo* experimental protocol was performed on mice. LPS was injected subcutaneously into the tissue pocket surrounding the calvaria and near the midline of the skull to induce osteolysis defects. LL37 was administrated, and then followed by injection of 1×10^6 MSCs or BMP2-modified MSCs. 3 weeks later, calvaria bones were harvest and examined by Micro-CT analysis. In addition, half specimens per group were decalcified and cut into 5 μ m sections for histological analysis.

RESULTS: We found that LL37 significantly induced cell differentiation, migration, and proliferation in both MSCs and BMP2 modified MSCs (Fig. 1). Additionally, LL37 inhibited LPS-induced osteoclast formation and bacterial activity in *in vitro* analysis. Furthermore, Combination of LL37 and BMP2 markedly promoted MSCs mediated bone repair and regeneration in LPS-induced osteolysis defects in mouse calvaria. Compared to the PBS control group, much more new bone formed in the LPS+mMSC/B2+LL37 group, which not only completely filled the bone loss defect, but also markedly increased the thickness of the calvaria bone (Fig. 2), demonstrating a robust effect of LL37 and MSCs/B2 on osteogenesis and suggesting that LL37 is more effective when combined with unmodified or BMP2-modified MSCs to treat inflammation-induced bone defects.

DISCUSSION: These findings demonstrated that this novel combination of LL37 and mMSC/B2 stimulates bone formation and is efficient to promote new bone formation for treatment of bone loss especially in inflammatory condition. LL37 can be a promising drug target for promoting osteogenesis, inhibiting bacterial growth and osteoclastogenesis.

SIGNIFICANCE: It appears that this system can be useful not only in osteolysis defect, but also in the filling of defects with limited accessibility or narrow cavities such as in periodontal bone repair as well as inflammatory bone loss.

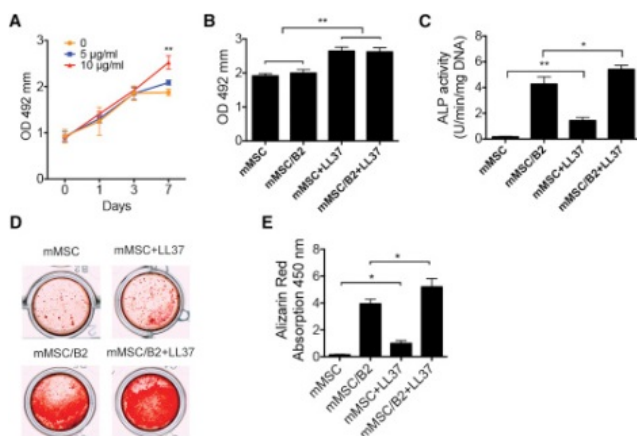


Figure 1. LL37 promotes proliferation, osteogenic differentiation, and mineralization of MSCs

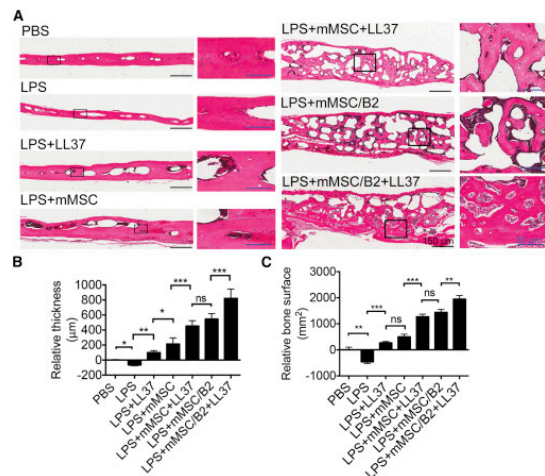


Figure 2. Histological evaluation of newly formed bone in LPS-Induced osteolysis

Multifaceted roles of IFT20 in osteoblast differentiation, proliferation and cell polarity influence bone development

Jormay Lim^{1#}, Xue Yuan^{2#}, Shuying Yang^{1,2*}

¹Department of Anatomy and Cell Biology, School of Dental Medicine, University of Pennsylvania; ²Department of Oral Biology, School of Dental Medicine, University of Buffalo, State University of New York, Buffalo, NY, United States.

[#]Equal contribution of authors

*Corresponding author: Dr. Shuying Yang, shuyingy@upenn.edu

This work was supported by a National Institute of Health grant DE023105 (S. Yang) and AR061052 (S. Yang)

Abstract

Intraflagellar transport proteins (IFT) are required for hedgehog (Hh) signaling in bone development. In particular, the role of IFT80 in balancing canonical Hh signaling and the non-canonical Hh-RhoA-cofilin/MLC2 signaling has been delineated previously in our lab. IFT20 is operating in the same transport complex-complex B as IFT80. On the other hand, IFT20 is different from IFT80 because it is also localized to the Golgi apparatus. Conditional knockout of IFT20 in the neural crest has caused craniofacial skeletal phenotypes. However, the role of IFT20 in bone development from the perspective of osteoblasts has not been characterized. We crossbred Osterix-cre (OC) and IFT20^{f/f} mice to obtain mice with the deletion of IFT20 in osteoblast (OB) precursor cells (OPC). Moreover, IFT20^{f/f} OPC has been isolated from neonatal calvaria and treated with Adenoviral-cre or Adenoviral-null for *in vitro* analysis. Employing the micro-CT method and *in vitro* cell differentiation assay of ALP activity and Alizarin Red staining, we found that OPC specific deletion of IFT20 in mice resulted in growth retardation and decreased bone mass with impaired OB differentiation. The failure of OB differentiation can be overcome by actin polymerization inhibitor cytochalasin D treatment or cytochalasin D treatment in combination with Hh. Therefore, the bone phenotypes are due to impaired Hh signaling depending upon the integrity of primary cilia. To further analyze the cellular roles of IFT20, we also performed cell proliferation analysis using WST-1 assay and found a significant reduction of cell proliferation in IFT20 deleted primary calvaria cells. Interestingly, IFT20 was localized in the mitotic spindle, and the dividing cells lacking IFT20 exhibited multi-polar mitotic spindle. The immunofluorescent staining of mitotic serine/ threonine kinase AURKA is reduced in the mitotic spindle of IFT20 deleted cells. Paradoxically, AURKA protein level is elevated by IFT20 deletion in the Western blot analysis especially upon treatment of Purmorphamine, an agonist of Smoothed of Hh signaling. To further study the role of IFT20 in cell polarity, we evaluated three-dimensional spheroid formation, and found that the total number and the size of the spheroids are not significantly different between the cells from OC control and IFT20^{f/f}, OC mice. However, the composition of medium or smaller size spheroids is markedly reduced in IFT20 deleted group. Additionally, the cells are less compact and less well organized in the IFT20 deleted spheroids compared to the control, implicating that IFT20 affects the cell arrangement and the patterning of the organ. In short, IFT20 is a versatile factor important for OPC proliferation, the osteoblast differentiation and the cell polarity, and thus impacts on bone development in a multifaceted manner.

Conditional Ablation of Osteoprogenitor YAP and TAZ during Bone Fracture Repair

Christopher D. Kegelman¹ and Joel D. Boerckel¹

¹University of Pennsylvania, Philadelphia, PA
ckeg@seas.upenn.edu

Disclosures: Christopher D. Kegelman (N) and Joel D. Boerckel (N)

INTRODUCTION: Bone fracture healing requires coordinated matrix remodeling and vascularization, which result from dynamic communication between bone cells, but the molecular mechanisms remain incompletely understood. Recently, we found that deletion of yes-associated protein (YAP) and transcriptional co-activator with PDZ-binding motif (TAZ) from skeletal cells resulted in impaired bone development characterized by disorganized matrix properties, increased osteoclast numbers, and decreased osteoblast number/activity¹; however, the roles of YAP and TAZ in osteogenesis remain controversial. The well-established YAP/TAZ downstream target of the CCN family, CYR61, has been implicated in upregulating proangiogenic factors leading to improved bone fracture healing², but the role of YAP/TAZ signaling in regulating these proteins in the context of fracture healing remains unknown. Here, we tested the hypothesis that osteoprogenitor YAP and TAZ promote bone fracture healing through CYR61 signaling.

METHODS: We generated two mouse models: 1) constitutive allele dosage-dependent YAP/TAZ conditional knockout mice and 2) adult-induced double homozygous conditional knockout mice (YAP^{fl/fl};TAZ^{fl/fl};TetOff-Osx-Cre, hereafter cDKOⁱ), by ablating YAP and/or TAZ by Cre-recombination under control of the Osterix1 promoter. All animal experiments were approved by the IACUC. In inducible knockouts, Cre expression was repressed by doxycycline (dox) administration from conception to 14 weeks of age, while constitutive knockouts were bred and raised without exposure to dox. Unilateral femoral fractures were created at 16 weeks of age. Fractured limbs were either snap frozen in liquid nitrogen-cooled isopentane prior to mRNA isolation or formalin-fixed, paraffin embedded prior to histological staining with Safranin-O/Fast Green (Saf-O) and immunostaining with anti-YAP and anti-CYR61 antibodies. Comparisons were made using Student's t-tests. Non-parametric Mann-Whitney tests were used if necessary. A p-value less than 0.05 was considered significant.

RESULTS: Both WT and cDKOⁱ mice exhibited callus formation in response to bone fracture (Fig.1 A). Compared to WT littermates, cDKOⁱ mice had significantly lower bone volumes, at both one and two weeks post-fracture ($p < 0.05$), but had equivalent total callus volumes (Fig.1 B-C, N = 6 - 12). At two weeks post-fracture, cDKOⁱ mice displayed increased positive Saf-O staining within the center of the callus (Fig.1 D). Fracture calluses from cDKOⁱ mice also showed lower overall positive YAP and CYR61 staining compared to fracture calluses from WT mice (Fig.1 D). Compared to WT littermates, cDKOⁱ mice displayed trends of increased Col10 and decreased Cyr61 mRNA expression levels at both 1 and 2 weeks post fracture (Fig. 1E-F).

DISCUSSION: YAP/TAZ deletion from osteoprogenitor cells reduced fracture callus ossification, but did not impair cartilaginous anlage formation, consistent with our prior observations in developmental endochondral ossification¹. However, remodeling of the callus to bone appeared delayed with cDKOⁱ mice having both increased Saf-O staining and Col10 mRNA expression levels at two weeks post fracture. Modest reductions in mRNA and protein expression levels of CYR61 at 2 weeks post fracture further validated reduced YAP/TAZ signaling in conjunction with the osteogenesis defect during fracture healing. Together, these data implicate YAP/TAZ in regulation of osteogenesis during endochondral fracture repair.

SIGNIFICANCE/CLINICAL RELEVANCE: A mechanistic understanding of how these proteins combinatorially regulate osteogenesis could guide future therapeutic strategies for bone regeneration.

REFERENCES: ¹Kegelman+ *BioRxiv* 2017, doi.org/10.1101/143982. ²Athanasopoulos+ *JBC* 2007, 282(37):26746-5,

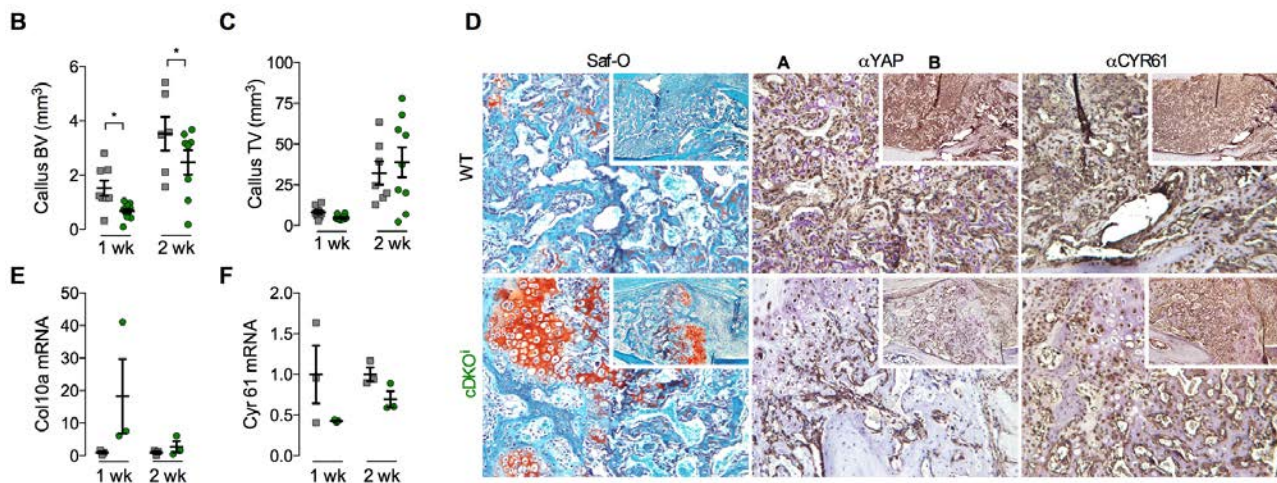


Figure 1: Inducible dual homozygous YAP/TAZ deletion impaired *in vivo* fracture healing. A) Representative 3D CT reconstructions at either 1 or 2-week post fracture. Quantification of callus B) bone and C) total volume at either 1 or 2-week post fracture. D) Representative micrographs stained for either Safranin-O, anti-YAP, or anti-Cyr61 at 2 weeks post fracture. mRNA expression levels for E) Col10 and F) Cyr61 from the callus lysate at either 1 or 2-week post fracture.

Resorbable Pins Enhance Retention of Nanofibrous Scaffolds in a Porcine Focal Chondral Defect Model

Mackenzie L. Sennett^{1,2}, Blair S. Ashley¹, Jay M. Patel¹, James M. Friedman¹, Robert C. Spiro³, Jason A. Burdick¹, James L. Carey¹, George R. Dodge^{1,2}, Robert L. Mauck^{1,2}

¹University of Pennsylvania, Philadelphia, PA, ²Translational Musculoskeletal Research Center, Philadelphia VA Medical Center, Philadelphia, PA, ³Aesculap Biologics, LLC, Breinigsville, PA

Disclosures: RCS (3A- Aesculap Biologics, LLC)

Introduction: The repair of focal cartilage lesions remains a challenging issue in orthopaedics. Left untreated, large focal lesions may progress to osteoarthritis, ultimately requiring total joint replacement [1]. Current interventions, such as microfracture, result in the formation of fibrocartilage and have poor long-term outcomes [2]. Emerging technologies that involve scaffold placement for cell delivery, such as matrix-induced autologous chondrocyte implantation (MACI), have recently been reported to have superior outcomes [3]. Indeed, the success of early scaffold based approaches has encouraged considerable innovation in the field of cartilage tissue engineering. As these new scaffolds and constructs emerge, one important consideration is the need for a reliable fixation technique for these various formulations. Previous work by our group evaluated the ability of a subchondral bone anchor (Mitek Microfix, Depuy) to support the retention of a 3D woven poly(ϵ -caprolactone) (PCL) scaffold in a full-thickness chondral defect in a large animal model [4]. While this fixation method provided adequate retention, it may not be suitable for all scaffold materials and resulted in notable disruption of the subchondral trabecular bone. Thus, the objective of this study was to evaluate additional fixation techniques that could be applied to multiple scaffold compositions in various defect geometries in a large animal model.

Methods: Full-thickness chondral defects were created unilaterally in the trochlear groove of 6 adult male Yucatan mini-pigs following a minimally invasive arthrotomy [5]. In 3 pigs, four 4mm-diameter defects (n=12 defects total) were created, with 10 receiving an electrospun nanofibrous hyaluronic acid (HA) scaffold. Scaffolds were fixed with press-fitting (n=2), fibrin glue (Tisseel, Baxter, n=2), or resorbable pin (Aesculap AG, n=6). In the other 3 pigs, two 8mmx4mm oblong defects were created (n=6 defects total), with five of the defects receiving nanofibrous PCL scaffolds fixed with two resorbable pins. All defects were subject to bone marrow stimulation via microfracture. The remaining two circular and one oblong defects served as microfracture controls. Animals were allowed to weight-bear immediately after surgery and were euthanized after 2 weeks. Gross evaluation, micro-computed tomography (micro-CT), and histology were used to assess scaffold retention, quality of adjacent and opposing cartilage surfaces, and bone morphometry. Additional biomechanical tests were performed to assess the failure load of the pin in ex vivo osteochondral samples. Pins were inserted into osteochondral explants with a loop of 4-0 vicryl suture around the head. The suture was tensioned at a rate of 0.05mm/s with an Instron mechanical tester until pin failure occurred (n=3). Fisher's exact test was used to compare retention rates between scaffolds fixed with pin to non-pin fixed scaffolds.

Results: Press-fitting and fibrin fixation resulted in no retention of HA scaffolds in the 4mm defects (PF: 0/2, Fib: 0/2). Pin fixation resulted in complete retention of HA scaffolds in the 4mm defects (6/6) and almost complete retention of PCL in the 8mm oblong defects (4/5). The overall retention rate for pin fixed scaffolds was significantly greater than non-pin fixed scaffolds (91% vs. 0%; p<0.05). Gross observation of the adjacent cartilage revealed no damage and India ink staining of the patella confirmed that no patterns of abnormal wear had occurred from the head of the pin. (Fig. 1). Micro-CT confirmed gross evaluation of scaffold retention and demonstrated normal trabecular architecture surrounding the pin (Fig. 2). Histological analysis revealed normal safranin O staining of the adjacent cartilage and very little staining of the repair tissue, which was fibrous and hypercellular at this early time point (Fig 3). Ex vivo mechanical testing of the pin showed that the failure strength was 7.4±1.8N, with pin failure occurring at the mid-substance.

Discussion: Our results conclusively show that bioresorbable polylactide pins provide reliable fixation of multiple scaffold materials in various defect geometries in a mini-pig chondral defect model. All adjacent and opposing cartilage surfaces were healthy and intact, indicating that these pins did not cause any detrimental mechanical wear during joint motion. Unlike the bone anchor we previously evaluated [4], this pin did not cause major disruption or incur remodeling of the subchondral bone. While histological analysis revealed proteoglycan-deficient, fibrous repair-tissue, we did not expect extensive repair at this early time-point. The ability of this pin to retain nanofibrous cartilage repair scaffolds in a focal chondral defect with no associated damage to surrounding cartilage or disruption to subchondral bone make it a promising fixation technique for long-term cartilage repair studies using advanced scaffold formulations.

Significance: These findings demonstrate a reliable fixation technique that will enable long-term studies of cartilage repair scaffolds in a clinically-relevant large animal model.

References: 1) Messner + 1996 Acta Orthop Scand. 2) Solheim + 2014 Knee Surg Sports Traumatol Arthrosc. 3) Saris + 2014 Am J Sports Med. 4) Friedman + 2017 Cartilage. 5) Bonadio + 2017 J Exp Orthop.

Acknowledgements: This work was supported by the American Orthopaedic Society for Sports Medicine.

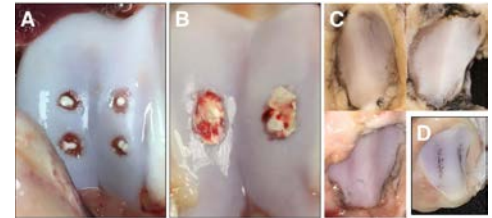


Fig 1: Post-mortem gross images. (A) HA scaffolds fixed with single pins in 4mm defects. (B) PCL scaffolds fixed with 2 pins in 8mm defects. (C) India ink-stained patellae demonstrating a lack of abrasions from pin implantation. (D) Control patella stained with India ink after ex vivo abrasion with scalpel (positive control for staining).

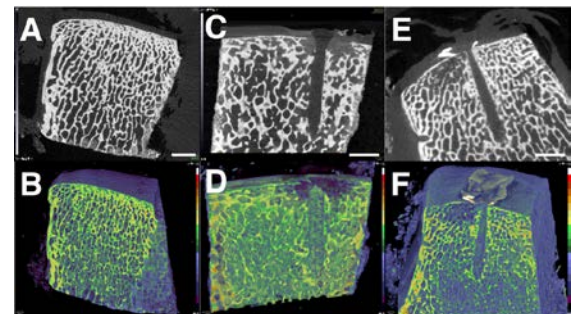


Fig 2: Micro-CT images and heat-mapped volume renderings (warmer colors indicate increased BMD). (A,B) Control sample from a non-operative limb showing healthy cartilage and normal trabecular architecture and bone mineral density for an adult mini-pig. (C) Image showing intact pin and HA scaffold within a 4mm defect. (D) Volume rendering shows normal trabecular architecture and bone mineral density. (E) Slice through 8mm oblong defect showing pin and radio-opaque PCL scaffold retained in the same plane as the surrounding cartilage. (F) Scaffold is firmly fixed above the subchondral plate. Cartilage not shown in volume rendered images. Scale bars = 2mm.

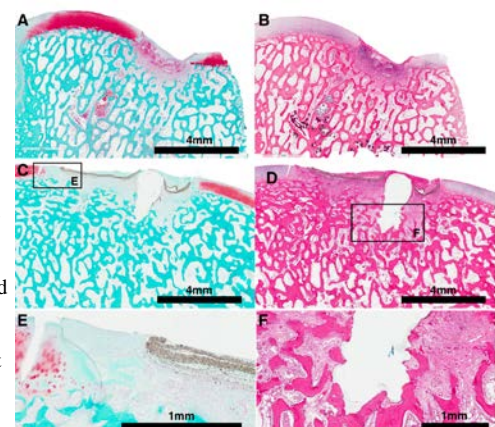


Fig 3: Histology of 4mm and 8mm defects. (A&B) Safo/FG and H&E staining of 4mm defect show HA scaffold retained above the subchondral plate. (C&D) Pin-fixed PCL scaffold retained above the subchondral plate. (E) Edge of scaffold and fibrous tissue at defect border. (F) Normal trabecular architecture surrounding site of pin insertion.

The Role of LPC and LPA in Osteoarthritis-Related Ossification and Pain

Emily Rumpf, Sonali Govande, Kennedy McKendall, Deepa S. Kurpad, Theresa A. Freeman, Ryan E. Tomlinson

Thomas Jefferson University, Philadelphia, PA

Introduction

Osteoarthritis is a common joint disorder that affects 10% of men and 13% of women over the age of 60 in the U.S.¹. The features of osteoarthritis include subchondral bone loss, cartilage fragmentation, and osteophyte formation, resulting in significant joint stiffness, inflammation, and pain. Furthermore, an estimated 15-25% of patients with osteoarthritis suffer from neuropathic pain². Recent reports have shown that lysophosphatidic acid (LPA) plays a critical role in the development of osteoarthritis (OA) and associated pain³. The interaction between LPA and the LPA1 receptor has previously been shown to induce local nerve demyelination, a causative factor in pain associated with osteoarthritis². Furthermore, LPA has been shown to induce chondrocyte proliferation and inhibit differentiation from mesenchymal stem cells inhibiting endochondral ossification⁴. Therefore, our overall hypothesis was that lysophosphatidylcholine (LPC) and/or LPA contribute to OA progression by inducing nerve demyelination, inhibiting angiogenesis, and promoting osteophyte formation. We directly tested these hypotheses using an *in vivo* model of endochondral ossification and *in vitro* studies of mesenchymal cell differentiation.

Results

Adult C57BL/6J mice were injected with Matrigel containing 2 ug/ml of bone morphogenic protein 2 (BMP2) and either vehicle (control), 5 mM LPC, 25 μ M LPA, or 5 mM LPC and 25 μ M LPA. The masses were excised after two and three weeks and analyzed using microCT and histology. After two weeks, masses treated with LPA had significantly decreased bone volume fraction as compared to the control, and the addition of LPC did not further affect ossification. In sections stained using hematoxylin and eosin (H&E), with Alcian blue (proteoglycan stain for chondrocytes), more chondrocytes were observed in masses treated with LPC and LPA as compared to control. In a separate group of mice, which express YFP in all nerves (Thy1-YFP mice), sections of masses were stained with antibodies against CD31 to evaluate angiogenesis and innervation. Here, control and LPC masses showed increased innervation and vascularization as compared to LPA treated masses. To further evaluate the roles of LPC and LPA on chondrocyte differentiation, C3H/10T1/2 cells were cultured in chondrogenic differentiation media containing transforming growth factor beta 1(TGF- β 1), then evaluated after one and three weeks. Western blot and real-time quantitative reverse transcription polymerase chain reaction (qRT-PCR) analysis revealed aberrant upregulation of the chondrogenic markers Col2, Runx2, and Sox9 in masses treated with LPC and LPA.

Conclusions

The results from our *in vivo* and *in vitro* studies illustrate that lysophosphatidic acid (LPA) has a negative effect on innervation, chondrocyte differentiation and endochondral ossification, suggesting a significant role in the osteophyte formation and pain associated with osteoarthritis. Understanding the mechanism(s) by which this phospholipid acts in the joint may be critical for the development of novel therapies for osteoarthritis.

1. Zhang, Y. et al 2010 Epidemiology of Osteoarthritis. *Clinics in Geriatric Medicine*, 26(3), 355–369
2. Nagai J et al. 2010 *Molecular Pain*, 6(78).
3. McDougall J et al. 2016 *Osteoarthritis and Cartilage*, 25(6), 926-934.
4. David M et al. 2014 *Journal of Biological Chemistry*, 289(10), 6551-64.

Intraflagellar transport proteins are required for jaw and tooth development

Chuanyun Fu^{1,3}, Xue Yuan^{2,4}, Shuying Yang^{1,2}

¹ Department of Anatomy and Cell Biology, School of Dental Medicine, University of Pennsylvania, ² Department of Oral Biology, School of Dental Medicine, University of Buffalo, The State University of New York, ³ Departments of Stomatology, Shandong Provincial Hospital Affiliated to Shandong University, ⁴ Department of Plastic and Reconstructive Surgery, University of Stanford, CA, United States

INTRODUCTION: Primary cilia and intraflagellar transport (IFT) proteins control a wide variety of processes during development and tissue homeostasis. Mutation of those proteins usually causes cilia defects and a wide range of diseases called ciliopathies. These disorders target multiple organs, of which bone and tooth are common ones. There are 22 identified IFT proteins that form two complex, IFT-A and IFT-B. IFT80 belongs to IFT-B complex and IFT80 deletion causes growth retardation and osteopenia. And mutations of IFT80 have been reported in human Jeune asphyxiating thoracic dystrophy (JATD) and short rib polydactyly type III. IFT20 also is a very important IFT complex B protein in assembling and maintaining many cilia/flagella, such as the motile cilia that drive the swimming of cells and embryos, the nodal cilia that generate left-right asymmetry in vertebrate embryos, and the sensory cilia that detect sensory stimuli in some animals. Although primary cilia have been observed in DPSCs and odontoblasts more than a decade ago, a few studies have investigated the role of primary cilia in tooth development, the roles of IFT20 and IFT80 in DPSC differentiation and function and teeth development are not well-addressed. The purpose of this study is to examine and compare the role of IFT20 and IFT80 protein in jaw and tooth development.

METHODS: OSX-Cre transgenic mice (also known as OSX1-GFP::Cre (Rodda and McMahon, 2006)) were crossed with IFT80f/f, IFT20f/f and IFT2080f/f to generate OSX-Cre;IFT80f/+ mice, OSX-Cre;IFT20f/+ mice, and OSX-Cre;IFT2080f/+ mice which were crossed with IFT80f/f, IFT20f/f and IFT2080f/f mice to obtain OSX-Cre;IFT80f/f mice (named as OSX;IFT80f/f), OSX-Cre;IFT20f/f mice (named as OSX;IFT20f/f), and OSX-Cre;IFT2080f/f mice (named as OSX;IFT2080f/f). Five 1-month old and 3-month old mice for each group were chosen for Micro-CT and Histological analysis. OSX-Cre mice were used as experimental controls (named as OSX;IFT+/+). A quantitative analysis of the gross bone morphology and microarchitecture was performed by micro-CT (μ CT35, Scanco Medical) in Mckay Orthopaedic Research Laboratory Micro-CT Imaging core facility of UPenn. Heads from 1-month old or 3-month old mice were scanned, and reconstituted as three-dimensional images. The region of interest (ROI) of the alveolar bone was manually established in the inter-radicular septal bone of the left mandibular first molar (M1). Bone volume/total volume (BV/TV, %), trabecular thickness (Tb.Th, mm), trabecular number (Tb.N. per mm), trabecular separation (Tb.Sp, mm), and bone mineral density (BMD), mineral density and volume of incisor and mandibular first molars were analyzed. Scanning electron microscopy (SEM) used to perform the analyses of dentin pattern. Mouse mandibles samples were sectioned and stained with H&E.

RESULTS: All the mice with conditional deletion of IFT20, IFT80 and IFT2080 showed a reduction in alveolar BV/TV, especially in OSX;IFT80f/f mice. The alveolar BV/TV decreased 83% in OSX;IFT80f/f mice, 64% in OSX;IFT20f/f mice and 81% in OSX;IFT2080f/f mice. Furthermore, conditional deletion of IFT80 and IFT2080 showed shorten molar root, less mineralized incisor enamel. There is no significant difference between IFT20f/f mice and OSX mice. Histological analysis revealed that the cervical loops and odontoblast layers were smaller in OSX;IFT80f/f and OSX;IFT2080f/f mice compared with those in OSX;+/+ mice. While conditional deletion of IFT20 and IFT2080 showed polarity abnormalities in odontoblasts of cervical loop. SEM also indicated the mice with IFT80 and IFT2080 deletion have defects in dentinal tubules and a decrease in tubules numbers.

SUMMARY: Our findings suggest that both IFT20 and IFT80 are essential for jaw development and bone development. IFT80 favors to regulate molar root development, incisor eruption, incisor enamel formation and odontoblast differentiation, while IFT20 likely has a more critical role in the polarity of odontoblasts. The results revealed that IFT proteins are likely new therapeutic targets for tooth and jaw and other tissue regeneration and treatment of various diseases.

RGS12 regulates osteoblast differentiation and bone formation through controlling Gai/calcium channel-calcium oscillation-ERK activity

Ziqing Li¹, Tongjun Liu², Alyssa Gilmore², Néstor Gómez¹, Claire Mitchell¹,
Merry J Oursler³, Shuying Yang^{1,2*}

¹Department of Anatomy and Cell Biology, School of Dental Medicine, University of Pennsylvania, Philadelphia, PA

²Department of Oral Biology, School of Dental Medicine, University of Buffalo, State University of New York, Buffalo, NY

³Department of Medicine, Endocrine Research Unit, Mayo Clinic, Rochester, MN

#Equal contribution of authors

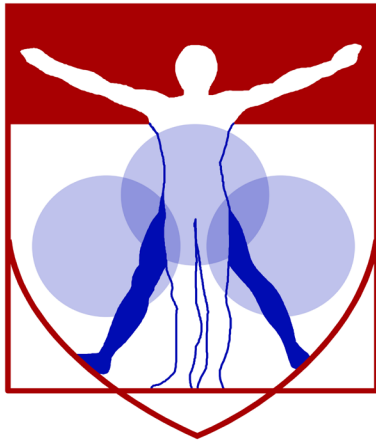
*Corresponding author: Dr. Shuying Yang, shuyingy@upenn.edu

Background: Bone homeostasis is intimately relied on the balance between osteoblasts (OBs) and osteoclasts (OCs). Pathological conditions such as osteoporosis, inflammation, and cancer break this balance through the disruption of communication and coupling between these two kinds of bone cells. Our previous studies have revealed that regulator of G protein signaling (RGS) protein 12 (RGS12), the largest, multi-domain and multi-functional protein in the RGS super family, is essential for osteoclastogenesis from both hematopoietic cells and OC precursors. However, the role of RGS12 in OB differentiation and function is poorly understood.

Methods and materials: To determine the role of RGS12 in osteoblast differentiation and function, we generated an OB-targeted RGS12 conditional knockout mice model by crossing RGS12^{ff} mice with Osterix-Cre transgenic mice. Bone architecture changes of 4 weeks and 12 weeks old mice were evaluated via micro CT, histology and histomorphometric analyses. For in vitro study, primary osteoblast precursors (POB) from RGS12^{ff} mice were transfected with CRE (ad-RGD-Cre) adenovirus, led to a deletion of RGS12 in the RGS12^{ff} POB. Molecular events were examined using qPCR, western blot, immunofluorescence and histochemical staining for OB differentiation markers, and live cell imaging for calcium (Ca²⁺) oscillation, extracellular Ca²⁺ influx and release of Ca²⁺ from endoplasmic reticulum (ER).

Results: Western blot and qPCR results showed that RGS12 was highly expressed in both pre-OBs and OBs, and that the expression of RGS12 gradually increased during OB differentiation. Furthermore, we found that conditional RGS12-KO mice exhibited a dramatic decrease in bone mass, evidenced by reduced bone formation rate, trabecular bone volume (BV/TV, 60%), trabecular number (Tb.N, 66%) and trabecular thickness (Tb.Th, 25%). Loss of RGS12 in POB significantly inhibited OB differentiation and the expression of OB marker genes including osteocalcin (OCN), alkaline phosphatase (ALP), Runx2 and collagen type I, resulted in suppression of OB mineralization. Ca²⁺ oscillations, along extracellular Ca²⁺ influx were impaired after deletion of RGS12 in POB. Further, Bay K8644 triggered L-type Ca²⁺ channel amplified influx and thapsigargin triggered Ca²⁺ releases from ER were also blocked in RGS12 deficient POB compared to the control cells. Basal expression of phosphorylated ERK was relatively lower in RGS12 deficient POB. The introduction of pertussis toxin (PTX), an inhibitor of G α i protein, or RGS12 overexpression partially rescued the defective OB differentiation and function via elevated expression of phosphorylated ERK in RGS12 deficient POB.

Conclusion: our findings suggest that (i) RGS12 is an important regulator in OB differentiation and function, and (ii) identify RGS12 as a potential therapeutic target for osteoporosis.



PENN

CENTER for

MUSCULOSKELETAL

DISORDERS

Miscellaneous Abstracts

Heparan Sulfate restricts BMP signaling and BMPR dynamics and interactions, mechanisms possibly altered in Hereditary Multiple Exostoses

Christina Mundy¹, Paul C. Billings¹, Hajime Takano² and Maurizio Pacifici¹

¹Division of Orthopaedic Surgery, The Children's Hospital of Philadelphia, Philadelphia, PA

²Department of Neurology, The Children's Hospital of Philadelphia, Philadelphia, PA

The bone morphogenetic protein (BMP) signaling pathway has critical roles in many processes including skeletal development and growth, and its perturbations can lead to diverse pathologies. A case in point is Hereditary Multiple Exostoses (HME), a pediatric musculoskeletal disorder caused by loss-of-function mutations in the heparan sulfate (HS)-synthesizing enzymes EXT1 and EXT2. HME is characterized by benign cartilaginous tumors (exostoses) that form next to the growth plates of various skeletal elements, causing multiple health problems. The HS chains, and the proteoglycans of which they are part, regulate signaling by key HS-binding proteins including hedgehogs and FGFs, but their roles in BMP signaling remain unclear. Previously we showed that interference with HS function by genetic or pharmacological means rapidly increases canonical BMP signaling, suggesting that HS normally limits BMP signaling by restricting ligand availability, BMP receptor (BMPR) dynamics and/or BMPR-ligand interactions. To analyze such possibilities, we transfected cell lines with constructs encoding Snap-BMPRII and/or Snap-BMPRIa fusion proteins. Co-transfected cells rapidly responded to BMP-2 treatment with major increases in pSMAD1/5/8 and interestingly, the same was seen after treatment with HS antagonist Surfen. To assess BMPR dynamics, we carried out fluorescence recovery after photobleaching assays and found that receptor mobility decreased significantly after treatment with BMP-2 or Surfen, suggesting that the receptors had transitioned to lipid rafts and/or had undergone oligomerization. To demonstrate that BMPRII population transitioned to lipid rafts, we carried out sucrose gradient ultracentrifugation to separate lipid raft and non-lipid raft cell surface domains. Indeed, treatment with Surfen recruited an abundant amount of BMPRII to the lipid raft domains compared to control-treated cells. Lastly, to show that BMPRIa and BMPRII undergo oligomerization during treatment with Surfen or heparitinase, we performed in situ proximity ligation assays. As indicated by increased number of cell surface fluorescent sites, treatment with Surfen or heparitinase did promote receptor-receptor interactions compared to the control-treated cells. Together, the data indicate that cell surface HS chains are important regulators of both BMP signaling and BMPR dynamics. The HS deficiency in HME may alter these important basic physiologic mechanisms, causing increases in local BMP signaling and promoting formation of exostoses.

Effect of Pro- and Anti-Angiogenic Factors on Vascular Response in the Rat Achilles Tendon after Injury

Corinne N. Riggan¹, Susan M. Schultz², Chandra M. Sehgal², Louis J. Soslowsky¹

¹McKay Orthopaedic Research Laboratory, University of Pennsylvania, PA, ²Department of Radiology, University of Pennsylvania, PA

Disclosures: Corinne N. Riggan (N), Susan M. Schultz (N), Chandra M. Sehgal (N), Louis J. Soslowsky (N)

Introduction: Tendons are hypovascular tissues that become hypervascular after injury. While vascular ingrowth is necessary for tendon healing, hypervascularization following tendon injury is not always believed to be beneficial [1], as degenerated tendons are also highly vascularized, and injured tendons do not regain their native properties [2]. Modulating the vascular response during healing could ultimately improve tendon healing. However, a method for vascular modulation, as well as the optimal vascular response during tendon healing, is unknown. Therefore, the objective of this study was to evaluate the effect of delivery of both pro- and anti-angiogenic factors on the rat Achilles tendon vascular response after injury using in vivo ultrasound imaging and ex vivo histological measures. We hypothesized that vessel properties such as vessel density, vessel size, and blood flow velocity will be increased due to the pro-angiogenic factor and decreased due to the anti-angiogenic factor.

Methods: Study Design: Under IACUC approval, 56 Sprague Dawley rats were used. All animals underwent a bilateral Achilles incisional injury, followed by injections of VEGF, anti-VEGF, or saline on 3 consecutive days. Ultrasound imaging was performed on days 7, 10, and 14 after injury and photoacoustic imaging was done for the anti-VEGF groups on days 7 and 14. Animals were sacrificed at either day 7 or 14 for histological evaluation. **Surgical Protocol:** A 1.5mm scalpel blade created a mid-substance incisional injury in the center of the Achilles tendon width and the tendon was left unrepaired. **Angiogenic Factor Injections:** To evaluate pro-angiogenic factor delivery, 5ug VEGF in 20ul saline (or 20ul saline only as control) was injected bilaterally intratendinously on either days 0-2 (early) or 4-6 (late) after surgery. To evaluate anti-angiogenic factor delivery, 50, 250, or 500ug anti-VEGF antibody (B20.4-1-1, Genentech) in 30ul saline was injected bilaterally intratendinously on days 4-6 after surgery (or 30ul saline as control). **Color Doppler Imaging:** Imaging (n=4-8) was performed using a Vevo 2100 ultrasound system (VisualSonics) with a 40 MHz transducer. Animals were anesthetized and positioned with the transducer parallel to the long axis of the tendon. The mean color level (MCL – average blood flow velocity), the fractional area (FA - % area of Doppler signal), and the color weighted fractional area (CWFA – weighted average of blood flow velocity/unit area) were quantified over the tendon area. Data was compared using a 2-way (treatment, time) ANOVA followed by post hoc t-tests. **Photoacoustic Imaging:** Photoacoustic imaging (n=6-8) was performed with the Vevo LAZR Photoacoustics Imaging System (VisualSonics) using the same transducer and positioning. Images were taken at two wavelengths (750 and 850 nm) based on the absorption spectrum of oxygenated (HbO₂) and deoxygenated hemoglobin (Hb), respectively. Blood oxygenation (sO₂ Avg), total hemoglobin (Hb Total), and relative tissue oxygenation (sO₂ Tot) were determined. Again, data was compared using a 2-way ANOVA followed by t-tests. **Histological Analysis:** After sacrifice, Achilles tendons were dissected and processed. Sections were stained with hematoxylin-eosin (H&E) and graded by 3 blinded, independent graders for cell shape (1 = spindle to 3 = round) and cellularity (1 = less cells to 3 = more cells). Additionally, sections underwent immunohistological staining for CD34, a vascular marker, and graded by 3 blinded, independent graders for vessel density (1 = less dense to 4 = more dense) and vessel size (1 = small diameter to 4 = large diameter). Data was compared using Mann-Whitney t-tests (n=4-8).

Results: VEGF Delivery: There was a significant increase in FA at days 7 and 14 in the late group and a trend towards a decrease at day 14 in the early group compared to saline (Fig1A). There were no changes in MCL (not shown). There was a significant increase in CWFA in the late group at day 7, a trending increase in the late group, and a trending decrease in the early group at day 14 compared to saline (Fig1B). Histology shows a trending increase in vessel density (Fig1C), a significant increase in vessel size (Fig1D), and significantly more rounded cell shape (not shown) in the late group compared to saline. There were no changes in cellularity (not shown). **Anti-VEGF Delivery:** There was a significant decrease in FA on days 7 and 10 in the mid B20 group, and a significant increase in the low B20 group compared to saline (Fig2A). There were no differences in MCL (not shown). There was a trending decrease in CWFA in the mid B20 group at day 7, a significant decrease in the mid B20 group at day 10, and a significant increase in the low B20 group at day 14 compared to saline (Fig2B). There were trending and significant decreases in Hb total in the B20 groups at day 7, and a significant increase at day 14 in the low and mid B20 groups (Fig2C). There were no changes in sO₂ avg (not shown). There was a significant decrease in sO₂ total in the mid and high B20 groups on day 7, and a significant increase in the low and mid B20 groups on day 14 (Fig2D). Finally, there was a significant decrease in vessel density (Fig2E), and a trending decrease in vessel size (Fig2F) in the mid B20 group on day 7, with no change in cell shape or cellularity (not shown).

Discussion: This study demonstrated that tendon vascular response after injury could be increased through the delivery of VEGF and decreased through delivery of anti-VEGF. Importantly, both dosage and timing are important factors in regulating the vascular response. The delivery of VEGF was only effective when delivered 4-6 days after injury, during the time when VEGF expression is naturally at a peak [3]. Additionally, the increase in vascularity seen with the delayed VEGF delivery coincided with a more rounded cell shape, suggesting a more active cellular state. When delivered early, vascular response was not increased, and trended toward a decrease at day 14, suggesting that this delivery may have shifted the VEGF expression time period earlier than normal. For delivery of anti-VEGF, the largest reduction in the vascular response was with the mid dosage. The lower dosage caused a compensation effect, with increased vascular measures at later time points. Histological measures of vascular size and density supported the changes seen with ultrasound.

Significance: This study establishes a model system for vascular modulation in a rat tendon injury model that can be used to evaluate the role of vascularity in tendon injury or degeneration, and potentially determine therapeutics for improved tendon healing.

References: 1) Tempfer et al., 2015, *Front Physiol*, 6:1-7. 2) Hope et al., 2007, *Foot Ankle Clin*, 12:553-67. 3) Boyer et al., 2001, *J Orthop Res*, 19:869-72.

Acknowledgements: Authors thank C Hillin, S Weiss, M Minnig, J Huegel, K Tiedemann, and the Small Animal Imaging Facility. This study was funded by a NIH/NIAMS (P30AR069619) supported Penn Center for Musculoskeletal Disorders Imaging Seed Grant and a NSF Graduate Research Fellowship.

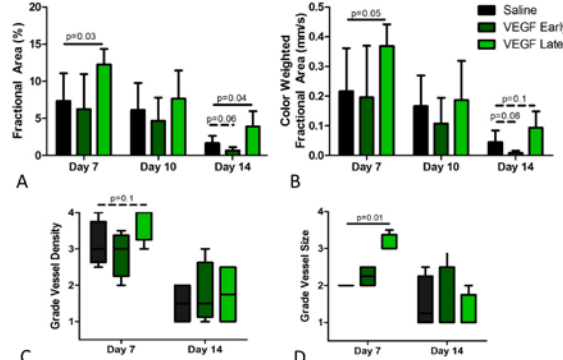


Figure 1: Color Doppler analysis of VEGF delivery showed an increase in (A) FA and (B) CWFA in the late group at days 7 and 14 compared to saline. CD34 staining showed an increase in (C) vessel density and (D) vessel size in the late group at day 7 compared to saline.

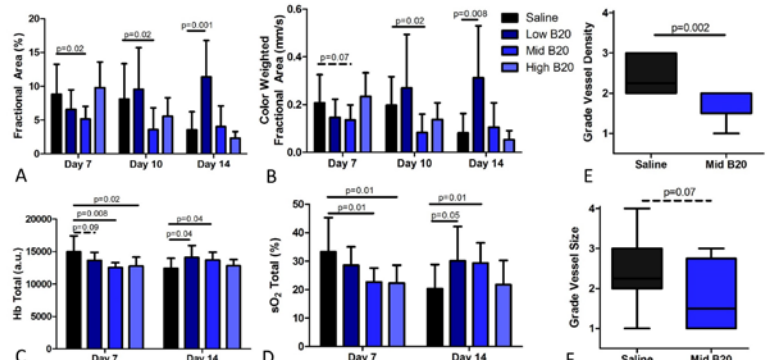


Figure 2: Color Doppler analysis of B20 delivery showed a decrease in (A) FA and (B) CWFA in the mid B20 group compared to saline on days 7 and 10. Photoacoustic analysis shows a decrease in (C) Hb Total and (D) sO₂ Total in the mid and high B20 groups at day 7 compared to saline. CD34 staining on day 7 demonstrated a decrease in (E) vessel density and a trend towards a decrease in (F) vessel size in the mid B20 group compared to saline.

MMP-1 Exposure Increases Neuronal Activity *in Vitro*

Meagan E. Ita¹, Olivia M.E. Leavitt², Beth A. Winkelstein^{1,3}

¹Bioengineering, University of Pennsylvania, Philadelphia, Pennsylvania 19104

²Biomedical Engineering, Worcester Polytechnic Institute, Worcester, Massachusetts 01609

Introduction: Joint degeneration is implicated in pain and osteoarthritis [1]. Pain is believed to be due either to stimulation of nerves by the biomolecules that increase in degenerative states or by loading through altered local tissue biomechanics from enzyme-mediated degradation [2,3]. Collagenases break down collagen in the extracellular matrix (ECM), and are implicated in joint degeneration [3,4]. Purified bacterial collagenase (BC) is an aggressive enzyme that hydrolyzes collagen molecules by attacking the Y-Gly bonds [5]. BC decreases neuron activity but increases the nociceptive neuropeptide substance P in mixed cultures [6]. Yet, BC lacks the non-ECM substrates of physiological collagenases like matrix metalloproteinases (MMPs) [4,7], limiting its utility in studying neuronal responses to collagenases involved in joint degeneration. Interstitial collagenase-1 (MMP-1) is a human enzyme that degrades collagen by cleaving it and has increased gene and protein expression in degenerated joints [3,4,7]. MMP-1 can interact with neural integrins and initiates signaling cascades independent of proteolysis [8]. Although this collection of reports suggests MMP-1 may have a role in painful joint degeneration, it has not been investigated. The goal of this study was to define temporal neuronal activity in response to MMP-1 exposure.

Materials & Methods: Rat embryonic dorsal root ganglia were harvested, dissociated, and plated at 3.0×10^5 cells/mL on glass [9]. At day 1, neurons were transduced with GCaMP6f (#AAV1.Syn.GCaMP6f.WPRE.SV40; 1:6,000) that fluoresces with increases in intracellular calcium [10]. On day 6, separate dishes were treated with MMP-1 ($6 \mu\text{g/mL}$) in DI water ($n=3$) or the same volume of DI water ($n=2$). Each dish was imaged on a Nikon Eclipse TE2000U microscope fitted with a spinning disk confocal and a CCD camera before (BL), immediately (Immediate), 1 hour (1hr), and 24 hours (24hr) after treatment [11]. The same 2 fields of view were imaged for each dish at each time to compare individual neurons over time (Fig. 1A). Images were recorded (20Hz for 1min) and analyzed with FluoroSNNAP [11]. Normalized fluorescence traces were calculated for each neuron to measure the number of calcium events using template-matching (Fig. 1A) [11]. Neurons with no calcium activity at any time point were omitted. A repeated-measures ANOVA compared the number of events over time within groups; a MANOVA with matched pairs detected differences in the number of events across groups.

Results & Discussion: Of the 104 neurons imaged, only 18 neurons in the control group and 32 in the MMP-1 group had calcium activity during at least 1 time point. There was no difference in activity from BL detected in either group immediately after treatment, or in the controls at 1hr (-0.78 ± 1.99 events) and at 24hr (-0.28 ± 2.93 events). Yet, MMP-1 increased activity from BL at both 1hr ($+1.09 \pm 2.02$ events; $p < 0.01$) and 24hr ($+1.41 \pm 1.96$ events; $p < 0.01$); calcium events increased in 14 neurons at 1hr and 19 neurons at 24hr after MMP-1 (Fig. 1B). The change from BL in MMP-1 treated neurons was also significant when compared across groups to the change in neurons at both 1hr and 24hr ($p < 0.01$) in controls. Other studies have shown that MMP-1 promotes neuroplasticity and dendritic complexity in hippocampal neuron cultures but that it can be cytotoxic [12,13]. Our data show that MMP-1 alone increases neuronal activity soon after exposure with sustained effects for at least 1 day in peripheral neurons.

Conclusions: This work implicates MMP-1 as a potential contributor to pain in degenerated innervated tissues. Since MMP-1 contributes to enzyme-mediated degradation it can alter the local microenvironment of joint afferents. Yet, the presence of MMP-1 *alone* may be sufficient to generate pain without any mechanical stress on the tissue.

Acknowledgements: Supported by NIBIB (U01EB016638) and Penn's CEMB NSF STC (CMMI15-48571). The GENIE Program at HHMI Janelia Campus provided the virus; the Meaney lab shared the spinning disk confocal.

Refs: 1 Neogi+ *Osteoarthr Cart* 21:1145-53, 2013 2 Miller+ *Curr Osteoporos Rep* 13:318-26, 2015 3 Kim+ *Osteoarthr Cart* 23:2242-51, 2015 4 Fields *J Biol Chem*. 288:8785-93, 2013 5 Zhang+ *Appl Environ Microbiol* 81:6098-107, 2015 6 Ita+ *SB3C #P123*, 2017 7 Visse+ *Circ Res* 92:827-39, 2013 8 Conant+ *J Biol Chem* 279:8056-62, 2003 9 Cullen+ *Tissue Eng A* 18:2280-9, 2012 10 Chen+ *Nature* 499:295-300, 2013 11 Patel+ *J Neurosci Meth* 243:26-38, 2015 12 Allen+ *Sci Rep* 6:35497, 2016 13 Vos+ *Exp Neurol* 163:324-30, 2000.

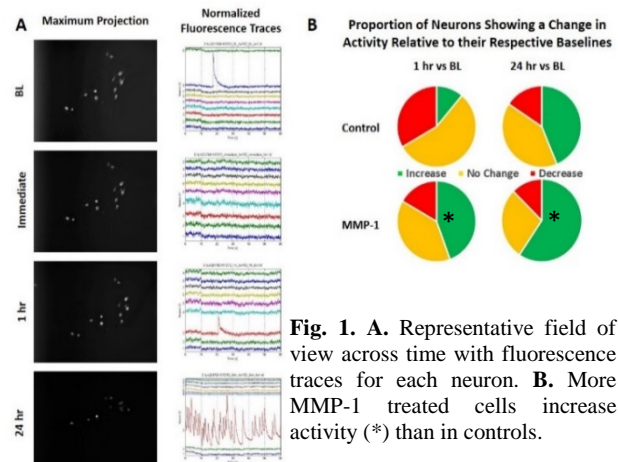


Fig. 1. A. Representative field of view across time with fluorescence traces for each neuron. **B.** More MMP-1 treated cells increase activity (*) than in controls.

Aberrant muscle tissue repair by mutant ACVR1/ALK2 FOP progenitor cells

Alexandra Stanley,^{1,3} Elisia Tichy,¹ Julia Haupt,^{1,3} Foteini Mourkioti,¹ and Eileen M. Shore^{1,2,3}

Departments of ¹Orthopaedics and ²Genetics, and the ³Center for Research in FOP and Related Disorders, Perelman School of Medicine, University of Pennsylvania

In the rare genetic disease fibrodysplasia ossificans progressiva (FOP), progenitor cells are mis-regulated to differentiate to heterotopic extra-skeletal bone in connective tissues. Mutations in the BMP type I receptor ACVR1/ALK2 cause FOP, with the R206H mutation as the most prevalent. Our lab previously identified the *ACVR1^{R206H}* mutation within the GS domain. This increases both BMP ligand-dependent and ligand-independent signaling to promote increased downstream chondro-/osteogenic gene expression and heterotopic ossification (HO) formation in FOP patients. HO formation is often initiated by injury to skeletal muscle. We have established that our *Acvr1^{R206H}* mouse model develops HO after cardiotoxin (CTX) injury, a myonecrotic agent commonly used for muscle injury. Our preliminary data show that quadriceps tissue from *Acvr1^{R206H}* mice 14 days after CTX injury is more fibrotic and severely damaged compared to muscle of CTX injured WT animals that is fully restored at 14 days, indicating that muscle repair is impeded by the *Acvr1^{R206H}* mutation. Additionally, *Acvr1^{R206H}* animals develop a substantial amount of HO within the muscle by 14-21 days after CTX injury. The regenerative potential of skeletal muscle is dependent on the function of muscle stem cells (MuSCs). Additionally, non-myogenic mesenchymal progenitor cells (or fibro/adipogenic progenitors, FAPs; CD4-CD31- α 7-integrin-PDGFR α +Sca1+) are in close association with regenerating muscle fibers and support myogenesis; these cells, considered mesenchymal progenitors based on their ability to differentiate to adipocytes and osteoblasts, are a source of pro-myogenic signals that support muscle regeneration. The efficiency of MuSCs to orchestrate regeneration of damaged muscle tissue is decreased by a stiffer tissue environment. I **hypothesize** that a stiffer tissue environment within damaged *Acvr1^{R206H}* tissue impairs the ability of MuSCs to regenerate muscle tissue, allowing expansion of other populations, such as FAPs within the muscle that are more prone to chondro-/osteogenic differentiation in the injured area. Using atomic force microscopy, I showed that *Acvr1^{R206H}* muscle tissue is stiffer than WT muscle tissue after injury. I examined the effect of the *Acvr1^{R206H}* mutation on MuSCs and FAPs alone by isolating the two populations using fluorescent activated cell sorting and analyzing proliferation based on BrdU incorporation. There appeared to be no significant differences between proliferation of MuSCs or FAPs from WT and FOP injured muscle tissue at day 3, day 5, and day 7 post-CTX injury in 2 month-old mice. I next investigated the ability of WT and FOP MuSCs to differentiate *in vitro*. I cultured WT and FOP MuSCs in myogenic fusion media and found that WT MuSCs differentiate normally and form branching myofibers (high fusion index) by day 7 of culture, but FOP MuSCs form underdeveloped fibers that fail to fuse (low fusion index). These data indicate that the *Acvr1^{R206H}* mutation does not affect MuSC proliferation, but has a negative impact on the ability of MuSCs to undergo myogenesis during muscle tissue regeneration. WT and FOP FAPs were equally able to undergo osteogenesis when given induction media. I examined the effect on myogenic differentiation *in vitro* of co-culturing WT/FOP MuSCs/FAPs. WT FAPs cultured with FOP MuSCs leads to proper myofibers formation and fusion, while FOP FAPs cultured with WT MuSCs form undeveloped fibers with a low fusion index. This suggests that the FAP population under the influence of the *Acvr1^{R206H}* mutation contributes largely to the poor muscle regeneration seen in FOP lesions. Future experiments will determine if FAPs with the FOP mutation contribute to the formation of heterotopic bone *in vivo*.

GMSC-derived Exosomes Promote Nerve Regeneration by Regulating Schwann Cell Dedifferentiation via c-JUN/Sox2 axis

Qin Mao^{1,2}, Pasha Shakoori³, Shihong Shi¹, Qunzhou Zhang¹, Neeraj Panchal^{1,3}, Anh D. Le^{1,3}

¹Department of Oral and Maxillofacial Surgery and Pharmacology, University of Pennsylvania School of Dental Medicine, Philadelphia, Pennsylvania; ²Department of Orthodontics, The Third Affiliated Hospital of Sun Yat-sen University, Guangzhou, China. ³Department of Oral & Maxillofacial Surgery, Penn Medicine Hospital of the University of Pennsylvania, Philadelphia, Pennsylvania

Objectives: Fully functional recovery following peripheral nerve injury represents one of the major challenges in clinic. Currently, autologous nerve grafts remain the “gold standard”, however, the morbidity and limited supply of donor nerves have significantly impeded their clinical application. Growing evidence has shown that mesenchymal stem cell (MSC)-derived exosomes confer therapeutic effects in various animal models of tissue injury and inflammatory diseases. In this study, we investigated whether exosomes secreted by human gingiva-derive MSCs (hGMSCs) could promote peripheral nerve regeneration and the potential mechanisms.

Experimental Methods: *In vivo*, hGMSC-derived exosomes (40µg/mice) were applied to the crush-injured site of mice sciatic nerves. Four weeks post-surgery, the sciatic nerve functional index (SFI), morphology, and histology of sciatic nerves were evaluated. *In vitro*, rat Schwann cells were co-cultured with hGMSCs or simulated with hGMSC-derived exosomes, and the expression of several key regulatory genes involved in Schwann cell dedifferentiation and myelination was determined by Western blot analysis.

Results: Improved clinical outcomes such as the sciatic nerve function index (SFI) were noted in experimental groups treated with GMSC-derived exosomes or transplantation of GMSCs as compared with the crush-injured control group, whereas the beneficial effect mediated by exosomes was more pronounced than that conferred by hGMSCs *per se*. Histologically, local application of GMSC-derived exosomes showed better effects on axonal regeneration and remyelination of injured nerves than hGMSCs. *In vitro*, stimulation of Schwann cells with hGMSC-derived exosomes robustly increased the expression of c-JUN, SOX₂ and SOX₁₀, three important positive regulators of Schwann cell dedifferentiation, but had no obvious effects on the expression of EGR2/Krox20, a major transcription factor that drives remyelination.

Conclusion: Taken together, our findings suggest that exosomes secreted by hGMSCs promote peripheral nerve repair/regeneration possibly by increasing the expression of c-JUN, SOX₁₀ and SOX₂, thus skewing dedifferentiation of Schwann cells toward a reparative phenotype.

Key words: Peripheral nerve regeneration, Gingiva-derived MSCs, exosomes, Schwann cells, c-Jun, SOX₁₀, SOX₂, EGR2/Krox20, dedifferentiation

This work was supported by OsteoScience Foundation Peter Geistlich Award and Resident Research Award and the Schoenleber Funding support.

Biocompatibility and Bioactivity of an FGF-Loaded Microsphere-Based Bilayer Delivery System

Dong Hwa Kim^{1,2}, Julianne Huegel^{1,2}, Courtney Nuss^{1,2}, Stephanie Weiss^{1,2}, Louis J. Soslowsky^{1,2}, Robert L. Mauck^{1,2}, and Andrew F. Kuntz^{1,2*}

¹University of Pennsylvania, Philadelphia, PA, ²Philadelphia VA Medical Center, Philadelphia, PA

Disclosures: DH Kim (N), J Huegel (N), C Nuss (N), S Weiss (N), LJ Soslowsky (N), RL Mauck (N), AF Kuntz (N)

INTRODUCTION: Biodegradable micro-particle systems have attracted increasing interest for use as delivery vehicles for drugs, proteins, and other factors [1-2]. Several new strategies have been developed to improve protein stability within such biodegradable polymer matrices [3]. For instance, sustained release of basic fibroblast growth factor (bFGF) from microspheres can promote proliferation and differentiation processes in a wide range of cells [4]. Albumin is commonly included in such formulations, both as a model protein to monitor release and as a carrier to preserve growth factor activity and prolong shelf-time [5]. In this study, we developed microspheres (MS) containing both Alexa-tagged BSA and bFGF and incorporated them into a Bilayer Delivery System (BiLDS) [6]. This system was designed to sequester MS in a defined pocket between two nanofibrous scaffolds, where the scaffold provides a template for new tissue formation while enabling independent and local release from the co-delivered MS. The objective of this study was to evaluate the biocompatibility and bioactivity of an FGF-loaded BiLDS system in vitro and in vivo.

METHODS: *Microsphere and BiLDS fabrication:* Microspheres were produced by combining 75:25 PLGA (0.15 g/mL, Mw=70 kDa) with/without 200 µg recombinant human bFGF and Alexa-BSA in dichloromethane. The external phase of the emulsion consisted of 5 mL of aqueous 1% poly(vinyl alcohol). To generate the bilayered delivery system (BiLDS), each MS formulation (Alexa-BSA MS and Alexa-BSA/bFGF MS) was suspended in 50 µl of PBS and placed onto the center of an aligned poly(ε-caprolactone) nanofibrous scaffold (6×8 mm) [6]. A second layer was placed on top and the two layers were sealed together by heat-annealing in a circular pattern around the microspheres using a custom heating device. ***Direct/indirect tenocyte culture:*** For direct culture, rat tenocytes (5000 cells/BiLDS) were seeded onto the BiLDS and cultured for 18 days in 1% FBS containing DMEM. For indirect culture, each BiLDS was incubated in basal media for 1 week at 37°C. Tenocytes were seeded (3×10^3 cells/well) into a 24-well plate and the conditioned media from each BiLDS was added. At regular intervals, cell viability (via MTT assay, n=4-5) and MS and cell morphology (via actin staining and SEM, n=3) was evaluated. ***BiLDS release in-vivo:*** BiLDS containing no MS, Alexa-BSA-MS, and Alexa-BSA/bFGF-MS (n=4/group) were fabricated and implanted into the rat's dorsal subcutaneous space. At 1, 2, and 4 weeks, samples were recovered and fluorescence images were taken to identify MS within the BiLDS and frozen sections were processed for hematoxylin and eosin (H&E) staining. Statistical analysis was performed by 2-way ANOVA with Tukey's post-hoc test.

RESULTS: SEM images demonstrated that MS were spherical with a smooth surface. Alexa-BSA and Alexa-BSA/bFGF MS ranged in diameter from 1.5-3 µm and 1.5-4.5 µm, respectively (not shown) (Fig. 1A, B). SEM images also showed a seal along the margin that effectively localized MS within the BiLDS (Fig. 1C) and cross-sectional views of the BiLDS showed large quantities of MS within the BiLDS (Fig. 1D). In direct culture, cell viability and proliferation of Alexa-BSA and Alexa-BSA/bFGF BiLDS increased during culture and were significantly higher than control at day 18 (Fig. 2A). Cells attached and spread along the BiLDS (Fig. 2B). SEM images confirmed this finding, and cross-sectional views showed that MS remained entrapped after 18 days (Fig. 2C). In indirect culture, after 4 and 7 days, proliferation in media from Alexa-BSA/bFGF BiLDS was higher than from no MS and Alexa-BSA BiLDS (Fig. 2D, E). After implantation, fluorescent images showed that MS remained within the BiLDS (Fig. 3A) and H&E staining revealed increased cellularity at the periphery with greater infiltration into nanofiber layers of the Alexa-BSA/bFGF BiLDS (Fig. 3B).

DISCUSSION: In this study, we developed a bilayered delivery system to deliver bFGF in a local manner using a clinically relevant and previously validated scaffold system. We previously showed that MS entrapped within the BiLDS system showed a somewhat attenuated release profile compared to free MS, and that protein release was sustained and continuous for up to 30 days [6]. Importantly, our new data show that cell viability and proliferation were enhanced in the context of Alexa-BSA/bFGF BiLDS, both in vitro and in vivo. MS delivered via the BiLDS system persisted in a localized area after implantation for at least 4 weeks, and bFGF release increased colonization of the implant. These data establish the BiLDS technology as a sustained in vivo drug delivery platform that can localize protein and other growth factor release to a surgical site. In future studies, we will explore the ability of this BiLDS technology to deliver growth factors to promote repair in a small animal model of rotator cuff injury.

SIGNIFICANCE: This work establishes the biocompatibility and bioactivity of a MS-loaded bilayered delivery system (BiLDS) for sustained release in a localized and clinically relevant fashion for tissue repair and regeneration.

REFERENCES: [1] Rafati+, 2012 J Control Release. [2] Ambrosch+, 2012 Acta Biomater. [3] Emma+, 2007 Biomaterials. [4] Rouch+, 2016 J Pediatr Surg. [5] Kratz+, 2008 J Control Release. [6] Kim+, 2017 ORS Proceedings.

ACKNOWLEDGEMENTS: This work was supported by the Department of Veterans' Affairs (O0979-R and RX001764) and the Penn Center for Musculoskeletal Disorders (P30 AR069619).

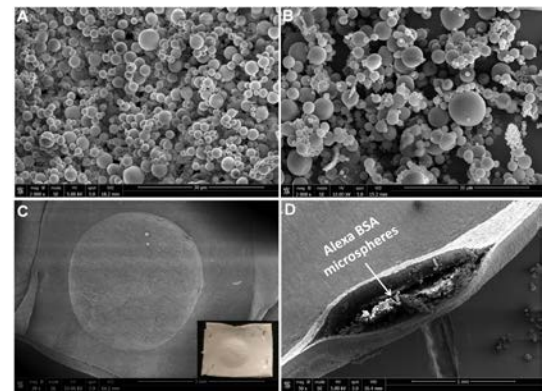


Figure 1. SEM of (A) Alexa-BSA and (B) Alexa-BSA/bFGF MS. (C) Top view and (D) cross-section showing MS within BiLDS (scale = 1mm).

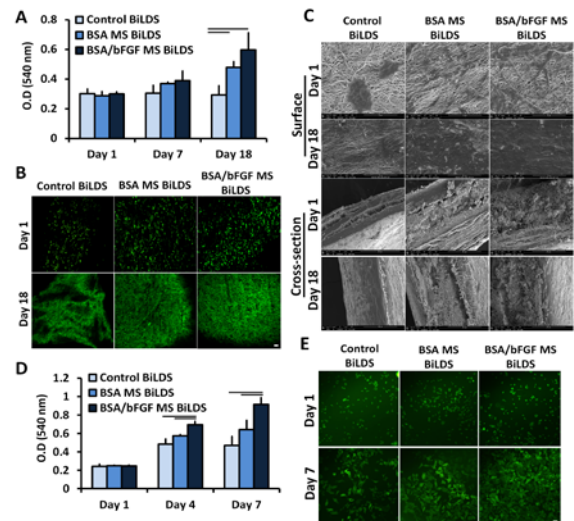


Figure 2. (A) Viability, (B) actin staining, and (C) SEM over 18 days with direct culture of tenocytes on BiLDS. (D) Viability and (E) actin staining over 7 days with indirect culture of tenocytes in media from BiLDS (Scale = 10 µm).

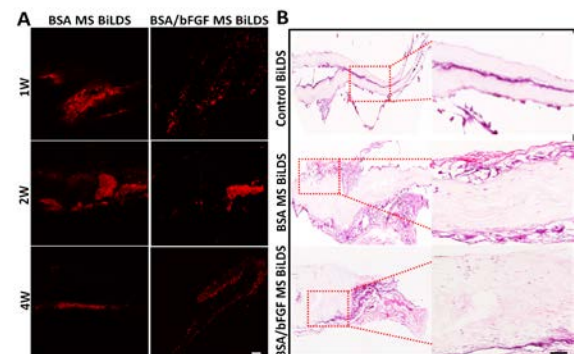


Figure 3. (A) Fluorescent images of Alexa tagged MS in BiLDS after implantation. (B) H&E staining after 4 weeks in vivo (scale = 200 µm).

Improved ELISpot Controls to Optimize the Predictive Power of a Novel Canine Disease Model in Gene Therapy for DMD

Leon Morales, Jake VanBelzen, Alock Malik, Yafeng Song, Christopher Greer, Samantha Globerman, Shira Rosenblum, Joe Kornegay*, Hansell H. Stedman

A specific iteration of a general problem in gene therapy is the potential for immune recognition of recombinant dystrophin in patients with Duchenne Muscular Dystrophy (DMD), as most cases are caused by multi-exon frame shifting deletions within the dystrophin gene. In contrast, the genetic basis of a widely used large animal model, Golden Retriever Muscular Dystrophy (GRMD), is a single base intron splice mutation that leaves the entire dystrophin coding sequence intact. Muscle from GRMD dogs has been found to express readily detectable amounts of near-full-length dystrophin on the basis of alternative exon splicing. This complicates the interpretation of preclinical studies in this model, as pre-existing tolerance to dystrophin may facilitate long term persistence of transgene products without the risk of autoimmune myositis. Early developmental expression of the dystrophin paralog utrophin in the thymus may confer central immunological tolerance against the peptide sequence. Here we address the immunogenicity of a synthetic version of utrophin (μ Utrophin) in which the rod domain has been internally deleted with an emphasis on preserving inter-repeat folding while minimizing neo-epitopes that can trigger T-cell responses. Neonatal GRMD dogs were given an intravenous injection of $10^{13.5}$ vg/kg AAV9- μ Utrophin without immunosuppression. Peripheral blood mononuclear cells (PBMCs) were collected at 5 and 8 weeks post injection. An interferon gamma ELISpot assay using utrophin-derived peptide pools revealed the absence of T-cell mediated reactivity, consistent with central immunological tolerance. Our initial positive control for this experiment was injection with Adenovirus-CMV-lacZ, which showed a positive response to lacZ peptide pools. To broaden our study of cell mediated immunity in the dog, we generated a second positive control by synthesizing a mini peptide pool composed of sequences derived from capsid proteins for canine distemper virus and parvovirus. To our surprise, PBMCs isolated from pre-vaccinated, asymptomatic 6 week-old wild type dogs resulted in strongly positive gamma-interferon responses to these control antigens, while still negative when tested against utrophin-derived peptides. Further studies are underway to track the potential expansion in reactive T cells post-vaccination in these dogs. These reagents will serve as standard positive controls in future pre-clinical gene transfer studies that explore immunological responses following expression of recombinant test proteins in canine disease models. We outline a rigorous translational approach using the recently characterized deletional-null GSHPMD canine model (VanBelzen, et al, Mol Ther in press). The GSHPMD model should be devoid of any immunological tolerance against all dystrophin-derived peptide epitopes and can therefore provide the most sensitive prediction of immune responses against recombinant dystrophin and/or utrophin expression.

Genetic inhibition of Notch pathway confers osteoclasts with reduced maturation and function

Goel PN^{1,2}, Hebb JH^{1,2}, Kaur G³, Hankenson KD^{1,4}, Ahn J^{1,2}, Ashley JW⁵

¹University of Pennsylvania, Philadelphia, PA; ²Corporal Michael J. Crescenz VA Medical Center, Philadelphia, PA; ³University of the Sciences, Philadelphia, PA; ⁴University of Michigan, Ann Arbor, MI; ⁵Eastern Washington University, Cheney, WA

Owing to a central role of osteoclasts in bone physiology and remodeling (including interaction with and stimulation of osteoblastic cells), manipulation of the maturation process provides an important potential therapeutic strategy for treating bone diseases. Notch signaling plays a crucial role in osteoclast maturation and function. Our lab has previously demonstrated that stimulating the Notch pathway in committed osteoclast precursors results in large multinuclear cells with increased resorptive activity whereas chemical inhibition of the same caused smaller osteoclasts with impaired resorption. Herein, we investigated osteoclast resorptive and coupling functions in the context of genetically inhibited Notch signaling. Notch activation requires cleavage of its intracellular domain NICD to translocate into the nucleus and interact with co-activators such as Mastermind-like1 (MAML) for transcriptional activation. Wild type (WT) [LysM-Cre/- dnMAML-/-] and dnMAML [LysM-Cre/- dnMAMLMye+/-] mice were utilized in this study. dnMAML mice express a dominant negative form of MAML that inhibits the transcriptional complex. Furthermore, this dnMAML expression is restricted to myeloid lineage cells, which include osteoclasts and their precursors. Using the dnMAML+ osteoclasts we observed that inhibition of Notch signaling results in osteoclast precursors that fail to mature and function without significant alterations in early osteoclastic gene expression. Osteoclasts from the dnMAML group showed defect in maturation process and were smaller in size and fewer in number compared to the wild type. The functionality of dnMAML+ cells upon stimulation with Notch signaling by Jagged-1 showed down-regulation of Hes1 (marker for Notch activation) compared with the wild type which is consistent with suppressed Notch signaling. TRAP activity in the condition media collected at regular intervals from osteoclasts seeded over bone slices showed marked reduction in the enzymatic activity due to lesser bone resorption by dnMAML+ osteoclasts.

In our present work, we have demonstrated that osteoclasts derived from dnMAML mice showed no significant differences in early osteoclastic gene expression compared to wildtype. However, osteoclasts with defective Notch signaling had decreased TRAP production and decreased bone resorption. These observations suggest that inhibition of Notch signaling impairs osteoclast maturation rather than early commitment and gene expression. Thus, the current work provides a mechanistic insight into osteoclast function and important pre-clinical data informing potential use of Notch signaling inhibition in osteoclasts to improve bone mass.

Stem Cell Regulation in Muscular Dystrophy

Elisia D. Tichy, David Sidibe, Yuwei Qi, Zachary Beethem, and Foteini Mourkioti

McKay Orthopaedic Research Laboratory, Perelman School of Medicine, University of Pennsylvania, Philadelphia, PA 19104

Skeletal muscle diseases or myopathies result in loss of muscle mass, degeneration and functional weakness. Duchenne muscular dystrophy (DMD) is the most common recessive chronic muscle disorder that results from lack of dystrophin, a cytoskeletal protein whose loss results in tearing of muscle during contraction. Muscle stem cells (MuSCs) are activated following muscle injury and are required for the repair of muscle tissue. Using MuSCs derived from mouse models of DMD, as well as from human patients, we found that dystrophic MuSCs undergo telomere shortening. Additionally, we found the NF- κ B signaling pathway was dysregulated in these dystrophic MuSCs. Using MuSC-specific mouse models, we queried the function of NF- κ B following induced injury. We have discovered that NF- κ B may play a critical role in the activation of MuSCs following injury. The exploitation of downstream mediators in this pathway may lead to future targeted therapies for the treatment of DMD.

Evolution of titin but not dystrophin correlates with the scalability of locomotive power

Christopher Greer¹, Andy Mead¹, Hansell H. Stedman^{1,2}

¹*Perelman School of Medicine & Pennsylvania Muscle Institute, University of Pennsylvania, Philadelphia, Pennsylvania, USA*

²*Corporal Michael J. Crescenz VA Medical Center, Philadelphia, Pennsylvania, USA*

Rapid locomotion in animals and unicellular eukaryotes is almost invariably powered by the motor proteins myosin and dynein, respectively. However, the earliest branching animal lineages retain dynein as the dominant locomotive power source^{1 2 3 4 5}. The evolutionary transition from dynein to myosin can be explained on the basis of geometric constraints imposed by their scaffolding organelles, cilia and sarcomeres, with critical implications for scalability. The emergence of sarcomeres in early metazoan evolution allows a detailed reconstruction of the molecular correlates of this pivotal transition based on genomes of extant species. Here we show that sarcomeres are only found in lineages with >100-fold tandem multiplications of an ancestrally solitary IgG-like domain in proteins orthologous to the chordate titins, while orthologs for the entire membrane spanning dystrophin protein complex can be inferred to predate this transition. We identify invertebrate lineages that retain the inferred ancestral titin supergene structure, providing a unified view of gene rearrangements that have complicated the delineation of gene orthology and the common origin of sarcomeres in animals with radial and bilateral symmetry. Surprisingly, the entire rod domain of dystrophin appears to have been coopted from a much larger ancestral spectropodin, a finding with significant implications for the mechanobiology of dystrophin and the design of recombinant proteins for therapeutic use in muscular dystrophy (2). Our reconstruction suggests that geometric constraints on cell morphology and body plan required a strong yet deformable connection between cytoskeleton and extracellular matrix before myosin could be safely arrayed, by titin, into sarcomeres at the density required to power scale-independent locomotion.

Comparison of equine synovial-derived mesenchymal stem cells (MSC) to bone-marrow derived MSCs for chondrogenesis

Mammone RM, Gale AL, Linardi RL, Ortved KF

University of Pennsylvania, New Bolton Center

Department of Clinical Studies

Reason for Performing the Study and Objective/Hypothesis

Traumatic injury to articular cartilage occurs commonly in the equine athlete and, due to the poor intrinsic healing capabilities of cartilage, can lead to osteoarthritis (OA) if left untreated. Mesenchymal stem cells (MSCs) have the potential to become an ideal source for cell-based treatment of cartilage lesions, before OA develops, as they are accessible and multipotent. The vast majority of cartilage repair efforts have been done using bone marrow-derived MSCs (BM-MSCs); however, full chondrogenic differentiation remains elusive. Synovium-derived MSCs (SD-MSCs) likely have superior chondrogenic abilities as synovium and cartilage share a common progenitor cell. Additionally, SD-MSCs can be easily harvested using minimally invasive techniques. The broad objective of this proposal was to compare the immunophenotype, proliferative capacity, and chondrogenic differentiation of BM-MSCs and SD-MSCs in order to optimize a cell source for treatment of cartilage lesions. We hypothesize that SD-MSCs will have a similar immunophenotype to BM-MSCs. However, SD-MSCs will also have superior proliferation and chondrogenesis *in vitro* compared to BM-MSCs.

Methods

Bone marrow collection and MSC isolation

Bone marrow was collected from the sternabrae of 6 healthy horses between 2-6 years of age under standing sedation and local anesthesia. Mesenchymal stem cells were cultured on T-175 plastic flasks in Dulbecco's Modified Eagle's Medium (DMEM), fetal calf serum (FCS) (10%), glucose (1%), 2mM L-glutamine, 1mM sodium pyruvate, 100U/ml penicillin/streptomycin, and 1ng/ml bFGF until 80% confluent and then passaged. Passage 2 cells were then collected with Accutase cell detachment solution (Innovative Cell Technologies, San Diego, CA) and re-suspended in phosphate buffered saline (PBS) prior to staining and flow cytometry analysis.

Synovium collection and MSC isolation

Synovial membrane was collected from 6 healthy horses between 2-6 years of age euthanized for reasons unrelated to musculoskeletal disease. Synovial membrane samples were collected from the dorsal middle and radiocarpal joints. Synovial membrane was washed with PBS, debrided with a sterile syringe plunger, and incubated at 37°C in 200µL FCS for 20 minutes. Samples were then re-suspended in DMEM, fetal calf serum (10%), glucose (4.5%), 2mM L-glutamine, 1mM sodium pyruvate, and 100U/ml penicillin/streptomycin until 80% confluent. Passage 2 cells were collected with Accutase and re-suspended in PBS prior to staining and flow cytometry analysis.

Cell surface marker analysis

Flow cytometric analysis using specific markers for "stemness" was performed in order to evaluate the immunophenotype of the different cell populations. Cells were stained with anti-CD29, CD44, CD90, CD105, CD45, CD-79 α , MHC I and MHC II antibodies prior to flow cytometry.

Chondrogenesis assay

Passage 2 SD-MSCs and BM-MSCs were pelleted in 96 well plates and cultured in chondrogenic induction medium for 21 days. Pellets were collected for histology, biochemistry, and gene expression analysis. Pellets for histology were fixed, sectioned and stained with toluidine blue to evaluate ECM synthesis. A DMMB assay will also be used to quantify glycosaminoglycan (GAG) content. RNA will be isolated using the Qiagen RNeasy kit and qRT-PCR will be performed to determine mRNA expression of cartilage specific genes including collagen type II, aggrecan, and SOX-9.

Results & Discussion

The immunophenotypes of BM-MSCs and SD-MSCs were similar with both cell types having positive expression of stem cell markers (CD29, CD44, CD90, CD105, and MHC I) and negative for exclusion markers (CD45, CD CD79 α , and MHC II) (**Fig 1**). At 24 and 48 hours, SD-MSCs and BM-MSCs had similar proliferation rates. SD-MSCs had a slightly increased proliferation rate at 72 hours. Passage 1 and 2 SD-MSCs had significantly increased proliferation at 96 hours compared to BM-MSCs (**Fig 2**). Chondrogenic differentiation, as evidenced by GAG content pellets, was superior in SD-MSCs compared to BM-MSCs.

Study Limitations and Scientific Relevance

Although MSCs were proposed as an ideal candidate for cartilage repair, adequate chondrogenesis has been challenging. We have demonstrated that SD-MSCs have a similar immunophenotype to BM-MSCs and that they can be culture expanded in the laboratory at an acceptable rate of proliferation. We also have preliminary histological evidence that SD-MSCs have superior chondrogenic differentiation capabilities compared to BM-MSCs. Synovial membrane is an easily accessible source of MSCs and could present a superior source of MSCs for joint disease.

Interactions of Bone Morphogenetic Proteins with Heparan Sulfate in Hereditary Multiple Exostoses Pathogenesis.

Evan Yang, Christina Mundy, Fouad Moussa, Maurizio Pacifici, Paul Billings

Abstract

Hereditary Multiple Exostoses (HME) is a pediatric bone disorder characterized by formation of osteochondromas/exostoses near the growth plates in multiple skeletal elements, including long bones. The majority of HME patients have mutations in *EXT1/2* which are Golgi-resident glycotransferases involved in heparan sulfate (HS) biosynthesis, resulting in HS deficiency. HS chains are constituents of cell surface and matrix-associated syndecans, glypicans and other heparan sulfate proteoglycans (HSPGs). A primary function of HSPGs is to sequester a wide variety of signaling proteins, including BMPs, and thus play an important role in cell signaling. We hypothesize that reductions in HS levels in HME patients leads to aberrant BMP signaling and exostoses formation. In this study we examined the interactions between BMPs and HS. In line with previous studies, we found that BMP2 and 4 contain a HS-binding domain (HBD) near the N-terminus. This domain bound HS with high affinity and interestingly, a recombinant form was sufficient to stimulate chondrogenic differentiation of mouse limb bud cells. Contrary to current literature, we discovered that the HBDs in BMP 5, 6 and 7 actually resides on the C-terminus and also stimulated chondrogenesis. Thus, our results suggest that the position of the HBDs residing in different BMPs may influence their distribution, activity and function. The stimulation of chondrogenesis by HBDs on their own indicates that the domains may modulate HS-growth factor interactions within the matrix and influence local cellular responses.

Myeloid specific deletion of IFT80 accelerates osteoclast differentiation, decreases bone mass and causes growth retardation in mice

Vishwa Deepak, Shuying Yang*

Department of Anatomy and Cell Biology, School of Dental Medicine, University of Pennsylvania, Philadelphia, PA, USA; email: shuyingy@upenn.edu

Primary cilia are nonmotile microtubule-based appendages protruding from the cell surface into the extracellular environment and can regulate cellular differentiation, proliferation, mechanotransduction and vertebrate development. Cilia assembly requires intraflagellar transport proteins (IFT) which are involved in import and export of ciliary proteins and are required for ciliary maintenance and sensing. Defects in the structure or function of the primary cilia are associated with various human diseases known as ciliopathies such as polycystic kidney disease (PKD), Bardet-Biedl syndrome, Jeune syndrome and Joubert syndrome causing defects in combinations of pathological changes in the kidney, retina, and skeleton. Our previous studies have shown that osteoblast-specific deletion of IFT80 leads to impaired osteoblast differentiation, reduced bone mass and growth defects in mice. However, the role of IFT80 protein in osteoclast formation and activity remains elusive.

By performing real-time PCR, we found a time-dependent increase and decrease of IFT80 gene transcription during osteoclast differentiation, indicating IFT80 might play a crucial role in osteoclastogenesis. Hence, we generated osteoclast precursor (monocyte)-specific IFT80 knockout mice by mating IFT80^{flox/flox} mice with those expressing Lysozyme M-Cre. Micro-CT and histological analysis results showed that IFT80^{flox/flox}, Lysm-cre mice displayed an osteopenic cancellous phenotype along with reduced body size and weight in comparison to wild-type control. Further *in vitro* primary culture studies showed that IFT80-deleted osteoclast precursors formed higher number of TRAP+ multinucleated osteoclasts than the IFT80^{flox/flox} control group ($p < 0.05$). Deletion of IFT80 enhanced the extracellular acidification by osteoclasts and osteoclast-mediated bone resorption ($p < 0.05$). Together these data show that IFT80 in osteoclast precursors is an important regulator of osteoclast formation and activity, bone homeostasis and growth.

Knee morphometric and alignment measurements with MR imaging in young adults with central cartilage lesions of the patella and trochlea

Sara Weintraub BA; Ronnie Sebro MD, PhD

Introduction: Osteoarthritis is a debilitating chronic musculoskeletal disorder associated with high health care costs, disability, and pain. The patellofemoral joint (PFJ) is an articulation between the patella and the femoral trochlea and is often affected by osteoarthritis, possibly related to the complex alignment and movement of the patella [1-5]. Identification of risk factors for patellofemoral osteoarthritis (PFO) is crucial, as lifestyle modification may prevent disease progression. Therefore, it is important to understand how the morphology of the patella and trochlea, and patellar alignment may contribute to the development of PFO. There are several studies evaluating the association between PFO and patellar alignment and trochlear and patellar morphology [6-10], but to our knowledge no studies have explicitly evaluated whether the patella and trochlear morphology and patellar alignment are associated with central cartilage lesions of the PFJ/central patellofemoral osteoarthritis (CPFJO). The goal of this study was to assess whether common measurements of patellar and trochlear morphology and patellar alignment are associated with central cartilage lesions of the patella and trochlea using MRI.

Methods: The MRI examinations of 58 patients (38 women, 20 men; mean age, 28.59 years [range: 19–35 years]) with central cartilage lesions of the patella and trochlea were retrospectively compared to those obtained in 102 control subjects (57 women, 45 men; mean age, 27.05 years [range: 20–35 years]). Patients had Modified Noyes Classification grade IIA, IIB, or III cartilage defects whereas control subjects had normal MRI examination of the knee as determined by two radiologists. Patellar measurements of facet asymmetry, patellar tilt, lateral patellofemoral angle, Insall-Salvati ratio, and patellochlear cartilage overlap were performed in patients and control subjects along with trochlear measurements of the trochlear depth and width, and sulcal angle. Multivariate logistic regression adjusted for age and body mass index was used to assess associations.

Results: The ratio of the lengths of the medial to lateral facets of the patella ($OR = 2.7 \times 10^{-3}$; $P < 0.001$), angle of the median eminence of the patella ($OR = 1.05$; $P = 0.040$), lateral patellofemoral angle ($OR = 0.91$; $P = 0.048$), Insall-Salvati ratio ($OR = 364.4$; $P < 0.001$) and edema in the superolateral aspect of Hoffa's fat pad ($OR = 6.52$; $P < 0.001$) were significantly associated with central cartilage lesions of the patella and trochlea.

Conclusion: Central cartilage lesions of the patellofemoral joint are associated with patellar and trochlear morphology, and patellar alignment. Our results may also help orthopedists identify patients who would benefit from trochleoplasties and patellar re-alignment procedures, because these procedures are done to recreate normal anatomy and alignment and to decrease the risk of development of osteoarthritis.

References

1. Arendt, Elizabeth A., et al. "Early osteoarthritis of the patellofemoral joint." *Knee Surgery, Sports Traumatology, Arthroscopy* 24.6 (2016): 1836-1844.
2. Mills, Kathryn, and David J. Hunter. "Patellofemoral joint osteoarthritis: an individualised pathomechanical approach to management." *Best Practice & Research Clinical Rheumatology* 28.1 (2014): 73-91.
3. Maquet, Paul. "Mechanics and osteoarthritis of the patellofemoral joint." *Clinical orthopaedics and related research* 144 (1979): 70-73.
4. Grelsamer, Ronald P., David Dejour, and Jason Gould. "The pathophysiology of patellofemoral arthritis." *Orthopedic Clinics of North America* 39.3 (2008): 269-274.
5. Lankhorst, N. E., et al. "Incidence, prevalence, natural course and prognosis of patellofemoral osteoarthritis; data of cohort hip and cohort knee study." *Osteoarthritis and Cartilage* 23 (2015): A42-A43.
6. Kalichman, L., et al. "The association between patellar alignment and patellofemoral joint osteoarthritis features—an MRI study." *Rheumatology* 46.8 (2007): 1303-1308.
7. Kalichman, Leonid, et al. "The association between patellar alignment on magnetic resonance imaging and radiographic manifestations of knee osteoarthritis." *Arthritis research & therapy* 9.2 (2007): R26.
8. Noehren, Brian, Stephan Duncan, and Christian Lattermann. "Radiographic parameters associated with lateral patella degeneration in young patients." *Knee Surgery, Sports Traumatology, Arthroscopy* 20.12 (2012): 2385-2390.
9. Macri, Erin M., et al. "Is tibiofemoral or patellofemoral alignment or trochlear morphology associated with patellofemoral osteoarthritis? A systematic review." *Arthritis care & research* 68.10 (2016): 1453-1470.
10. Stefanik, Joshua J., et al. "Association between measures of trochlear morphology and structural features of patellofemoral joint osteoarthritis on MRI: the MOST study." *Journal of Orthopaedic Research* 30.1 (2012): 1-8.

Longitudinal Genome-Wide Association Analyses and Heritability Estimates of Pediatric Bone Mineral Density

Diana L. Cousminer, PhD, Alessandra Chesi, PhD, Jonathan A. Mitchell, PhD, Heidi J. Kalkwarf, PhD, Joan M. Lappe, PhD, Vicente Gilsanz, MD, Sharon E. Oberfield, MD, John A. Shepherd, PhD, Andrea Kelly, MD, Shana E. McCormack, MD, Benjamin F. Voight, PhD*, Babette S. Zemel, PhD*, and Struan F. A. Grant, PhD*

*equal contribution

Background: SNP heritability (h^2_{SNP}) assesses the trait variance attributed to genotyped genetic factors. h^2_{SNP} for bone mineral density (BMD) is known to vary across skeletal sites and with age, and assessments of h^2_{SNP} and genome-wide association studies (GWAS) have typically been performed using cross-sectional data in adults. In contrast, systematic longitudinal assessment of h^2_{SNP} in the pediatric context has not yet been conducted. Thus, we sought to determine h^2_{SNP} estimates for BMD and bone mineral content (BMC) across specific clinically important skeletal sites using modeled longitudinal pediatric growth curves. We also performed complementary GWAS in search of novel bone-related loci.

Methods: In the multicenter, multiethnic Bone Mineral Density in Childhood Study (BMDCS) of healthy children aged 5 to 20 years old with up to 7 annual measurements each, BMD and BMC of the spine, total hip, femoral neck, distal radius and total body less head were measured in up to 1,876 boys and girls. We used GCTA-Restricted Maximum Likelihood (GREML) to estimate h^2_{SNP} for Super Imposition by Translation and Rotation (SITAR)-modeled longitudinal growth parameters (*size*, *tempo*, and *velocity*) at each skeletal site, adjusting for population ancestry. Subsequently, sex and ancestry-specific standardized SITAR-modeled growth parameters were subjected to GWAS analyses using GEMMA, which also accounts for population ancestry.

Results: In general, h^2_{SNP} was higher for the *size* parameter than for the *tempo* and *velocity* parameters, and was comparable to previously published cross-sectional estimates. h^2_{SNP} for *size* ranged from 0.52 (SE=0.093, $P=2.0 \times 10^{-8}$) for femoral neck BMD to 0.20 (SE=0.09, $P=0.011$) for radius BMD. GWAS recapitulated the known signal at *CPEDI* for female radius BMD as associated with the radius *size* parameter, but also yielded a number of novel genetic signals associated with *size*, *tempo*, and *velocity* that varied across skeletal sites.

Conclusions: We generated skeletal site-specific longitudinal estimates of h^2_{SNP} for pediatric BMC and BMD that are comparable to previous estimates but expand to more detailed skeletal resolution and capture growth longitudinally. Both h^2_{SNP} and the most prominent GWAS-implicated loci vary across skeletal sites. These results provide new insights into the process of skeletal bone acquisition, which is vital to optimizing the reduction in later-life osteoporosis risk.

Unsuspected osteochondroma-like outgrowths in the cranial base of Hereditary Multiple Exostoses patients and treatment with a BMP antagonist in mice

Sayantani Sinha¹, Christina Mundy¹, Till Bechold³, Federica Sgariglia¹, Paul Billings¹, Kristein Carroll², Eiki Koyama¹, Kevin Jones² and Maurizio Pacifici¹

¹ Division of Orthopaedic Surgery, The Children's Hospital of Philadelphia

² Department of Oncological Sciences and Huntsman Cancer Institute, University of Utah School of Medicine, Salt Lake City, Utah

³ Departments of Orthodontics and Orofacial Orthopedics, University Hospital Tuebingen, Tuebingen, Germany

Hereditary Multiple Exostoses (HME) is a rare autosomal-dominant pediatric disorder that affects about 1 in 50,000 individuals worldwide. HME is characterized by formation of cartilaginous outgrowths—called osteochondromas—next to the growth plates of many axial and appendicular skeletal elements. Because of their size, large number and location, the osteochondromas can cause severe problems such as skeletal deformities, chronic pain and early onset osteoarthritis. Surprisingly, it is not known whether such tumors also form in endochondral elements of the craniofacial skeleton. Here, we carried out a retrospective analysis of cervical spine MRI and CT scans from 50 consecutive HME patients that included cranial skeletal images. Interestingly, nearly half of the patients displayed moderate defects or osteochondroma-like outgrowths in the cranial base and specifically in the clivus. In good correlation, osteochondromas developed in the cranial base of mutant *Ext1^{fl/fl};Col2-CreER* or *Ext1^{fl/fl};Aggrecan-CreER* mouse models of HME along the synchondrosis growth plates. Because chondrogenesis requires bone morphogenetic protein (BMP) signaling, we asked whether osteochondroma formation could be blocked by a BMP signaling antagonist. Systemic administration with LDN-193189 effectively inhibited osteochondroma growth in conditional *Ext1*-mutant mice. In vitro studies with mouse embryo chondrogenic cells clarified the mechanisms of LDN-193189 action that turned out to include decreases in canonical BMP signaling pSMAD1/5/8 effectors but interestingly, concurrent increases in such anti-chondrogenic mechanisms such as pERK1/2 and *Chordin*, *Fgf9* and *Fgf18* expression. Our study is the first to reveal that the cranial base can be affected in patients with HME and that osteochondroma formation is amenable to therapeutic drug intervention.

A Novel Role of miR-150 in Bone Homeostasis

Fouad Moussa, Gregory Sondag, Thomas Mbimba, Michael Erossy, Bryson Cook, Paul Nemer, Kimberly Novak, Fayez Safadi

MiRNA are small, non-coding RNA molecules that consist of about 22 nucleotides, which target mRNA and trigger its degradation or repress translation. MiR-150 is highly expressed in immature B cell stages, and targets c-Myb, a transcription factor that is important for lymphocyte development. However, the role of miR-150 on bone has not been documented. Our lab shows that miR-150 is expressed in mouse long bone and calvaria, and its expression is increased with age, thus suggesting that miR-150 might play a role in bone homeostasis. Here, we show a novel role of miR-150 in osteoblast differentiation and function, where miR-150 gene expression is maximum at early stage (cell proliferation) and decreases at later stage (matrix mineralization) of osteoblastogenesis *in vitro*. In this study, we reveal that miR-150 knockout (miR-150 KO) mice have decreased bone mass reflected by less bone volume to tissue volume ratio; and a significant reduction of *in vitro* mesenchymal stem cells (MSCs) proliferation. Interestingly, there is an increase in *in vitro* osteoblast differentiation and function compared to wild type (WT) mice. Osteoclasts (OCs) are also significantly reduced in proliferation and function *in vitro* furthering characterizing the effects of this miRNA on bone.

Mid-Infrared Spectroscopic Monitoring of Engineered Cartilage Culture Media

R.J. Kyada¹, F. Yousefi¹, M.V. Padalkar¹, M. Unger², N. Pleshko¹

¹Temple University, Department of Bioengineering; ²Anasys Instruments

DISCLOSURES: R.J. Kyada(N), F. Yousefi(N), M.V. Padalkar(N), M. Unger(N), N. Pleshko(N)

INTRODUCTION: Osteoarthritis is a musculoskeletal joint disease affecting nearly 12% of the American population and is characterized by articular cartilage degeneration. Disappointment with long-term outcomes of current clinical methods for reducing disease progression has stimulated interest in developing functional engineered replacement tissues.¹ One such tissue engineering method involves seeding synthetic polyglycolic acid (PGA) scaffolds with harvested bovine articular chondrocytes and culturing the construct over several weeks. During the culture, the PGA polymers in the scaffold degrade as chondrocytes proliferate and deposit more cartilaginous extracellular matrix; as chondrocytes consume glucose present in the cell medium, they undergo anaerobic glycolysis, releasing lactate, which can travel back out of the construct and into the medium. It is speculated that glucose and lactate levels reflect the overall quality of the developing construct and hence can be used to assess when the construct is most optimal for implantation. Traditionally, biochemical assays are used to monitor these metabolite concentrations during the culture, but these are often time-consuming, difficult, and complex to carry out. However, these metabolites can be sensitively, noninvasively, and rapidly monitored across the duration of the cell culture using mid-infrared (MIR) spectroscopy.⁴ In this spectroscopic technique, MIR photons of specific frequencies are absorbed by various functional groups, typically from molecules with highest concentration within the sample.² For this project, MIR spectra were collected using a novel 10 μm thick flow cell that can average out the much stronger water peak to sensitively delineate the weaker solute peaks. The goal here is to identify and spectroscopically monitor the major metabolites released into the cell culture media by the constructs over time.

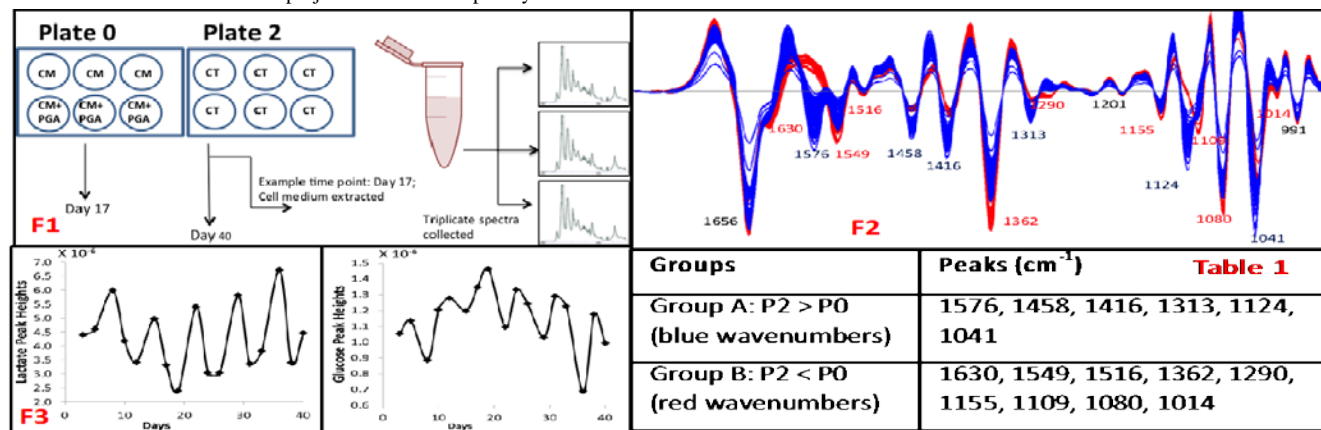
METHODS: I. Cell Harvesting, Scaffold Seeding, and Cell Culture: The chondrocyte harvesting, PGA scaffold seeding, and culturing of the engineered construct were carried out as shown in McGoverin et al.³ As shown in Fig. 1, there were 2 Plates: Plate 0 was the acellular control while Plate 2 included the cell-seeded constructs. During the culture, media were extracted from the wells 3 times a week for 6 weeks for Plate 2 and 2.5 weeks (17 days) for Plate 0. II. Mid-Infrared Spectroscopy: Spectra were collected via the MBIO AquaSpec technology (Cetics Healthcare Technologies, Esslingen, Germany). One hundred μL of media samples were added to the 10- μm thick flow cells to collect transmission FTIR spectra. These spectra were then ratioed to the background of water. In total, 126 spectra were collected for Plate 0 and 306 spectra for Plate 2. III. Data Analysis: The media sample spectra were analyzed using Unscrambler X (CAMO Software, Oslo, Norway). The spectra were smoothed and reduce-averaged. 2nd derivative spectra were obtained with a 13-point Savitzky-Golay smoothing window. Paired t-tests were performed for assessing statistical significance in differences between second derivative peak values (set at $P < 0.05$). IV. Biochemical Assays: Colorimetric glucose assays and fluorometric lactate assays (Cayman Chemicals, Ann Arbor, MI) were performed as gold standard comparisons to spectral data.

RESULTS: Peaks differing significantly between the two plates were determined with t-tests as shown in Fig. 2. Correlation analysis revealed two groups of peaks: A and B summarized in Table 1. Peaks in Group A correlated negatively with those in Group B, indicating that one component is possibly getting converted to the other. Since the 1576 cm^{-1} peak has previously been assigned to the carboxyl stretch in lactate and the 1155 cm^{-1} to the C-O-C glucose ring vibration, Group A peaks are attributed to lactate and Group B peaks to glucose. To understand how glucose and lactate change across the duration of the culture, each of their characteristic peaks (1576 cm^{-1} for lactate and 1155 cm^{-1} for glucose) were plotted with respect to time, as shown in Fig. 3. Two major aspects can be noted: 1) both curves are periodic and 2) while the lactate curve is concave-up, the glucose one is concave-down.

DISCUSSION: The periodicity in the glucose and lactate curves in Fig. 3 can be explained by the fact that the cell media for the constructs were changed 3 times a week. However, it is unclear why on there are sudden changes in the glucose and lactate peak heights every Monday (Days 8, 15, 22, 29, and 36). The curves, alongside the strong negative correlation coefficient ($r = -0.92$; $P < 0.05$) between the two peaks for all time points, also indicate that at low glucose levels, lactate levels are higher and hence much of that glucose is used for anaerobic glycolysis. However, this lactate production minimizes around Day 19; this may indicate the scaffold has reached a post-proliferation peak cell density, which would physically hamper glucose diffusion within the construct, partly explaining the lower glucose consumption.

REFERENCES: 1. Makris et al, "Repair and tissue engineering techniques for articular cartilage," *Nature Reviews Rheumatology*, Vol. 11, pp. 21-34, 2015. 2. Baker et al, "Using Fourier transform IR spectroscopy to analyze biological materials," *Nature Protocols*, Vol. 9, pp. 1771-91, July 2014. 3. McGoverin et al, "Non-destructive assessment of engineered cartilage composition by near infrared spectroscopy," *Ann. Biomed. Eng.*, Vol. 44, pp. 680-92, January 2016. 4. Rhiel et al, "Real-time in situ monitoring of freely suspended and immobilized cell cultures based on mid-infrared spectroscopic measurements," *Biotechnology and Bioengineering*, Vol. 77, pp. 174-85, January 2002

ACKNOWLEDGMENTS: The project was funded in part by NIH R01 AR056145.



F1: Experimental schematic. **F2:** Second derivative spectra of cell culture media; red = control Plate 0 (Days 3-17) and blue = cell-containing Plate 2 (Days 3-40). Blue wavenumbers = peak values in P2 > P0; red wavenumbers = peak values in P2 < P0. For all wavenumbers $P < 1.0 \times 10^{-5}$ ($n = 7$). **F3:** Time plots indicating behavior of lactate (left) and glucose (right) over the duration of the culture. These are produced by plotting inverted second derivative peak heights for the 1576 cm^{-1} (lactate) and 1155 cm^{-1} (glucose) peaks with respect to time. **Table 1:** grouping of the major peaks based on their relative values in the control and construct-containing plates.

Quantification of bone mineral crystallinity by FTIR and Raman spectroscopy

William Querido¹, Ramyasri Ailavajhala¹, Mugdha Padalkar¹, Nancy Pleshko¹
¹Department of Bioengineering, Temple University, Philadelphia, PA
 william.querido@temple.edu

INTRODUCTION: Properties of the mineralized bone matrix play a major role in determining bone strength and resistance to fractures. In particular, the crystallinity of bone mineral is directly associated with the mechanical properties of the tissue [1,2]. The gold-standard method to quantify bone mineral crystallinity is X-ray diffraction (XRD), which provides a measurement of the size of the calcium phosphate apatite crystals. However, alternative approaches are needed to evaluate samples that cannot be analyzed by XRD, such as histological sections and very small biopsies. Vibrational spectroscopy methods, including infrared and Raman, present a great alternative, as label free and non-destructive modalities that require little to none sample preparation, very small sample size, and can be coupled to a microscope to evaluate and image regions of interest. Transmission Fourier transform infrared (FTIR) spectroscopy is often used to estimate bone mineral crystallinity based on the 1030/1020 cm^{-1} peak ratio, which correlates to XRD assessment [3]. However, it is unclear whether this same approach is applicable to other infrared sampling modes, such as the very straightforward attenuated total reflection FTIR (ATR-FTIR). Further, the use of Raman for bone mineral crystallinity assessment has yet to be fully investigated. Our objective in this study is to verify and establish approaches by which FTIR (transmission and ATR) and Raman spectroscopy can be used to determine bone mineral crystallinity.

METHODS: We analyzed 13 poorly crystalline apatite samples, including native bones, deproteinized bones and synthetic mineral with different maturation stages. The powdered samples were analyzed by gold standard XRD, Raman spectroscopy, transmission FTIR spectroscopy and ATR-FTIR. Crystal size was determined by the broadening of the (002) reflection in the XRD pattern [4]. Several approaches were used to analyze the Raman, FTIR and ATR-FTIR spectra, as described below. Correlation levels were assessed based on the Pearson R-values and significance with $P < 0.01$.

RESULTS AND DISCUSSION: XRD showed typical patterns of poorly crystalline apatite for all samples, with an isolated peak indexed as the (002) reflection of hydroxyapatite (Fig. 1a). The crystal size of the minerals varied from around 10 to 25 nm in length, which is well within the range of crystallinity expected for bone apatite. The Raman spectra were also very characteristic of bone mineral, showing the clear phosphate peak around 960 cm^{-1} (Fig. 1b). The FTIR spectra also showed the typical phosphate peaks of bone apatite in the 1200-900 and 700-500 cm^{-1} region (Fig. 1c). However, we noticed striking differences between the raw spectra from FTIR (Fig. 1c, full orange line) and ATR-FTIR (Fig. 1c, dotted blue line). To analyze the underlying peaks in more detail, we evaluated the second derivative spectra, and found previously undocumented differences in phosphate peaks in the 1200-900 cm^{-1} region (Fig. 1d). In particular, the peaks around the 1030-1020 cm^{-1} region were markedly different: in FTIR spectra, the peak around 1030 cm^{-1} was clearly seen in the samples, often split with another peak around 1020 cm^{-1} (Fig. 1d, full orange line); whereas in ATR-FTIR spectra, only the peak around 1020 cm^{-1} was seen, with the 1030 cm^{-1} peak appearing at most as a faint shoulder (Fig. 1d, dotted blue line). This original observation is of high relevance because the absence of this peak would certainly impair a valid crystallinity assessment based on the 1030/1020 cm^{-1} ratio by ATR-FTIR. It was then necessary to search for alternative peak ratios that could be used to estimate mineral crystallinity by ATR-FTIR, such as using the well crystalline apatite peaks around 1095 and 960 cm^{-1} and the less crystalline apatite peak around 1120 cm^{-1} (Fig. 1d). Several original approaches using Raman, FTIR and ATR-FTIR spectroscopy showed strong correlation with mineral crystallinity determined by XRD (Table 1).

SIGNIFICANCE AND CLINICAL RELEVANCE: The approaches we describe here using vibrational spectroscopy can be applied for the quick and reliable quantification of bone mineral quality in clinically relevant samples, such as specific regions of interest in histological sections and very small bone biopsies. These approaches can be readily implemented in many orthopedic and biomineralization studies, for instance, evaluate samples that cannot be analyzed by XRD and to complement and enrich standard histomorphometry methods.

REFERENCES: [1] Yerramshetty et al. Bone. 2008;42(3):476-82. [2] Donnelly et al. Calcif Tissue Int. 2010;87(5):450-60. [3] Boskey et al. Biomaterials. 2007;28(15):2465-78. [4] Farlay et al. J Bone Miner Metab. 2010;28(4):433-45.

ACKNOWLEDGEMENTS: Supported by NIH R01 AR056145 and NIH R21 AR071704

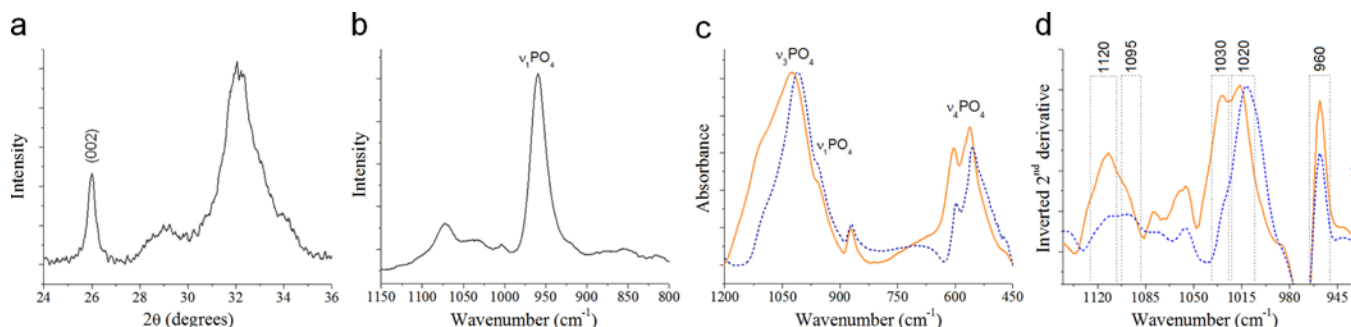


Fig. 1: (a) XRD pattern. (b) Raman spectrum. (c) FTIR (full orange line) and ATR-FTIR (dotted blue line) raw spectra. (d) (c) FTIR (full orange line) and ATR-FTIR (dotted blue line) second derivative spectra. A bovine compact bone sample was chosen to illustrate the results.

Table 1: Correlation coefficient (R) between XRD crystallinity and Raman, FTIR and ATR-FTIR approaches.

	Spectral analysis approach	R-value
Raman	$\nu_1\text{PO}_4$ maxima wavenumber	0.92
Transmission-FTIR	1030/1020 cm^{-1} ratio in the second derivative spectra	0.94
	$\nu_1\text{PO}_4$ maxima wavenumber	0.93
ATR-FTIR	1030/1020 cm^{-1} ratio	Not adequate
	960/1120 cm^{-1} ratio in the second derivative spectra	0.91
	1095/1115 cm^{-1} ratio in the second derivative spectra	0.88
	$\nu_1\text{PO}_4$ maxima wavenumber	0.95

FT-IRIS for the Evaluation of Treatment Strategies in a Pre-Clinical Arthrofibrosis Model

Jessica M Falcon¹, Jolanta Fertala², Andrzej Steplewski², Antonia Chen², Andrzej Fertala², Nancy Pleshko¹

¹Department of Bioengineering, Temple University, Philadelphia, PA

²Department of Orthopaedic Surgery, Sidney Kimmel Medical College, Thomas Jefferson University, Philadelphia, PA

Falcon@temple.edu

INTRODUCTION: Fibrotic deposits formed within joint tissues in response to injury mainly consist of collagen I-rich fibrils. These deposits, cause joint stiffness that severely limits the range of motion (ROM), thereby altering patients' quality of life [1]. The pathomechanisms of joint contracture include: (i) inflammation, (ii) proliferation of activated cells, and (iii) enhanced production of extracellular matrix macromolecules that form collagen-rich fibrotic tissue that may be deposited in the intraarticular and periarticular areas [3]. Treatments to improve the ROM include physical therapy, splinting or casting, as well as anti-inflammatory medications. Recently, Steplewski et al. engineered a recombinant antibody that targets the formation of collagen fibrils, the main component of fibrotic deposits that contribute to joint stiffness [3]. Although this antibody was effective in blocking the formation of new collagen fibrils produced in response to knee injury, this antibody is ineffective in reducing the mass of already-formed fibrous deposits. While bacterial collagenase is applied in Dupuytren's contracture to digest collagen-rich deposits, treatment with this enzyme is significant risk of damaging healthy tissues. While bacterial collagenases cleave the triple-helical domains of collagenous proteins, trypsin cleaves only at specific sites of the telopeptide regions of collagen molecules. In this study, we tested a possibility of using trypsin to cleave collagen telopeptides, thereby breaking collagen cross-linking that stabilize fibrotic deposits. The aim of the current study is to understand the effects of antibody-based and trypsin-based methods to reduce the effects of excessive collagen fibril formation due to joint injury in a rabbit model. We applied Fourier transform infrared imaging spectroscopy (FT-IRIS) to study key characteristics of collagen-rich arthrofibrotic tissues [2].

METHODS: **Animals:** A rabbit joint contracture model represents clinical features associated with post-traumatic joint stiffness in human patients. Female New Zealand White rabbits (Covance, Inc), 8- to 12- months old, were used. All animal studies were approved by the Thomas Jefferson University Institutional Animal Care and Use Committee. **Surgical Procedure and Antibody Engineering:** The model and antibody production was described in detail in [3], and involved knee injury caused by intra-articular fracture and mechanical disruption of the posterior capsule (PC). The injured knees were maintained in a flexed position for 8 weeks with the use of Kirschner (K) wires. The un-operated contralateral leg serves as control. Following 8 weeks of immobilization and delivery of pegylated or non-pegylated antibody, the K-wires were removed and the rabbits are allowed free cage activity for 2 weeks (N = 2 rabbits, 4 legs, injured and contralateral control) then sacrificed. In the trypsin-treated group, trypsin was injected into the knee joint once during the Kwire removal. As the PC is the main contributor to knee contracture in the rabbit model, the PCs were dissected from the limbs for histological and spectroscopic evaluation. Tissues were formalin-fixed paraffin embedded, and sectioned at 5 microns for FT-IRIS. **Spectroscopy:** FT-IRIS data were obtained using a Perkin Elmer Spectrum Spotlight 400 imaging spectrometer (Perkin Elmer). Tissues were sampled in reflection mode using a reflective substrate, MirrIR low-e microscope slides (Kevley Technologies). Data were acquired in the mid IR range (2000 to 750 cm⁻¹) in imaging mode at a pixel resolution of 25 μm, spectral resolution of 8 cm⁻¹ and 2 co-added scans. **Data Analysis:** Imaging data for injured and uninjured PC tissues were analyzed using ISyS 5.0 software (Malvern, UK). Spectral images are first processed to mask out paraffin and noise followed by second derivative calculation to resolve underlying peaks. Second derivative spectra were used to calculate peak height ratios to quantify the amount of collagen to total protein. The spectral peaks of interest were 1656 cm⁻¹ (Amide I – total protein quantity) and 1338 cm⁻¹ absorbance (that arises from collagen side chain vibrations). To evaluate collagen maturity, which may be related to cross-linking [2], peak height ratios of spectral peaks 1660 cm⁻¹ to 1690-1 were used. Significant differences among treatment groups were determined by one-way ANOVA and student t-test with * indicating a p<0.0001 and indicating a p<0.0002 (JMP Pro 13 Statistical Software).

RESULTS: Histology images can be seen in Figure 1A. The first two images are of injured posterior capsules after antibody and trypsin treatment. The last image is of an uninjured healthy control capsule. Figure 1B are infrared spectral images collected from identical sections of the histology images. The spectral maps visualize the distribution of collagen in the tissue. Areas that appear red reveal higher intensity of collagen to total protein for that particular pixel. Figure 2 supports the visual distribution of collagen in Figure 1B. The peak height ratio of collagen to total protein drops in both the antibody treated and trypsin treated groups when compared to the healthy control. From this data, it can be understood that the antibody and trypsin treatments had a direct interfering effect on collagen formation. Figure 3 represents the quantitative peak height ratio of mature cross-links to immature cross-links. The trypsin treated group had a higher ratio of mature to immature cross-links when compared to the healthy control.

DISCUSSION: Infrared spectroscopy is an effective tool for quantifying and assessing the collagen content and distribution. The presence of absorbance peaks specific for collagen and collagen cross-links allows for quantification and understanding of the direct impact of antibody-based and trypsin-based approaches on arthrofibrosis. Interestingly, figure 3 shows that there are relatively more mature cross links in the trypsin treated group than immature crosslinks. This information could indicate that trypsin digestion leads to the reduction of fibrils stabilized by immature cross-links rather than those stabilized by mature ones. Thus, we hypothesize that the main target of trypsin treatment are newly-formed collagen fibrils that are produced in response to the joint injury.

SIGNIFICANCE: Targeted disruption of fibrotic collagen deposits formed due to arthrofibrosis is an unmet clinical need. Additional insight into collagen distribution in preclinical models of post-traumatic joint contracture could improve understanding of therapeutic protocols.

REFERENCES 1. Fergusson, Dean, Brian Hutton, and Andrea Drodge. "The Epidemiology of Major Joint Contractures." *Clinical Orthopaedics and Related Research* 456 (2007): 22-29. 2. Boskey, A., and N. Pleshko Camacho. "FT-IR Imaging of Native and Tissue-engineered Bone and Cartilage." *Biomaterials* 28.15 (2007): 2465-478. 2. 3. Steplewski, Andrzej, Jolanta Fertala, Pedro K. Beredjikian, Joseph A. Abboud, Mark L. Y. Wang, Surena Namdari, Jonathan Barlow, Michael Rivlin, William V. Arnold, James Kostas, Cheryl Hou, and Andrzej Fertala. "Auxiliary Proteins That Facilitate Formation of Collagen-rich Deposits in the Posterior Knee Capsule in a Rabbit-based Joint Contracture Model." *Journal of Orthopaedic Research J. Orthop. Res.* 34.3 (2016): 489-501.

ACKNOWLEDGEMENTS: # DoD grant W81XWH-13-1-0393 awarded to AF. AF and AS have a pending patent application to protect the amino acid sequence of the antibody used in this study. OREF 16-009 awarded to AC.

Near Infrared Spectral Assessment of Free and Bound Water in Bone

Ramyasri Ailavajhala¹, Jack Oswald¹, Mugdha V. Padalkar¹, William Querido¹, Nancy Pleshko¹

¹Department of Bioengineering, Temple University, Philadelphia, PA

Ramya.Ailavajhala@temple.edu

INTRODUCTION: Bone is a tri-phasic tissue consisting of type 1 collagen, hydroxyapatite and water. Bone mineral density (BMD) is clinically used to indicate bone quality, and has been shown to decrease with age and in disease states. However, factors such as water content associated with mineral and collagen have been emerging as markers for bone quality¹. Gravimetric analysis is an established technique to determine water content in bone, but this technique is time consuming, destructive, and only yields information on bulk water content. Water is approximately 10% of cortical bone wet weight and exists as free and bound¹. Free water is surface water associated with collagen and hydroxyapatite, and bound water is found within the molecular structure of collagen and hydroxyapatite. The various water compartments have synergistic effects to mechanically stabilize bone tissue. Currently, magnetic resonance imaging (MRI) based on ultra-short TE (UTE) is being developed to assess bone water in clinical and pre-clinical applications^{2,3}; however, detecting water in its various states as bound to collagen or mineral has not yet been confirmed. In musculoskeletal tissues such as bone and cartilage, near infrared spectroscopy (NIRS) has been used to evaluate key compositional information including bound water and free water (cartilage), and organic components (cartilage and bone)^{4,5}. NIRS (frequency range 4000-12000 cm⁻¹) is a nondestructive technique that is sensitive to molecular vibrations, and permits a depth of penetration into tissues from millimeters to centimeters⁴. Recently we showed that specific absorbances in the NIRS region are sensitive to water in bone, and also correlate to water content as determined by UTE data⁴. Here, we assign absorbances that arise from free and bound water, and develop a water calibration based on correlation to gravimetric data. These data will help build the foundation for the application of NIRS to pre-clinical studies of bone quality.

METHODS: Tissues: Bovine tibiae (n=6) were collected from 2-month-old animals (Research 87). Tibiae were cut by into segments with a bone band saw (Mar-Med Inc.), and ultrasonicated in 1% tergazyme solution for 2 hours at 38°C to remove bone marrow. Marrow-free bones were sliced into 500 µm thick, cross-sectioned slices using a diamond wafering saw (Buehler Isomat 1000), and stored in 1x phosphate buffer saline (PBS) at -20°C. **Preparation for spectral data collection:** To obtain tissues with varying amounts of water, bone samples were dried in ambient conditions for 15 and 30 minutes, and then lyophilized for 24 hours. At time points 0, 15, 30 minutes and at 24 hours with lyophilization, gravimetric data was collected prior to spectral data collection. Spectral data were also collected from lyophilized Bio-Oss (Geistlich) which is a mineralized substrate that is comparable to hydroxyapatite in human bone, and from lyophilized pure collagen type 1 (Elastin Products). **Spectral data collection and analysis:** NIRS data was collected using a Perkin Elmer Spotlight 400 imaging spectrometer at 16 cm⁻¹ spectral resolution with 32 co-added scans and at 50 microns pixel resolution. An 8x8 pixel image took approximately 2 minutes for data collection. During the ambient drying section of the study, data were collected with samples placed on a glass slide (relative humidity: 50%). After lyophilization, samples were placed in a chamber supplied with low humidity by dry air (relative humidity 3%). Spectra from individual infrared images were averaged and the second derivative peak heights of collagen and water absorbances, reflecting relative quantity of these components, were determined with Isys 5.0 software (Malvern Instruments). NIR absorbances of interest for water, collagen and hydroxyapatite are as follows (Figure 1A& 1B), water: 5192 cm⁻¹, 6560 cm⁻¹, 7008 cm⁻¹, collagen: 4600 cm⁻¹ and hydroxyapatite (P-OH vibration) : 6984 cm⁻¹. Percent water content in samples were calculated by:
$$\frac{\text{Wet weight}_{(T)} - \text{dry weight}_{(L)}}{\text{Wet weight}_{(T)}} *$$

100. Wet weight (T) = sample weight at a particular time point, Dry weight (L) = sample weight with 24 hours of lyophilization. Statistical analysis: One way ANOVA was performed using JMP (SAS) to determine differences for spectral data parameters with significance set at p < 0.05. Linear regression models and Pearson correlations were performed for spectral data versus gravimetric data with significance set at p<0.05.

RESULTS: Water absorbances at 5192 cm⁻¹ and 7008 cm⁻¹ were determined to arise from combined free and bound water, as the peak intensities were reduced with lyophilization, but did not completely disappear (Figure 1A). The 7008 cm⁻¹ absorbance shifted to a lower frequency of 6976 cm⁻¹ after lyophilization. The 6560 cm⁻¹ absorbance was determined to arise from only free water because the absorbance becomes insignificant with lyophilization (Figure 1A). This data confirms that in bone, water existing in bound and free states can be assessed by NIRS. The gravimetrically calculated percent water content for bone samples ranged between 8-14%. The percent water content was calculated to quantify the change in water content over time. Second derivative peak heights of water (5192 cm⁻¹, 6560 cm⁻¹, 7008 cm⁻¹) were ratioed to the collagen peak (4600 cm⁻¹), and all ratios decreased with time and lyophilization (Figure 2). All three water peaks were significantly correlated to the gravimetric data, but only data for the best model to predict water content is shown here: 5192 cm⁻¹ combination water peak (r= 0.91, p <0.001, y=-14.84 +10.42x (x: ratio of water/collagen, y: gravimetric data % water content.)).

DISCUSSION: The current study demonstrates the utility of NIRS to detect compositional differences in water compartments in bone. The gravimetric measured water content is positively correlated to the NIR water absorbances, and the decreases in water content were directly related to the increase in collagen peak intensities. The NIR absorbance of the P-OH vibration from mineral is very small and needs to be further validated.

SIGNIFICANCE: NIRS sensitivity to detect water changes associated to collagen can be useful in pre-clinical applications for bone quality assessment.

ACKNOWLEDGEMENT: Supported by NIH R21 071704

References: 1. Unal, Mustafa, and Ozan Akkus. *Bone* 81 (2015): 315-326. 2. Allen, Matthew R., et al. *Journal of Bone and Mineral Research* 30.8 (2015): 1441-1444. 3. Li, Cheng, et al. *Radiology* 272.3 (2014): 796-806. 3. Rajapakse, Chamith S., et al. *Bone* 103 (2017): 116-124. 4. Padalkar, M. V., R. G. Spencer, and N. Pleshko *Annals of biomedical engineering* 41.11 (2013): 2426-2436

Transcutaneous Assessment of Bone by Near Infrared Spectroscopy

James P. Karchner¹, Jina Ok¹, Mary F. Barbe², Sayed Ali³, Cathleen L. Raggio⁴, Nancy Pleshko¹

¹Department of Bioengineering, Temple University, Philadelphia, PA, ²Department of Anatomy and Cell Biology, Temple University School of Medicine, Philadelphia, PA, ³Department of Radiology, Temple University Hospital, Philadelphia, PA, ⁴Department of Orthopedic Surgery, Hospital for Special Surgery, New York, New York.
james.karchner@temple.edu

DISCLOSURES: James P. Karchner (N), Jina Ok (N), Mary F. Barbe (N), Sayed Ali (N), Cathleen L. Raggio (2-Alexion, 2-Biomarin), Nancy Pleshko (N)

INTRODUCTION: Diseases of bone fragility such as osteoporosis and osteogenesis imperfecta require monitoring of bone health, typically by X-ray or dual X-ray absorptiometry (DXA), modalities based on ionizing radiation. DXA scans provide information on bone density that is related to overall bone fracture risk, and X-rays are typically used for qualitative assessment of fracture incidence or healing. However, a quantitative “bone health index” (BHI), has recently been proposed for quantitative assessment of hand X-rays. BHI is calculated based on cortical thickness, length, and width of metacarpals and is related to bone quality.¹ Near-infrared (NIR) fiber optic spectroscopy utilizes non-ionizing radiation that spans the frequency range from ~4000-11000 cm^{-1} and has previously been used for evaluation of bone and cartilage.² Absorbances at specific wavenumbers arise due to certain vibrations in molecular bonds, which also correspond to the type of material or tissue that is being detected. Due to the limitations in penetration depth of the radiation, previous studies have only investigated harvested tissues by NIR spectroscopy. However, there is a frequency window where the NIR radiation can penetrate through skin, and if thin enough, to sample bone. Here, we investigate whether bone from metacarpal 2, which is covered by a very thin layer of skin and fascia, ~ 2 mm thick, is accessible transcutaneously by NIR spectroscopy. To investigate this, NIR spectra were collected from metacarpals of human hands from cadavers, and from individual tissue layers through to bone. Further, we investigate whether the BHI index calculated only from metacarpal 2 significantly correlates with the BHI from the average of the three metacarpals. These studies will demonstrate feasibility of using NIR fiber optic spectroscopy to evaluate bone quality by detecting bone spectra through skin and fascia, providing a foundation to develop this technique that eliminates exposure to ionizing radiation.

METHODS: Institutional Biosafety approval was obtained from Temple University prior to this study. Hands were acquired from human cadavers (n=1 female, n=3 male) ranging in age from 51-84. Digitized posterior-anterior X-Rays were obtained for the calculation of BHI.¹ Measurements of metacarpal length and width, and cortical bone thickness, of metacarpals 2, 3, and 4 (M2-4) were obtained utilizing Fiji software (Fig 1). NIR spectra were collected using a Remspec NIR fiber optic probe coupled to a Nicolet ISSN FT-NIR spectrometer at a spectral resolution of 16 cm^{-1} with 512 co-added scans. Spectra were collected from M2 in the center of the bone. M2 was selected over other metacarpals due to the lack of interference from extensor tendons, minimizing interference from other tissues. Initially, spectra were collected transcutaneously through an intact M2. Then skin was removed and spectra were collected through fascia, and then fascia was removed and spectra were collected from the bone only. Spectra were then collected from all of the layers of tissue, without any bone underneath. To investigate depth of penetration of NIR radiation, spectra from polystyrene, which has unique spectral absorbances, were collected, and from skin and fascia on top of the polystyrene, to determine whether NIR radiation penetrated deep enough through skin and fascia to detect the polystyrene signals. *Unscrambler* software (Camo) was utilized to evaluate the spectra by second derivative processing to resolve underlying peaks, and *Microsoft Excel* was used to calculate BHI values and determine Pearson correlations, with $p < 0.05$ considered significant.

RESULTS: BHI values were calculated for each hand and ranged from 5.63-7.93, similar to values reported in the literature, with the female hand having the lowest BHI, as expected.² The BHI values from M2 were found to significantly correlate with the average BHI values of M2, M3, and M4 ($R = 0.99$, $p = 0.0013$), indicating that a BHI calculated from M2 measurements only was feasible. NIR Penetration: There are four peaks in the second derivative spectra that are specific to polystyrene, which were detected through the skin and fascia at wavenumbers higher than 5900 cm^{-1} (Fig 2). Thus, the NIR radiation penetrates through skin and fascia, supporting the prospect of sampling bone through skin and fascia. NIR bone absorbances: There is no strong mineral peak in the NIR region, but rather absorbances from collagen and bone water. Two peak heights significantly correlated between spectra collected transcutaneously through the hand surface, and spectra collected directly from the bone only. The first peak is 6560 cm^{-1} ($R = 0.99$, $p = 0.006$), which arises from an O-H first overtone from water. The second peak is 8490 cm^{-1} ($R = 0.98$, $p = 0.018$), which arises from a C-H second overtone from collagen. No significant correlation was seen between spectra collected transcutaneously through the hand surface and spectra collected directly from skin and fascia.

DISCUSSION: The correlation of all metacarpal BHI values with M2 BHI values justifies the use of M2 as a general indicator of the bone health, and supports NIR data collection from this location. Detecting polystyrene peaks through the skin and fascia that overlay M2 confirms that the NIR radiation penetrates deep enough to detect the underlying bone. It also provides a better understanding of spectral ranges that should be focused on when attempting to detect peaks arising specifically from bone, because the radiation only penetrated deep enough at wavenumbers above 5900 cm^{-1} . The significant correlation between spectra collected through the hand surface and spectra collected directly from bone supports the hypothesis that bone absorbances can be detected transcutaneously by NIR radiation. Further supporting this hypothesis is the lack of significant correlations between spectra collected only from skin and fascia when compared to spectra collected transcutaneously through the surface of the hand. This validates that the 6560 cm^{-1} and 8490 cm^{-1} peaks are arising from bone, rather than skin and fascia. In future work, correlations with BHI values and NIR spectra will be investigated.

SIGNIFICANCE: Current gold-standard methods to evaluate bone quality are costly and expose patients to ionizing radiation. Non-invasive NIR evaluation of bone would provide a safer and cheaper alternative to monitoring the bone quality of patients with bone diseases, and could also be investigated for assessment of healing of fractures in bone near the surface of the skin.

REFERENCES: 1. Thodberg et al (2016). *Arch Osteoporos*, 11(1), 17. 2. McGovern et al (2014). *Appl Spectrosc*, 68(10), 1168-1175.

ACKNOWLEDGEMENTS: Supported by NIH R21 071704 (NP) and MARC U-STAR grant NIH T34 087239-06 (JPK).

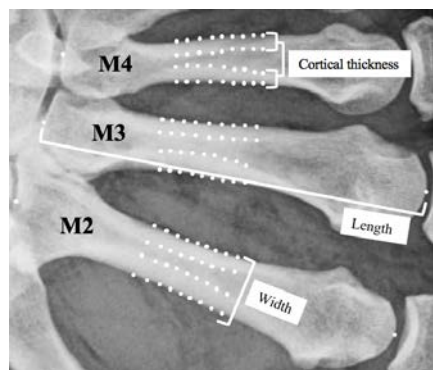


Figure 1. Locations of measurements for width, length, and cortical thickness of the three metacarpals studied.

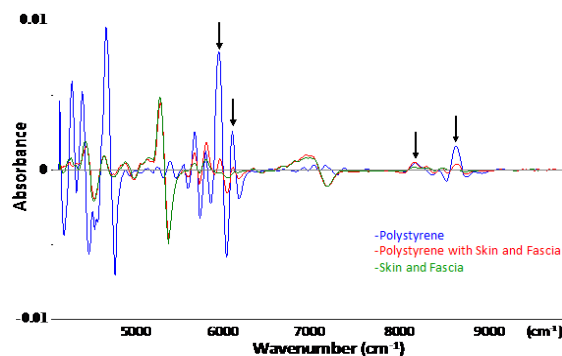


Figure 2. Inverted NIR second derivative spectra showing detection of polystyrene peaks through skin and fascia.

Effects of transcription factor Mohawk on tenogenic gene expression in equine tenocyte-derived induced pluripotent stem cells

Feikun Yang¹, Filipa Pinto², Spencer Szczesny³, Su-Jin Heo³, Aiwu Zhang¹, Robert L. Mauck³,
Dean W. Richardson¹

¹ Department of Clinical Studies New Bolton Center, University of Pennsylvania, 382 West Street Road, Kennett Square, PA 19348

² Institute for Regenerative Medicine, University of Pennsylvania, 421 Curie Blvd., Philadelphia, PA 19104

³ Department of Orthopaedic Surgery, Perelman School of Medicine, University of Pennsylvania, 36th Street and Hamilton Walk, Philadelphia, PA 19104

Tendon, a unique form of connective tissue transforming the force from muscle to bone, is highly prone to injury or overuse, leading to the development of tendinopathy in both human and horses. Cell-based therapeutic strategies may afford major potential advantages in tendon repair because the natural healing of injured tendon is poor. Mohawk (MKX), a homeobox gene, is highly expressed in developing tendon and appears to be an important regulator of tenogenic differentiation. However, its role in horse tendon repair/regeneration remains unknown. In this study, equine MKX gene (accession number: XM_014737017.1) was amplified from total cDNA of fetal equine tenocytes and identified by DNA sequencing. The gene was sub-cloned into backbone vectors 6His-HA-pcDNA3, or pHAGE lentiviral vector, and its expression and subcellular localization were determined by western blotting and immunofluorescent microscopy. Lentivirus encoding equine MKX assembled in HEK293 cells were used to infect tenocyte-derived induced pluripotent stem cells (teno-iPSCs). Quantitative real-time PCR (qPCR) analysis showed that: 1- ectopic introduction of MKX increased the mRNA levels of Scleraxis (Scx) and Egr1, two known tenogenic-associated transcription factor in teno-iPSCs; 2 - the mRNA level of SOX9, a master regulator of chondrogenesis, was only slightly greater than the GFP-expressing controls. On the other hand, application of uniaxial cyclic mechanical loading increased the expression of SCX and MKX in teno-iPSCs. Their levels were further increased when mechanical loading was utilized with the re-introduction of MKX. Our data suggest that ectopic expression of transcription factor Mohawk combined with mechanoinduction may facilitate the tenogenic differentiation capacity of teno-iPSCs in horse.

Tailoring supramolecular guest-host hydrogel properties with covalent double networks

Claudia Loebe¹, Amal Ayoub², Jonathan H. Galarraga¹, Olga Kossover², Haneen Simaan-Yameen², Dror Seliktar² and Jason A. Burdick¹.

¹University of Pennsylvania, Dept. of Bioengineering, United States, ²Technion-Israel, Institute of Technology, Israel.

Statement of Purpose: Supramolecular chemistry has enabled the design of tunable biomaterials that are potentially injectable and that mimic the dynamic nature of the extracellular matrix¹. However, the noncovalent nature of supramolecular bonds renders them inherently weak, limiting their applicability to many biomedical applications. To address this, we formulated double network (DN) hydrogels through a combination of supramolecular guest-host (GH) hyaluronic acid (HA) assemblies and covalently crosslinked PEGylated fibrinogen and tested properties such as mechanics and cell encapsulation towards their use in tissue engineering.

Methods: HA was modified with β -cyclodextrin (CD-HA) or adamantane (Ad-HA) and mixed to form GH hydrogels² (Fig. 1A). DN hydrogels were formed with the addition of acrylate-PEG (10 kDa) modified fibrinogen (8 mg/mL) and PEG-diacrylate (PEG-DA, 10 kDa) into the GH materials and crosslinking with ultraviolet (UV) light³ (Fig. 1B). Mechanical analysis was performed in compression (DMA), by tensile testing (Instron), and with oscillatory rheology. The viability of encapsulated mesenchymal stem cells (MSCs) was investigated in DN hydrogels through Live/Dead staining.

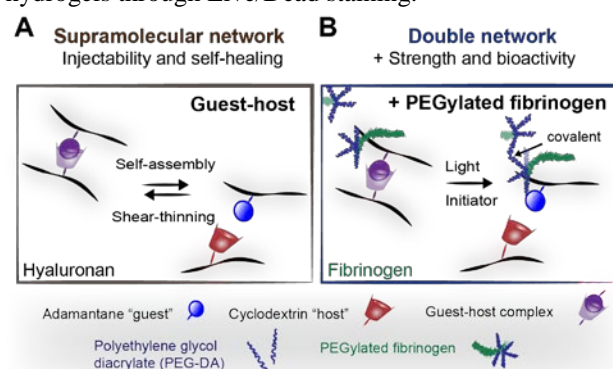


Figure 1. Schematic of hydrogels from guest-host (A, interaction of Ad/CD) and combined guest-host and covalent (B, acrylate photopolymerization) networks.

Results: DN hydrogels were formed through the mixture of supramolecular GH networks with covalently crosslinked networks (Fig. 1) and the concentration of the GH component, as well as the amount of PEG-DA were altered to tune the material properties. Fibrinogen was included to impart enzymatic degradation and cell adhesion to the DN system. The networks were initially soft and injectable (not shown), enabled by the rapid self-healing of the GH bonds, but their compressive moduli then increased after photopolymerization to magnitudes based on PEG-DA concentration (Fig. 2A).

Increased DN compressive moduli were coincident with improved failure stresses and increased toughness (Fig. 2B,C). While the GH concentration had little influence

over the compressive moduli across groups (Fig. 2A), an increase in the GH concentration resulted in more viscous behavior of the DN hydrogels as indicated by the linear increase of the loss tangent ($\tan(\delta)$), Fig. 2D). PEG-DA levels also decreased $\tan(\delta)$ for a given GH concentration. High encapsulated MSC viability was observed for DN hydrogels at 72 hours across all groups (>88%, Fig. 2E).

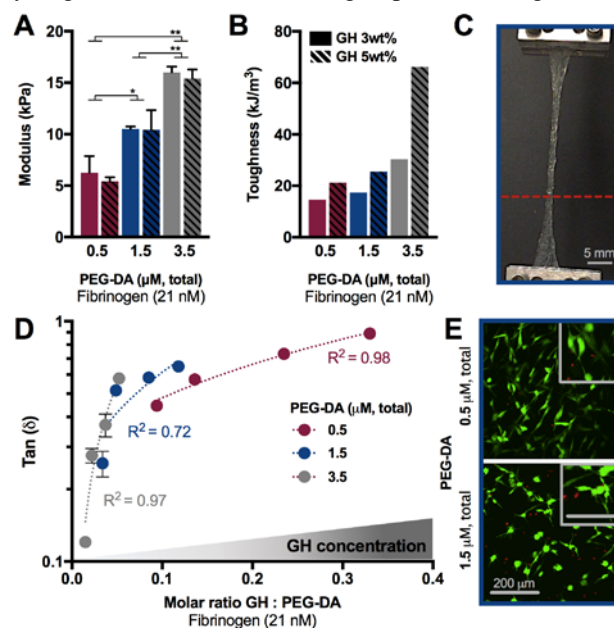


Figure 2. DN hydrogel compressive modulus ($n = 3$, mean \pm SD, $*p \leq 0.05$, $**p \leq 0.01$) (A) and toughness (B) with varied PEG-DA and GH content. Image of DN network (GH 5wt%, PEG-DA 1.5 μ M) during loading with the starting position of top grip indicated with dotted line (C). Loss tangent ($\tan(\delta)$) across variable hydrogel formulations ($n = 3$, mean \pm SD) (D). MSC viability within DN hydrogels (GH 5wt%, 72 hours) (E).

Conclusions: The combination of supramolecular and covalent chemistries enabled the formation of DN hydrogels with tunable properties, including injectability (reversible GH network) and enhanced moduli and toughness through network entanglement (covalent PEGylated fibrinogen network). The inclusion of HA and fibrinogen provide bioactive cues towards stem cell differentiation as well as enzymatic degradations. Moreover, conserving the supramolecular interaction of the GH network holds promise as means to customize DN hydrogels towards repair of visco-elastic tissues. Ongoing work is to better understand these biological interactions and utility for tissue repair.

References: ¹(Webber MJ. Nat. Mater. 2015;15:13-26.)
²(Rodell CB. Biomacromolecules. 2013;14, 4125-4134.)
³(Dikovski D. Biomaterials. 2006;8:1496-1506.)

Hyaluronic Acid Modification Alters CD44 Binding in Soluble and Hydrogel Forms

Mi Y. Kwon¹, Chao Wang², Lin Han², Robert L. Mauck^{1,3}, Jason A. Burdick¹

¹Departments of Bioengineering and ³Orthopaedic Surgery, University of Pennsylvania

²School of Biomedical Engineering, Drexel University, Philadelphia, PA

Statement of Purpose: Hyaluronic acid (HA) is a linear polysaccharide of alternating D-glucuronic acid and N-acetyl-D-glucosamine that is native to numerous tissues and interacts with cells via cell-surface receptors, primarily CD44¹. HA has been extensively studied as a modified macromer for use in the design of glycomaterials, such as hydrogels and macroporous scaffolds², including for chondrogenesis of mesenchymal stem cells (MSCs)³. However, the effect of HA modification on CD44 binding has not been quantitatively explored. To address this, we investigated how the modification level of norbornene-modified HA (NorHA) alters CD44 binding in both soluble and hydrogel forms.

Methods: Cells (hMSCs, Lonza) were stained with a CD44 antibody (Biolegend, clone IM7) to verify cell-surface CD44 presentation through imaging and flow cytometry. NorHA was synthesized through the reaction of HA tert-butyl ammonium salt with 5-norbornene-2-methylamine; NorHA of different modifications was produced, as verified by ¹H NMR. Dextran (Dex) and PEG were used as controls. For cell-binding studies, hMSCs were blocked with 10 µg/mL unmodified HA for 30 minutes on ice, washed, and treated with 100 µg/mL FITC-tagged polymer for 30 minutes on ice, washed, and analyzed for bound FITC signal. For adhesion force analysis, atomic force microscopy (AFM) was performed on mechanics-matched (DMA) hydrogels using polystyrene beads conjugated with human CD44. The max adhesion force was measured as the greatest change from baseline of the retraction curve after indentation.

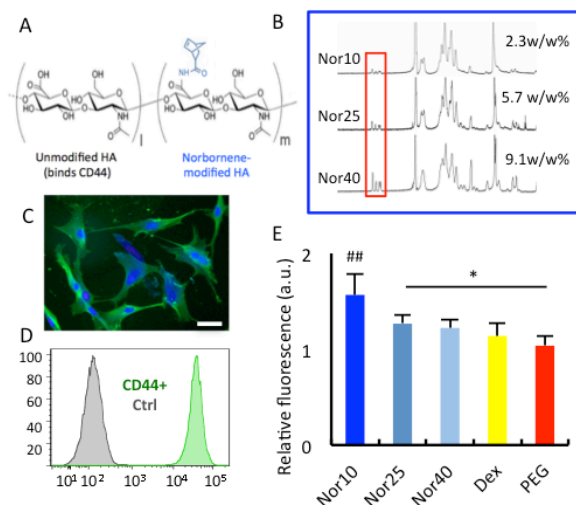


Figure 1. Norbornene modification of HA quantified by ¹H NMR (A,B). CD44+ human MSCs in 2D (C, scale bar = 100 µm) and 3D (D, flow). 2D competitive binding of NorHA-FITC to hMSCs quantified as fluorescence relative to autofluorescence control (E). **p*<0.05, ##*p*<0.01 to all groups.

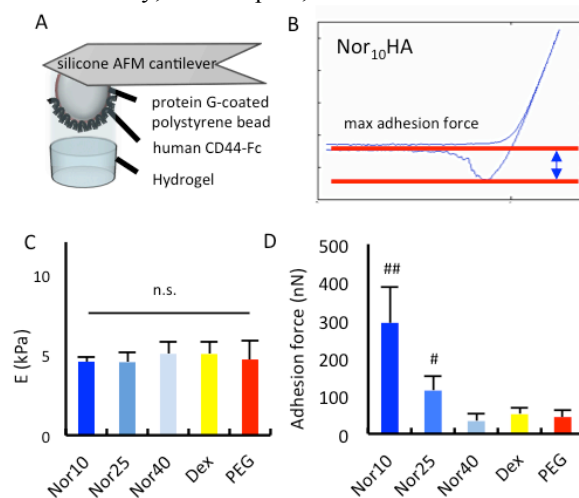


Figure 2. AFM to probe CD44-HA adhesion forces (A) and example adhesion force curve (B). Mean bulk elastic moduli of hydrogels (C). Adhesion forces of CD44-hydrogel interactions (D). #*p*<0.05, ##*p*<0.01 to all groups.

Results: HA modification with norbornene yielded macromers with 10, 25, and 40% modification (indicated as Nor10, Nor25, and Nor40), as measured by ¹H NMR (Fig. 1B). The mass contribution of norbornene was accounted for in all studies (Fig. 1B). hMSCs showed robust CD44 cell-surface expression, illustrating potential to bind HA (Fig. 1B,C). Studies of NorHA competitive binding to hMSCs plated in 2D showed decreased binding of highly modified (Nor25, Nor40) macromers compared to Nor10, indicating a lower avidity to CD44 relative to unmodified HA. Dextran and PEG controls showed low binding.

To investigate the influence of HA modification on CD44-HA adhesion to HA hydrogels, AFM was performed with custom bead tips (Fig. 2A,B). Different macromer-crosslinker ratios were used to yield gels with different modification/material but matched mechanics (shown: elastic modulus, Fig. 2C). Higher-mod gels exhibited lower adhesion forces compared to low-mod (Fig. 2D). Thus, CD44 avidity to modified HA depends on the extent of HA modification.

Conclusions: HA interaction with hMSCs is influenced by the extent of its modification, where increased norbornene modification (here, up to 40% mod) shows a downward trend in binding and adhesion force. This work suggests that the modification of polysaccharides is important to consider in their biological activity when processed as biomaterials. Ongoing work includes considerations of modification site selection and the influence of modification on encapsulated cell behavior.

References: 1. Aruffo A. Cell. 1990; 61:1303-1313. 2. Burdick JA, Prestwich GD. Adv Mater. 2011; 23:H41-H56. 3. Kim IL. Biomaterials. 2011; 32:8771-8782.

Combinatorial hydrogels with biochemical gradients for probing cell-ECM interactions

Sebastián L. Vega¹, John Durel², Michelle Kwon¹, Robert L. Mauck^{1,3}, Jason A. Burdick¹

¹Department of Bioengineering, University of Pennsylvania, Philadelphia, PA

²Department of Biomedical Engineering, University of Virginia, Charlottesville, VA

³Department of Orthopaedic Surgery, Perelman School of Medicine, University of Pennsylvania

Abstract

Due to the multifactorial nature of the stem cell niche and its impact on cell behavior, there is a growing appreciation of high-throughput systems for evaluating the cooperative influence of multiple parameters on cell function. Here, light-mediated thiol-norbornene chemistry is used to create hyaluronic acid hydrogels with spatially continuous gradients of multiple biochemical signals. To validate the utility of this platform as a screening tool, mesenchymal stem cells (MSCs) were encapsulated within hydrogels featuring orthogonal concentration gradients of peptides that mimic cell-cell (HAV) and adhesive cell-ECM (RGD) signals present during mesenchymal development. Fluorescence-imaging based analysis of MSCs revealed HAV/RGD combinations that induce the expression of early (1-week) chondrogenic markers within combinatorial hydrogels and long-term (8-week) formation of cartilage-specific matrix within discrete hydrogels. The versatility of this platform is further demonstrated by evaluating how HAV and RGD regulate MSC mechanosensing across a physiological range of ECM stiffness. Preliminary findings show that the mode in which HAV regulates nuclear YAP/TAZ localization of MSCs is largely dependent upon HAV concentration and underlying substrate stiffness. Together, these findings present a novel combinatorial hydrogel system to probe the effects of multiple parameters on cell behavior, with applications ranging from regenerative medicine to mechanobiology.

Association between lateral patellar osteoarthritis and knee morphology and alignment in young adults

Sara Weintraub BA; Ronnie Sebro MD, PhD

Introduction: Osteoarthritis is a debilitating chronic disease associated with high health care costs and estimated to become the fourth leading cause of disability by 2020 in today's aging population.[1] It is a progressive rheumatic disease, starting with cartilage edema/fissuring and progressing to full-thickness cartilage loss with bone-on-bone contact and subchondral edema at the end-stages.[2] Identifying risk factors for osteoarthritis may lead to earlier recognition of the disease when cartilage may still have regenerative capacity.[2] The knee is commonly affected and abnormalities in the morphology of the trochlea have been associated with increased risk for patellar lateral subluxation and abnormal articulation with the lateral facet of the patella.[3-10] Similarly, abnormalities in the position of the patella and relative malalignment of the quadriceps tendon insertion onto the patella and patella tendon insertion onto the tibial tubercle have been associated with patellar maltracking.[4,7] Anecdotally, there are individuals who present with different patterns of osteoarthritis/chondrosis (OAC) of the patellofemoral joint: involving the medial patellofemoral joint, involving the central patellofemoral joint or involving the lateral patellofemoral joint. It is unknown whether lateral patellofemoral compartment OAC is influenced by patellar and trochlear morphology or the alignment of the patella. The hypothesis of the present study was that the patellar and trochlear morphology are associated with OAC of the lateral patellofemoral compartment.

Methods: Magnetic resonance imaging (MRI) images of 183 subjects (81 cases, 102 controls) aged 21–35 years of age were evaluated. Quantitative measurements of patella and trochlea morphology and patellar alignment were obtained. Axial and sagittal MRI images were reviewed to grade the severity of focal cartilage defects along the lateral facet of the patella. Controls had knees without any abnormalities and were compared to cases with mild and severe lateral patellar OAC. Multivariable logistic regression was used to assess associations between measurements and lateral patellar OAC adjusting for body mass index.

Results: Cases were more likely to have higher Insall–Salvati ratios (OR=350; $p<0.001$), shorter ratios of the medial to lateral facets of the patella (OR=1.63×10⁻³; $p<0.001$), a shallower (angle closer to 180°) median eminence of the patella (OR=1.063; $p=0.009$), decreased trochlear cartilage overlap with the patellar cartilage (OR=0.086; $p=0.023$), and a less angulated lateral patellofemoral angle (OR=0.903; $p=0.028$), compared to controls. Cases were also more likely to have patellar tendinosis (OR=5.265; $p=0.045$) and edema in the superolateral aspect of Hoffa's fat pad (OR=9.872; $p<0.001$).

Conclusion: Patellar and trochlear morphology and patellar alignment are associated with lateral patellofemoral compartment OAC in young adults. Our results may help orthopedists identify patients who would benefit from trochleoplasties and patellar re-alignment procedures aimed at recreating normal knee anatomy.

References

1. Woolf, Anthony D., Bruce Pfleger. "Burden of major musculoskeletal conditions." *Bulletin of the World Health Organization* 81.9 (2003): 646-656.
2. Madry, H., et al. "Early osteoarthritis of the knee." *Knee Surg Sports Traumatol Arthrosc* 24.6 (2016): 1753-62.
3. Ali, Syed A., Robert Helmer, Michael R. Terk. "Analysis of the patellofemoral region on MRI: association of abnormal trochlear morphology with severe cartilage defects." *American Journal of Roentgenology* 194.3 (2010): 721-27.
4. Diederichs, Gerd, Ahi S. Issever, and Sven Scheffler. "MR Imaging of Patellar Instability: Injury Patterns and Assessment of Risk Factors 1." *Radiographics* 30.4 (2010): 961-981.
5. Grelsamer, Ronald P., Jason Saleh, and James Gladstone. "Congruous versus incongruous patellar tilt: a preliminary study." *Bulletin of the NYU hospital for joint diseases* 70.4 (2012): 232.
6. Guilbert, S., et al. "Axial MRI index of patellar engagement: a new method to assess patellar instability." *Orthopaedics & Traumatology: Surgery & Research* 99.8 (2013): S399-S405.
7. Monk, A. P., et al. "The patho-anatomy of patellofemoral subluxation." *J Bone Joint Surg Br* 93.10 (2011): 1341-1347.
8. Noehren, Brian, Stephan Duncan, Christian Lattermann. "Radiographic parameters associated with lateral patella degeneration in young patients." *Knee Surgery, Sports Traumatology, Arthroscopy* 20.12 (2012): 2385-90.
9. Perrild, Claus, Niels Hejgaard, and Arne Rosenklint. "Chondromalacia patellae: a radiographic study of the femoropatellar joint." *Acta Orthopaedica Scandinavica* 53.1 (1982): 131-4.
10. Fucentese, Sandro F., et al. "The patella morphology in trochlear dysplasia—a comparative MRI study." *The knee* 13.2 (2006): 145-50.